Simulating the lattice thermal conductivity of iron-bearing bridgmanite with implications on core-mantle boundary heat flux

Benjamin John Todd

Submitted in accordance with the requirements for the degree of
Doctor of Philosophy

The University of Leeds
School of Earth and Environment

December 2019

This candidate confirms that the work submitted is his own and that appropriate credit has been given where reference has been made to the work of others.

Acknowledgements

First and foremost, I must thank my team of supervisors for their guidance and willingness to meet with me every week. I would not have completed this thesis in absence of their generosity with time and patience. Stephen and Andrew kept me on track when my ambition and motivation waned, and I doubt I would be writing these acknowledgements were my mentors anyone else. I am very grateful to Jon also, whose insight we called into meetings when the path (or paperwork) was unclear. I hope the experience of putting this thesis together was as valuable for you all as it was for me, and at the very least we can add a fancy green book to our shelves!

I would like to thank my examiners Chris Davies and Lidunka Vočadlo for giving me a somewhat enjoyable viva experience. The big old list of corrections was less enjoyable, but the thesis is better for them. I am grateful that you took such a keen interest in my work, and allowed me to be an expert, even if just for a day! A final thanks to Chris for dealing with my response to the corrections so close to ~~Christmas~~ AGU. You'll be on the nice list for sure!

In addition to my academic and pastoral support, I would like to thank Fiona Gill for her role as a postgraduate research tutor for wellbeing within the department. We met exactly once, and that was all I needed, to be told that sometimes academia sucks (my words, not hers), but to be assured that everyone suffers through it at some point and help is out there.

A large amount of this thesis was written on my laptop, for which I am very grateful to David Appleyard. He helped me set up and maintain hardware and software, and never kept me waiting.

I would like to give a special thanks to Maeve, who was extremely helpful in providing her expertise to plot Figures 1.6 and 1.7.

My past and present office buddies from 8.152 derserve a shoutout, for providing a proper pleasant environment to be a PhD student. Where else am I going to get the opportunity to sample such a wide array of donated sweets and biscuits? Look after my spider plants when I am gone.

I started this journey with Ruth and Tom, and although I am finishing it a fair bit later, I am grateful for the inspiration to finish, for showing me there is life at the end of the PhD tunnel! Thanks to Ruth for enabling the exploitation of free Cafe Nero drinks, and the odd complete loyalty stamp card she donated

when I couldn't take advantage of the O2 priority offer. It's the little things that count. I would like to extend this section to include Huw and Ruth (Tom's Ruth not Ruth Ruth), who altogether made AGU '17 and the subsequent excursions so memorable. I couldn't have asked for better company than y'all.

My parents have always been supportive of me, no matter what the future looked like. I may not have been able to explain it very well, but they always took an interest in my work. I couldn't ask for you to have done any more, and wouldn't trade you for anyone else. Thank you mum and dad (for the food parcels...).

Finally, I must thank Claire for sticking with me through the last few months of crunch time. It hasn't always been easy for you to be around me, and I am sorry for the times I was difficult. I would recommend Claire as moral support for anyone trying to finish a thesis, her editorial skills are second to none and she has a keen eye for improving figures and data tables. Without you I would likely have not finished this work in the current decade, or without a few all-nighters, the value of which is hard to quantify. Cheers bev.

Do it!
Just do it!

Don't let your dreams be dreams.
Yesterday you said tomorrow, so just do it!
Make your dreams come true!
Just do it!

Some people dream of success,
while you're gonna wake up,
and work hard at it!
Nothing is impossible!

You should get to the point,
where anyone else would quit,
and you're not going to stop there.
No, what are you waiting for?

Do it!
Just do it!
Yes you can!
Just do it!

If you're tired of starting over,
stop
giving
up.

Shia LeBeouf

Abstract

In this thesis, I calculate the thermal conductivity of bridgmanite across a range of lower mantle conditions, with particular focus on the core-mantle boundary (CMB). Thermal conductivity of the lowermost mantle has direct implications on the heat flux from the core. Heat flux, and its lateral variations, control dynamic processes on both sides of the CMB, affecting the core geodynamo, the mantle convective cycle, and plate tectonics at the surface.

Thermal conductivity is difficult to determine at the high pressures and temperatures of the CMB using experimental methods, but computational approaches are able to reproduce these physical conditions. The thermal conductivity of bridgmanite has previously been modelled under limited conditions, but here, I model the full range of CMB conditions including temperatures from 1000–5000 K, and the effects of adding Fe^{2+} impurities (i.e., the full suite of $MgSiO_3$ to $FeSiO_3$-endmember composition).

I compare two different molecular dynamic approaches to determine thermal conductivity: the direct method and the Green-Kubo method, previously not compared in application to bridgmanite at CMB conditions. In atomic-scale simulations, finite system sizes can misrepresent the properties of the bulk material, leading to inaccurate estimates of thermal conductivity in the case of this study. Finite-size effects in the Green-Kubo method are easily addressed, and the Green-Kubo results can then be used to evaluate finite-size effects in direct method simulations. I present a comprehensive analysis of finite-size effects at 1000 K and 4000 K, and 136 GPa, identifying where simulations from existing literature may be incorrect. I also suggest minimum direct method system sizes (2×2 at 4000 K, lengths of 8–24 unit cells) for computing the thermal conductivity of bridgmanite at the CMB, which could be implemented in density functional theory calculations. It is possible to use the direct method to calculate thermal conductivity at lower mantle conditions, but care must be taken to avoid finite-size effects. I conclude that accurate results are more easily obtained using the Green-Kubo method.

Using the Green-Kubo method, I investigate the effects of iron impurities across a wide range of temperatures (1000–5000 K) at a CMB pressure of 136 GPa. At a CMB pressure and temperature (4000 K), I calculate lattice thermal conductivity to be 7.07 ± 0.06 $Wm^{-1}K^{-1}$ for bridgmanite, 5.30 ±

0.05 $Wm^{-1}K^{-1}$ for the $FeSiO_3$ endmember, and 5.46 ± 0.05 $Wm^{-1}K^{-1}$ for the 50% (Mg,Fe)SiO_3 solid solution. I find that adding impurities (introducing phonon-defect scattering) causes conductivity to decrease, but the rate of the decrease decays with impurity concentration. The conductivity reduction due to temperature (increased phonon-phonon scattering) is more significant than the conductivity reduction due to impurities. I identify saturation in thermal conductivity as phonon-phonon and defect scattering increase, where the relative significance of these scattering mechanisms determines the reduction in conductivity as a function of temperature and composition.

I combine the temperature and compositional-dependence of thermal conductivity to create a new combined model. I use this model with a simple representation of the large-scale structure of the lower mantle to investigate CMB heat flux. The results from thermochemical LLSVP models show that in order to reproduce LLSVP shear velocity anomaly and heat flux across the CMB, the values of lateral thermal boundary layer temperature range and LLSVP Fe content range from 100 K and 10% Fe, to 1000 K and 4% Fe. For simplified models of large low shear velocity provinces (LLSVPs), where the seismic anomaly is caused by lateral variation in mantle temperature, I find larger lateral variation in CMB heat flux than for models where the equivalent seismic anomaly is caused by lateral variations in the Fe^{2+} content. However, absolute values of the integrated CMB heat flux and its variability depend on the temperature at the CMB as well as the origin of LLSVPs, and will be sensitive to other phases and impurities found in the lower mantle.

It is only by investigating the effect of finite system size on atomic-scale modelling that it is possible to obtain reliable conductivity estimates. By determining a comprehensive suite of thermal conductivity values across a range of temperature and composition, I produce a new combined model and show how this can be used to inform on dynamic processes both sides of the CMB.

Contents

List of Figures

List of Tables

Nomenclature

List of acronyms

ACF	**A**uto-**c**orrelation **f**unction
bdg	**b**ri**dg**manite
BPT	**B**allistic **p**honon **t**ransport
CMB	**C**ore-**m**antle **b**oundary
CSA	**C**ross-**s**ectional **a**rea
DAC	**D**iamond **a**nvil **c**el
DFT	**D**ensity **F**unctional **T**heory
DM	**D**irect **M**ethod
EMD	**E**quilibrium **M**olecular **D**ynamics
FSE	**F**inite-**s**ize **e**ffects
GK	**G**reen-**K**ubo
LAMMPS	**L**arge-scale **A**tomic/**M**olecular **M**assively **P**arallel **S**imulator
LD	**L**attice **D**ynamics
LEMA	**L**eeds **E**arth **M**odelling **A**pparatus
LLSVP	**L**arge, **l**ow-**s**hear-**v**elocity **p**rovince
MD	**M**olecular **D**ynamics
MFP	**M**ean **f**ree **p**ath
NEMD	**N**on-**e**quilibrium **M**olecular **D**ynamics
NPT	Molecular dynamics simulation at constant pressure and temperature

NVE	Molecular dynamics calculation at constant volume and energy
NVT	Molecular dynamics calculation at constant volume and temperature
ppv	**p**ost-**p**ero**v**skite
pv	**p**ero**v**skite
TBL	**T**hermal **b**oundary **l**ayer
UC	**U**nit **C**ells
ULVZ	**U**ltra **l**ow **v**elocity **z**one

List of symbols

α	Thermal diffusivity
$\bar{M}$	Mean atomic mass
χ	Measure of resistance to the effects of impurity scattering
ΔT_{LM}	Range of lateral variation in lower mantle temperature
δ	TBL thickness
κ	Thermal conductivity
κ_V	Voigt average of conductivity
κ_∞	Conductivity of bulk material
κ_b	Phonon-boundary scattering effect
κ_d	Phonon-defect scattering effect
κ_{ph}	Phonon-phonon scattering effect
κ_{SS}	Thermal conductivity of the solid solution
∇T	Temperature gradient
ω_0	Phonon frequency at which phonon-phonon scattering and phonon-defect scattering contributions to the MFP are equal
ω_D	Debye frequency

ρ	Density
σ	Standard deviation
τ	Phonon relaxation time
B	Thermal expansion coefficient
b_{ij}	Pre-exponential repulsive parameter for a pair of atoms
C_1	Scaling factor between relaxation time and phonon frequency
C_v	Volumetric heat capacity
C_v	Volumetric isochoric heat capacity
C_{Fe}	Iron content
c_{ig}	van der Waals parameter
J	Heat flux through a cross-sectional area
$K.E.$	Kinetic energy
k_B	Botlzmann constant
k_x, k_y, k_z	Cartesian components of the phonon wave vectors
L	Cell length
l	Phonon mean free path
L_z	Length of the simulation cell in the z-direction
m	Mass
N	Number of atoms
q	Heat flux
$q*$	Lateral variation in heat flux
q_i	Local heat flux
q_i, q_j	Atomic charges
Q_{CMB}	Core-mantle boundary heat flux

R	Interatomic distance
r_{CMB}	Core-mantle boundary radius
t	Correlation length
T_0	Temperature associated with ω_0
T_{CMB}	Core-mantle boundary temperature
T_{LM}	Lower mantle temperature
U	Buckingham interatomic potential
V	Simulation cell volume
v	Average phonon velocity
v	Velocity
V_s	Mean shear wave velocity
g	Acceleration due to gravity
H	Radiogenic heat production per unit mass
Ra	Rayleigh number

Chapter 1

Thermal conductivity and the Earth's interior

Heat flux across the core-mantle boundary is a crucial component of the Earth's energy budget and affects many aspects of the planet's dynamic processes. On the mantle side, the ratio of internal heating to heating from the core controls how mantle dynamics are driven (e.g., *Lay et al.*, 2008), the significance of plume upwellings compared with slab downwellings (e.g., *Garnero and McNamara*, 2008), and the effect this has on plate tectonics. The amount of heat that leaves the core through the mantle controls the vigour of core convection, and thus the power available to the geodynamo and the behaviour of the Earth's magnetic field (e.g., *Gubbins et al.*, 2007).

Core-mantle boundary heat flux is directly proportional to lower mantle thermal conductivity, a parameter with complex dependence on temperature and composition. Despite this, we know little about the thermal properties of lower mantle materials. Experiments can measure the conductivity of material, but not at the high pressure/temperature conditions found in the deep Earth. Computer simulations allow materials and their conductivities to be modelled on an atomic-scale, but appropriate simulation parameters must be determined in

order to obtain realistic results.

In this thesis, I investigate the sensitivity of different methods of atomic-scale simulation to: (1) determine the thermal conductivity of bridgmanite, the dominant mineral in the lower mantle; (2) investigate the effect of iron content on bridgmanite conductivity; and (3) explore the ways in which core-mantle boundary heat flux is influenced by conductivity and large low shear velocity province (LLSVP) structures. In Chapter 1, I provide the context for this work by introducing the structure of the Earth and outlining the key heat transfer processes that will be discussed throughout this thesis. I also review the existing state of knowledge around the conductivity of bridgmanite, considering computational and experimental studies.

1.1 Structure of the Earth

The Earth is comprised of several layers across its radius of 6371 km. Moving from the surface toward the centre of the Earth, the properties of these layers change dramatically. Through seismic studies, we know that the Earth has a solid inner core, a liquid outer core, and a solid mantle (e.g., *Fowler*, 1990). The crust is enriched in silicon, whilst the mantle is Si-depleted. Within the mantle, it is expected that there is both 4-fold coordinated Si in the upper mantle and this transitions to a high-pressure, high density 6-fold coordinated Si in the lower mantle (*Knittle and Jeanloz*, 1989; *Hu et al.*, 2017).

In this thesis, I focus on the lower mantle, particularly the region close to the core (the core-mantle boundary, CMB). Events in the lower mantle influence (and are influenced by) the upper mantle and lithosphere above, and the core below (Fig. 1.1). Heat transport throughout the Earth is influenced by thermal conductivity, which in turn affects the dynamics of the system, the surface expression of this being plate tectonics. Heat flow also affects the core geodynamo,

which produces the Earth's magnetic field.

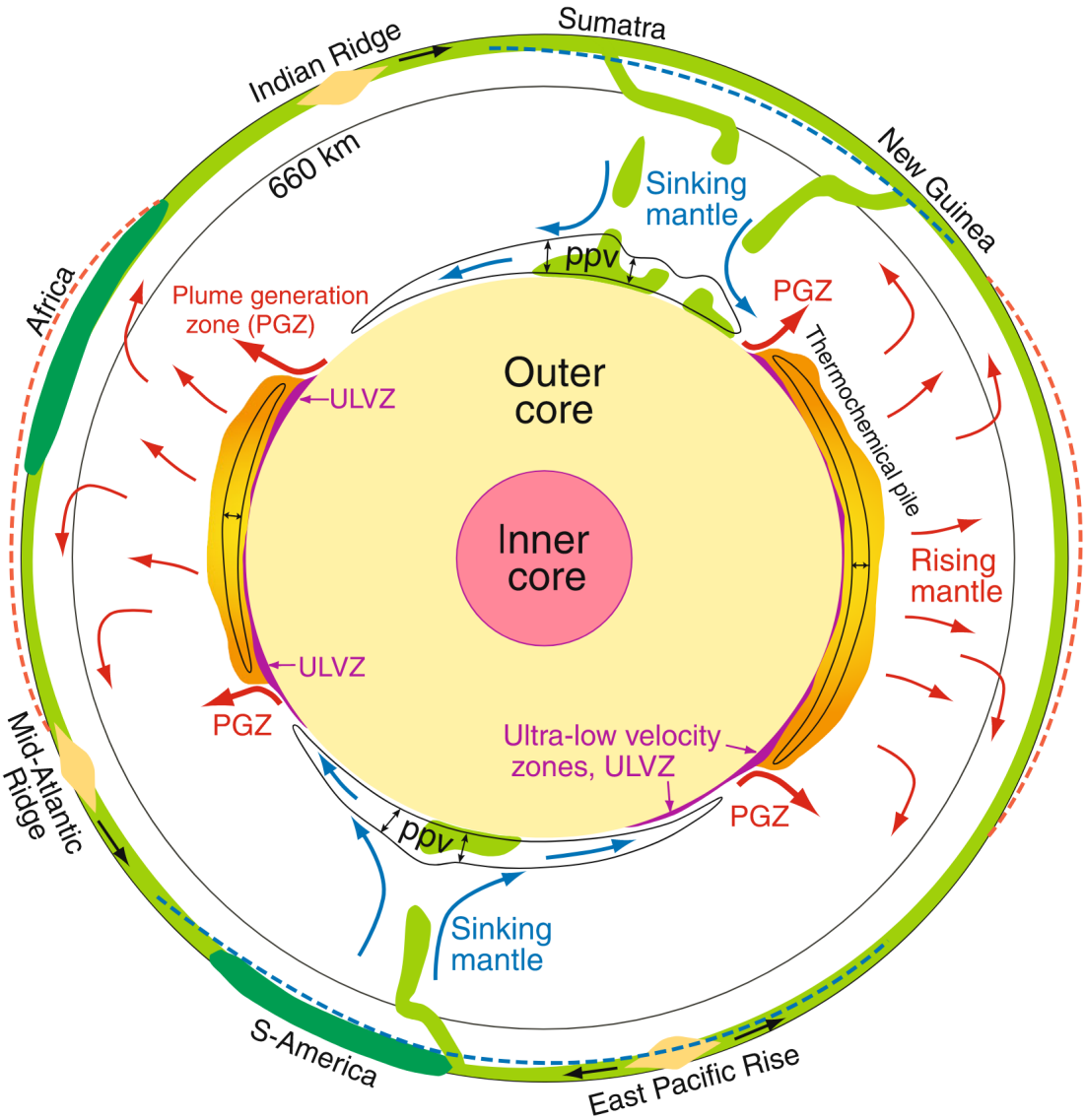

Figure 1.1: Schematic equatorial Earth section, reproduced with permission from *Trønnes* (2009). Not drawn to scale, and some thicknesses are exaggerated.

1.1.1 Lithosphere and mantle transition zone

The crust and upper mantle lie above the transition zone (down to 660 km depth), the bottom of which marks the top of the lower mantle. Although the chemical composition of these regions is similar to that of the lower mantle, the physical conditions and mineral phases are different. Eruptive and subductive behaviour

associated with plate tectonics is perhaps the most obvious consequence of mantle dynamics at the Earth's surface, and generally to humanity.

The "rocky" portion of the Earth (from the surface down to CMB) is largely composed of magnesium silicates and oxides, with a significant amount of iron, aluminium and calcium.

The two main chemical changes from the Earth's surface to the top of the lower mantle are pyroxene to garnet (40% composition), and olivine through wadsleyite to ringwoodite (60%, see Fig. 1.2 *Trønnes*, 2009). The olivine to wadsleyite phase change occurs at 410 km, marking the top of the mantle transition zone. Wadsleyite transitions to ringwoodite through this zone until 660 km, at which point it breaks down into lower mantle bridgmanite and ferropericlase.

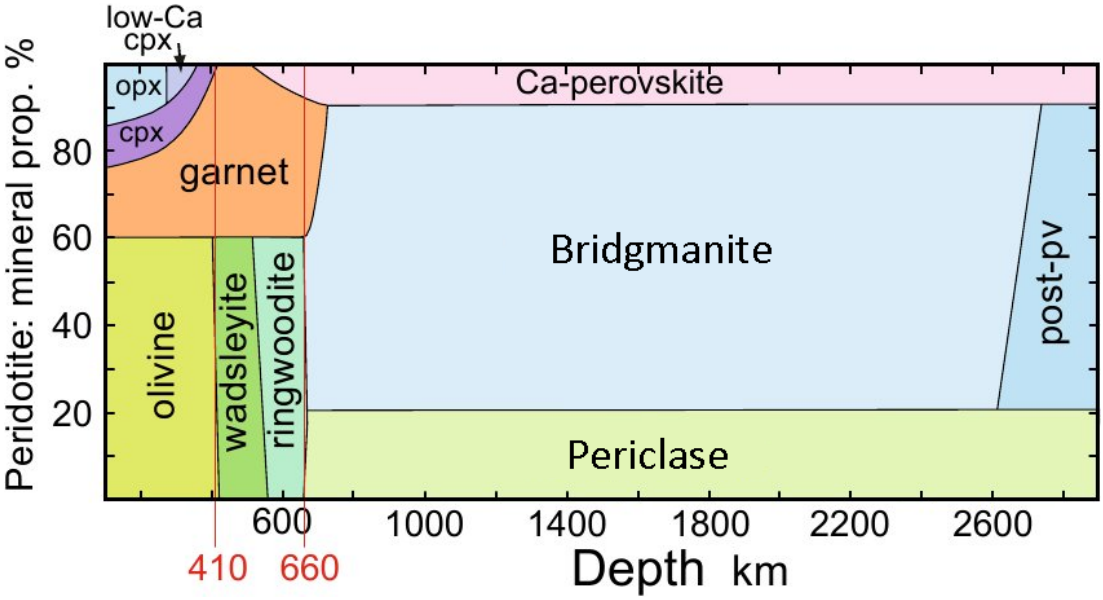

Figure 1.2: Approximate mineral proportions in peridotite (pyrolite) compositions as a function of mantle depth, where peridotite compositions contain ∼70% bridgmanite, ∼20% periclase, and ∼10% Ca-perovskite. Modified with permission from *Trønnes* (2009).

1.1.2 Lower mantle

The lower mantle encompasses the region below the mantle transition zone (660 km deep, ∼1900 K, ∼25 GPa) to the CMB (2900 km deep, ∼4000 K,

136 GPa). The mineral proportion of this region is thought to be ∼70% bridgmanite ($MgSiO_3$, perovskite structured magnesium silicate), ∼20% periclase (MgO, magnesium oxide), and ∼10% calcium silicate ($CaSiO_3$) perovskite (*Lee et al.*, 2004; *Trønnes*, 2009, see Fig. 1.2). Bridgmanite undergoes a pressure-driven phase transition in the lowermost mantle to post-perovskite (*Oganov and Ono*, 2004).

The bridgmanite crystal structure is $MgSiO_3$ perovskite (Fig. 1.3). The crystal lattice can be thought of a regular, repeating pattern of an atomic arrangement with translational symmetry. Bridgmanite and periclase are insulators with the potential for the inclusion of iron impurities (and aluminium in the case of bridgmanite). Ferrous (2+) and ferric (3+) iron enter the bridgmanite structure by replacing magnesium atoms (Fig. 1.3), which have varying electron spin states depending on pressure. The concentration of iron is not partitioned evenly between silicates and oxides, with periclase taking a larger proportion than bridgmanite (*Muir and Brodholt*, 2016). The nature of partitioning changes with composition, where aluminium can enrich Fe^{3+} content in bridgmanite (*McCammon*, 1997), and post-perovskite (the high-pressure phase of bridgmanite; Fig. 1.3) may behave differently to bridgmanite.

Moving from the average 1D structure of the earth, to considering the 3D structure, there are two large-scale features on the CMB. Two large low shear velocity provinces (LLSVPs, see *Garnero and McNamara*, 2008) can be found roughly underneath Africa and the Pacific. They are identified seismically by a ∼3% reduction in shear wave velocity. An associated feature is the ultra-low velocity zones (ULVZs, see *Rost et al.*, 2005), identified around the edges of LLSVPs. These can be observed seismically by a 25% reduction in shear wave velocity, but the reason they exist is unclear. It is suggested they are "thermo-chemical features", hotter and denser than the regular lower mantle (*Garnero and McNamara*, 2008). Increasing temperature and density

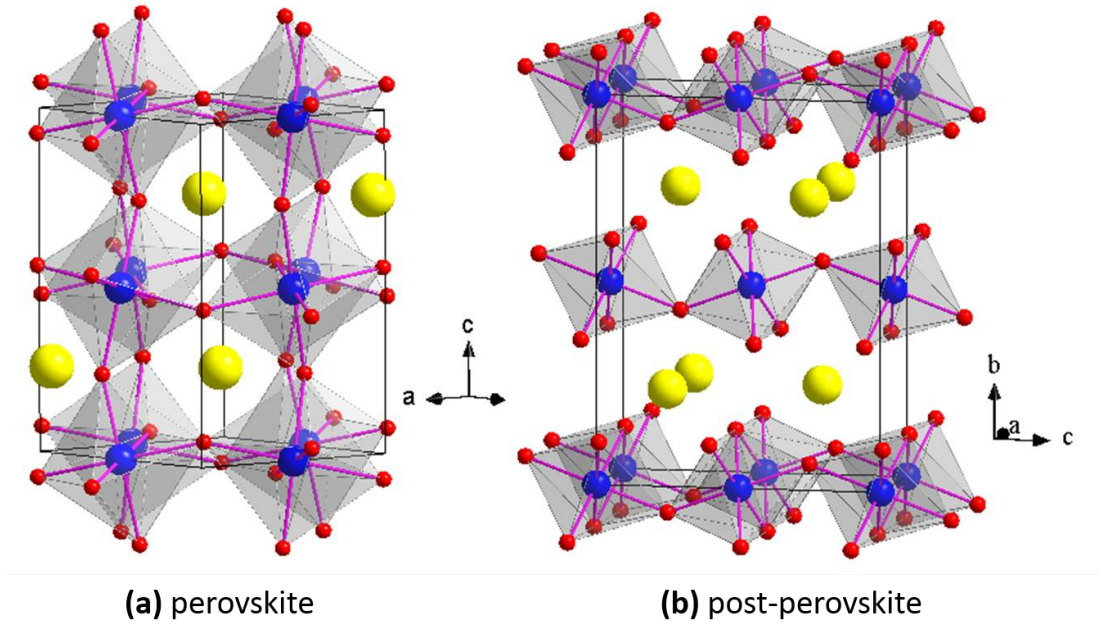

Figure 1.3: Crystal structure of **(a)** perovskite (bridgmanite) and **(b)** post-perovskite, where yellow shows magnesium atoms, red shows oxygen atoms, and the blue shows silicon atoms in the centre of the silicon-oxygen tetrahedra. Reproduced with permission from *Cai et al.* (2016).

tend to reduce seismic velocity, with increased density to offset the additional buoyancy from raised temperature. "Thermo" intuitively refers to the change in temperatures, while "chemical" changes are required to explain density increase. As a result, thermal conductivity will vary within these regions. Adding impurities such as iron would be a possible cause for density increase, such that the conductivity change should be quantified.

It is widely believed that bridgmanite is stable in the lower mantle until the bottom few 100 km, where it undergoes a pressure-driven phase change to post-perovskite (*Murakami et al.*, 2004; *Oganov and Ono*, 2004). In places, close proximity to the CMB might transform post-perovskite back to perovskite structure due to the increased temperature. This "double crossing" of the bridgmanite stability range can be imaged seismically, where lens-like bands of post-perovskite are shown to pinch out laterally (*Lay et al.*, 2006).

Imaging the post-perovskite double crossing and its lateral pinching from

seismic velocity anomalies can be used to make inferences on the mantle temperature structure (Fig. 1.4). At a given depth/pressure, crossing the post-perovskite to bridgmanite transition means an increase in temperature. The centre of a cool downwelling may have the seismic signature of post-perovskite, transitioning to that of bridgmanite as it warms next to the surrounding mantle. The pinching-out of post-perovskite lenses towards the edges of LLSVPs shows a temperature increase, which could be associated with the thermochemical composition of an ULVZ and/or the buoyancy of a mantle plume root.

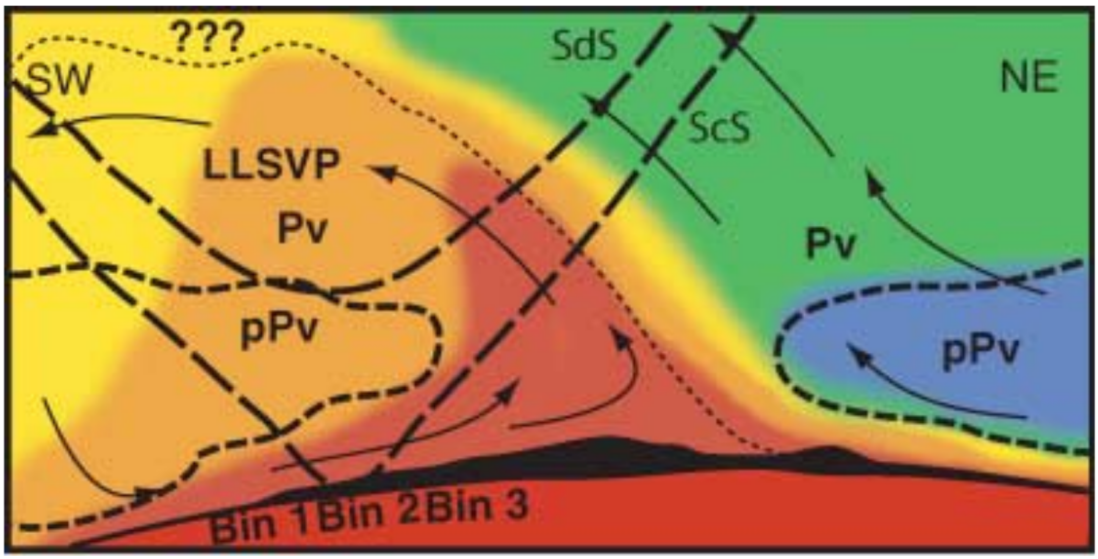

Figure 1.4: Cartoon showing a cross section of the lower mantle with LLSVP region, where the dashed line marks the bridgmanite/post-perovskite phase transition. Colour refers to relative temperature, where red is warmest and blue is coolest. Reproduced with permission from *Lay et al.* (2006).

1.1.3 Inner and outer core

The region below the CMB (starting at 2900 km depth) is the core, comprised of its outer and inner sections. The liquid outer core extends to 5100 km depth, where the pressure-driven transition to solid inner core occurs. The composition of the core is dominated by iron, with various light elements suggested as possible alloying components (e.g., *Allègre et al.*, 1995; *Alfè et al.*, 2007).

Relative to the lower mantle, the outer core is a vigorously convecting system, and the core side of the CMB can be considered to be an isothermal boundary. Heat transfer across the CMB depends on mantle conductivity and temperature. A second issue is possible chemical transfer between core and mantle, where iron from the core would be exchanged with various light mantle elements. Fe-content may increase in the lower mantle with CMB proximity, which in turn could affect conductivity and the temperature profile for CMB heat flux (*Knittle et al.*, 1991).

1.2 Heat transport in the Earth

Within the lower mantle, thermal conductivity influences the rate at which heat is transferred from core cooling towards the surface, and more importantly the mechanisms by which it does so (*Lay et al.*, 2008). High thermal conductivity systems will preferentially transport heat by conduction. Systems will convect where there is too much heat to be transported by conduction alone (i.e., low conductivity conditions).

Observations of plume structures and spatial correlations of high P- and S-wave velocities (see *Garnero and McNamara*, 2008) suggest convective behaviour in the lower mantle. Thermal conductivity is poorly constrained in this region and obtaining a comprehensive depth profile of the conductivity is not a trivial task. Additional difficulties are pressure, temperature, and compositional dependences, including isotopic variation (*Tang and Dong*, 2010; *Dalton et al.*, 2013; *Tang et al.*, 2014) and inclusion of impurities (*Manthilake et al.*, 2011; *Ammann et al.*, 2014; *Ohta et al.*, 2014). Thermal conductivity in the deep Earth influences dynamic processes such as mantle convection and heat loss from the core (*Lay et al.*, 2008). In this section I discuss the prominent thermal conductivity-dependent processes.

1.2.1 Mantle dynamics

Convection in the mantle is dependent on thermal conductivity, and will occur if heat cannot be sufficiently transported by conductive processes. The value of the Rayleigh number (Ra) describes the behaviour of heat flow in a fluid, relative to a critical value for the system (Ra_C). The Rayleigh number for the mantle is estimated to be at least 3×10^6 (bottom heated, *Davies*, 2001). *Schubert et al.* (2001) give a range of realistic values for the mantle Rayleigh number of $1 - 3 \times 10^7$, although indicate that the Rayleigh number could be as high as 10^9. These estimates are much higher than the critical value for the mantle, which is expected to be on the order of 1000 (*Davies*, 2001). *Schubert et al.* (2001) give critical values in a range of 384–1707, depending on the specific boundary conditions and mode of heating. When the Rayleigh number is lower than the critical value, conduction is the dominant process. When the Rayleigh number is greater, the ratio between it and the critical value describes the vigour and style of convection. The Rayleigh number is inversely proportional to thermal conductivity. If thermal conductivity is high, Ra decreases and thus so does $\mathrm{Ra}/\mathrm{Ra}_C$.

The Rayleigh number related to bottom heating (Ra_T) of the mantle from the core can be expressed as

$$\mathrm{Ra}_T = \frac{g\rho_0^2\beta\Delta T_{SA}D^3C_P}{\eta\kappa} \ , \tag{1.1}$$

where g is the acceleration due to gravity, ρ_0 is the reference density, β is the thermal expansion coefficient, ΔT_{SA} is the superadiabatic temperature across the mantle, D is the depth in the mantle, C_P is the specific heat capacity at constant pressure, η is dynamic viscosity, and finally κ is thermal conductivity.

A Rayleigh number can also be calculated considering internal heating (Ra_H)

of the mantle

$$\mathrm{Ra}_H = \frac{g{\rho_0}^2 \beta H D^5}{\eta \alpha \kappa} \ , \tag{1.2}$$

where H is radiogenic heat production per unit mass, and α is the thermal diffusivity. In the mantle, there is a combination of bottom heating (i.e., heat loss from the core) and internal heating (i.e., radiogenic heating). By assuming the existence of a thermal boundary layer, I explicitly consider bottom heating of the mantle later when considering a model of heat flux in the Earth (Chapter 5).

The Rayleigh number is used as a numerical expression of the conditions in the lower mantle, but we also know about the realistic changes in this region of the Earth. In the lower mantle thermal conductivity changes with pressure, temperature, and composition, influencing features on a large scale. For example, *Naliboff and Kellogg* (2006) used numerical models of mantle convection to show size and stability of convective plumes are sensitive to thermal conductivity above the CMB. They showed that increasing the thermal conductivity at depths below 2000 km increased the size and stability of thermal upwellings, whereas decreasing the conductivity in this region has a comparatively small effect on such upwellings.

Dubuffet and Yuen (2000) investigated the effects of temperature ($\kappa_{\mathrm{lat}} \propto T^{-0.3}$, $\kappa_{\mathrm{rad}} \propto T$) and pressure-dependent ($\kappa_{\mathrm{lat}} \propto P$) thermal conductivity (scaling relations originally from *Hofmeister*, 1999) on mantle convection, finding that this reasonable depth-dependent thermal conductivity encouraged heat transport via convective plumes. Compared to a constant conductivity model, vertical heat transfer was concentrated to these "pipe-like" structures, despite the horizontally-averaged heat flow for both systems being around the same value. Variable conductivity, even in one dimension, increased the spatial and temporal stability of convection. Plumes were thicker, had heads of larger surface area, and were hotter, compared to the uniform conductivity mantle model.

Tosi et al. (2013) perform two-dimensional numerical simulations of mantle convection with varying composition, thermal expansivity, and thermal conductivity. The reasonable depth ($\kappa \propto z$) and temperature-dependent ($\kappa \propto T^{-d}$, where $d = 0.3 - 0.6$) conductivity implemented in models leads to a higher bulk mantle temperature, which then inhibits plume buoyancy and their effect on mantle dynamics.

When variable thermal conductivity and expansion are considered together, slabs can be observed to stagnate and move laterally at the transition zone. Changes in mantle behaviour affect the presence of post-perovskite above the CMB, which itself affects the mantle by having a different thermal conductivity to bridgmanite. These outcomes show thermal conductivity is an important property for mantle dynamics simulations to consider, in order to produce Earth-like behaviour.

1.2.2 Heat flow

The most accessible estimate of the Earth's energy is the total heat flow at the surface, with total heat flow estimated at 46 ± 3 TW by *Lay et al.* (2008), and more recently at 47 ± 2 TW by *Davies et al.* (2015). Contributions to the energy budget include: radiogenic heating (20 ± 3 TW); mantle cooling (8–28 TW); and the conduction of heat across the CMB from core cooling (*Lay et al.*, 2008). Conductive heat flow is constrained by thermal conductivity, a model of which is not well constrained for realistic mantle compositions.

Better constraints on thermal conductivity are required to estimate CMB heat flow. This in turn would tell us more about the temperatures either side of the CMB, as well as the presence and nature of the lower mantle thermal boundary layer (TBL). Employing the most commonly used value for lower mantle conductivity, 10 $\mathrm{Wm^{-1}K^{-1}}$, heat flow across the CMB is expected to be

5–13 TW (*Lay et al.*, 2008). Both higher and lower values have been proposed, as discussed in Section 1.6. The wide range of values for CMB heat flux is due to the significant uncertainty in the temperature gradient above the CMB. Even if thermal conductivity was known for all conditions, uncertainty in heat flow values would still arise from constraining the temperature gradient at the CMB.

1.2.3 Geomagnetism

It is possible to use shear wave velocity as a proxy for CMB heat flow (e.g., *Bloxham*, 2000; *Olson and Christensen*, 2002; *Christensen and Olson*, 2003). Considering this, *Gubbins et al.* (2007) showed that variations in mantle temperature gradients above the CMB can influence Earth's geodynamo. The present day magnetic flux patches align with regions of fast shear wave velocity on the CMB. Specifically these patches are found in the east of Canada and Russia, and southwest of South America and Australia. Grouping these patches by lines of longitude, they fall inbetween the African and Pacific LLSVPs. Ignoring compositional effects in the mantle, seismically-fast regions can be assumed to be cold. Colder regions facilitate larger heat flows through steeper temperature gradients from the isothermal CMB (see Equation 1.3).

Gubbins and Bloxham (1985) and *Bloxham and Gubbins* (1985) were some of the first studies to present the idea that regions of downwelling in the core correspond to high shear wave velocities in the lower mantle (i.e., higher than LLSVP regions, see also *Gubbins et al.*, 2003). The mantle surrounding LLSVPs therefore also has higher heat flux than LLSVP regions. Core material flows towards regions of downwelling, which concentrates the magnetic field under regions of high CMB heat flux (i.e., non-LLSVP regions). Alfvén's theorem states how magnetic flux is imagined to be frozen into fluid in the absence of diffusion. Convergence of downwelling core fluid means a similar convergence

and concentration of magnetic flux under regions of high CMB flux.

Gubbins et al. (2007) showed that core dynamics models with heterogeneous (i.e., laterally varying) heat flux conditions at the CMB allow magnetic flux lobe structures to form. These lobe structures can be observed at the surface, and they have been relatively stationary throughout recorded history. This infers that lateral variations in heat flux on the CMB are also relatively stationary, and thus long-lived. Recorded history in this context unfortunately refers to around 400 years of human observations (*Jackson et al.*, 2000). This timescale is about the same as that of core convection overturn, and inferences beyond this become ambiguous (e.g., *Korte et al.*, 2009). While assumptions about the longevity of magnetic flux patches and high heat flow regions seem reasonable, certainty of coupling between the two requires a much longer sample period (i.e., on the order of mantle convection, see *Gubbins*, 2003).

Gubbins et al. (2007) recreated the geomagnetic observation of the aforementioned lobes using a core geodynamo simulation, where the upper boundary (CMB) condition was a laterally varying heat flux. Knowing the thermal conductivity, especially as it changes with temperature, would better constrain mantle boundary conditions used in this and similar core dynamics models (*Ammann et al.*, 2014).

1.3 Defining thermal conductivity

The transfer of thermal energy can occur between an object and its surroundings, two bodies brought into contact, or along a temperature gradient within an object. The possible mechanisms by which this can occur are conduction, convection, and radiation. Conduction is the transfer of heat by atomic vibrations and electron transport in metallic substances (such as in the outer core, e.g., *Pozzo et al.*, 2012). Convection is the transfer of thermal energy via a moving medium, generally in

liquids and gases (but expected in the mantle). Density differences are the driving force for convection, due to the volume change associated with thermal expansion. Radiation refers to the transport of heat by electromagnetic radiation in the form of photons.

Thermal conductivity is a material property, indicative of the ease with which heat is transferred through conduction. Fourier's law relates heat flux (q) through a material to its thermal conductivity (κ), and the temperature gradient (∇T) across the body

$$q = -\kappa \nabla T \ . \tag{1.3}$$

In this thesis, I focus on lattice conduction through the lower mantle, and secondly the convective behaviour therein. The radiative component of thermal conductivity in the mantle is thought to be small (0.54 $\mathrm{Wm^{-1}K^{-1}}$, *Goncharov et al.*, 2008). In the event that radiation contributes significantly to the effective thermal conductivity (10 $\mathrm{Wm^{-1}K^{-1}}$, *Keppler et al.*, 2008), it can simply be added to the lattice component. Although I do not determine the radiative component of thermal conductivity, I discuss results from previous studies that include the radiative component (Section 1.6).

1.3.1 Technical applications considering thermal conductivity

Knowledge of the thermal conductivity of solids is key for a wide range of technological applications, in addition to developing our understanding of natural systems. I suggest that the methods developed in thesis could also be applied to nano-scale engineering problems and material science. While everyday technological applications may not approach CMB conditions of 136 GPa and 4000 K, the atomic-scale behaviour and the effect of impurities remain key questions in thermal conductivity studies.

For known substances thermal conductivity spans about six orders of magnitude, from silica aerogels with 0.005 $Wm^{-1}K^{-1}$ (*Lee et al.*, 1995) to graphene with 5000 $Wm^{-1}K^{-1}$ (*Balandin et al.*, 2008). Conductivity determines whether a material is a conductor or insulator of heat, both of which have many uses, technological or otherwise. Oven gloves introduce an insulating, low conductivity layer between our hands and a hot object which would otherwise cause injury. Vacuum flasks are designed to have a low conductivity construction to keep liquids hot, houses have wall insulation to keep the heat in. While a saucepan may have an insulating rubber handle, it may also have a conductive copper base, allowing it to heat up quickly with an even temperature distribution.

Heat exchangers are found in many systems, where one substance is used to cool or heat another. While the heat transfer is affected by the thermal conductivity of the media in question, the material that separates the two must have high conductivity for the system to be efficient. Domestic examples include central heating system, fridges, and cars. Industrial examples include solar water heating, and power plants, from geothermal to nuclear.

Thermoelectric materials convert waste heat into electricity, thereby improving the efficiency of domestic, automotive, and industrial processes. They are proposed to increase the sustainability of our current electricity base, but suitable materials must have a low thermal conductivity (*Snyder and Toberer*, 2008).

1.4 Mechanisms of thermal conductivity

The transport of heat, rather than the transport of hot material, can be split into three mechanisms which contribute to the overall thermal conductivity of a material. These transport mechanisms can be explained on an atomic level, and in the case of this study within a crystal lattice.

1.4.1 Conductivity by electron motion

Electrical thermal conductivity refers to the transport of heat via free electrons in an atomic structure. Close parallels exist between thermal and electrical conduction. The conduction of thermal energy in metals is predominantly due to the motion and interaction of free electrons. Heat is transferred as electrons move and collide in the lattice. There is no net transport of electrons in order to maintain charge neutrality within the lattice. Lower mantle minerals are insulators, and thus electrical thermal conductivity is of little significance unless very high concentrations of iron minerals exist.

1.4.2 Conductivity by photon emission

Radiative thermal conductivity is the transport of heat via photons, or packets of electromagnetic energy. Any body with a non-absolute zero temperature emits thermal radiation as light, or photons. Radiative thermal conductivity is determined by a material's optical absorptivity, which describes how heat is transferred by electromagnetic radiation. On the atomic scale, electrons in an excited state emit photons when the electron drops back to its ground state. Energy is transferred from one particle to another when this light is scattered or absorbed. The transfer of heat by radiation is limited similarly to the transfer of visible light, with difficulty passing through opaque media. Unlike lattice conductivity at mantle conditions, radiative conductivity increases with temperature (*Hofmeister*, 1999). This relation has been used to assume thermal conductivity could be constant through the lower mantle if radiative processes are significant, where the lattice component decreases at the same rate the radiative component increases (*Tang et al.*, 2014).

1.4.3 Conductivity by lattice vibrations: phonons

Phonons are quantised packets of vibrational energy (*Kittel*, 2005). They are quasiparticles used to describe atomic motions which contribute to lattice thermal conductivity (often referred to as just "conductivity" elsewhere in this thesis) and hence are studied in an area of solid state physics called "lattice dynamics" (*Dove*, 1993). Considering a crystalline arrangement of atoms, there is long-range structure and well-defined bonds between atoms. Much like standing waves on a string, atoms can vibrate in-phase. Phonons can be thought of as patterns of vibration and can be differentiated by wavelength and the relative motions of atoms.

There are two types of phonon, acoustic and optic (*Kittel*, 2005, Fig. 1.5). Both types can be longitudinal or transverse, referring to the motion of atoms relative to the direction of energy propagation. Longitudinal means atoms move only in the direction of motion with no perpendicular displacement. Transverse refers to perpendicular displacement of atoms away from the direction of propagation, with no lateral motion along it. The former is like extention/compression of a spring, the latter a standing wave on a string.

Acoustic phonons are propagated by atoms displaced in-phase from their equilibrium positions, generating forces on their neighbours and thus subsequent displacement. Optic phonons are propagated by out of phase motion of adjacent positive and negatively-charged ions (conserving momentum, the lighter atom moves further). This motion is generated from the electric fields of external electromagnetic radiation, and is typically of a higher energy than its acoustic counterpart.

Similar to photons, phonons also have wave particle duality (i.e., properties of energy and matter). This is useful for explaining how phonon waveforms (as in Fig. 1.5) interact with structural discontinuities and in phonon-phonon collisions,

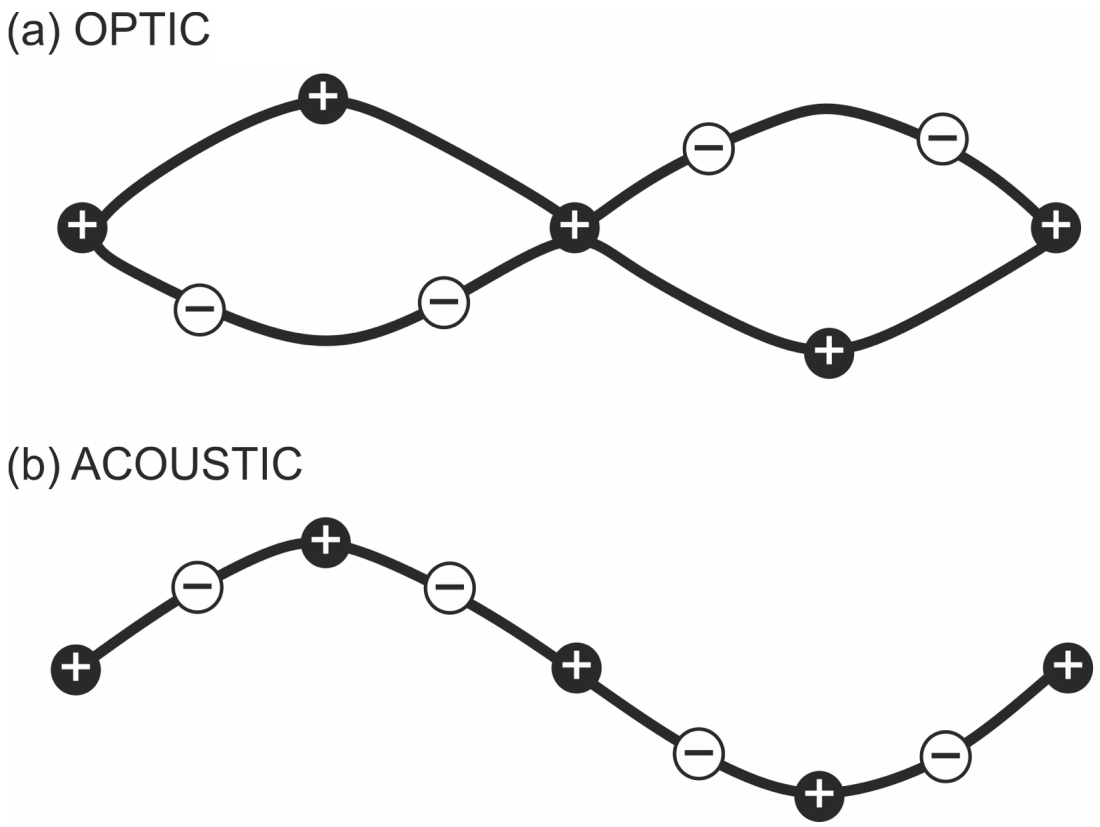

Figure 1.5: Schematic sketches of transverse (a) optic and (b) acoustic phonons in a diatomic linear lattice, where plus and minus symbols refer to ion polarity. Adapted with permission from *Kittel* (2005).

as particles they are able to scatter off of structure and one another (*Kittel*, 2005). A phonon particle is a quantised packet of vibrational energy moving from hot to cold regions, but there is no net motion of atoms within the lattice.

The mean free path (MFP) of a phonon is the average distance it travels before scattering (*Kittel*, 2005). The longer the MFP, the more efficient the heat transport and thus higher the thermal conductivity. There are several different phonon scattering mechanisms, collisions with (1) other phonons in the lattice, (2) boundaries in the material, and (3) defects in atomic structure. In a phonon-phonon scattering event, the wave vector is conserved over the collision. This can sometimes lead to scenarios where two wave vectors pointing in a similar direction create a resultant wave vector in the opposite direction (due to the periodic nature of crystalline materials).

The MFP can be determined via Matthiessen's rule (see *Klemens*, 1959), which states the total thermal resistivity (inverse of conductivity, the lattice component in this case) is equal to the sum of individual resistivities,

$$\frac{1}{\kappa_{\mathrm{lat}}} = \frac{1}{\kappa_{\mathrm{ph}}} + \frac{1}{\kappa_{\mathrm{b}}} + \frac{1}{\kappa_{\mathrm{d}}} \ , \tag{1.4}$$

where κ_{ph}, κ_{b}, and κ_{d} represent phonon, boundary, and defect scattering effects, respectively. The MFP is proportional to conductivity, thus inversely proportional to resistivity. The shorter the phonon path of a scattering mechanism, the more it influences and contributes to, or detracts from, the MFP. This is apparent in Equation 1.4, where the inverse of the smallest number contributes the most to the sum.

Boundary scattering effects are negligible in this study, as the spacing of boundaries in this context depends on the grain size. Crystal grains are significantly larger than any MFPs in the lower mantle, so phonons scatter off each other many times before ever approaching a boundary (i.e., $1/\kappa_{\mathrm{ph}} > 1/\kappa_{\mathrm{b}}$). The effect of defect scattering will be discussed extensively in Chapter 4.

1.5 Factors influencing thermal conductivity

Lattice thermal conductivity can be expressed (e.g., *Schelling et al.*, 2002; *Stackhouse et al.*, 2010) as a simplification of kinetic theory in the form

$$\kappa_{\mathrm{lat}} = \frac{1}{3} C_{\mathrm{v}} v l \ , \tag{1.5}$$

where C_{v} is the volumetric heat capacity, v is the average phonon velocity, and l is the phonon mean free path.

Previous studies have shown that there are many factors that influence lattice

thermal conductivity (κ_{lat}), and these are explored further in Section 1.6. These factors are further complicated by the range of numerical and experimental methods that are used to study thermal conductivity. Despite these complexities, there are three key factors that influence conductivity: temperature, pressure, and composition. In this study, I directly address temperature and composition.

1.5.1 Temperature-dependence

Conductivity increases with the volumetric heat capacity, until the heat capacity saturates at a material's Debye temperature (Fig. 1.6). Lattice conductivity is proportional to the MFP (Equation 1.5), so also increases with temperature up to the Debye limit. Assuming heat capacity (C_{v}) and phonon velocity (v) remain constant above the Debye temperature, conductivity is dependent on the phonon mean free path (l). The MFP decreases above the Debye temperature, corresponding to a decrease in conductivity.

The effect of phonon-phonon scattering increases with temperature past the Debye temperature. Conductivity change is inversely proportional to temperature at this point, decreasing, and eventually saturating (Fig. 1.7), to a minimum value as the MFP reaches its minimum (on the order of atomic spacing). While I observe this saturation effect, there is debate within the community whether phonons actually reach a minimum MFP and therefore a minimum conductivity. Other studies (e.g., *Ghaderi et al.*, 2017; *Zhang et al.*, 2017) suggest that rather than reaching a minimum MFP and therefore saturating, the conductivity instead continues decreasing with increasing temperature (i.e., past those expected in the mantle), but at a much slower rate of decrease than at lower temperatures.

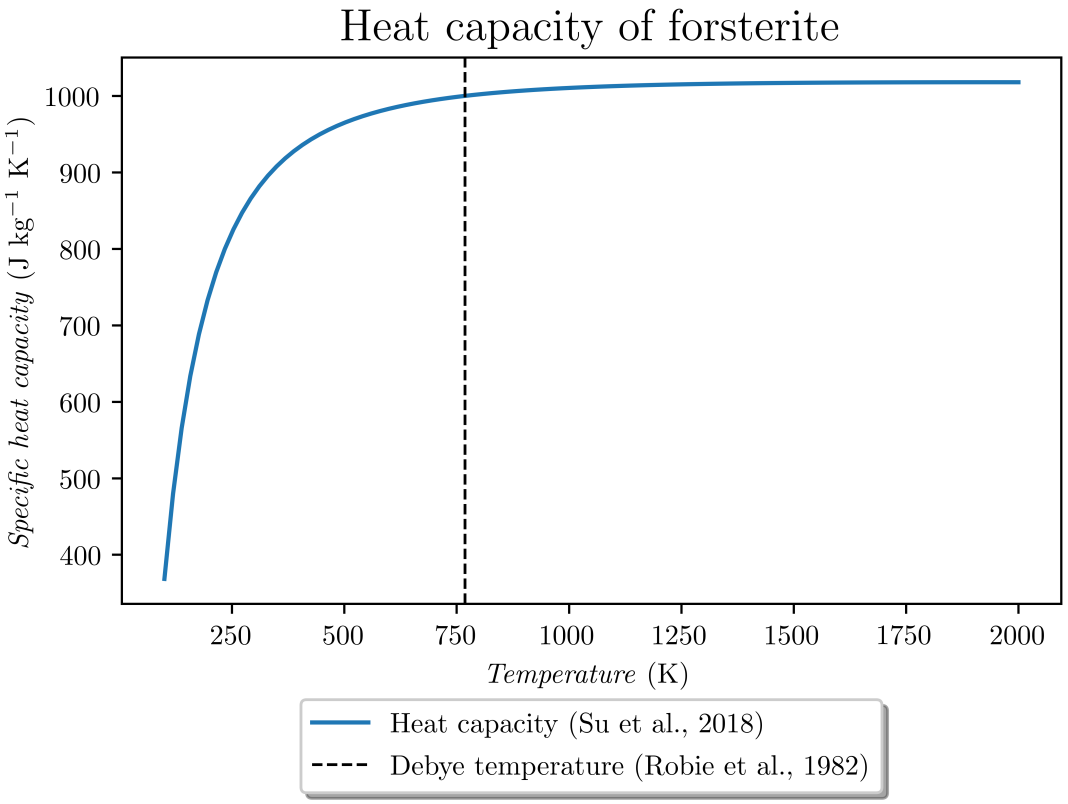

Figure 1.6: Heat capacity as a function of temperature, where heat capacity uses functions from *Su et al.* (2018). The Debye temperature is indicated by the dashed line (*Robie et al.*, 1982).

1.5.2 Pressure-dependence

The volume of material decreases with increasing pressure and thus with increasing depth into the Earth. Higher pressure increases the harmonicity in atomic oscillations, thus causing the phonon velocity to increase (*Kittel*, 2005). As phonon-phonon scattering is the main scattering mechanism in bridgmanite (*Okuda et al.*, 2017), increased phonon velocity leads to a higher conductivity (as in Equation 1.5).

The temperature-dependence of thermal conductivity may itself be pressure-dependent. While the magnitude of conductivity and thus its rate of change will increase with pressure, the general behaviour is expected to be the same at different pressures, assuming thermal conductivity saturates with

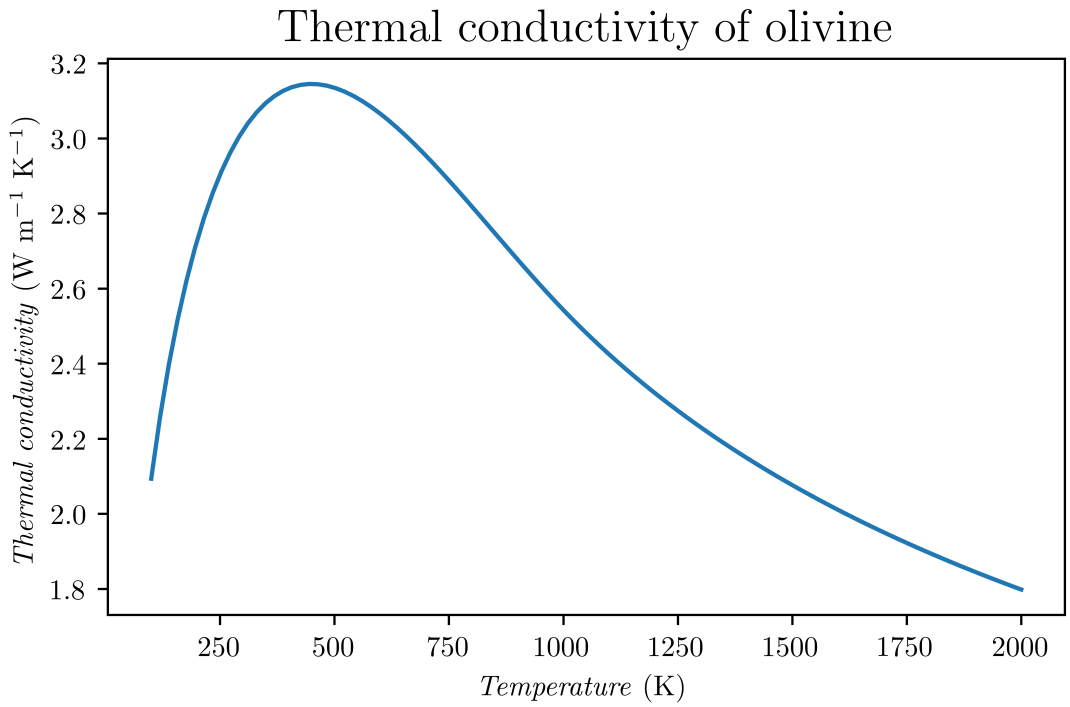

Figure 1.7: Thermal conductivity as a function of temperature, using functions from *Xu et al.* (2004) and *Su et al.* (2018).

temperature. Pressure-dependence is not considered in this study, and would require a full analysis of how finite-size effects vary with pressure in order to be included in thermal conductivity calculations.

1.5.3 Composition

Considering an end member of a solid solution, like $MgSiO_3$ bridgmanite, the main source of scattering is phonon-phonon (phonon-boundary scattering exists, but is of small significance). Addition of impurities, such as in (Mg,Fe)SiO_3 perovskite, introduces phonon-impurity scattering and can reduce conductivity (Equation 1.5). The effect of impurities is less significant at high temperatures, when conductivity is already reduced by phonon-phonon sacttering. When the phonon-impurity path is much shorter than those of other scattering sources however, impurities can greatly reduce conductivity (via Matthiessen rule, above).

Because of these relations, impurities will affect conductivity more higher in the mantle, with the effect reducing towards the CMB. The effect of impurities on thermal conductivity will be discussed extensively in Chapter 4.

1.6 Existing estimates of the thermal conductivity of the lower mantle

A range of experimental and atomic-scale simulation methods are available to determine the lattice thermal conductivity of materials. Many studies assume lowermost mantle thermal conductivity to be 10 $\mathrm{Wm^{-1}K^{-1}}$ (e.g., *Lay et al.*, 2008), but as discussed later, uncertainty in the extrapolation of experimental results made at low pressures and temperatures gives a range of 4–16 $\mathrm{Wm^{-1}K^{-1}}$ (*Brown*, 1986; *Osako and Ito*, 1991; *Hofmeister*, 1999; *Goncharov et al.*, 2009; *Manthilake et al.*, 2011). Computational methods are invaluable for calculating thermal conductivity at conditions which are inaccessible to experiments, i.e., the extreme conditions found in the Earth's lower mantle.

The significance of radiative thermal conductivity, the transport of heat by photonic processes, is an ongoing discussion in terms of the lower mantle (see Section 1.6.3). The components can simply be added to determine the total conductivity (ignoring electrical conductivity), a correction that could be applied to my results at a later date.

Next, I review experimental and computational determinations of the thermal conductivity of Earth materials at relevant conditions (the Green-Kubo and direct methods are elaborated on in Chapter 2). I focus on determining the conductivity of bridgmanite, as this makes up a more significant proportion of the lower mantle ($\sim$70%) compared to ferropericlase ($\sim$20%) or Ca-perovskite ($\sim$10%).

1.6.1 Experimental estimates of thermal conductivity

There have been several experimental studies to measure the lattice thermal conductivity of bridgmanite at CMB conditions. *Osako and Ito* (1991) obtained the lattice thermal conductivity of $MgSiO_3$ perovskite from observing temperature variations across a periodically heated sample. They investigated a temperature range of 160–340 K at ambient pressure. At 300 K, a conductivity of 5.1 $Wm^{-1}K^{-1}$ was obtained. This value is reported to be consistent with chemical and structural analogues, $MgSiO_3$ enstatite (5.0 $Wm^{-1}K^{-1}$, *Horai*, 1971) and $CaTiO_3$ perovskite (4 $Wm^{-1}K^{-1}$, *Touloukian et al.*, 1970). *Osako and Ito* (1991) extrapolated the value to lower mantle conditions via a semi-empirical relation, neglecting the radiative component of thermal conductivity. Based on their extrapolation, they predicted a value of 3.0 $Wm^{-1}K^{-1}$ just beneath the mantle transition zone at 1900 K, and 12.0 $Wm^{-1}K^{-1}$ at the top of the D″ layer at 2500 K, a four-fold increase.

Manthilake et al. (2011) measured the thermal conductivity of $MgSiO_3$ perovskite at 26 GPa and 473–1073 K, and periclase at 8 and 14 GPa between 373–1273 K. They showed that adding 3% of $FeSiO_3$ to $MgSiO_3$ decreased measured thermal diffusivity from 2.90 ± 0.09 mm^2/s to 1.29 ± 0.28 mm^2/s (at 26 GPa and 573 K). In order to estimate values of thermal conductivity at the top and bottom of D″ for a lower mantle compositional model of 4 perovskite : 1 periclase, the authors extrapolated their measurements to high temperature and pressure. For an iron-free mantle, thermal conductivities of 18.9 ± 1.6 $Wm^{-1}K^{-1}$ and 15.4 ± 1.4 $Wm^{-1}K^{-1}$ were estimated for the top of D″ and CMB respectively. Similarly, for a mantle composition with Fe, thermal conductivities of 9.1 ± 1.2 $Wm^{-1}K^{-1}$ and 8.4 ± 1.2 $Wm^{-1}K^{-1}$ were calculated for the same regions (lower than the 12.0 $Wm^{-1}K^{-1}$ estimated by *Osako and Ito* (1991) for a Fe-free mantle). This highlights the importance of impurities in

controlling thermal conductivity in the lower mantle. The authors mention the inhibiting factor that iron is likely to have on the radiative component of heat transport, and perform their experiments in a manner to reduce the radiative effect.

Ohta et al. (2012) measured the lattice thermal diffusivity of $MgSiO_3$ perovskite and post-perovskite at room temperature and temperatures up to 436 K, and pressures up to 144 GPa (using a diamond-anvil cell and light heating thermoreflectance). Using the temperature effect of thermal conductivity proposed by *Manthilake et al.* (2011), they extrapolated their results to give conductivity at higher P-T conditions. These results suggest a majority perovskite lowermost mantle would have conductivity of $\sim$11 $Wm^{-1}K^{-1}$, and that parts of the lowermost mantle where post-perovskite is stable will have a conductivity approximately 60% higher. The authors suggest that these differences in conductivity between phases will not have a large effect on CMB heat flux, assuming the double-crossing perovskite phase model. The lattice conductivity of $MgSiO_3$ perovskite is shown to increase with pressure and decrease with temperature as expected. The inclusion of impurities is expected to decrease lattice thermal conductivity.

Hsieh et al. (2017) measured the lattice thermal diffusivity of Fe-bearing bridgmanite up to 120 GPa with time-domain thermoreflectance in a diamond-anvil cell. They find conductivity to increase with pressure but drop around 45 GPa due to a pressure-induced lattice distortion on the iron sites. They extrapolate their experimental conditions along a mantle geotherm to show that iron causes a significant conductivity decrease. The conductivity of bridgmanite (the Mg endmember) at 120 GPa is 9 $Wm^{-1}K^{-1}$, and Fe-bearing bridgmanite with 9% iron has half the conductivity. The study concludes that while variations in CMB heat flux are dominated by lateral temperature variations, the conductivity and variation thereof is also a controlling factor on heat flux.

The main benefit of experiments is that they allow direct measurement of thermal conductivity, however from reviewing the literature, I suggest that the main problem with experimental results is the replication of CMB conditions, or the assumptions in extrapolation of low pressure/temperature results. Particularly, it is not currently possible to simultaneously replicate the CMB conditions *and* measure thermal conductivity. Impurities are observed to have a significant effect, but different compositions require individual experimental runs and synthesis of new samples. For considering a wide range of temperatures and compositions, computational approaches will allow me to be flexible in choosing conditions of interest.

1.6.2 Numerical estimates of thermal conductivity

Haigis et al. (2012) used the Green-Kubo method (Section 2.8) with advanced ionic interaction potential (parameterised from density functional theory) to calculate the lattice thermal conductivity of bridgmanite, post-perovskite, and periclase at lower mantle conditions (ignoring effects of radiative heat transport). Assuming an isotopically corrected iron-free composition with four parts bridgmanite to one part periclase, they constructed a model of density and temperature-dependent thermal conductivity along a geotherm. This model suggests great variation over the lower mantle, with a value of 9.5 $\mathrm{Wm^{-1}K^{-1}}$ at the top and 20.5 $\mathrm{Wm^{-1}K^{-1}}$ above D″. Based on the results of *Manthilake et al.* (2011), *Haigis et al.* (2012) suggest the inclusion of iron will lower thermal conductivity by up to half, bringing their result in line with the accepted value of 10 $\mathrm{Wm^{-1}K^{-1}}$(*Lay et al.*, 2006).

Dekura et al. (2013) used *ab initio* anharmonic lattice dynamics with density functional theory (DFT) to calculate the lattice thermal conductivity of bridgmanite. At temperature of 300 K, they found conductivity increases

from 9.8 $Wm^{-1}K^{-1}$ at 23.5 GPa to 43.6 $Wm^{-1}K^{-1}$ at 136 GPa. At 100 GPa conductivity decreases from 28.1 $Wm^{-1}K^{-1}$ at 300 K to 2.3 $Wm^{-1}K^{-1}$ at 4000 K. They approximate the effect of radiative conductivity as a function of temperature, and show that total conductivity increases along a typical geotherm, the radiative component being proportional to the increasing temperature and offsetting the decrease in lattice component. From their results they calculated a Rayleigh number (Ra) of 10^5–10^7 for the mantle, in agreement with previous estimates (3×10^6, see Section 1.2.1). These results suggest that a CMB region at 136 GPa and 3200 K will have a conductivity of 5.3 $Wm^{-1}K^{-1}$.

Ammann et al. (2014) used the direct method, a non-equilibrium molecular dynamics technique for different interatomic potentials, to calculate the lattice thermal conductivity of bridgmanite and post-perovskite under D″ conditions. They found the conductivity of post-perovskite to be around 50% larger than bridgmanite for the same conditions (12 $Wm^{-1}K^{-1}$ compared to 8.5 $Wm^{-1}K^{-1}$). This relation is true even in the TBL, where increases in temperature reduce lattice conductivity for all $MgSiO_3$ phases.

Ammann et al. (2014) also investigated the effects of impurities on conductivity, substituting magnesium with iron. The lower mantle distribution of iron is not yet well-understood, specifically the partitioning between bridgmanite, post-perovskite, and periclase. Interestingly, the authors observed saturation in the conductivity reduction associated with atomic impurities for any Fe concentrations (Fig. 1.8). Extrapolations of variable-composition experimental results must be applied carefully, increasing iron content past a certain point will not reduce conductivity any further.

Tang et al. (2014) performed first-principles calculations to assess the thermal conductivity of $MgSiO_3$ and the effect of Fe inclusions therein, using the Peierls-Boltzmann kinetic phonon transport equation. These results feed into a model of conductivity (including radiative, see Section 1.6.3) along a lower mantle

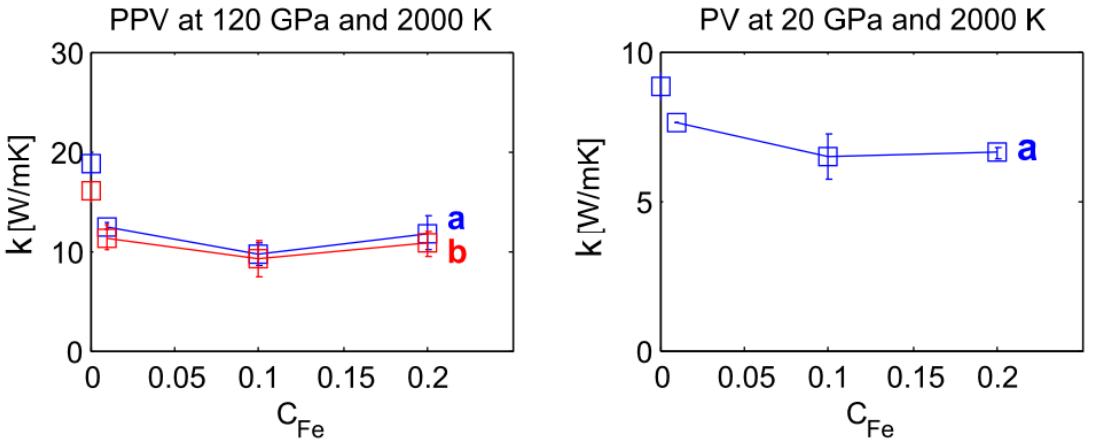

Figure 1.8: Thermal conductivity decrease due to inclusion of impurities is shown to saturate with increasing Fe-content, for $MgSiO_3$ post-perovskite and perovskite phases. **a** and **b** refer to crystallographic directions along which conductivity was calculated. Figure from *Ammann et al.* (2014) with permission.

geotherm, of aggregate composition 4 bridgmanite : 1 periclase with 12.5% Fe impurities. Their calculations model (Mg,Fe)SiO_3 by increasing atomic mass, but not changing the force constants, in a manner similar to *Ammann et al.* (2014). The inclusion of impurities has little effect at 136 GPa–4000 K, on the order of a few percent, but they note MgO should be affected more considering its higher conductivity. The observation that conductivity is reduced less when it is already small due to the effect of temperature, matches the saturation described in *Ammann et al.* (2014). *Haigis et al.* (2012) report conductivity of their aggregate approximately halving however, showing the large uncertainty when extrapolating data especially when considering the (temperature-dependent) effect of impurities.

Stackhouse et al. (2015) did *ab initio* molecular dynamics using the direct method to determine lattice thermal conductivity of bridgmanite. They found 6.9 ± 0.9 $Wm^{-1}K^{-1}$ at core-mantle boundary conditions. They also identified saturation effects in thermal conductivity with temperature, attributed to the phonon mean free path approaching the atomic spacing. In this study, they also used seismic tomography to be indicative of heat distribution within the lower

mantle. Using this, they show that the temperature-dependence of conductivity creates lateral variations in heat flux across the CMB, an idea that will be explored further in Chapter 5 of this thesis.

Ghaderi et al. (2017) investigate the lattice conductivity of bridgmanite using *ab initio* lattice dynamics calculations, considering a range of pressures at room temperature (mirroring previous experimental measurements). $MgSiO_3$ conductivity is found to increase from 10.7 $Wm^{-1}K^{-1}$ at 0 GPa, to 59.2 $Wm^{-1}K^{-1}$ at 100 GPa. Conductivity is extrapolated to lower mantle conditions and determined for a sample geotherm. The value initially increases with depth as the effect of increasing pressure dominates, until around 400 km above the CMB where temperature effects take over and conductivity reduces. A value of $\sim$5.2 $Wm^{-1}K^{-1}$ is given for bridgmanite at CMB conditions of 136 GPa and 4000 K.

The concept of a minimum phonon mean free path is discussed by *Ghaderi et al.* (2017), the idea that a minimum MFP causes conductivity to saturate at high temperatures, showing a dependence different to the expected $1/T$. The authors suggest an explanation for this phenomena, which is radiative heat transport. The cause of low MFP is called into question, whether it be small group velocities, or short phonon lifetimes. In any case, the authors assume the minimum MFP to not be correct, and extrapolate to high temperatures with a $1/T$ relation.

Zhang et al. (2017) characterize phonon quasiparticles numerically through a hybrid approach combining first-principles molecular dynamics and lattice dynamics. They find no lower-bound limits on the MFP in bridgmanite, contradicting the idea it reaches a minimum value on the order of the lattice constant. While they calculate path lengths and MFPs below the lattice parameters, they also show that conductivity decreases sharply with temperature (with a 1/T dependence) up to 4000 K across a range of lower mantle pressure

conditions. Regardless of the dependence used, conductivity does tend towards a minimum value with increasing high temperature, even if the temperature required increases with pressure. They also determine the pressure-dependence of lattice conductivity for a range of temperatures from 300 K to 4000 K. They find the dependence to be linear for all temperatures, but the value of conductivity and the rate of increase with pressure decreases sharply with temperature. This appears to be an effect of saturation, the effect of phonon-phonon scattering at high temperatures severely dampens the conductivity increase with pressure. Their computed conductivity for bridgmanite at CMB conditions of 4000 K and 136 GPa is around 2 $\mathrm{Wm^{-1}K^{-1}}$.

Numerical results for thermal conductivity of bridgmanite at CMB conditions (including those extrapolated to these conditions) range from 2 to 8.5 $\mathrm{Wm^{-1}K^{-1}}$ (Table 1.1; *Ammann et al.*, 2014; *Stackhouse et al.*, 2015; *Ghaderi et al.*, 2017; *Zhang et al.*, 2017). The most similar results (6.8 ± 0.9 $\mathrm{Wm^{-1}K^{-1}}$ and 8.5 $\mathrm{Wm^{-1}K^{-1}}$) come from two direct method calculations, which are comparable when considering the error. Conductivity results for bridgmanite across a full range of lower mantle conditions are plotted in Figure 1.9.

Results calculated using the direct method (see Table 1.1) are similar to the experimental values from *Ohta et al.* (2012) for bridgmanite at CMB conditions, who obtain a value of 9 ± 1.6 $\mathrm{Wm^{-1}K^{-1}}$. Thermal conductivity at CMB conditions has also been calculated for bridgmanite and periclase aggregates, including iron. The results of these are also on the same order of magnitude, e.g., 8.2 $\mathrm{Wm^{-1}K^{-1}}$ (Green-Kubo method; *Haigis et al.*, 2012) compared with 5.5 $\mathrm{Wm^{-1}K^{-1}}$ (Peierls Boltzmann method; *Tang et al.*, 2014).

From reviewing the literature, it is clear that multiple methods have been used to estimate thermal conductivity. The Green-Kubo method is advantageous in that it gives the full conductivity tensor and allows investigation of anisotropy. The Green-Kubo method, however, requires long simulation times for the auto

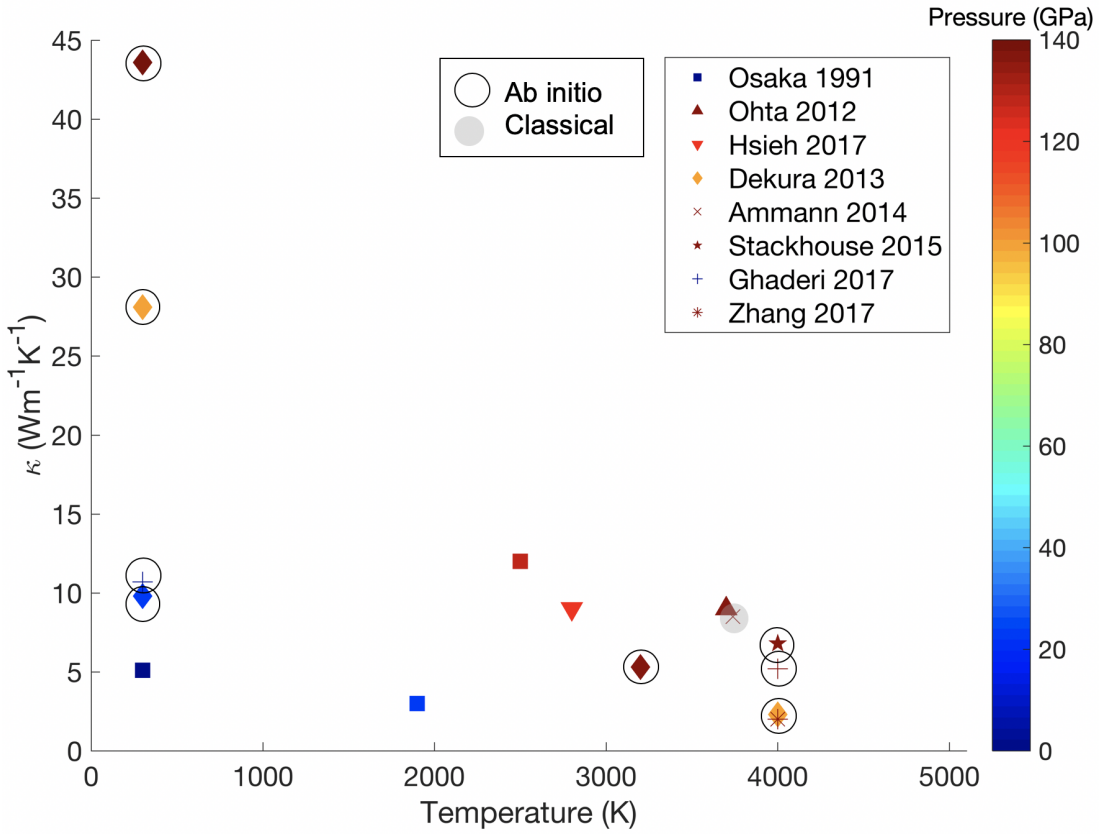

Figure 1.9: A comparison of bridgmanite thermal conductivity results across a range of lower mantle conditions from existing literature, including experiments and calculations as shown in Table 1.1. Calculations are differentiated into classical methods (shaded circles) and *ab initio* methods (hollow circles). Uncircled points show experiments.

correlation function to decay, and so results are only reliable once a sufficient simulation time has been identified. The Green-Kubo method is also difficult to calculate from first principles. The direct method has more experimentation in parameters than the Green-Kubo method, and thus requires a more detailed setup, for example through a more robust determination of finite-size effects and suitability of temperature gradients across a system. If finite-size effects are resolved and appropriate simulation parameters identified, the direct method provides robust estimations of thermal conductivity. Lattice dynamics has also been used to estimate thermal conductivity, and can be used to calculation phonon properties (such as frequencies and lifetimes). This means that it can

offer a better breadth of results than other methods, including calculation of the full conductivity tensor. Lattice dynamics, however, can be problematic at high temperatures (such as CMB conditions), when the harmonic approximation breaks down. In this thesis, I will be using both the Green-Kubo method and the direct method further, as reviewing the literature presents these as the most reliable methods for estimating thermal conductivity.

The full extent of the effects of finite system size are not always considered however, due to the computational cost associated with density functional theory calculations, or incomplete results for partial investigations (i.e., not considering the really long cells or large cross-sectional areas). Calculated results suffer from the same uncertainties as experimental results when extrapolated, particularly considering the effects of composition, where conductivity may not be affected in the same manner for all compositions. In this thesis, I investigate large system sizes and constrain finite-size effects for bridgmanite at core-mantle boundary conditions. I also investigate the full range of Fe^{2+} inclusions into bridgmanite, up to the Fe-endmember, seeing how conductivity varies with the amount of impurities across multiple temperatures, ultimately combining the two into a conductivity model as a function of temperature and composition at the CMB.

1.6.3 Existing estimates of radiative conductivity

Hofmeister (1999) produced a model of thermal conductivity for the entire mantle using data from infrared reflectivity methods. The radiative component at maximum was found to be small compared to the lattice conductivity, between 10–15% depending on the geotherm model used. This corresponds to radiative conductivity values of 0.67–0.82 $Wm^{-1}K^{-1}$ compared to 5.8–6.7 $Wm^{-1}K^{-1}$ for the total conductivity at the top of D″.

Keppler et al. (2008) studied the near-infrared and optical absorption spectra

of silicate perovskite up to pressures of 125 GPa at room temperature. From both their tests and visual inspection, it was shown that their synthesised perovskite remains transparent at high pressures. Extrapolating their results to high temperatures (4500 K) they suggest that the maximum radiative thermal conductivity above the CMB is around 10 $\mathrm{Wm^{-1}K^{-1}}$, implying that radiative conductivity is likely to be an important component of the total conductivity at lower mantle conditions. The study does not measure the variation of absorption spectra with temperature and pressure, which is currently unfeasible for experiments.

Goncharov et al. (2008) performed a similar optical absorption spectra analysis up to 133 GPa, but reached the opposite conclusion to *Keppler et al.* (2008). They agreed the radiative conductivity was dependent on the amount, redox state, and spin state of iron, but disagreed with its significance. *Goncharov et al.* (2008) estimated radiative conductivity would not exceed 0.54 $\mathrm{Wm^{-1}K^{-1}}$ at the top of the D″ layer, a value in line with *Hofmeister* (1999) but at odds with *Keppler et al.* (2008).

Tang et al. (2014) re-evaluated the works of *Keppler et al.* (2008) and *Goncharov et al.* (2008) to create a profile of radiative conductivity in the lower mantle. *Tang et al.*'s profile suggests that the previous works have a more reasonable agreement than they show, reducing the order of magnitude difference to a factor of 2 or 3, and a value around 4 $\mathrm{Wm^{-1}K^{-1}}$ at CMB conditions. Radiative heat transfer is inhibited in the same way as conductive, by impurities and grain boundaries which are not considered when calculating this upper bound. Unlike lattice thermal conductivity, radiative conductivity increases with temperature, strongly in the mantle thermal boundary layer. When the opposing temperature dependencies of lattice and radiative conductivity are considered together, they suggest that the thermal conductivity of the lower mantle is largely temperature-independent above the D″ region at around 3 $\mathrm{Wm^{-1}K^{-1}}$.

Thermal conductivity is found to increase to 5.5 $Wm^{-1}K^{-1}$ in the TBL, due to the increased significance of the radiative component.

More recently, *Lobanov et al.* (2017) determine the radiative conductivity of post-perovskite (1.2 ± 0.2 $Wm^{-1}K^{-1}$, 10% Fe), bridgmanite (2.2 ± 0.4 $Wm^{-1}K^{-1}$, 10% Fe), and ferropericlase (0.2 ± 0.1 $Wm^{-1}K^{-1}$, 15% Fe) at 130 GPa and ∼3000 K. They measure optical absorption from diamond anvil cell experiments, extrapolating radiative conductivity from absorption coefficients to lower mantle conditions (∼130 GPa, 4000 K). While the model shows radiative conductivity generally increasing towards the CMB, it decreases from bridgmanite to post-perovskite. Ferropericlase is found to have a lower radiative conductivity than either of the (Mg,Fe)SiO_3 phases, with all of the considered minerals having higher lattice conductivities compared to radiative. The authors conclude that the lattice conductivity will decrease faster than radiative with the inclusion of Fe-impurities, changing the relative significance from low to high Fe content. The results from this study agree with the previous works, that although lattice conductivity is the dominant mechanism of heat transport, radiative conductivity is also important and affects the overall thermal conductivity in the lower mantle.

Table 1.1: Comparison of previous lower mantle thermal conductivities. [c] indicates a classical method, whilst [a] indicates *ab initio*

Paper	Type	Material	Pressure (GPa)	Temp (K)	κ ($Wm^{-1}K^{-1}$)	Notes
Osako and Ito (1991)	Experiment	$MgSiO_3$ perovskite	0	300	5.1	Measurement, w/ analogues
		$MgSiO_3$ enstatite	0	300	5	
		$CaTiO_3$	0	300	4	
		$MgSiO_3$ perovskite	24	1900	3	Extrapolation
			127	2500	12	
Manthilake et al. (2011)	Experiment	4 $MgSiO_3$ pv: 1 periclase	127	2600	9.1 ± 1.2	Extrap., mantle model (w/ Fe)
			136	4100	8.4 ± 1.2	
			127	2600	18.9 ± 1.6	Extrap., mantle model (no Fe)
			136	4100	15.4 ± 1.4	
Ohta et al. (2012)	Experiment	$MgSiO_3$ perovskite	136	3700	9.0 ± 1.6	Extrapolation
		$MgSiO_3$ post-perovskite			16.8 ± 3.7	
		4 $MgSiO_3$ pv: 1 periclase			11.0 ± 2.0	
		4 $MgSiO_3$ ppv: 1 periclase			17.8 ± 3.9	
Haigis et al. (2012)	Green-Kubo Calculation[c]	4 $MgSiO_3$ pv: 1 periclase	24	2200	9.5	Calculation
			127	2900	20.5	
		Pv/periclase aggregate	136	3739	16.4 ± 2.7	Extrapolation, mantle model
		Ppv/periclase aggregate			16.6 ± 2.7	
		Pv/periclase aggregate w/Fe			8.2	
		Ppv/periclase aggregate w/Fe			8.3	
Dekura et al. (2013)	Lattice Dynamics[a]	$MgSiO_3$ perovskite	23.5	300	9.8	Calculation
			136	300	43.6	
			100	300	28.1	
			100	4000	2.3	
			136	3200	5.3	Extrapolation

Table 1.1 continued from previous page

Paper	Type	Material	Pressure (GPa)	Temp (K)	κ ($Wm^{-1}K^{-1}$)	Notes
Ammann et al. (2014)	Direct method[c]	$MgSiO_3$ perovskite $MgSiO_3$ post-perovskite	136	3739	8.5 12	Calculation
Tang et al. (2014)	Peierls Boltzmann[a]	4 $MgSiO_3$ pv: 1 periclase	24 127 136	2000 3000 4000	2.5 3.5 5.5	Including Fe, with radiative
Stackhouse et al. (2015)	Direct method[a]	$MgSiO_3$ perovskite	136	4000	6.8 ± 0.9	Calculation
Ghaderi et al. (2017)	Lattice dynamics[a]	$MgSiO_3$ perovskite	0 140 136	300 300 4000	10.7 78.8 5.2	Extrapolation
Hsieh et al. (2017)	Experiment	$MgSiO_3$ perovskite $(Mg,Fe)SiO_3$ perovksite	120	2800	9 4.5	Extrapolation along geotherm
Zhang et al. (2017)	Hybrid molecular /lattice dynamics[a]	$MgSiO_3$ perovskite	136	4000	2	Calculation

1.7 Aims, objectives, and thesis outline

The aim of the work presented in this thesis is to model thermal conductivity in the lower mantle, a key parameter in determining heat flux across the core-mantle boundary and the nature of planetary dynamics. I perform atomic-scale simulations of bridgmanite at high pressure and varying temperatures, in order to consider the effect of composition between the bridgmanite and its iron endmember. To do this, I have several goals within the project, which have associated objectives as presented below.

While other studies may have accomplished individual goals, none have consolidated the effects of finite simulation size at lower mantle conditions, to the effect conductivity has on CMB heat flux. I compare the Green-Kubo and direct method at lower mantle conditions for the first time, I conduct one of the most comprehensive fifnite size effect analyses, and I incorporate composition-dependent thermal conductivity results into a model of core-mantle boundary heat flux for the first time.

1. **Establish method of simulating bridgmanite at lower mantle conditions**
   (a) Validate the *Oganov et al.* (2000) potential for bridgmanite.
   (b) Establish computational tools and respective limitations for calculations of thermal conductivity.
2. **Determine the accuracy of various atomic-scale modelling approaches.**
   (a) Determine the simulation parameters required to calculate thermal conductivity at lower mantle conditions, i.e., ensuring simulations are converged for given timescales.

(b) Quantitatively determine thermal conductivity at core-mantle boundary conditions.

(c) Compare the direct method with the Green-Kubo method for calculating thermal conductivity of bridgmanite.

(d) Consider fully the effects of finite system size on computed conductivity results.

(e) Evaluate existing observations of finite-size effects.

(f) Analyse conductivity results to calculate phonon mean free paths.

3. **Investigate how impurities affect conductivity at lower mantle conditions**

(a) Determine how iron can be incorporated into Green-Kubo calculations of thermal conductivity.

(b) Perform Green-Kubo calculations of thermal conductivity across the full range of lower mantle temperatures and a range of composition (i.e., $MgSiO_3$ to $FeSiO_3$ endmembers).

(c) Create model to fit compositional- and temperature-dependence of conductivity to allow thermal conductivity to be estimated at any temperature and composition at the core-mantle boundary.

(d) Quantify the mean free path of phonon-defect scattering.

4. **Incorporate the thermal conductivity results into a model of core-mantle boundary heat flux to investigate LLSVP conditions.**

(a) Investigate appropriate numerical representations of LLSVP distribution in the lower mantle.

(b) Investigate the sensitivity of core-mantle boundary heat flux to lateral variations to temperature gradient and composition, and therefore

thermal conductivity.

(c) Evaluate thermal, chemical, and thermochemical LLSVP models to determine likely LLSVP parameters.

Chapter 2

Computing thermal conductivity

In Chapter 1, I introduced the key concept of thermal conductivity and showed how this is determined, both experimentally and numerically. One of the project objectives is to investigate the magnitude of thermal conductivity throughout the deep Earth, considering the effect of physical conditions and Fe impurities. In this chapter, I introduce how numerical simulations can be used to calculate conductivity and I show the fundamental system setup and parameter convergence.

The theory presented in Chapter 2 is then applied in later chapters to investigate how conductivity is affected by system shape and size (Chapter 3), and by adding impurities to an otherwise regular crystal structure (Chapter 4).

2.1 Atomic-scale modelling

Knowledge of thermal conductivity is important for modelling the deep earth, but there are significant challenges associated with experimentally determining thermal conductivity at core-mantle boundary conditions. Atomic-scale simulations sidestep experimental limitations, but system size must be chosen carefully in order to determine accurate conductivity values.

Atomic-scale simulation begin with a box of atoms. The box has size and shape, and atoms of known positions within it (i.e., atomic structure). By representing the atomic interactions using the Buckingham potential (see Section 2.4), the energy between two atoms at a given separation can be found, and thus the energy of the box by considering all atomic interactions. The force acting on an atom is equal to the change in energy that would be observed if an atom was displaced over a given distance. Once the forces are determined, Newtons laws of motion are applied to the system to perform molecular dynamics calculations.

A range of atomic-scale simulation methods are available to determine the lattice thermal conductivity of materials. These are invaluable for calculating thermal conductivity at conditions of which experiments are difficult, e.g., the extreme conditions found in the Earth's lower mantle (pressures and temperatures up to 136 GPa and 4000 K at the core-mantle boundary).

Before the material properties of interest can be calculated, the specific theoretical approach of atomic-scale modelling needs to be chosen. This refers to how the atoms are set up to interact with one another, before considering the magnitude of interactions or parameters used to replicate a material. There are multiple regimes for doing so, several of which are described below.

2.2 Molecular dynamics

In a molecular dynamics (MD) calculation, atoms in a simulation cell have masses, velocities, and forces acting between them. At each computational timestep the net force on each atom is calculated from all the other atoms. Accelerations are then calculated from Newton's second law of motion, which are used to update the velocities and positions of the atoms. The process is repeated, iteratively updating parameters every timestep (Fig. 2.1).

As I am utilising molecular dynamics approaches, I use the Verlet algorithm

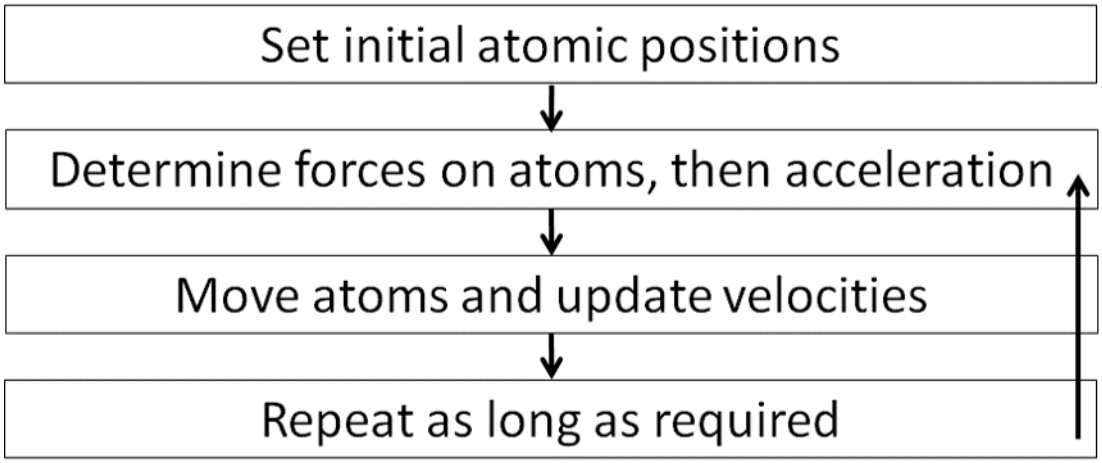

Figure 2.1: Flowchart of process in molecular dynamics simulations

(*Verlet*, 1967; *Leach*, 2001) to integrate the equations of motion. Considering a timestep δt, the Verlet algorithm uses the positions ($\mathbf{r}$) and acceleration ($\mathbf{a}$) of atoms at the current time (t), the positions from the previous timestep ($t - \delta t$), to calculate the positions at the next timestep ($t + \delta t$). The positions of the next and previous timesteps can be written in terms of the current timestep, and the parameters defined above along with the velocity ($\mathbf{v}$)

$$\mathbf{r}(t + \delta t) = \mathbf{r}(t) + \delta t \mathbf{v}(t) + \frac{1}{2}\delta t^2 \mathbf{a}(t) + \ \cdots, \tag{2.1}$$

$$\mathbf{r}(t - \delta t) = \mathbf{r}(t) - \delta t \mathbf{v}(t) + \frac{1}{2}\delta t^2 \mathbf{a}(t) - \ \cdots. \tag{2.2}$$

These are combined into one equation for the position of the next timestep

$$\mathbf{r}(t + \delta t) = 2\mathbf{r}(t) - \mathbf{r}(t - \delta t) + \delta t^2 \mathbf{a}(t) \ . \tag{2.3}$$

The atomic velocities do not appear explicitly, but can be calculated by dividing the change in position by the timestep. The Verlet algorithm has a modest computational cost, but is not without limitation. Drift in the converged values of

parameters can be observed when using molecular dynamics if the simulation time is very long (Fig. 3.11). This is due to inaccuracies in integrating the equations of motion. The first is in the choice of timestep, where too coarse a temporal sampling can lead to inaccurate estimations of the simulated behaviour. While I employ a fine timestep (1 fs) throughout all molecular dynamics calculations in this body of work, even small errors can compound over time. The second inaccuracy is in the truncation of Taylor series that describe the atomic motions, for example the position is given by

$$\mathbf{r}(t+\delta t) = \mathbf{r}(t) + \delta t\mathbf{v}(t) + \frac{1}{2}\delta t^2\mathbf{a}(t) + \frac{1}{6}\delta t^3\mathbf{b}(t) + \frac{1}{24}\delta t^4\mathbf{c}(t) + \ \cdots, \tag{2.4}$$

where b is the rate of change of the acceleration, and so on. Again, the fine timestep used means these higher-order coefficients are likely to be of minor significance, but may become relevant for long simulations.

From the atomic velocities in MD simulations, the temperature of a system with N atoms can be calculated. To do this, the summed kinetic energy ($K.E.$) of all atoms in the system is calculated by

$$K.E. = \frac{1}{2}\sum_{i}^{N} m_i v_i^2 \ , \tag{2.5}$$

where m is mass and v is velocity and the sum is overall all i atoms in the section. Kinetic energy can also be given by the equipartition theorem by

$$K.E. = \frac{3}{2}Nk_{\mathrm{B}}T \ , \tag{2.6}$$

where k_{B} is the Boltzmann constant, and T is the average temperature of the section. Equating these equations and rearranging for T gives

$$T = \frac{\sum_i^N m_i v_i^2}{3Nk_{\mathrm{B}}}. \tag{2.7}$$

At zero temperature, a parameter such as unit cell volume will converge, but this is not true when finite temperatures are considered. Temperature fluctuations due to the transfer of potential energy to kinetic, and vice versa, mean cell volume will constantly change, regardless of simulation length. The solution is to take the cumulative average of a parameter over many timesteps, which eventually converges.

The pressure in a molecular dynamics situation is given by

$$P = \frac{1}{V}\left[Nk_BT - \frac{1}{3}\sum_{i=1}^{N}\sum_{j=i+1}^{N} r_{ij}f_{ij}\right], \tag{2.8}$$

where V is system volume, N is the number of atoms, k_B is the Boltzmann constant, T is temperature, r_{ij} is the separation between two atoms, and f_{ij} is the force acting between them, where f_{ij} is calculated by

$$f_{ij} = \frac{dv(r_{ij})}{dr_{ij}}\ , \tag{2.9}$$

where v is the contribution to the virial. The virial is defined in Equation 2.8 as the summation of the products of the particle coordinates and the forces acting on them.

There are three thermodynamic ensembles that I will use over the course of this project to perform different kinds of calculations. These are NPT, NVT, and NVE, where N refers to the number of atoms, P to pressure, T to temperature, V to volume, and E to energy. The number of atoms is kept constant in all cases presented here.

In NPT and NVT simulations, a thermostat is used to bring the system to a specified temperature. In NPT a barostat is also set, and the cell volume is allowed to equilibrate with the pressure and temperature conditions. This kind of simulation is performed before calculating parameters like thermal conductivity,

in order to recreate physical conditions (like the CMB, i.e., 136 GPa, 4000 K). One cannot simply equilibrate the system at high pressure and then run temperature initialisation, this adds the effect of thermal pressure. If this equilibration is performed incorrectly, it is possible to end up with a CMB at 145 GPa for example, ultimately causing conductivity results to be overestimated (as they increase with pressure). When considering temperature while barostatting, thermal pressure will increase system volume accordingly whilst achieving the target pressure.

Once the cell is of a suitable volume for the conditions of interest, the temperature of the system (via the velocities of the atoms) can be initialised through computation in the NVT regime. Freedom to control the initial temperature condition is great for studies where repeatability or gathering a sample of data is important. The structure, conditions, and subsequent computation workflow do not change, but the result will varying in a given distribution from the random nature of atomic velocities and motion. While pressure is free to change, it will remain constant assuming the aforementioned NPT equilibration is performed to obtain a suitable cell volume. Volume and temperature are fixed parameters, so there are no fluctuations in thermal pressure.

A Nosé-Hoover thermostat (*Nosé*, 1984; *Hoover*, 1985) is used throughout this study to equilibrate the system to a target temperature. In simple terms, a "heat bath" is simulated alongside the system. The total energy of the system and the bath is conserved, but energy can move between the two. This is facilitated by altering the atomic velocities, to add energy to the system from the bath (or to remove energy to the bath). This changes the temperature of the system, and over a long enough equilibration time causes temperature to fluctuate around a specified average value.

The next step is to establish how the atoms will interact with one another in the simulation cell. This means the forces that act between them, how things like

atomic separation and charge are considered. There are varying forms of varying complexity available, with multiple parameterisations to describe the interaction.

Once a reasonable distribution, a steady average temperature, and atomic interactions are constrained, a system can be computed in the NVE ensemble. Conductivity results are determined in this regime for both the direct and Green-Kubo methods. The kinetic and potential energies of the atoms are held constant, allowing local temperature variations. The same point about variable pressure applies here as well as with NVT, but an overall consistent average temperature means a similarly average pressure. NVE is used over the similar NVT when calculating parameters, as thermostatting can artificially influence the dynamics of the system.

MD functions below the Debye temperature, but stops working as the temperature approaches zero Kelvin. In MD, zero Kelvin means zero kinetic energy, and so the atoms stop moving. This is not realistic, because there is always a minimum energy, called zero-point motion.

2.3 Lattice dynamics

An alternative approach to MD is lattice dynamics (LD), where the response of all atoms to the motion of one is considered (e.g., *Dove*, 1993; *Gale*, 1997).

LD is a useful methodology for describing how atoms move in a crystalline structure. Where there are N atoms in a system, a 3N $\times$ 3N matrix holds the force constants for each atom, in each direction, due to the effect of moving each other atom in each other direction. This matrix is then multiplied by the reduced masses of the atoms, which effectively controls what effect the force constant have on an atom (where light atoms move more readily, they require a smaller force than a heavier atom to move a given distance). The product of these matrices is the dynamical matrix, which fully describes the motion of the atoms.

The dynamical matrix can then be diagonalized to obtain eigenvalues (which describe the vibration frequencies) and eigenvectors (which give the direction of displacement for an atom). As the eigenvalues cannot be zero, the atoms have quantised frequencies, even at zero kelvin. The energy cannot drop to zero, which means LD avoids the zero point motion associated with MD.

The force constant matrix takes significant time to compute compared to a single MD timestep, but can be used to calculate various material properties once obtained. The focus of this study will be on MD approaches, but LD results from the literature will be reviewed for comparison.

LD do not have the same limitations as MD when approaching temperatures of zero Kelvin. There are, however, other limitations to LD, for example, the harmonic approximation of atomic oscillations breaks down at high temperatures as the behaviour becomes inharmonic.

2.3.1 Density functional theory

Density functional theory (DFT) is a way of determining accurate interatomic forces. The properties of the electrons are considered along with the nuclei, which increases the computational cost and simulation run time. This additionally limits the size of systems, or number of atoms (on the order of thousands), that can be considered. Calculating from first principles in this manner should only be considered if the system parameters required to obtain converged results are known, and the simulations can be completed on a suitable timescale. I will be opting for a different approach, as I wish to investigate bigger systems ($>16\times2\times2$), potentially for multiple compositional variations.

2.3.2 Classical interatomic potentials

The alternative to DFT is to use empirically-derived potentials to calculate the interatomic forces. Whereas calculating from first principles considers the interactions of atoms and their outer shell electrons, interatomic potentials use an approximation of the electronic potential component (i.e., a classical atomic model).

The potential energy of the system (E) is split into components for each atom, and groups of atoms

$$E = \sum_i e_1(\mathbf{r}_i) + \sum_i \sum_{j>i} e_2(\mathbf{r}_i, \mathbf{r}_j) + \sum_i \sum_{j>i} \sum_{k>j} e_3(\mathbf{r}_i, \mathbf{r}_j, \mathbf{r}_k) + \cdots, \qquad (2.10)$$

where $\sum i \sum j > i$ notation indicates summation over the pairs i and j without counting any pair twice, with the same consideration for the triple terms, and i, j, and k denote unique atoms. e_1 refers to the self-energy, e_2 refers to the pair-wise energy, and e_3 refers to the energy of a triplet of atoms, and so on (*Allen and Tildesley*, 2017).

Systems on the order of millions of atoms can be considered with atomic potentials, due to significantly reduced computational cost compared to DFT. The trade-off is accuracy however, which is controlled by the characteristics of the employed potential. These potentials are set up to reproduce a set of experimental results, but the is no certainty they reflect true values outside their calibrated range of conditions. A realistic model reproduces the structural, elastic, and thermal properties of a material. A common feature of classical potentials is to underestimate the diagonal terms of the elastic constant tensor, and overestimate the off-diagonal, where the discrepancy increases with pressure (*Chen et al.*, 2012).

The interatomic potential function includes ionic, covalent, and van der Waals

components. The dominant long-range term is the Coulomb interaction, and the short-range interactions are described using a Buckingham potential with the Born-Mayer potential, and a C/r^6 van der Waals term. The equation for pair-wise potential (summed for potential energy of the system) takes the form

$$E_{ij}^{\text{Buck}} = \frac{1}{4\pi\epsilon_0}\frac{q_i q_j}{r_{ij}} + b_{ij}\ exp\left(\frac{-r_{ij}}{\rho_{ij}}\right) - \frac{c_{ij}}{{r_{ij}}^6}\ , \tag{2.11}$$

where q_i and q_j are the charges of atoms i and j, r_{ij} is the distance between them, b_{ij} is the pre-exponential repulsive parameter for the pair, ρ_{ij} is the repulsion exponent, and c_{ij} is the van der Waals parameter. This potential is illustrated in Figure 2.2 as a function of atomic separation.

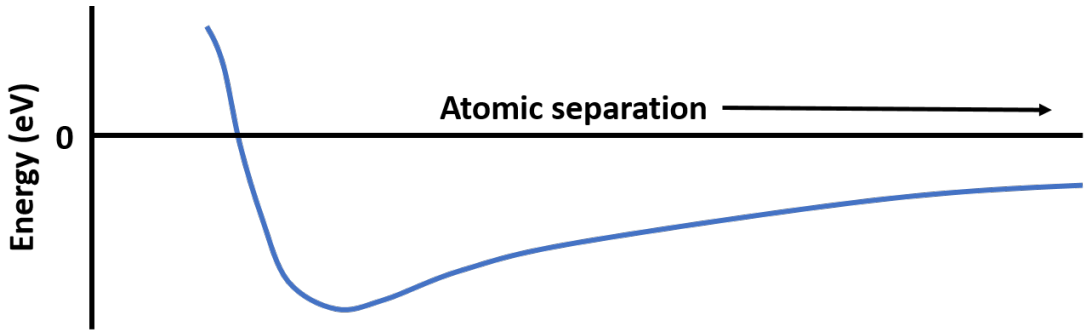

Figure 2.2: Illustration showing energy between two atoms as a function of their separation.

2.4 Oganov's bridgmanite potential

The interatomic potential used in this project was developed by *Oganov et al.* (2000). Many potentials exist for $MgSiO_3$ perovskite (e.g., *Chen et al.*, 2012), but the aforementioned is robust up to lower mantle pressures and temperatures. In addition to calculating thermal conductivity, the *Oganov et al.* potential has also been used for modelling melting under lower mantle conditions (*Di Paola and Brodholt*, 2016), dislocation glide at high P-T conditions (*Kraych et al.*, 2016), prediction of mechanical twinning in post-perovskite (*Carrez et al.*, 2017), and

defect modelling (*Goryaeva et al.*, 2017). The use of this potential in such varied studies shows both the versatility and robustness of the functional form.

There are three sets of these parameter, for each of the interacting atomic pairs (shown in Table 2.1). The charges for Mg, Si, and O atoms are 1.9104, 2.9043, and −1.6049, respectively. To obtain these parameters, *Oganov et al.* (2000) first calculate the ionisation potentials (ρ; see Section 4.2.1 for calculation within this study). The O-O short range potential is taken from *Gavezzotti* (1994). Using lattice dynamics, they then fit four independent parameters: the atomic charges for the magnesium and silicon atoms (where the charge of the oxygen is calculated from these terms), and the pre-exponential repulsive parameters (b), which are for the Mg-O and Si-O interactions. They fit to experimental data of crystal structure (*Ross and Hazen*, 1989) and the elastic constants tensor (*Yeganeh-Haeri*, 1994).

Table 2.1: Parameters used to define *Oganov et al.* (2000)'s $MgSiO_3$ perovskite potential.

Bond ij	b_{ij} (eV)	ρ_{ij} (Å)	c_{ij} (eV.Å^6)
Mg-O	1041.435	0.2866	0
Si-O	1137.028	0.2827	0
O-O	2023.800	0.2674	13.83

2.4.1 Cutoff calibration

Part of applying classical potentials is setting up the distance over which they act, the maximum separation between two atoms before they are not paired for force calculation. Too small a cut-off distance, and the material is not being replicated faithfully. Too large a cut-off means more calculations are being performed than are required, thereby increasing computation time. The potential between two atoms is inversely proportional to their separation (see Equation 2.11), "cutting off" in this manner is acceptable when the potential is tending towards zero with

increasingly large interatomic distance. I consider two cut-off distances, for both the Coulombic and the Buckingham interactions.

I choose to use Buckingham and Coulombic cutoffs of 14 Å and 8 Å respectively. This choice was influenced by other works, and size of the bridgmanite unit cell. As shown in Figure 2.3a & b, the choice of Coulombic cutoff is of low significance. Figure 2.3c & d show the convergence of both energy and a with increasing Buckingham cutoff. The difference between a cutoff of 14 Å and higher values is on the picometer scale, we use the former in the interests of computational efficiency. The Coulombic terms are calculated using an Ewald summation (*Ewald*, 1921) to speed up computation.

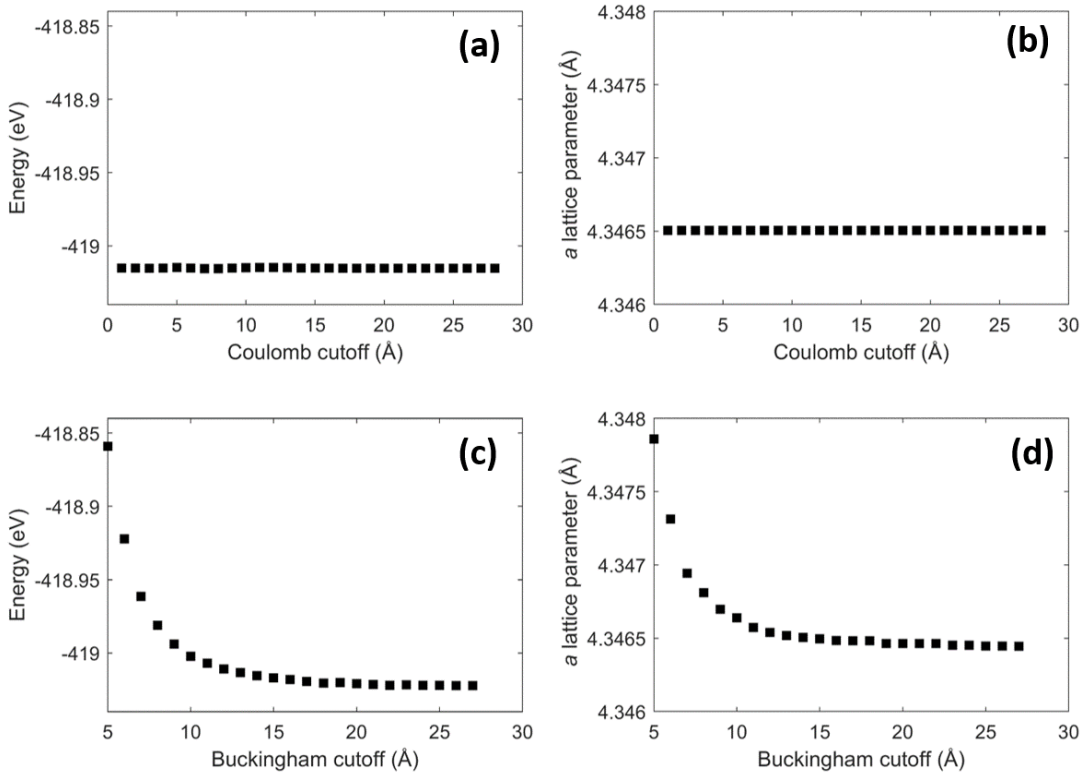

Figure 2.3: For a given Buckingham cutoff of 14 Å **(a)** Relationship between energy and Coulomb cutoff and **(b)** Relationship between a lattice parameter and Coulomb cutoff. For a given Coulomb cutoff of 8 Å, **(c)** relationship between energy and Buckingham cutoff and **(d)** relationship between a lattice parameter and Buckingham cutoff. Geometry optimisation was performed at a pressure of 136 GPa.

2.4.2 Comparison of results

For my calculations to be valid, I have to be able to reproduce other results calculated using the *Oganov et al.* (2000) potential in LAMMPS. *Oganov et al.* provide lattice parameters for a unit cell, along with elastic constants and the bulk and shear moduli. I reproduced their results to acceptable accuracy (see Table 2.2), using LAMMPS and the lattice dynamics code GULP (*Gale*, 1997). Of particular note in this table is the agreement (within 0.0001 Å) of the static LAMMPS and GULP results, showing the potential has been implemented identically for both codes. The agreement between the LAMMPS and GULP results are always within 1%, although the exact variation of the percentage error changes as a function of pressure and temperature. The standard error on the LAMMPS values is smaller than the difference with the GULP values, this disparity is caused by the use of lattice dynamics (LD) opposed to molecular dynamics (MD). The GULP (LD) values are believed to be more accurate in this case, as lattice dynamics performs better at temperatures closer to zero.

Ammann et al. (2014) used GULP and the *Oganov et al.* (2000) potential, and provide unit cell lattice parameters for sample lower mantle pressures and temperatures. I reproduced their data to within 0.15% (Table 2.3), and I observe the discussed difference between LD and MD reducing at increased temperatures.

2.5 Computational tools

LAMMPS (Large-scale Atomic/Molecular Massively Parallel Simulator) is a classical molecular dynamics code (*Plimpton*, 1995). I use it to look at large systems (up to the order of 10^5 atoms) and assess how size and shape of the simulation cell affects results. While calculations using interatomic potentials are not as accurate as those using DFT, a main focus of this work will be on

Table 2.2: Comparison of bridgmanite properties calculated using the *Oganov et al.* (2000) potential at 0 GPa

Property	*Oganov et al.* (Static)	GULP (Static)	LAMMPS (Static)	GULP (LD, 300 K)	LAMMPS (MD, 300 K)
a (Å)	4.7822	4.7875	4.7875	4.8074	4.8022
b (Å)	4.8960	4.9001	4.9002	4.9193	4.9140
c (Å)	6.9322	6.9366	6.9366	6.9598	6.9530
V (Å^3)	162.31	162.73	162.73	164.59	164.08
C_{11} (GPa)	500	507	507	492	487
C_{22} (GPa)	509	519	519	502	498
C_{33} (GPa)	398	411	411	395	395
C_{12} (GPa)	116	125	125	117	116
C_{13} (GPa)	210	209	209	205	201
C_{23} (GPa)	188	192	192	185	184
C_{44} (GPa)	174	177	177	172	170
C_{55} (GPa)	189	189	189	186	184
C_{66} (GPa)	102	108	108	103	102
K_H (GPa)	270.4	276.5	276.5	266.8	269.9
G_H (GPa)	146.3	150.1	150.0	145.2	145.7

a, b, c, and V represent lattice vectors and unit cell volume. C_{xx} denotes elastic constants. K_H and G_H are the Voigt-Reuss-Hill averaged bulk and shear moduli. The MD LAMMPS elastic constants have standard error on the order of 0.1.

Table 2.3: Comparison of calculated bridgmanite unit cell parameters with *Ammann et al.* (2014)

Pressure (GPa)	Value	Lattice parameter (Å) at a given temperature (K)								
		1000			2000			3000		
		a	b	c	a	b	c	a	b	c
20	My work	4.7281	4.8336	6.8215	4.7701	4.8676	6.8670	4.8220	4.9102	6.9127
	Standard error	0.0001	0.0001	0.0001	0.0001	0.0001	0.0001	0.0006	0.0006	0.0006
	Ammann et al.	4.7281	4.8342	6.8221	4.7708	4.8685	6.8653	4.8293	4.9169	6.9070
	% Difference	0.00	0.01	0.01	0.02	0.02	0.02	0.15	0.14	0.08
130	My work	4.3787	4.5180	6.3290	4.3985	4.5265	6.3495	4.4191	4.5352	6.3706
	Standard error	0.0001	0.0001	0.0001	0.0001	0.0001	0.0001	0.0001	0.0001	0.0001
	Ammann et al.	4.3807	4.5192	6.3236	4.4003	4.5244	6.3438	4.4203	4.5347	6.3691
	% Difference	0.05	0.03	0.08	0.04	0.05	0.09	0.03	0.01	0.02

Data produced using LAMMPS is compared with the GULP results of *Ammann et al.* (2014), across a range of pressure/temperature conditions. The standard error is calculated from 1E6 timesteps of NVT simulation. The percent difference refers to the variation between my work and *Ammann et al.*'s.

the observations of conductivity change between systems of varying size. The $Wm^{-1}K^{-1}$ result is less important as confirming phonon behaviour is not being artificially influenced.

GULP (General Utility Lattice Program) is an alternative programme to LAMMPS for performing molecular dynamics simulations (*Gale*, 1997). It can also be used for lattice dynamics on a wide range of materials and different styles of atomic interaction. In this project, I use GULP to perform the parameter fitting required to ensure that my addition of iron to the *Oganov et al.* (2000) potential is representative of bridgmanite behaviour in LAMMPS.

I use Advanced Research Computing (ARC) services, which are part of the High Performance Computing facilities at the University of Leeds. I run LAMMPS on these supercomputers to enable consideration of very large systems in this project. I run parallelised code which uses multiple nodes to speed up calculations.

Finally, ARCHER is a national supercomputer, again used to decrease the time needed to produce results. Having access to both ARCHER and ARC allows simultaneous model runs on each supercomputer facility.

2.6 Computing thermal conductivity

I will be using two approaches, both utilising classical interatomic potentials, to calculate thermal conductivity throughout this thesis. They will be explained later in this section, and are as follows,

(1) The non-equilbrium molecular dynamics-based "direct method", where thermal conductivity is calculated from an imposed heat flux and corresponding temperature gradient via Fourier's Law (*Müller-Plathe*, 1997; *Nieto-Draghi and Avalos*, 2013). The specific method adopted here is outlined further in Section 3.1.

(2) Equilibrium molecular dynamics based on the Green-Kubo relations

to determine the thermal conductivity from heat flux fluctuations and their time-dependence (*Green*, 1954; *Kubo*, 1957, 1966; *Schelling et al.*, 2002). The specific approach adopted in this thesis is outlined further in Section 3.2.

Stackhouse and Stixrude (2010) review other methods to compute thermal conductivity, including the above, but also

(3) Anharmonic lattice dynamics (*Tang and Dong*, 2009).

(4) Combined quasiharmonic lattice dynamics and molecular dynamics method (*de Koker*, 2009).

The Green-Kubo and direct method use the same underlying atomic model, but calculate thermal conductivity differently. They have their own unique system setup procedures, data processing work flows, and they both produce results that can depend on their respective system size. These methods were chosen for comparison over the lattice dynamics approaches as they have previously yielded similar results (see Section 2.9), and can both be performed within LAMMPS.

Computational techniques are not hindered by the reproduction of physical conditions like experiments, this does not mean they are without limitations however. Finite-size effects refer to when the number of atoms, or system shape and size, affects the computed result, compared to that of an infinite system. In the case of thermal conductivity, the problem arises when phonons are truncated by boundaries in the simulation cell. As discussed in Chapter 1.4.3, phonons have wave-like properties, including wavelength.

When a simulation cell is shorter than a phonon's wavelength, that phonon cannot be represented in the system. This will mean a calculation is tending to underestimate conductivity, the phonon population is not being fully represented. Another scenario is if the phonon mean free path is longer than the distance between boundaries in a system, in this case phonon scattering behaviour is not being reproduced accurately. This leads to overestimations, where phonons are able to transport heat unimpeded, and conductivity is strongly dependent on

system size (*Tadano et al.*, 2014).

The finite-size effects (FSE) observed for a material change with thermal conductivity/phonon MFP, and thus are sensitive to pressure, temperature, and composition. Requiring a minimum simulation cell size to recreate phonon behaviour accurately can be a problem when employing DFT calculations, where large system sizes (generally >16×2×2) are highly computationally expensive. Testing system size is also a problem, as calculations of large systems must be performed to check convergence of small system results.

In the following sections, I consider both the direct method and the Green-Kubo method, before a review of literature comparing the two, and how I will use them to analyse their FSE.

2.7 Direct method

The direct method is the computational implementation of a typical experiment to measure thermal conductivity using Fourier's law, where the heat flux (q) is controlled, and the temperature gradient (∇T) is observed, to determine thermal conductivity (κ)

$$q = -\kappa \nabla T \ . \tag{2.12}$$

2.7.1 System setup

In the direct method energy is transferred from one group of atoms to another at regular time intervals, creating hot and cold regions between which heat flows (Fig. 2.4.a). This heat transfer process is implemented by taking the velocity of the lowest energy atom in the hot section, and swapping it with the highest energy atom in the cold section (the approach from *Müller-Plathe*, 1997). The resultant temperature gradient is measured by calculating the temperature of atoms within a section along the direction of the heat flux (Fig. 2.4.a). Thermal conductivity

is equal to the ratio of imposed heat flux to the resulting temperature gradient. This can be shown in a rearranged version of Fourier's law

$$\kappa = -\frac{\langle J \rangle}{\langle dT/dx \rangle} \ , \tag{2.13}$$

where κ is thermal conductivity, $\langle J \rangle$ is time-averaged heat flux through a unit cross-sectional area, and $\langle dT/dx \rangle$ is the time-averaged temperature gradient between hot and cold regions. $\langle J \rangle$ is obtained by summing the energy transferred by swapping the atomic velocities between the hot and cold regions.

Simulation cells tend to be long relative to their cross-sectional area, defined as height by width (Fig. 2.5). Cell boundaries are periodic and the hot and cold sections are half the cell length apart, meaning heat flows in both directions from hot to cold (one of which is across the length-end periodic boundary). This results in two similar temperature gradients which can be averaged.

2.7.2 Data processing

In the immediate vicinity of hot and cold regions, the temperature gradient exhibits non-linear behaviour (Fig. 2.4b) due to the non-Newtonian nature of the heat exchange. Care must be taken to measure the linear portion, which is located roughly in the middle third of the temperature gradient.

The finite size of the simulation cell truncates the mean free path, underestimating conductivity compared to that of the bulk material (κ_∞). Using results from simulations of varying cell length (L), conductivity is extrapolated to a length-independent value (where b is a material-dependent parameter),

$${\kappa_L}^{-1} = bL^{-1} + {\kappa_\infty}^{-1} \ . \tag{2.14}$$

Inverse conductivities from direct method simulations are plotted against

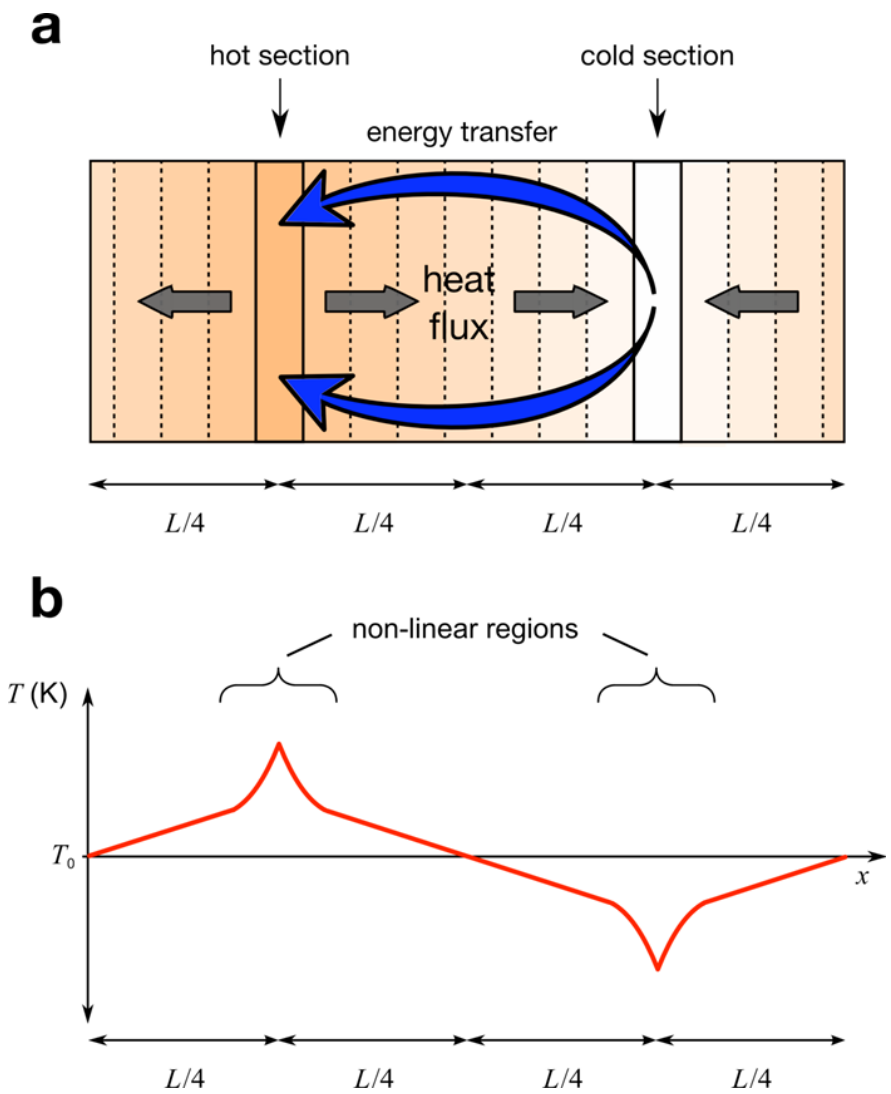

Figure 2.4: **(a)** Movement and distribution of heat in the direct method. Orange to white scale represents temperature; **(b)** Temperature profile along DM simulation cell. Modified with permission from *Stackhouse et al.* (2015)

corresponding inverse cell lengths. A straight line is fit to the data and extrapolated to the y-axis (at which the inverse cell length equals zero and real length equals infinity), where the intercept gives the inverse of the bulk material conductivity (*Schelling et al.*, 2002).

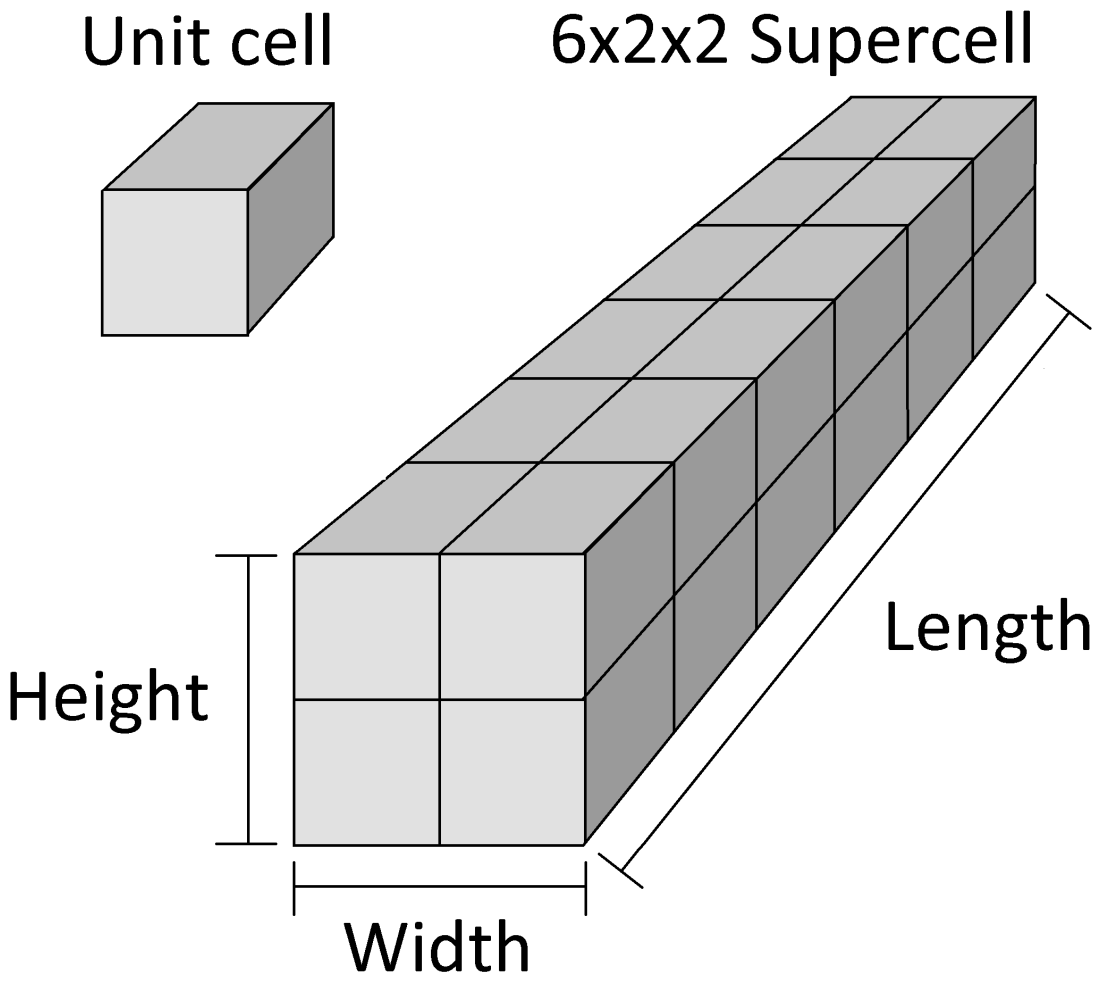

Figure 2.5: Schematic of a unit cell and supercell. The unit cell represents the smallest box of atoms that can be replicated to produce a crystal structure. A supercell is an arrangement of unit cells.

2.7.3 Finite-size effects

From kinetic theory, conductivities computed by the direct method (κ_L) are dependent on length of simulation cell

$$\kappa_L = \frac{1}{3} C_V v l_L \ , \tag{2.15}$$

where C_v is the volumetric heat capacity, v is the average phonon drift velocity, and l_L is the phonon mean free path.

Problems arise when the data do not support the aforementioned linear trend.

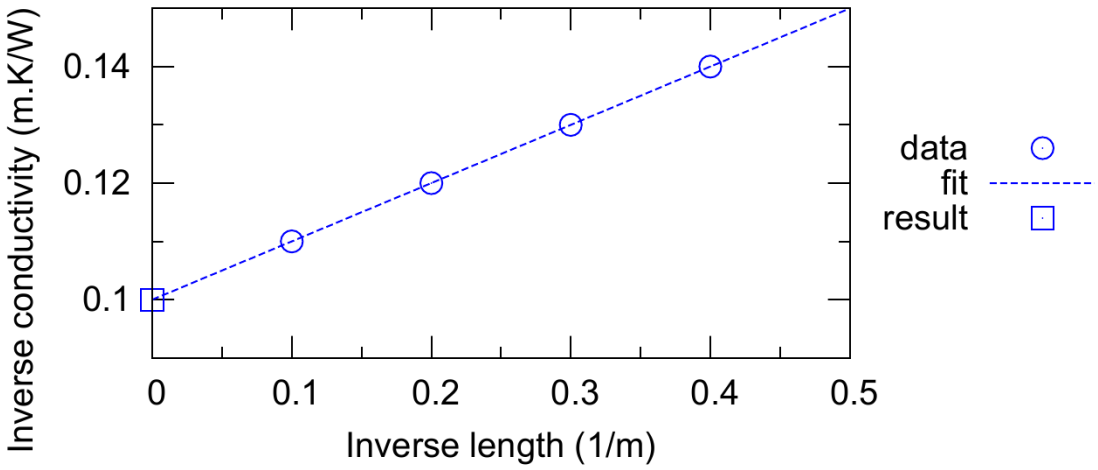

Figure 2.6: Inverse conductivity as a function of inverse simulation cell length, showing an idealised linear extrapolation procedure, where extrapolation to y-axis gives conductivity of an infinite system length, i.e., the bulk material.

There are two effects of finite system size that can cause an individual direct method simulation to diverge away from an inferred/expected linear trend, both of which result in overestimation of the length-dependent conductivity data point. First, when the distance between hot and cold sections (controlled by cell length) is shorter than the MFP, phonons travel ballistically (i.e., without any scattering events) from heat source to sink (*Sellan et al.*, 2010). Conductivities in shorter length cells are overestimated when this occurs, reducing the gradient of the linear fit and thus underestimating the extrapolated conductivity.

For a given length, conductivity is dependent on the CSA, or aspect ratio of the simulation cell. Conductivity is overestimated due to an underestimation of phonon-phonon scattering, from sparse phonon phase sampling in cells where cross section is small compared to length. Phonons that aren't resolved cannot contribute to phonon-phonon scattering effects. Reduced scattering means heat transport is artificially more efficient than expected from the bulk material.

2.8 Green-Kubo

Equilibrium molecular dynamic (EMD) simulations consider systems with constant average temperatures, and a net heat flux of zero. The Green-Kubo method is a way of using EMD to compute thermal conductivity, looking at heat flux caused by temperature fluctuations. The lattice thermal conductivity of the system is related to the duration of these variations. I use the Green-Kubo method to both compute and validate the workflow and results of the direct method. While the direct method has complex finite-size effects based on length and cross-sectional area, Green-Kubo is simpler in that number of atoms is the main factor. As long as the system is of sufficient size, which will be explored in Chapter 3, there is no need to care about arranging the cells or extrapolation procedures.

2.8.1 Methodology

The Green-Kubo method uses auto-correlation functions (ACFs) to quantify time-dependence of heat fluxes (shown in Fig. 2.7, and Equation 2.16). Instantaneous heat fluxes can be used to determine how energy is dissipated within a system.

The heat flux data required to generate the ACF is obtained from MD simulation in the NVE regime. As always, it is necessary to perform the NPT cell size convergence, and preliminary NVT to populate the atomic velocities.

For a timescale up to a chosen correlation length, the auto-correlation function is obtained over the series of net heat flux in each crystallographic direction

$$ACF_i = \langle J_i(0) \cdot J_i(t) \rangle \,, \tag{2.16}$$

where i specifies direction, J is heat flux, and t is the correlation length. Heat

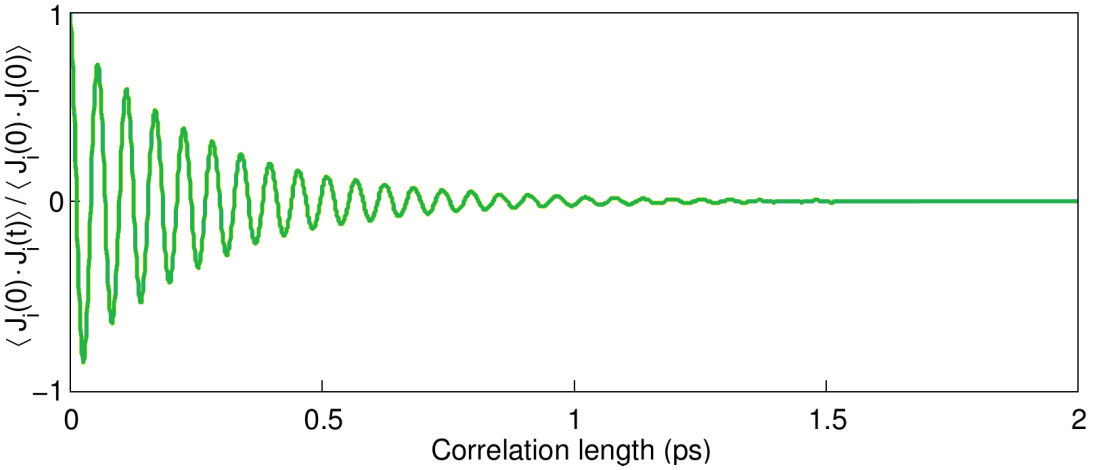

Figure 2.7: Normalised ACF. Correlation is taken over a longer length than shown on this plot (100 ps), however the function decays to less than 1% of its initial value at 2 ps. It continues to oscillate about zero, with a positive average value.

flux is calculated using

$$J = \frac{1}{V}\left[\sum_m e_m \mathbf{v}_m + \frac{1}{2}\sum_{m<n}(\mathbf{f}_{mn}\cdot(\mathbf{v}_m+\mathbf{v}_n))\mathbf{x}_{mn}\right], \tag{2.17}$$

where e is the energy of the mth atom, v is the velocity of the mth atom, $\mathbf{f}$ is the force acting on the mth atom, and $\mathbf{x}$ is the separation between the mth and nth atoms.

This acts as a cut-off, the significance of correlating points far apart in time decreases with the separation. The correlation length could be as long as the simulation length, but for large time differences there would be fewer and fewer heat flux pairs. This means there would be increased uncertainty on points of decreasing relevance. The correlation lengths I use are much shorter than the simulation length.

The integral of heat flux ACF is proportional to thermal conductivity via the Green-Kubo equation (see Fig. 2.8 and Equation 2.18),

$$\kappa_i = \frac{V}{k_B T^2}\int_0^\infty \langle J_i(0)\cdot J_i(t)\rangle \, dt \ , \tag{2.18}$$

where V is the simulation cell volume, k_B is the Boltzmann constant, and T is the average temperature of the system. The Green-Kubo equation is obtained from the fluctuation-dissipation theorem (*Kubo*, 1966), and relates the time-dependence of heat flux events to material properties, in order to obtain thermal conductivity. This means that the length of time over which the heat flux events autocorrelate represents the conductivity of the material, i.e., a short correlation length represents a rapid dissipation of heat, meaning the material efficiently transports heat and therefore has a high lattice thermal conductivity. In this study I use Green-Kubo results as an independent check on the direct method, as they do not have the same finite-size effects. Obtaining a converged conductivity result simply depends on using a large enough cell volume/number of atoms.

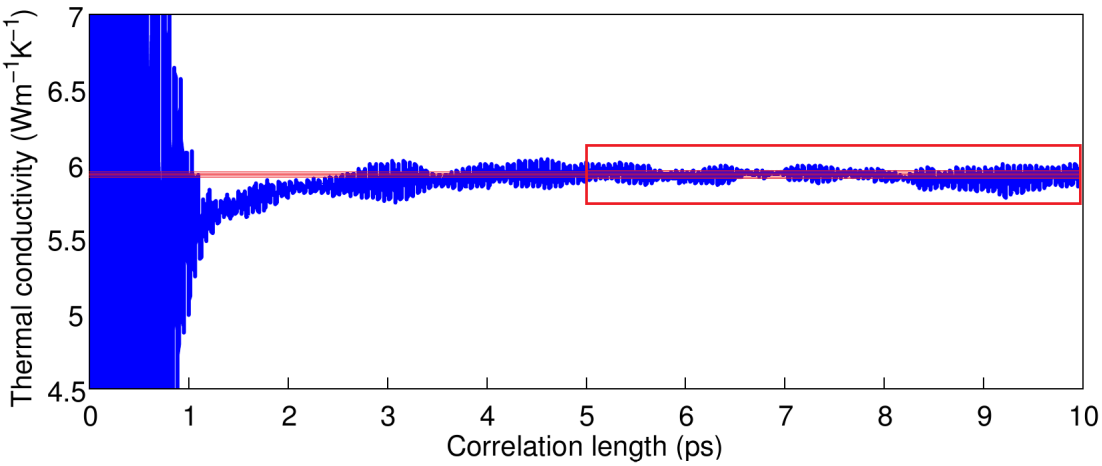

Figure 2.8: Integrated ACF, multiplied by constants to get thermal conductivity. Large variation in the first 1 ps corresponds to the correlation time where the ACF is unconverged (still decaying/large oscillations). Thermal conductivity is averaged from correlation time of 5 – 10 ps (region in red box).

2.8.2 Data processing

The individual integrals obtained from the Green-Kubo show variation from the average combined integral on the order of the mean. Many simulations from

different initial temperature conditions are required in order to ensure good sampling of conductivity, as well as ensuring the computation time for each is long enough for convergence. This makes Green-Kubo a computationally expensive method, especially for large systems.

From a large sample of integrals, the mean integral is examined to find a time window of convergence. This region exists after the initial large variations, and before any drift behaviour. This correlation window is then applied to all integrals separately, yielding a population of conductivities and uncertainties. I then applied a weighted average to this information, obtaining a conductivity for the entire population.

The ACF should decay to zero as correlation time tends to infinity, however noise in the ACF prevents this. This will ultimately cause the integral to diverge/drift on long timescales. *Howell* (2012) fits a series of exponential decays to their ACF, forcing the expected decay to zero and subsequent (constant) integral convergence. This represents a significant improvement on the conductivity estimate at long correlation lengths, but is mostly similar with the un-fit integrals early in the correlation.

2.9 Previous comparisons of Green-Kubo and direct method

A wealth of data comparing the conductivities yielded by non-equilibrium and equilibrium molecular dynamics is available for silicon, at temperatures around 1000 K. *Schelling et al.* (2002) consider Sillinger-Weber silicon, and find good agreement in conductivity results, once FSE are addressed. *Sellan et al.* (2010) consider the same material and find the two methods do not agree at a lower temperature of 500 K, although it is argued by *Howell* (2012) that their direct

method finite-size scaling was inappropriate. *Howell* (2012) performs their own calculations and review of literature, finding consistent results between the methods and the suite of studies considered. *Wang and Ruan* (2017) contribute further results consistent with *Howell* for Sillinger-Weber Si at 1000 K, as well showing agreement between methods for graphene and silicene (a two-dimensional allotrope of silicon) at 300 K.

Dong et al. (2018) show consistency between NEMD and EMD for silicene and Si nanowires. *Turney et al.* (2009) show very coherent agreements for Lennard-Jones argon across a range of simulation methods, including NEMD, EMD Green-Kubo, along with Boltzmann transport equation and lattice dynamics approaches.

Although the existing literature suggests good agreement between calculations run using the direct method and the Green-Kubo method, none of the existing studies consider a material as complicated as bridgmanite. Therefore in the next chapter, I computed conductivities using the direct and Green-Kubo methods, and investigate the agreement between the two.

2.10 Conclusion

In this chapter I introduced atomic-scale modelling, how it can be performed, and how atoms can be made to behave like realistic materials. I outlined molecular dynamics methodologies for computing thermal conductivity, and potential problems associated with them.

In this chapter, I have shown how the *Oganov et al.* (2000) potential can be used in LAMMPS to reproduce the behaviour of bridgmanite. I did this by calibrating the cutoff distances associated with the Buckingham and Coulomb cutoffs. I calculated structural parameters (e.g., lattice parameters, unit cell volume, elastic constants, and the bulk and shear moduli). Using LAMMPS, I

compared the structural parameters from calculations using my implementation of the potential with other calculations using the same potential. The main conclusion from this chapter is that bridgmanite is well replicated at the atomic scale using the *Oganov et al.* (2000) potential in LAMMPS.

In Chapter 3 I use the validated potential to calculate thermal conductivity and study the effects of finite simulation size on computed bridgmanite conductivity results. I first determine the finite-size effects for the Green-Kubo method, and then I use the Green-Kubo result to investigate finite-size effects in the direct method.

2.11 Summary

1. In this Chapter, I introduced atomic-scale modelling concepts and methods of computing thermal conductivity.

2. I implemented the *Oganov et al.* (2000) potential for bridgmanite and reproduced structural parameters at CMB conditions, finding good agreement (within 1%) with the results from previous implementations.

3. I gave a review of comparisons between the Green-Kubo and direct method, which have only previously been compared for simpler systems than bridgmanite at CMB conditions.

Chapter 3

Examining finite-size effects in thermal conductivity computations

A range of atomic-scale simulation methods are available to determine the lattice thermal conductivity of materials. These are invaluable for calculating thermal conductivity at conditions of which experiments are difficult, e.g., the extreme conditions found in the Earth's lower mantle (pressures and temperatures up to 136 GPa and 4000 K at the core-mantle boundary), however there are limitations to these methods, which will be investigated further in this chapter.

In this chapter, I explore how finite-size effects (FSE) influence the results of calculations performed using both the Green-Kubo method and the direct methods. I find that the finite-size effects in the Green-Kubo method are easily addressed, and so I then use the Green-Kubo result to independently verify the direct method calculations. By comparing these methods, I will reduce the current uncertainty around the temperature-dependence of FSEs. Quantifying the FSEs for the direct method is challenging, but the direct method is one of the ways in which conductivity is computed using *ab initio* methods. *Ab*

initio methods using the Green-Kubo method, on the other hand, are not readily available. Therefore the quantification of FSEs presented here, using interatomic potentials, could be used to inform the appropriate application of *ab initio* methods, e.g., quantifying FSEs in the direct method using interatomic potentials to inform appropriate cell geometries for DFT calculations, such as *Stackhouse and Stixrude* (2010); *Stackhouse et al.* (2015).

As previously discussed, it is important to ensure simulations represent material properties and physical properties as accurately as possible. Perhaps most obvious is ensuring the chemistry is correct, and that the atoms have correct charges, masses, and interactions with neighbours. Even if this chemical information is accurate, simulations can produce inaccurate results if the shape and size of the modelled cells do not reproduce the bulk material behaviour. In the case of thermal conductivity, this means ensuring the phonon population and interactions between phonons are both accurately reproduced.

Previous studies report that the finite-size effects can influence calculated thermal conductivity values (e.g., *Sellan et al.*, 2010; *Stackhouse et al.*, 2015; *Hu et al.*, 2011). Thermal conductivity is underestimated if the length of the system is comparable with or smaller than the dominant heat-transporting phonon wavelengths (*Sellan et al.*, 2010). This is because phonons with longer wavelengths than the size of the simulation box cannot be represented in a molecular dynamics simulation. Such phonons cannot then contribute to heat flow. Another way the effect of finite system size can be observed is in the reproduction, or failure, of thermal resistance. During phonon-phonon scattering, heat flow is impeded.

If simulation cells of sufficient length to support phonon mean free paths are used, phonon-phonon scattering in the direction of heat flow will be accurate. What will not necessarily be correct is the phonon-phonon scattering in the directions perpendicular to this. The above principal applies, if the system has

too small a cross-sectional area (compared to its length), the phonons involved in lateral scattering cannot be resolved. This reduces thermal resistance within the system, thereby overestimating conductivity. A longer cell length inherently has more phonons within the cell; this means the cell requires a proportionally larger cross-sectional area in order to reproduce phonon behaviour.

The FSE discussed in this chapter are therefore those that are observed considering the cell size in terms of the phonon mean free path and also the scattering effects. I find that when using the direct method (Section 3.2.7), FSE are observed when the cell length is of comparable magnitude to the phonon mean free path or when the CSA is too small to accurately reproduce phonon-phonon scattering. The same effects are apparent but more easily addressed in calculations using the Green-Kubo method (Sections 3.1.4).

I not only investigate thermal conductivity at CMB conditions, but also at conditions at which conductivity will be largest, i.e., low temperatures, high pressures, and no impurities. I am primarily interested in the conductivity at the CMB, 136 GPa and 4000 K, and I also investigate the FSE at 136 GPa and 1000 K, both considering chemically and isotopically pure $MgSiO_3$ bridgmanite.

I assume that Green-Kubo finite-size effects have been removed, and then compare the results to those from direct method calculations to inform on the FSE in the direct method. These results present one of the most in-depth analyses of FSE, and the conclusions of this could be further applicable within the field of material science.

3.1 Green-Kubo procedure

Here I outline my approach for applying the Green-Kubo method for computing conductivity to bridgmanite at lower mantle conditions (Fig. 3.1). First I show accurate results can be obtained within the chosen correlation length. I then

show how results represent a large sample of possible conditions, and a way of minimising error by combining multiple heat flux autocorrelation functions (ACFs). Finally I show that all these components are valid with respect to total simulation time, before presenting how finite simulation size affects conductivity results.

3.1.1 Correlation length convergence

As described in Section 2.8.1, I compute ACFs up to correlation lengths of 100 ps for all calculations, with (100,000) 1 fs timesteps. This length is longer than required but selected to show convergence in the conductivity result, and check for drift in the integrals for long correlation times. Figure 2.7 shows that the magnitude of the ACF decays to less than 1% of its initial value at a correlation time of about 2 ps, inferring the start of convergence for the integral and thus conductivity.

Considering bridgmanite at lower mantle pressures, I find correlation time windows of 2–30 ps to be suitable. This allows the initial high variability in integral value to be ignored and is long enough for good sampling of the integral, but short enough to ignore the drift-effects. The magnitude and range of the window typically increases with conductivity (or with decreasing temperature at constant pressure), the correlation window is 2–8 ps at 3000 K (Fig. 3.2b), and 10–30 ps at 1000 K (Fig. 3.3b). These correlation lengths are on the same order of magnitude as used by *Haigis et al.* (2012), who used the Green-Kubo method and observed convergence in MgO conductivity results after 30 ps, albeit at a temperature of 3000 K.

As shown in Figures 3.2c & 3.3c, the integral drifts considerably outside of the chosen correlation window. This effect needs to be resolved before accurate conductivity results can be determined, and is caused by an increase in the ACF

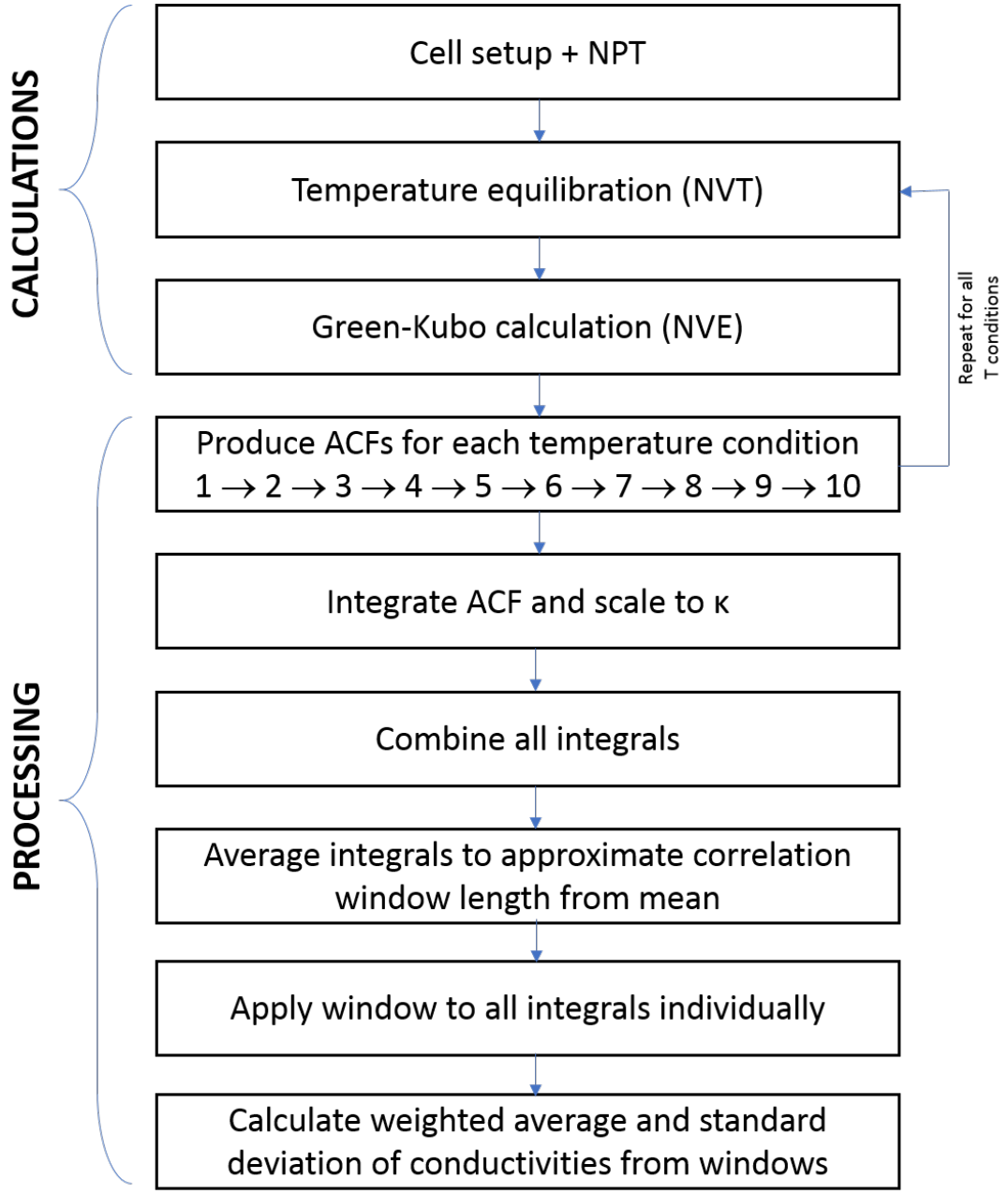

Figure 3.1: Flowchart showing the Green-Kubo procedure. The total run time of a simulation for each initial temperature condition (given for each supercell geometry in Tables 3.1 and 3.2) is split into ten, to produce that many ACFs. Simulation time is split in this manner to guarantee computational feasibility, where restarting calculations bypasses maximum job run times in addition to improving subsequent sample averaging of integrals.

signal to noise ratio at long correlation lengths. Theoretically, the ACF tends to zero as correlation length tends to infinity. In practice this doesn't happen because of noise, but it can be thought of as the signal tending to zero and the

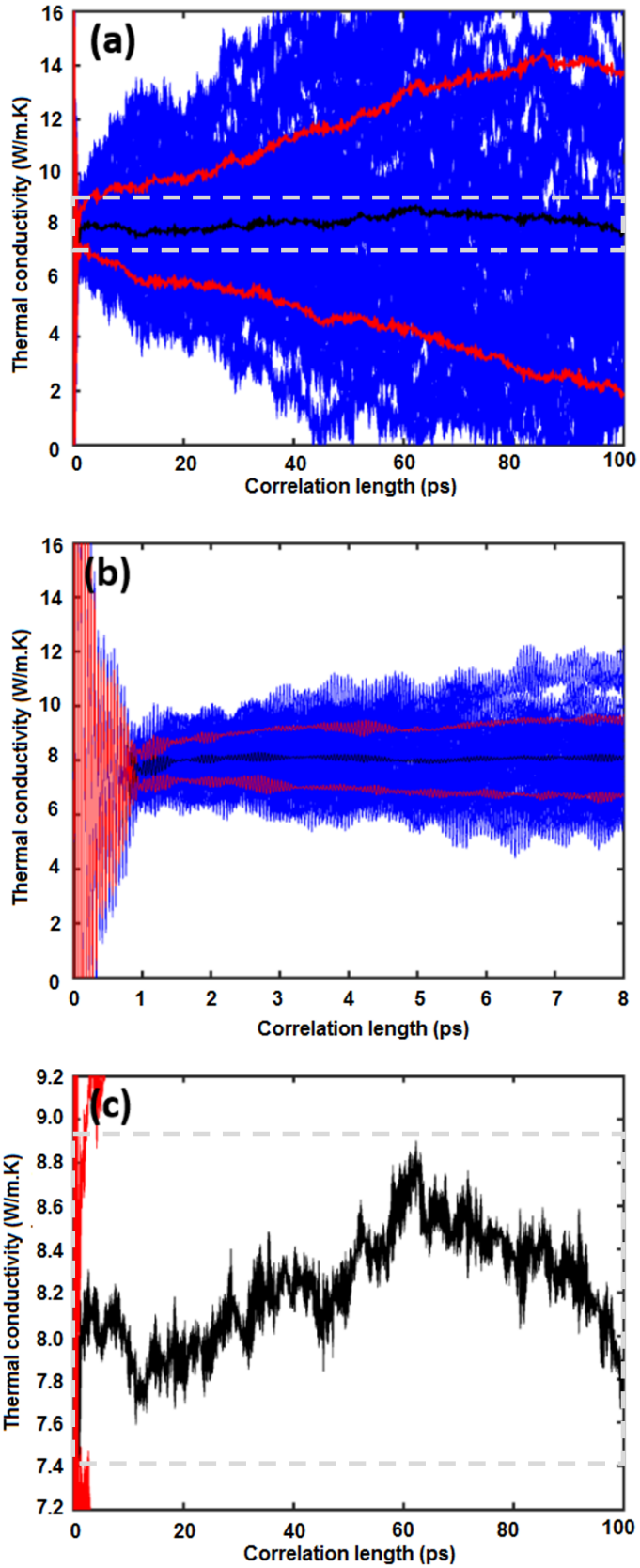

Figure 3.2: Integral populations (blue) from GK calculation at 3000 K, with mean integral and plus/minus standard deviation (red). **a.** shows the range of conductivity series over the full correlation length. Dashed box shows position of data series shown in (c). **b.** shows the series up to the end of the correlation window (8 ps, the window starts at 2 ps). **c.** focuses on the mean integral over all the correlation length, past the correlation window where it begins to drift away from a converged value.

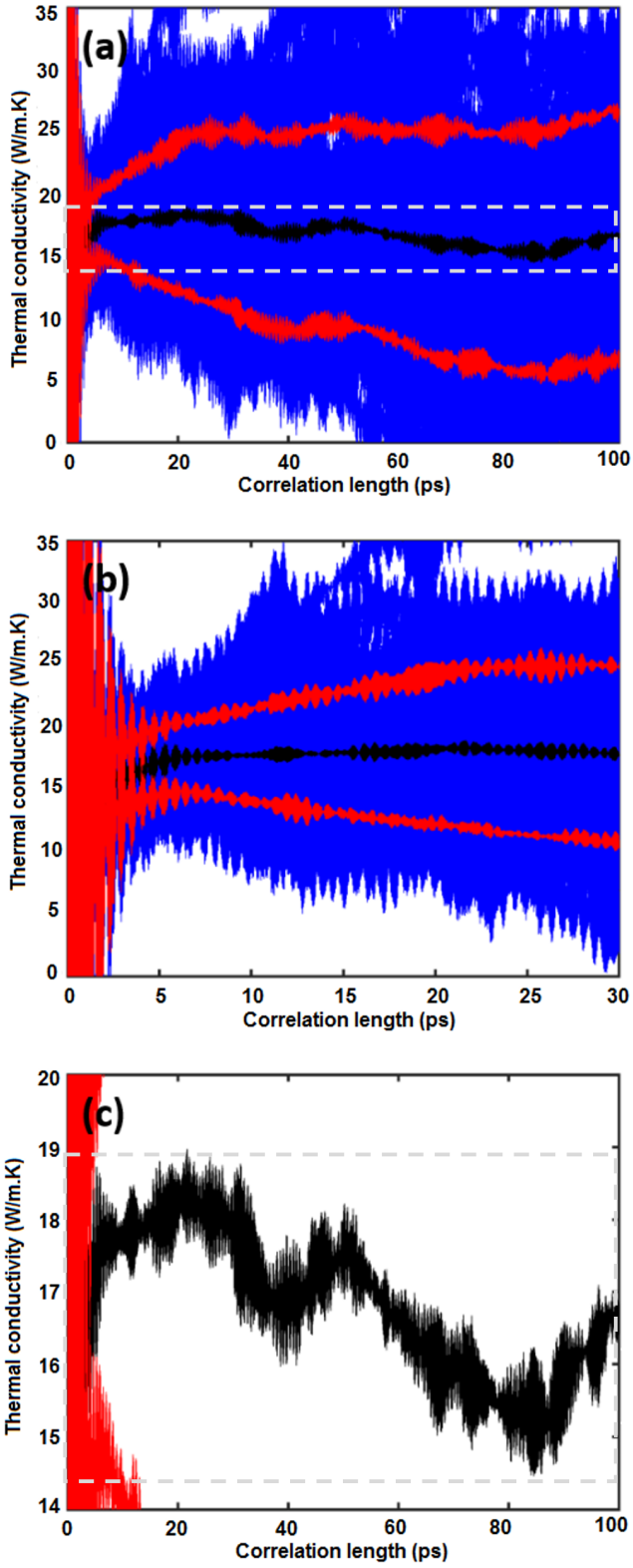

Figure 3.3: Integral populations (blue) from GK calculation at 1000 K, with mean integral and plus/minus standard deviation (red). **a.** shows the range of conductivity series over the full correlation length. Dashed box shows position of data series shown in (c). **b.** shows the series up to the end of the correlation window (30 ps, the window starts at 10 ps). **c.** focuses on the mean integral over all the correlation length, past the correlation window where it begins to drift away from a converged value.

noise remaining finite.

3.1.2 Integral sample convergence

ACFs produced by each simulation are integrated separately, and averaged into a single series. From this combined integral I pick by eye a window of correlation lengths to capture a flat, converged region (or the section just after the 'bottleneck' if convergence is not obvious, and before the integral drift). The sections of the individual integrals within the correlation window are averaged, to give a population of windowed averages (with uncertainty relating to the spread of the integral within each window). Based on these uncertainties, a weighted average is taken of this population (i.e., the greater the uncertainty, the less the value contributes to the average). This weighted average gives a single value with standard deviation, and this value is directly proportional to thermal conductivity, as given by Equation 2.18.

3.1.3 Simulation length convergence

In this section, I calculate the auto-correlation functions at different points throughout a simulation, to determine the effect of simulation length on the conductivity result (and the convergence of these values with increasing simulation time). To investigate this, I process the auto-correlation function every 1 ns up to a simulation length of 10 ns (Fig. 3.4). There is little variability in conductivity result average with increasing simulation length. The variation is ± 0.02 on an average of 6.80 $\mathrm{Wm^{-1}K^{-1}}$.

While the results in Figure 3.4 suggest that the conductivity is converged with respect to simulation length, it does not mean the constituent integrals have converged to a single value. Figure 3.5a corresponds to an individual simulation length of 1 ns, and 3.5b shows a simulation length of 10 ns. This shows that

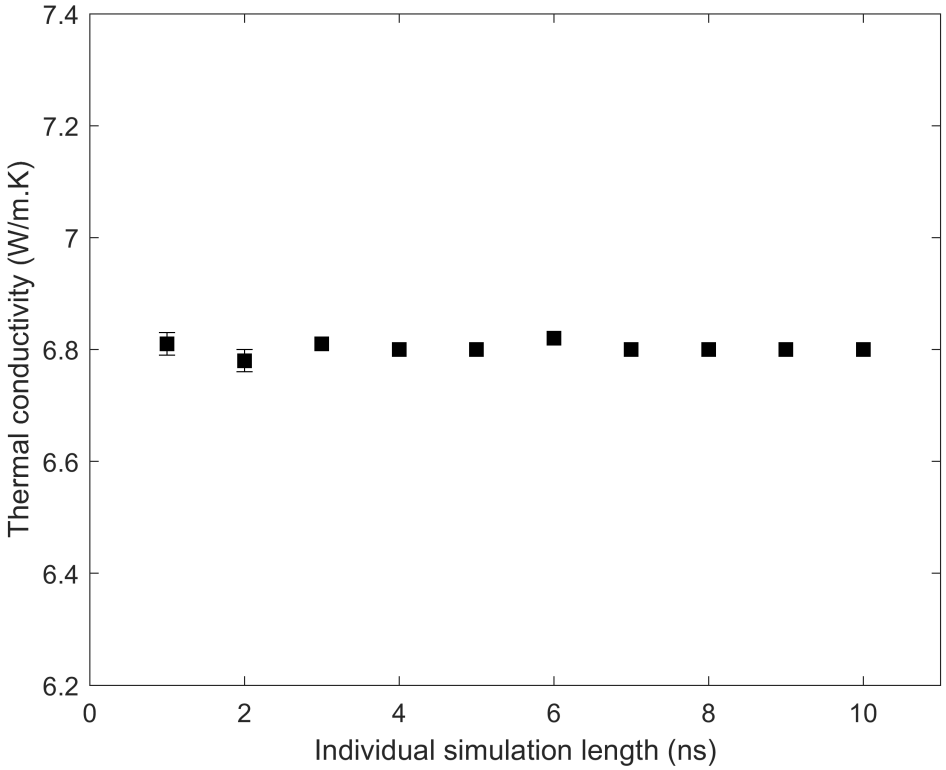

Figure 3.4: Thermal conductivity as a function of effective simulation time for Green-Kubo simulations. Error bars show one standard deviation and are smaller than symbol size.

although the conductivity value is similar, the individual integrals converge on the mean, reducing the spread and standard deviation. Negative conductivities can be seen on 3.5a, which is obviously unphysical, reinforcing the idea that averaging a large enough sample of integrals is more important than the simulation time that went into producing a single series.

In the simulation lengths I tested, the conductivity result already appeared converged to a stable value. To explore this further, I showed that as simulation length increased, the range of integral values decreased. Therefore conductivity values obtained for simulation lengths of 10 ns have a smaller error than those obtained at 1 ns (Fig. 3.4). It is possible that simulation lengths below those tested here (1 ns) could show incorrect (i.e., non-converged) values for the conductivity of bridgmanite at lower mantle conditions. The simulation length

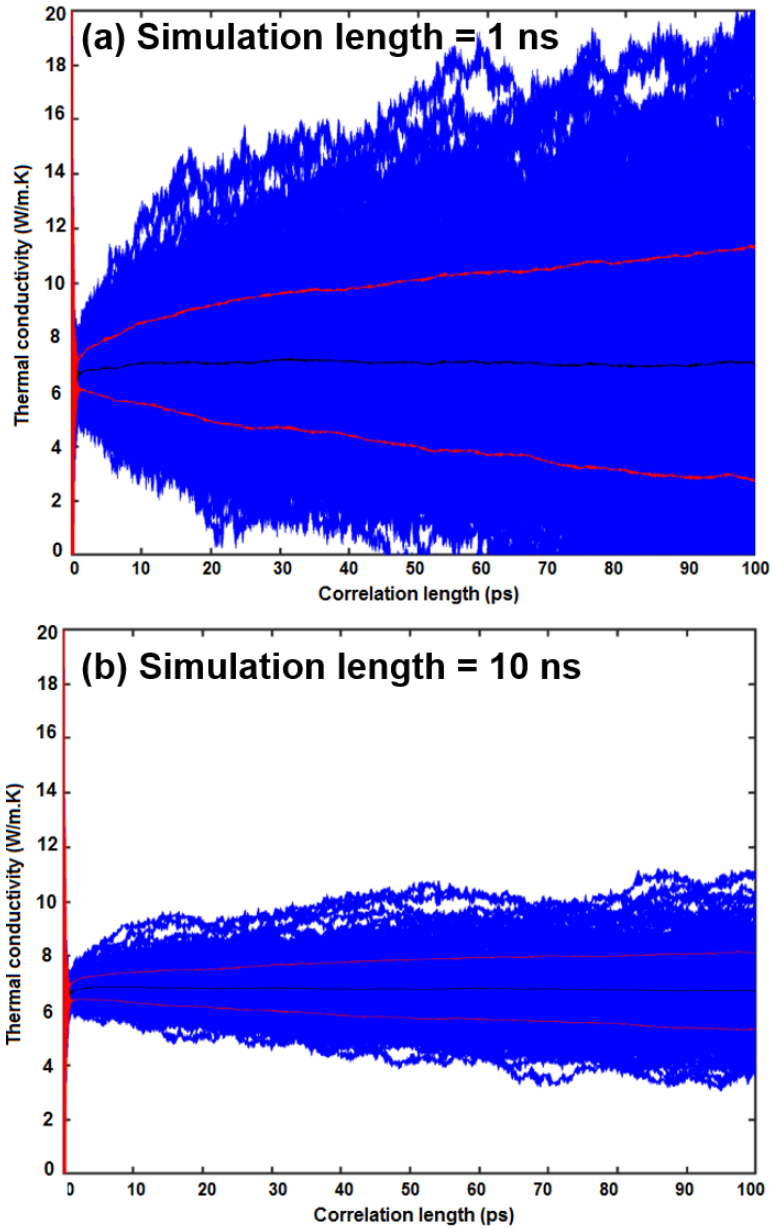

Figure 3.5: Conductivity as a function of correlation length. Integral populations (blue) from GK calculation at 4000 K, with mean integral and plus/minus standard deviation (red). Both show series over full correlation length, where the simulation length is **(a)** 1 ns and **(b)** 10 ns.

is therefore less important than the number of integrals and their correlation length, assuming that the simulation length is exceeds the required correlation length window.

3.1.4 Finite-size effect convergence

The bridgmanite unit cell is orthorhombic (i.e., a:b:c = 1:1:1.4), so I assemble supercell structures of 3×3×2, 4×4×3, 5×5×4, and 6×6×4 to make a supercell arrangement approximating a cube (Tables 3.1 and 3.2). These supercells contain 360, 960, 2000, and 2880 atoms respectively (20 atoms in the unit cell). The goal here was to minimise the height to area ratio in each direction, while increasing the atom count.

The supercell arrangement of 3×3×2 fails to reproduce the conductivities of the larger cells for both temperatures (Figs 3.6a & 3.6b). Although there is no clear convergence shown in Figure 3.6a, the variation in thermal conductivity between the simulation cells ≥4×4×3 is on the order of 0.1 $Wm^{-1}K^{-1}$. At 1000 K, the agreement between simulation cells ≥4×4×3 is more obvious (Fig. 3.6b). I use the 4×4×3 supercell as the conductivity obtained is in good agreement (within 0.5 $Wm^{-1}K^{-1}$) with the larger cells.

This a useful result in terms of computation efficiency, as 6×6×4 supercells are 3 times as large as 4×4×3. I investigate the finite-size effects at conditions of both 4000 K (Fig. 3.6a, Table 3.1) and 1000 K (Fig. 3.6b and Table 3.2).

Table 3.1: A summary of the simulations performed at 4000 K, corresponding to the data shown in Figure 3.6a.

Supercell	Simulation length	# initial conditions	Total run time	
3×3×2	10 ns	20		2 μs
4×4×3	10 ns	30		3 μs
5×5×4	5 ns	20	1 μs	1.7 μs
	1 ns	70	0.7 μs	
6×6×4	1 ns	80		0.8 μs

Table 3.2: A summary of the simulations performed at 1000 K, corresponding to the data shown in Figure 3.6b

Supercell	Simulation length	# initial conditions	Total run time
3×3×2	1 ns	20	0.2 μs
4×4×3	1 ns	50	0.5 μs
5×5×4	1 ns	50	0.5 μs
6×6×4	1 ns	50	0.5 μs

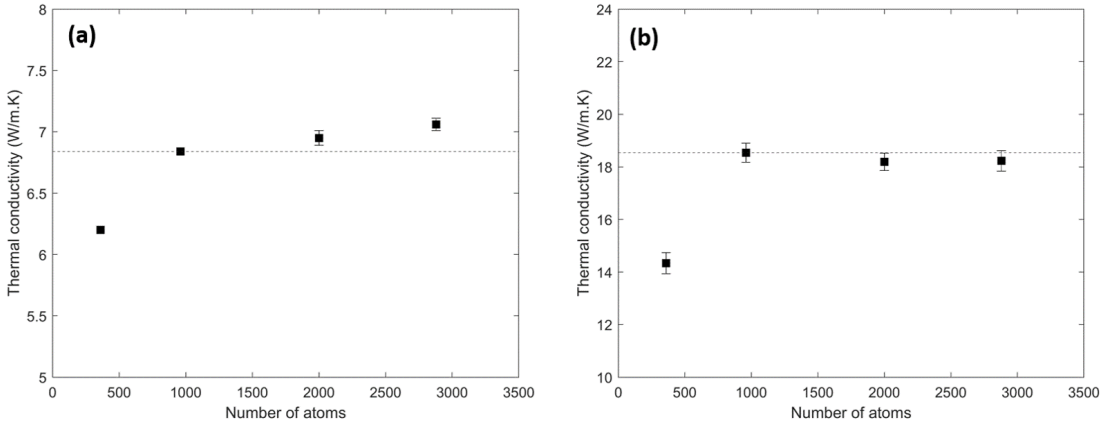

Figure 3.6: Finite-size effects at **(a)** 4000 K and **(b)** 1000 K. Thermal conductivity as a function of the number of atoms in the simulation. Error bars show one standard deviation. Full data given in Table 3.1.

3.2 Direct method

In this section I outline how I apply the direct method to compute the thermal conductivity of bridgmanite (Fig. 3.7). I outline the initial system setup, the supercell geometry and how the system is divided into sections to determine the temperature gradient. I then discuss properties which must be controlled to ensure accurate results, namely the magnitude of the temperature gradient, and the convergence of computed conductivity with respect to total simulation time. I briefly introduce the data processing methodology, before explaining how the effects of finite system size are considered and mitigated.

Finally I discuss my results with respect to theoretical predictions (i.e., *Hu et al.*, 2011), and discuss the required system size to compute the conductivity of bridgmanite at lower mantle conditions.

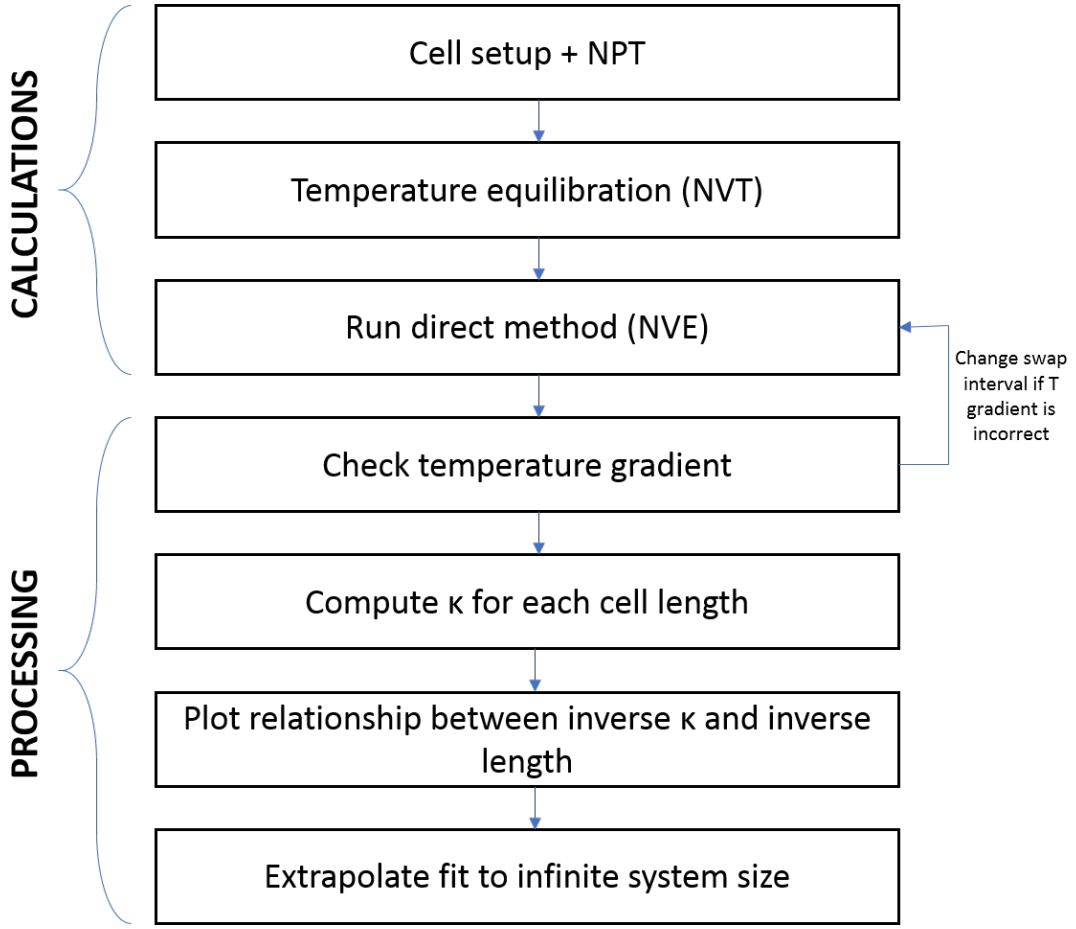

Figure 3.7: Flowchart showing the direct method procedure.

3.2.1 Constructing supercells

In order to investigate how FSE can affect the results of DM calculations, I use very large cells, both in length and cross-sectional area. I use supercells of 6, 8, 10, 12, 16, 24, 48, and 96 unit cells long and with corresponding cross sections of 1×1, 2×1, 2×2, 4×4, 8×8, and 12×12 (see Tables 3.3 and 3.4).

In the direct method, the simulation supercell is split into sections along its length (Fig. 3.8). The temperature of each section is calculated using the kinetic energy, as described in Section 2.2. The symmetry of the bridgmanite crystal system allows unit cells to divided into two, such that the width of sections is half a unit cell along the length of the supercell (the direction of heat flow).

Two of these sections, half the supercell length apart, are designated as the

Table 3.3: Simulation run times (ns) for each simulation cell cross-sectional area, and each simulation length, at 4000 K

	Length							
	6	8	10	12	16	24	48	96
1×1	5	5	5	5	5	5	5	5
2×1	5	5	5	5	5	5	5	5
2×2	50	50	50	50	50	50	50	10
4×4	10	10	10	10	10	10	10	n/a
8×8	1	1	1	1	1	1.5	1.5	n/a
12×12	1	1	1	1	1	1	0.6	0.6

Table 3.4: Simulation run times (ns) for each simulation cell cross-sectional area, and each simulation length, at 1000 K

	Simulation length							
	6	8	10	12	16	24	48	96
1×1	10	10	10	10	10	10	10	10
2×1	10	10	10	10	10	10	10	10
2×2	10	10	10	10	10	10	10	10
4×4	10	10	10	8	5	3	2.5	1.4
8×8	1	1	1	1	1	0.8	0.4	0.18

heat source and heat sink. It is within these sections that the kinetic energy of the atoms is swapped. Heat flows in both directions from the hot section because of cell periodicity (see Section 2.7.1), meaning there are two temperature gradients and the average temperature can be determined for equivalent sections.

Where L is the supercell length in unit cells and S (= 2L) gives the number of sections, there are S/2 + 1 temperature points to fit the gradient to. The width of a section, S_W, is half that of a single unit cell. As the temperature gradient is non-linear around the heat source and sink, I ignore S/12 sections (rounded to the nearest integer) from both ends of the temperature gradient. For a given simulation cell, S/3 + 1 points are used to fit the temperature gradient with a linear least squares fit. The minimum supercell length considered is 6 unit cells (12 sections, 5 data points for fitting), in order for an accurate sampling of the temperature gradient.

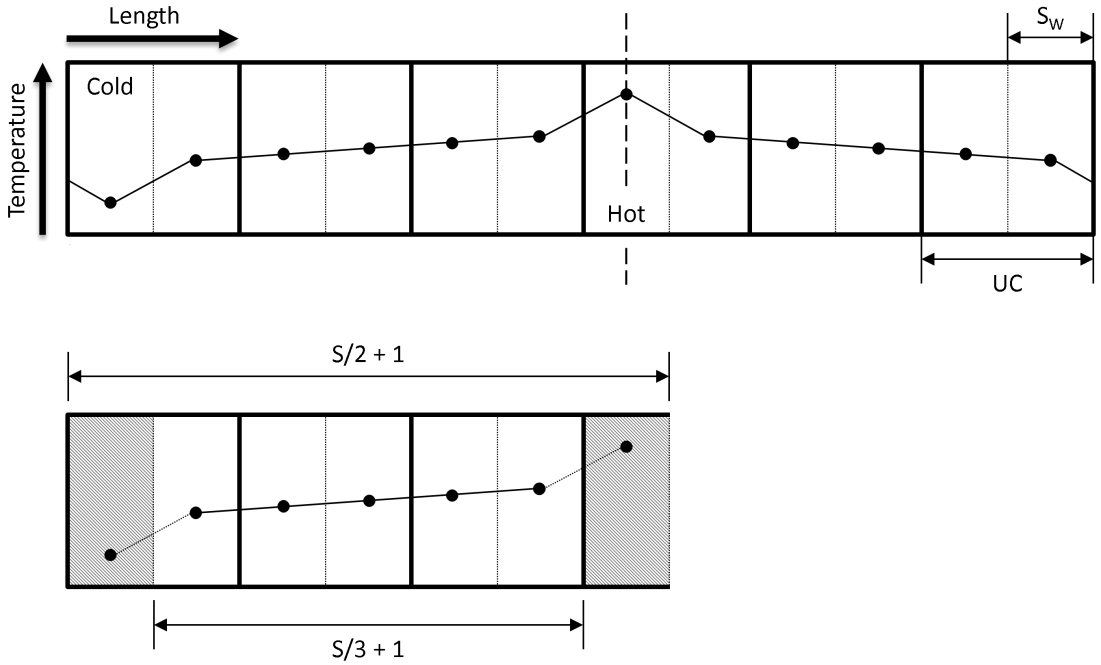

Figure 3.8: Temperature profile and geometry schematic for a cell 6 unit cells long. The temperature profile is non-linear, steeper gradient than the surrounding, immediately around the heated sections. In longer cells, the non-linear region will be wider than one section, requiring more sections to be ignored. The temperature profile is folded over onto itself to average one temperature gradient. The equations discussed hold as long as a unit cell is divided into two sections, and a twelfth of the total sections are removed from each end of the combined gradient.

3.2.2 Influence of section width

I investigated changing the width of the heated sections and found that the section width has no effect on the resultant conductivity value, assuming there are enough temperature points to fit the linear gradient. Furthermore, changing the width (and thus number) of temperature bins has no effect on the sampled gradient, assuming resolution is large enough to capture the non-linear region around the heat source/sink (Fig. 3.9).

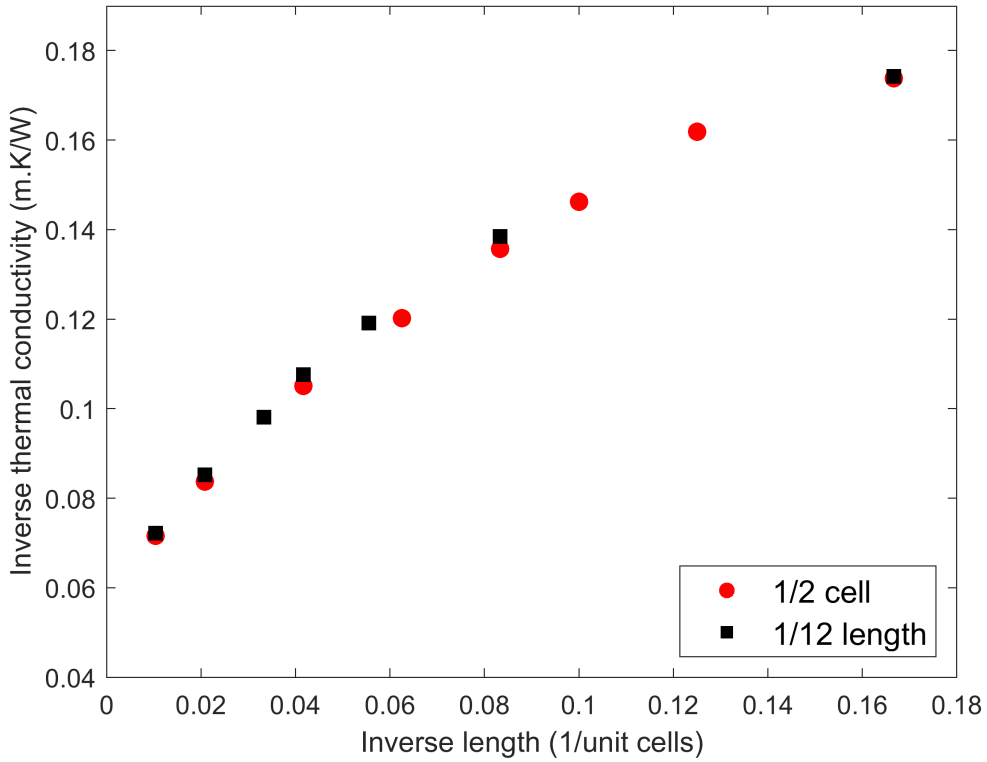

Figure 3.9: Conductivity results from direct method when temperature is calculated from sections half a unit cell wide, and also a twelfth of the total length. The amount of points in the temperature gradient changes when the section width depends on the unit cell, but not on the length (i.e., there are always twelve sections, the gradient is fit to five data points).

3.2.3 Temperature gradient

In the direct method, it is important to control the magnitude of the temperature gradient, such that Fourier's law (Equation 2.12) remains valid, i.e., conductivity is constant along the length of the cell. Thermal conductivity is strongly temperature-dependent at upper lower mantle conditions (1000 K), it is therefore undesirable to have a large temperature gradient across the cell, because this results in varying thermal conductivity. The opposite case is also true, the difference in temperature between hot and cold sections must be larger than the uncertainty in the average system temperature.

In all of my simulations, I keep the temperature difference between the ends

Table 3.5: Intervals used for swapping atomic velocities in the hot and cold sections, for each simulation cell cross-sectional area at 4000 K.

	Cell length (UC)							
	6	8	10	12	16	24	48	96
1×1	40	50	100	100	125	125	250	250
2×1	40	50	100	100	125	125	250	250
2×2	40	50	100	100	125	125	250	250
4×4	20	20	25	25	40	50	100	n/a
8×8	5	5	8	8	10	20	25	n/a
12×12	1	1	2	2	4	5	8	10

Table 3.6: Intervals used for swapping atomic velocities in the hot and cold sections, for each simulation cell cross-sectional area at 1000 K.

	Cell length (UC)							
	6	8	10	12	16	24	48	96
1×1	40	40	40	100	100	125	250	500
2×1	40	40	40	100	100	125	250	500
2×2	10	10	20	20	25	40	50	100
4×4	1	2	4	5	8	10	20	25
8×8	1	1	1	1	1	2	4	5

of the gradient to 20% the mean temperature. I control the magnitude of the gradient by altering the interval at which heat is exchanged (at the intervals shown in Tables 3.5 and 3.6), via swapping atomic velocities in the hot and cold sections (see Section 2.7.1). To produce the desired gradient magnitude as outlined above, shorter intervals are required as cell length decreases, cross-sectional area increases, and the mean cell temperature decreases. The easier it is for heat to flow from hot to cold (smaller distance between, more area for heat transport, lower temperature/less thermal resistance), the more heat must be transported (in the form of shorter intervals between heat swaps) to maintain a temperature gradient.

3.2.4 Simulation time convergence

A plot of thermal conductivity versus time shows large variability in conductivity as the temperature gradient evolves and approaches steady-state (Fig. 3.10). This

is related to the setup of the temperature gradient and its transition to steady behaviour. For this reason, the timesteps containing this behaviour are ignored when determining conductivity. This simply means removing the temperature gradient and heat flow data from the rest of the series. How this is applied varies in practice, but on a 1 ns simulation, I typically ignore the first 100 ps (10% simulation time).

The cumulative average of conductivity tends towards a constant value while the uncertainty decreases (Fig. 3.10). This is a simple check to ensure accurate results, where the simulation can be extended if more data is required.

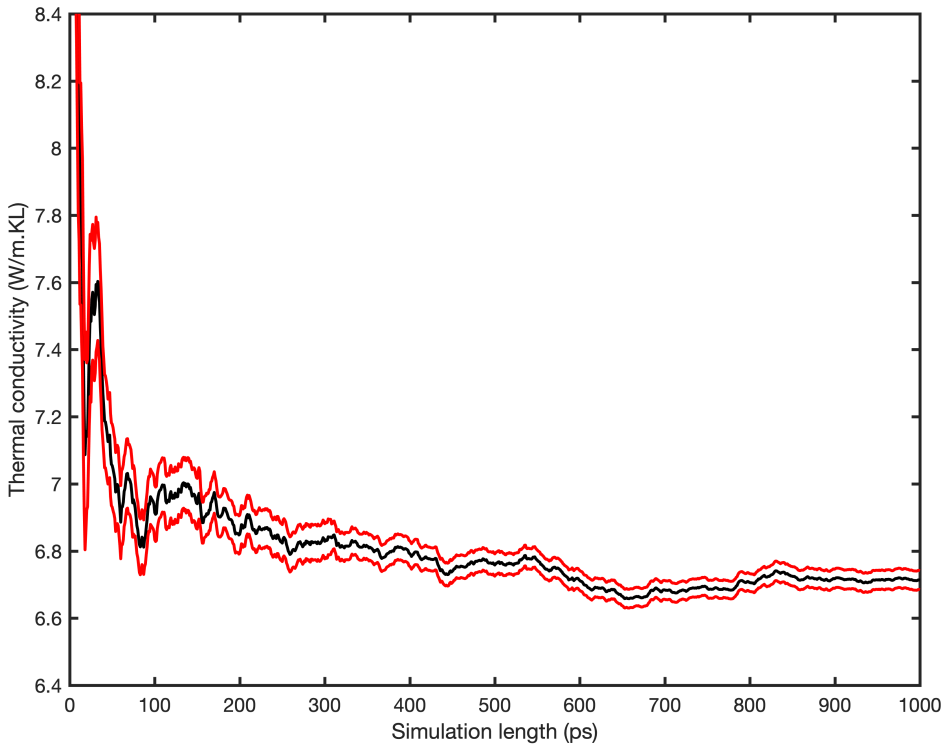

Figure 3.10: Thermal conductivity as a function of simulation time, showing convergence with increasing time. Cell size = 48×2×2. Conditions = 4000 K. Black shows cumulative average, red shows upper and lower bounds of error (1σ).

It is also possible for a simulation to be too long however, where the conductivity result will drift from its converged position (Fig. 3.11). This is due to inaccuracies in the molecular dynamics integrator (Section 2.2). It is

difficult to spot by just looking at the conductivity result and uncertainty, but easy to observe in the time series and/or graphically. The conductivity value obviously begins to change erratically, and the uncertainty begins to increase. The uncertainty would never increase if the result was still converging, making this a useful marker to look for in the series.

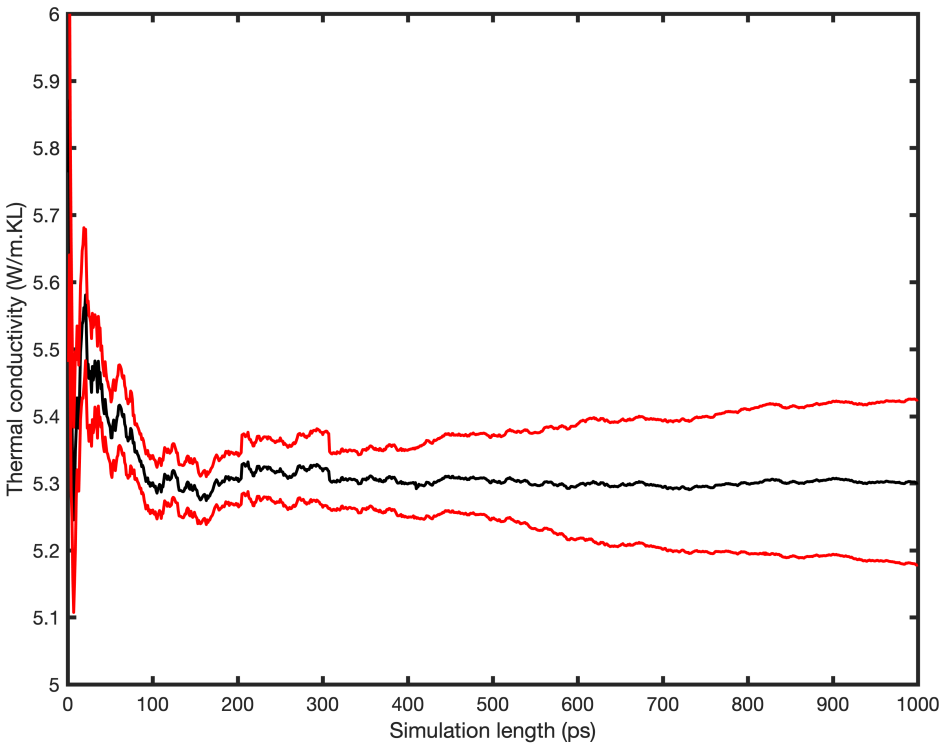

Figure 3.11: Thermal conductivity as a function of simulation time, showing drift with increasing time. Cell size = 8×2×2. Conditions = 4000 K. Black shows cumulative average, red shows upper and lower bounds of error (1σ).

3.2.5 Data processing

Thermal conductivity is calculated from Fourier's law (Equation 1.3). The cumulative average of conductivity is calculated, along with the errors, which are calculated as one standard deviation of the mean (e.g., Fig. 3.10).

3.2.6 Inverse extrapolation procedure

As discussed in Section 2.7.2, the results from simulations of varying cell lengths are used to determine the conductivity of the bulk material (Fig. 3.12). The lack of a linear relationship indicates finite-size effects (Fig. 3.12a).

3.2.7 Finite-size effects and convergence issues

To explore the FSE and convergence issues for calculations using the direct method, I first show results at 4000 K and then at 1000 K. In each case, I determine conductivities for varied cell cross-sectional areas. I conclude by showing that the nature of FSE on conductivity results varies for different conditions.

FSE at 4000 K

It is clear in Figure 3.12a that supercell CSAs of 1×1 and 2×1 overestimate conductivity (underestimate inverse conductivity) with respect to the larger CSAs. As discussed earlier (Section 2.6), this can be attributed to unrealistic biasing of phonon scattering within a narrow simulation cell. For the supercells with shorter lengths (larger inverse length), increasing CSA (to 2×2) brings the results into alignment. Although the variation between the larger (>2×2) CSAs appears significant, this is due to the inverse axis and the absolute difference in conductivity estimates is on the order of 0.5 $\mathrm{Wm^{-1}K^{-1}}$.

Another problem is apparent when looking closely at the shortest cells in the series (highest inverse length). They appear to overestimate conductivity with respect to the expected linear fit through the other short cells (see the linear trend on Fig. 3.12a). This can be explained by the cell being on the order of the phonon MFP, as discussed later in Section 3.2.9, allowing for phonons to travel from hot to cold without any scattering events (Ballistic Phonon Transport). This means

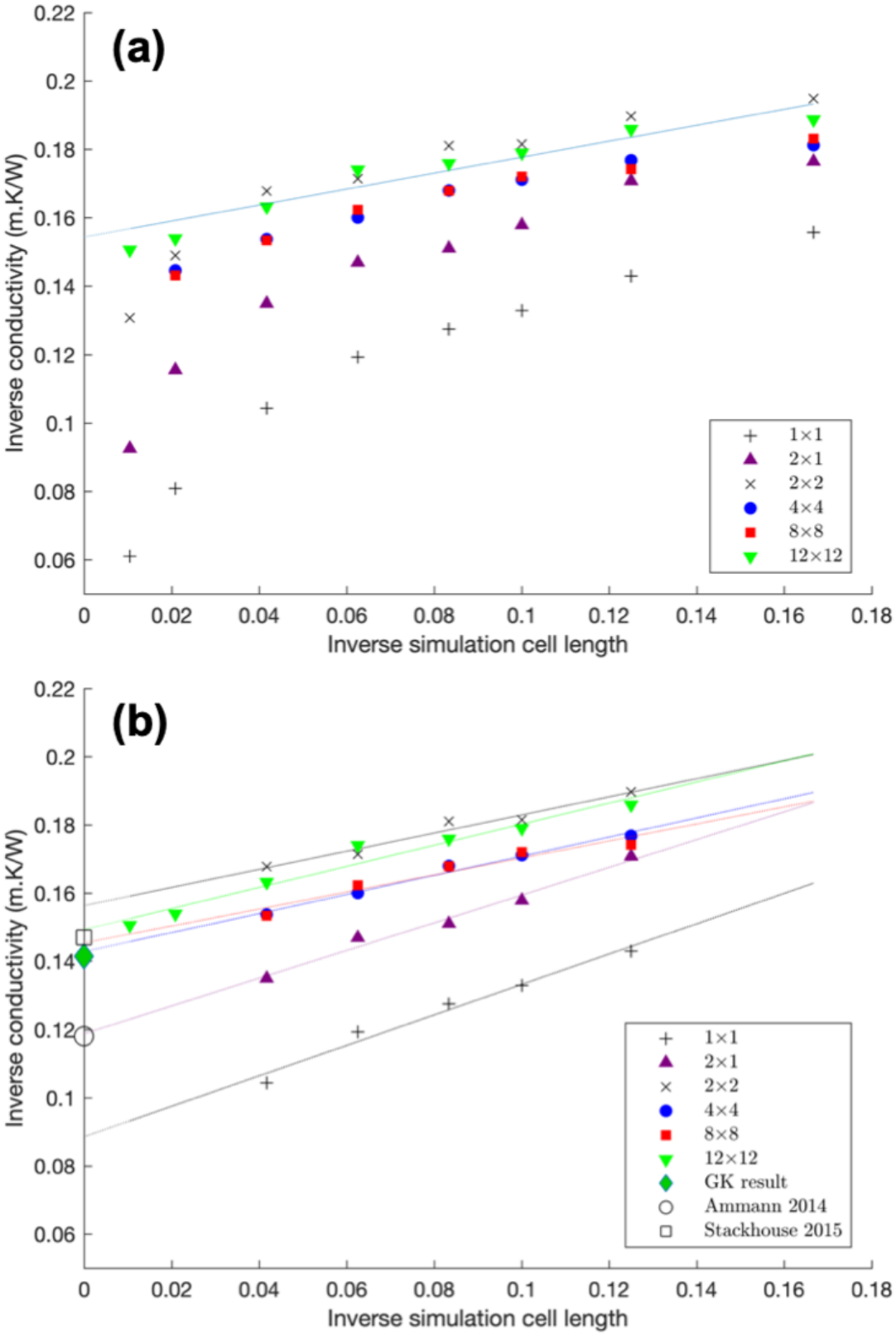

Figure 3.12: Inverse conductivity plotted against (a) all inverse simulation cell lengths and (b) for cell lengths between 8 and 24 UC, both for direct method simulations performed at 4000 K. Dotted line shows linear least squares fit. Error bars for results from this study showing one standard deviation are smaller than symbol size. Also shown are extrapolated direct method results from *Ammann et al.* (2014) and *Stackhouse et al.* (2015).

the simulation does not have thermal resistance representative of the material. No correction can be applied here, the 6 UC length supercells must be excluded from the extrapolation.

The effect of removing the shortest cell length is subtle, but it improves the fit to the remaining series and the agreement with the Green-Kubo estimate of thermal conductivity. Although the 8×8 supercell with length 8 (inverse length of 0.125) also shows a slightly anomalous conductivity result, it is still considered in the fit, as the results for all other CSAs at length 8 fit with their respective trends. The argument of removing short cells is further discussed with respect to the results at 1000 K, where the effect is much more significant (e.g., Fig. 3.15).

While the shorter cells across all cross-sectional areas produce similar conductivity results (Fig. 3.12), they diverge from the expected linear trend with length. The magnitude of this divergence appears to decrease with increasing CSA. This suggests that there is an aspect ratio finite-size effect, as reported by *Hu et al.* (2011). This is similar to the CSA effect mentioned above, whereby phonon-phonon scattering behaviour is not being modelled correctly. This explains why the effect is larger the smaller the CSA, where there are fewer phonons to participate in scattering events.

The divergence is not observed for 12×12 CSA (Fig. 3.12a). Such a large cross-sectional area has a high computational cost, however, and is not really a viable option for employing the direct method to calculate conductivity at many P-T conditions. The largest CSA (i.e., 12×12) show the greatest scatter about the trendline. This is likely due to convergence issues and could be improved by averaging repeated simulations, however this is computationally intensive.

The 12×12 simulations give the only results that do not show divergent behaviour with increasing length. The results in Figure 3.12b show that smaller CSAs (>2×2) can provide equally robust results, if the divergent behaviour is identified and removed from the extrapolation to infinite system size. In order

to avoid divergence of thermal conductivity results with respect to increasing cell length, I recommend ignoring cells with lengths longer than 24 Unit Cells (UC). Cells that are 24 UC or shorter in length are converged with respect to CSA and GK (Fig. 3.12b). Computational cost increases with length, as does the divergence from linear behaviour. I can still produce accurate results using the cell lengths where 2×2 CSA cells produce the same results as those from 12×12 (Fig. 3.12b), with significantly reduced computational cost. These key dimensions are somewhat arbitrary, only inferred from observations of the finite-size effects. Different materials require their own FSE analysis, despite any similarities in chemistry to bridgmanite or conditions to the lower mantle.

Comparison with the equivalent Green-Kubo point shows good agreement for the extrapolations from CSAs 2×2 and above. The 12×12 series extrapolates to 6.7 $Wm^{-1}K^{-1}$, the spread of the other extrapolations is $\pm$ 0.3 $Wm^{-1}K^{-1}$, with the GK point at around 7.0 $Wm^{-1}K^{-1}$(Fig. 3.12b). Therefore using a cross-sectional area of 12×12 produces a result that is converged with respect to Green-Kubo. Using this result, I determine that cells with a cross-sectional area of 2×2 are also converged when the cell length is less than 24 UC. Using a CSA of 2×2 is therefore a good compromise between computational cost and result accuracy.

In summary, accurate bridgmanite conductivity results can be produced with the direct method when the cell CSA is greater than 2×2, and the length between 8–24 UC. This will be the most efficient use of computational resources. Different lower mantle minerals may require different simulation geometries, making them easier or more difficult to compute.

FSE at 1000 K

Everything is different with the FSE analysis at 1000 K (Fig. 3.14a). It still appears that the 1×1 and 2×1 CSAs overestimate conductivity, and that the smallest, 6 unit cell length data point overestimates conductivity compared to a

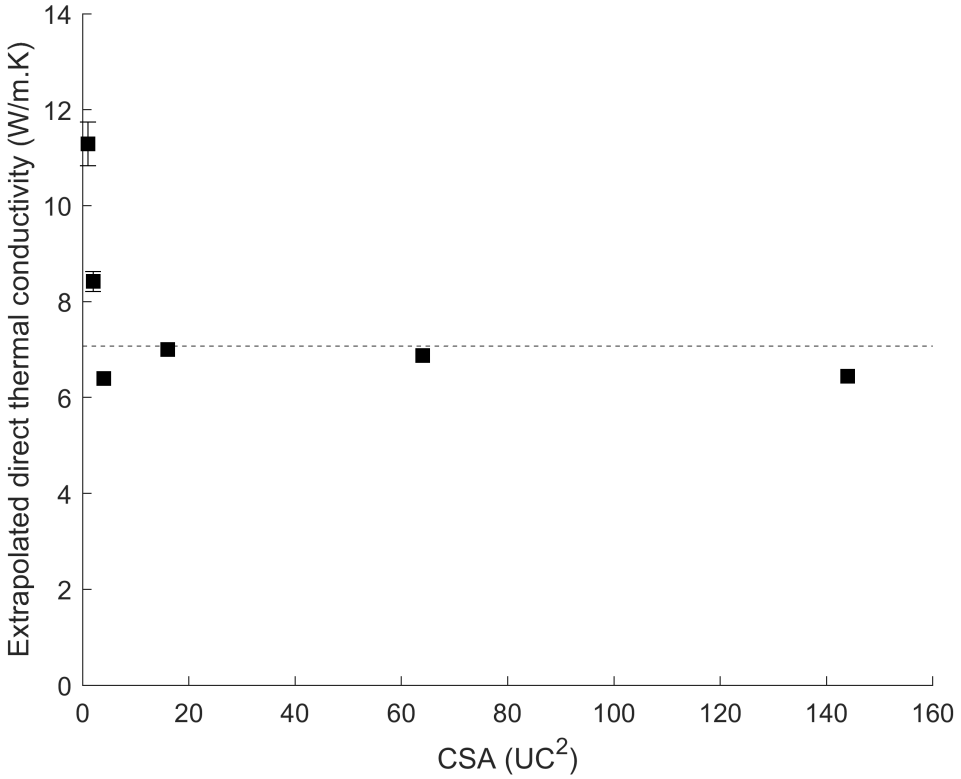

Figure 3.13: Extrapolated thermal conductivity, calculated using the direct method, as a function of CSA at 4000 K. Error bars show one standard deviation and are in most cases smaller than symbol size. Dotted line shows Green-Kubo result.

hypothetical linear fit through the other points. Using cells between 8–24 UC for extrapolation does not produce conductivity results which agree with GK however (Fig. 3.14b).

The discrepancy is around 5 $\mathrm{Wm^{-1}K^{-1}}$, 12.5 $\mathrm{Wm^{-1}K^{-1}}$ from direct method and 17.5 $\mathrm{Wm^{-1}K^{-1}}$ from Green-Kubo. The best CSA series to fit appears to be the 2×1. To get agreement between the two methods at these conditions for CSAs of 2×2 or greater, cells with lengths of 48 UC or larger should be considered (Fig. 3.15). Using these cell parameters, the conductivity result produced is approximately the same as the Green-Kubo results, suggesting convergence of the minimum CSA to the GK result.

Unlike the results at 4000 K, the longest simulation cells provide similar

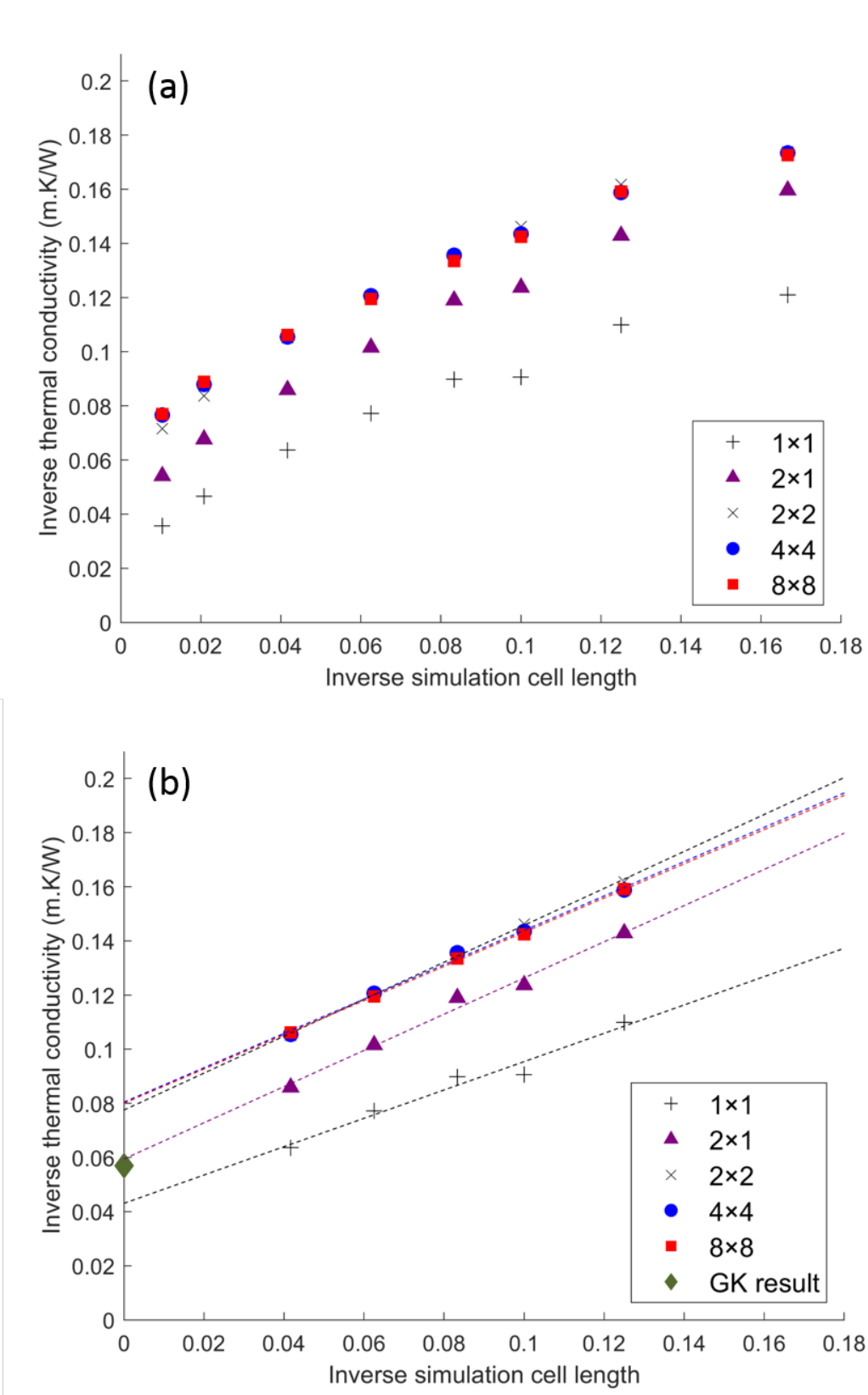

Figure 3.14: Inverse conductivity plotted against **a** all inverse simulation cell lengths and **b** for only 48 and 96 UC. All direct method simulations performed at 1000 K. Error bars showing one standard deviation are smaller than symbol size.

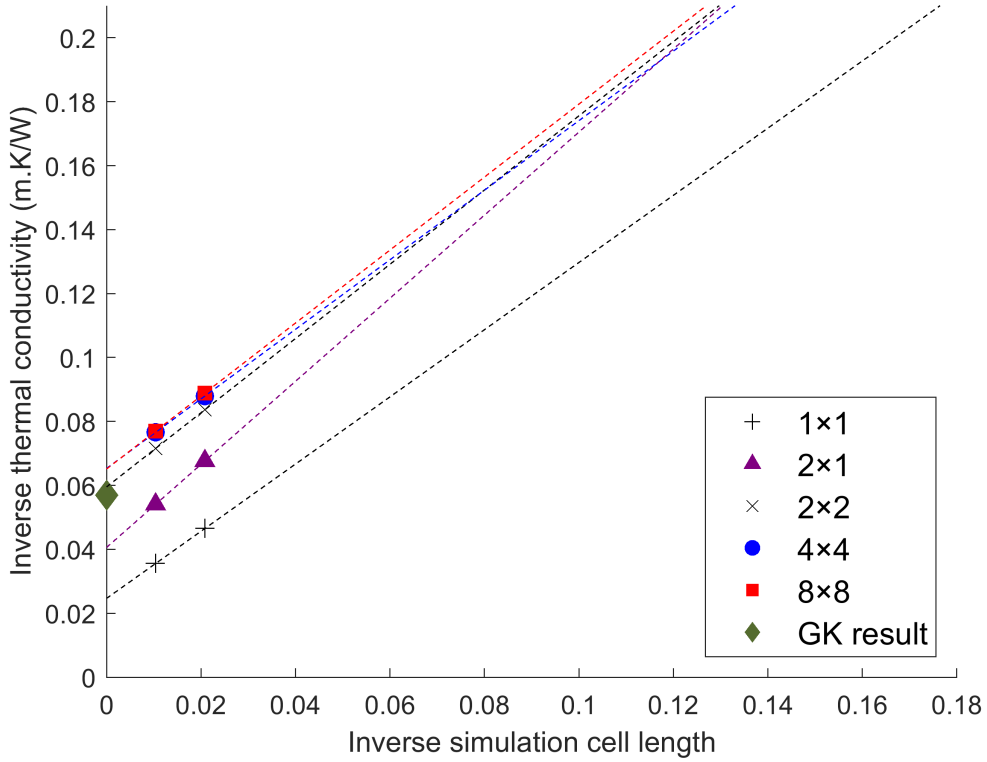

Figure 3.15: Inverse conductivity plotted against inverse simulation cell length, for direct method simulations performed at 1000 K, for lengths of 48 and 96 UC. Dotted lines show linear least squares fit for each cross-sectional area data series $> 2\times2$. Green-Kubo result is shown in green. Error bars showing one standard deviation are smaller than symbol size. Largest converged cells agree with Green-Kubo result.

conductivity estimates to the Green-Kubo result at 1000 K. At 4000 K, the only cell length that was ignored for being too short was 6 UC. This was because the phonon MFP exceeded the cell length, and therefore phonon scattering was misrepresented. However, at 1000 K, the conductivity is higher, and thus the MFP is longer. This means that the MFP exceeds the length of more of the simulation cells, requiring a higher minimum cell length, and thus more simulations must be ignored to obtain a result similar to Green-Kubo. At 1000 K, longer cells are used for extrapolation, as they exceed the length of the MFP, and therefore appropriately capture phonon scattering events. From the data series here, only two points appear to have sufficient cell lengths to exceed the MFP.

The fit, therefore, should not be considered robust, but is more similar to the Green-Kubo result than the fit that includes the shorter cell lengths.

3.2.8 Explaining CSA effect

Hu et al. (2011) presented a numerical model of thermal conductivity using the direct method, where they demonstrated that increasing simulation cell length and keeping the cell cross-sectional area constant leads to diverging thermal conductivity at very long cell lengths (Fig. 3.16). They suggest that this is because of discrete phonon phase space sampling, leading to behaviour characteristic of one-dimensional systems. The thermal conductivity (κ) model presented by *Hu et al.* (2011) is an approximation for one acoustic phonon, summed over the phonon wave vectors

$$\kappa = \frac{C_1 k_{\mathrm{B}}}{3A\pi} \sum_{k_x} \sum_{k_y} \tan^{-1}(k_{\mathrm{z}}/(k_x^2 + k_y^2)^{1/2})/(k_x^2 + k_y^2)^{1/2}|_{\pi/L_z}^{\pi/a} \ , \tag{3.1}$$

where C_1 is a scaling factor between relaxation time and phonon frequency, k_B is the Boltzmann constant, A is the cross-sectional area, k_x, k_y and k_z are the Cartesian components of the phonon wave vectors, L_z is the length of the simulation cell in the z-direction, and a is the lattice parameter.

When the phonon wave vectors in the x- and y-directions tend toward zero, and the cell length is significantly longer than the lattice parameter, the conductivity from Equation 3.1 becomes directly proportional to L_z by

$$\kappa(k_x = k_y = 0) = \frac{C_1 k_B}{3A\pi^2} L_z \ , \tag{3.2}$$

where κ represents the contribution of the divergent term (Fig. 3.16). As k_x and k_y tend toward zero, the divergent term contributes more to the total conductivity. When phonons perpendicular (x and y) to the direction of heat transport (z)

become insignificant, phonon-phonon scattering is diminished and the system tends towards length-dependent conductivity characteristic of one-dimensional systems.

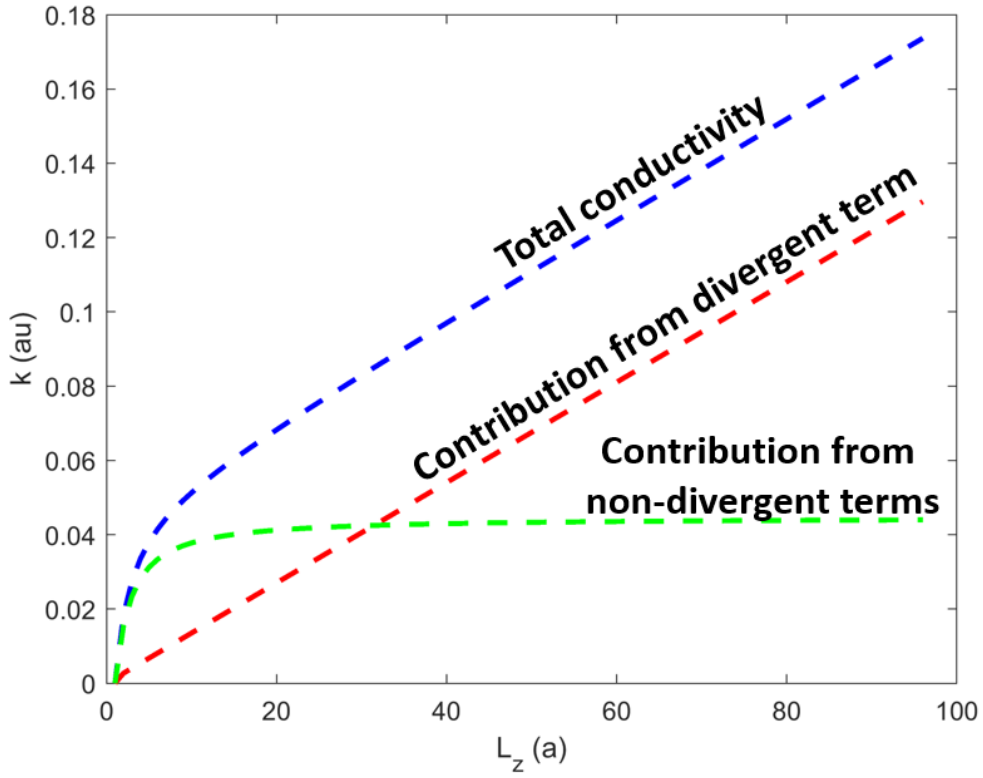

Figure 3.16: Analytical model from *Hu et al.* (2011) showing how thermal conductivity increases with structure length. Total conductivity is calculated by Equation 3.1. Contribution from the divergent terms is calculated in Equation 3.2. The contribution from non-divergent terms is obtained from the difference between Equation 3.1 and Equation 3.2. Divergent conductivity results are observed when the total conductivity deviates from the non-divergent portion, i.e., when the cell length is too long with respect its CSA and the divergent terms become significant.

Here, I compare the forms (considering the shape of the data rather than the absolute magnitudes) of the thermal conductivity results obtained via the direct method in this study with the form of the analytical model presented by *Hu et al.* (2011). I use the results obtained using a 2×2 cross-sectional area at 1000 K (Fig. 3.17b) and 4000 K (Fig. 3.17c), as shown in Figures 3.14 and 3.12, respectively. The analytical model from *Hu et al.* (2011) diverges with

length, i.e., the longest simulation cell lengths diverge away from the linear trend seen at shorter cell lengths (see Fig. 3.17a, at around x=0.05). This point of divergence is considered here to be the "turning point" in the model. I suggest that when data points calculated using the direct method fall within the linear portion of the inverse-space *Hu et al.* model (Fig. 3.17a), these points can be extrapolated to give a conductivity result at infinite system size that agrees with the corresponding Green-Kubo result.

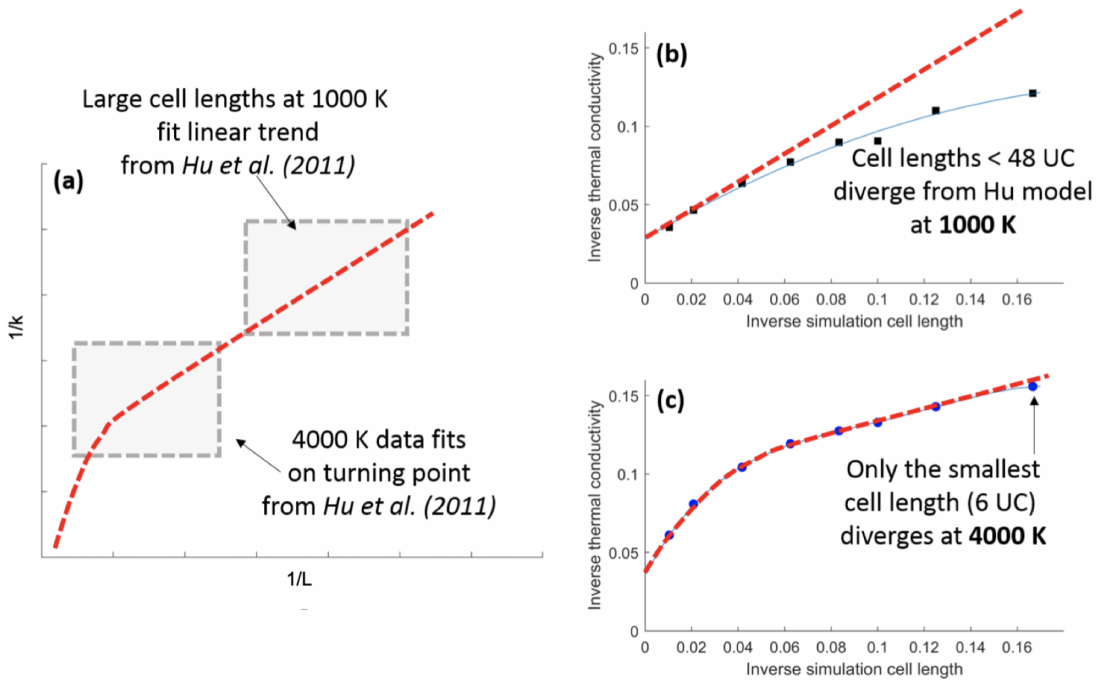

Figure 3.17: **(a)** Inverse conductivity as a function of inverse sample length, according to the analytical model from *Hu et al.* (2011), with annotations showing where the direct method conductivity results from this study plot; **(b)** the direct method results for 1000 K using a 2×2 CSA, with red-dashed line illustrating how the data would map onto the *Hu et al.* model; **(c)** the direct method results for 4000 K using a 2×2 CSA, with red-dashed line illustrating how the data would map onto the *Hu et al.* model.

I show illustratively that from the 1000 K data (Fig. 3.17b), the largest cells fit with the linear portion of the *Hu et al.* trend, whilst the shortest cells (<48 UC) diverge from the analytical model (shown by the red dashed line in Figure 3.17b). This divergence occurs because the cell lengths are too short relative to the phonon mean free paths at those conditions, which leads to ballistic phonon

transport and over-estimations of conductivity (as described by *Sellan et al.*, 2010). This concept gives further justification for my use of only 2 data points in the calculation of conductivity at 1000 K shown in Figure 3.15.

The 4000 K data (Fig. 3.17c) matches the *Hu et al.* model, for all simulation cell lengths. The exception to this is the smallest cell length from this study, as the data at 6 UC diverges from the *Hu et al.* model.

Although the 4000 K data from this study maps well to the *Hu et al.* model, this is not to say that if extrapolated, it will produce a reliable conductivity result that matches the Green-Kubo result. This is because only data corresponding to the linear (i.e., non-divergent) portion of the *Hu et al.* model (plotted on inverse conductivity against inverse length axes, as in Figure 3.17a) can be extrapolated to appropriate conductivity values, as the non-linear portion exemplifies the impact of FSE, i.e., when cell lengths are too long compared to their cross-sectional area.

Considering Figure 3.16, when the "Total conductivity" runs parallel to the "Contributions from the divergent term", the conductivity has diverged due to excessive length and started behaving in the one-dimensional regime. The conductivity from cell lengths where "Total conductivity" follows the "Contribution from non-divergence terms" will produce accurate extrapolated conductivity results. In Figure 3.17a, Figure 3.16 is converted into inverse space. The linear portion in inverse space corresponds to when "Total conductivity" follows the "Contribution from non-divergence terms", and can be extrapolated accurately. The nonlinear in inverse space (3.17a) relates to when "Total conductivity" runs parallel to the "Contributions from the divergent term", i.e., conductivity is diverging with length and the system is behaving in the one-dimensional regime.

Length-dependent conductivity due to excessive length relative to cross-sectional area, i.e., one-dimensional behaviour, is always undesirable when

simulating materials that are not one dimensional (in the case of this study). This is an unwanted side effect of trying to maintain the minimum simulation size in the interest of computational efficiency. As discussed in Section 3.2.7, using the minimum CSA is not always problematic, as long as cells of reasonable length are used. The finite-size effects that can be observed in the direct method depend on the physical conditions and the material being simulated, and must be investigated on a case by case basis.

3.2.9 Back-calculating mean free path

The size of the simulation cell is important in relationship to the length of the phonon mean free path, because as discussed in this chapter, the cell length must be larger than the mean free path length. An important parameter therefore, is the length of the mean free path, however this information is not directly accessible while performing simulations. It is however possible to infer the phonon mean free path from direct method conductivity results.

The conductivities from supercells (κ_L) of varying length (L) obtained via direct method calculations fit the form

$$\frac{1}{\kappa_L} = \left[\frac{12}{C_\mathrm{v} v}\right] \frac{1}{L} + \left[\frac{3}{C_\mathrm{v} v} \frac{1}{\Lambda_{\mathrm{ph-ph}}}\right], \tag{3.3}$$

where C_v is the volumetric isochoric heat capacity, v is the phonon group velocity, and $\Lambda_{\mathrm{ph-ph}}$ is the mean free path associated with phonon–phonon scattering (modified from *Schelling et al.* (2002), via *Stackhouse and Stixrude* (2010)). When the inverse conductivities are plotted against the inverse cell lengths, extrapolation to the y-axis ($1/L = 0$) gives the bulk material ($L \to \infty$) conductivity, and its associated phonon mean free path. The two square-bracketed terms in the above equation represent the gradient and intercept respectively, of such a line fit to data and extrapolated (as in Fig. 2.6).

I can rewrite Equation 3.3 with the following simplifications

$$M = \left[\frac{12}{C_{\mathrm{v}} v}\right], \text{ and } \frac{M}{4} = \frac{3}{C_{\mathrm{v}} v} ,$$

giving

$$\frac{1}{\kappa_L} = M \frac{1}{L} + \left[\frac{M}{4}\frac{1}{\Lambda_{\mathrm{ph-ph}}}\right]. \tag{3.4}$$

When $1/L = 0$ (i.e., a cell of infinite size), the extrapolated conductivity can be equated to the gradient and effective mean free path

$$\frac{1}{\kappa} = \frac{M}{4}\frac{1}{\Lambda} ,$$

and thus

$$\Lambda = \frac{M}{4}\,\kappa . \tag{3.5}$$

Using the gradient and conductivity from direct method calculations at 136 GPa, 4000 K, and a supercell cross-sectional area of 12×12, the mean free path is equal to 0.23 ± 0.03 nm. This value is roughly half the width of the unit cell in the direction of heat flux, or the width of a direct method temperature section. The mean free path length estimate is on the same order of magnitude as that by *Stackhouse et al.* (2015), who estimated MFP at 145 GPa and 4000 K as 0.8±0.4 nm. Although there is a slight discrepancy between these values, the estimate by *Stackhouse et al.* (2015) is at a higher pressure. Decreasing the pressure would decrease the mean free path length, bringing it more in line with the estimate reported here.

Calculating the MFP can help to understand which cell lengths are likely to yield appropriate thermal conductivity results. The smallest cell length explored in this study (6 UC) gave anomalous results and was excluded (see Fig. 3.12a and 3.12b), despite having five sections across the length (Section 3.2.1 and Fig. 3.8)

of temperature gradient. The length over which the temperature gradient is considered is approximately five times the phonon mean free path, and yet the conductivity result is deemed invalid. I therefore suggest that the relationship between minimum cell length and phonon mean free path is more complicated. I show that the minimum cell length yielding appropriate conductivity values for bridgmanite at lower mantle conditions is 8 UC.

The mean free path length can also be calculated at 136 GPa and 1000 K, and is equal to 2.13 nm. The conductivity result at L=0 (i.e., infinite cell size) is extrapolated from only two direct method conductivity results (Fig. 3.15b) in order to be comparable with the Green-Kubo estimate of conductivity (Section 3.2.7), and due to the number of data points, the mean free path length error cannot be calculated. In this case, the mean free path length is longer than at 4000 K, and it therefore makes sense that smaller cell lengths <48 UC (i.e., inverse cell length values >0.03) do not correctly simulate longer mean free path lengths. The MFP at 1000 K is on the same order of magnitude as the MFP calculated by *Stackhouse et al.* (2015) for a pressure of 110 GPa and a temperature of 1000 K. As mentioned previously with reference to the *Stackhouse et al.* (2015) study, the pressures used are slightly different to those in this study, giving reason to the difference in MFP estimates.

3.3 Discussion

In this Chapter I have presented conductivity results for bridgmanite at temperatures of 1000 K and 4000 K, both at 136 GPa, using firstly the Green-Kubo method and secondly the direct method in order to constrain FSE. The quantitative results are shown in Table 3.7.

The conductivity estimates at 4000 K are similar to those reported for the same conditions by *Ghaderi et al.* (2017), who found conductivities of

Table 3.7: Table of thermal conductivities using the Green-Kubo and direct methods, at 136 GPa, and for temperatures of 1000 K and 4000 K. Direct method results given for CSA of 2×2.[1] no errors are available for the direct method at 1000 K, because only 2 points were used for the extrapolation (see Fig. 3.15).

	1000 K	4000 K
Green-Kubo	17.51±0.27	7.07±0.06
Direct method	16.81[1]	6.39±0.11

5.2 $Wm^{-1}K^{-1}$. *Ammann et al.* (2014) also estimated a conductivity value of 8.5 $Wm^{-1}K^{-1}$ for bridgmanite at 3739 K and 136 GPa. Both studies used simulations in their estimates, where *Ammann et al.* (2014) used the direct method with interatomic potentials, and *Ghaderi et al.* (2017) used *ab initio* lattice dynamics. *Stackhouse et al.* (2015) also used the direct method with DFT to estimate bridgmanite conductivity at 145 GPa and 4000 K, with a value of 9±2 $Wm^{-1}K^{-1}$. An extrapolation of an experimental study from *Ohta et al.* (2012) suggest bridgmanite conductivity of 9±1.6 $Wm^{-1}K^{-1}$ at 3700 K and 136 GPa, again similar to the values found in my study.

Conductivity estimates at 1000 K and 136 GPa are less available in the literature, because these are unrealistic conditions. *Stackhouse et al.* (2015) use the direct method with DFT to estimate thermal conductivity of bridgmanite at 110 GPa and 1000 K. They obtained a value of 16±5 $Wm^{-1}K^{-1}$.

The similarity of these results (and *Ammann et al.*'s) to estimates found in this study might be expected based on use of the direct method, with differences arising from how finite-size effects are identified and managed. Removing the influence that the direct method might have on any results, comparison of *Stackhouse et al.* (2015) with the Green-Kubo results still show agreement within error.

The results of my calculations using the Green-Kubo method show that this method is an efficient way of calculating thermal conductivity for bridgmanite at lower mantle conditions. This is because the thermal conductivity results are converged for a low number of atoms (<1000), and are thus computationally efficient. This is significantly more efficient than the direct method simulations, where multiple simulations are required with atom counts up to 2000. The main strength of Green-Kubo as a theoretical method is statistical averaging which allows multiple datasets to be obtained simultaneously, whereas the direct method requires a series of calculations where each result is dependent on the complete calculation of the previous result (i.e., as shown in Fig. 3.7). There is also more processing of calculations required when using the direct method, and this leads to increased subjectivity when evaluating temperature gradients and the extrapolation of results.

In this Chapter, I have shown that cross-sectional area affects thermal conductivity estimates of bridgmanite at CMB conditions when the simulation cell is smaller than 2×2 UC. The influence of FSE was also discussed by *Stackhouse et al.* (2015). They calculated thermal conductivity estimates using varied simulation cell cross-sectional areas (1×1 and 2×1) and they concluded that their results were identical within uncertainty. I suggest that their results are an overestimate of thermal conductivity, as I obtain a value of ∼7 $Wm^{-1}K^{-1}$ compared to their value of 9 $Wm^{-1}K^{-1}$. The difference between the results is expected due to the cross-sectional areas considered by *Stackhouse et al.*

(2015). As I showed by considering much larger cross-sectional areas (up to 12×12, Fig. 3.13), the CSAs used by *Stackhouse et al.* (2015) result in a conductivity overestimate. The results in this chapter show that simulation cells with area 2×2 produced converged estimates of conductivity with respect to larger cross-sectional areas, which was not possible to investigate using the computationally expensive *ab initio* approach of *Stackhouse et al.* (2015).

We observe non-linearity in the thermal conductivity results using the direct method (Fig. 3.12a), as previously described by *Sellan et al.* (2010). The non-linearity can be observed around the inverse length corresponding to the simulation with a unit length of 6 UC, which has higher conductivity than expected from the linear fit through the data from longer simulation cells (>6 UC). When this shortest cell length (i.e., highest inverse value) is included in the extrapolation, this reduces the gradient of the fit, raising the intercept and thus causing conductivity to be underestimated.

Considering again the study from *Stackhouse et al.* (2015), they considered a limited range of simulation cell lengths (6–12 UC). Using the results from my study, I suggest that the longer simulation cells (≥8 UC) produced a valid thermal conductivity result. However, I speculate that the inclusion of the result at 6 UC could have influenced the overall linear fit to the data in the same way observed in this study. This would lead to an underestimate of thermal conductivity and gives just one example of a study where FSE may not have fully been explored and quantified.

I therefore have identified a possible overestimation due to small cross-sectional areas (<2×2), and possible underestimation due to shorter simulation cell length (<8 UC at 4000 K). In the case of *Stackhouse et al.* (2015), using a small cross-sectional area has a more significant effect than a short cell length. I suggest that these parameters (simulation cell length and cross-sectional area) should be more fully considered in the design of future studies using the

direct method.

I investigated the impact of the cell length on conductivity measurements further in this chapter by comparing the form of the conductivity results with that from *Hu et al.* (2011), where they showed that conductivity diverges with cell length for a fixed cross-sectional area. I showed, using the 1000 K data, that the cell length can be too short. I suggest this is an additional complexity to the conductivity divergence which is not incorporated into the *Hu et al.* model, but would improve the use of the analytical model to understand finite-size effects in the direct method.

In this study, by increasing the simulation cell cross-sectional area to 12×12 at 4000 K, I was able to observe the aspect ratio-dependent divergence as reported by *Hu et al.* (2011). This is to say that for a given simulation cell length, there is an ideal cross-sectional area which reproduces the phonon-phonon scattering found in the bulk material. Using a cross-sectional area smaller than this ideal size causes conductivity values to be overestimated (i.e., the difference between Figures 3.12a and 3.12b). This can be observed in the longest simulation cell lengths (i.e., lowest inverse length values), where the conductivity values are higher than expected from the linear fit through the data from shorter simulation cell lengths ($\leq$24 UC). When these longer cell lengths (i.e., lowest inverse values) are included in the extrapolation, this increases the gradient of the fit, lowering the intercept and thus causing conductivity to be overestimated. Using this conclusion that cells can be too long to produce accurate conductivities for a given cross-sectional area. Discarding simulations with cell lengths that are considered too long also provides the additional benefit of reducing computational costs, and so should be considered in the design of direct method studies.

I suggest this effect can also be observed in the data presented by *Ammann et al.* (2014), who studied the variation in conductivity and heat flux at the CMB. They plot the conductivity of post-perovskite as a function of

inverse simulation-cell length (Fig. 3.18). Looking at the thermal conductivities calculated from interatomic potentials (blue data points), I suggest the value of thermal conductivity extrapolated to infinite system size (the filled diamond) could be over-estimated due to the influence of the longest cell sizes. At inverse simulation cell lengths less than 0.05, I suggest the conductivity results are over-estimated due to FSE, thus steepening the gradient of extrapolation. I have shown in this chapter that previous estimates of FSE were incomplete, and this is just one example of how FSE can influence a thermal conductivity estimate.

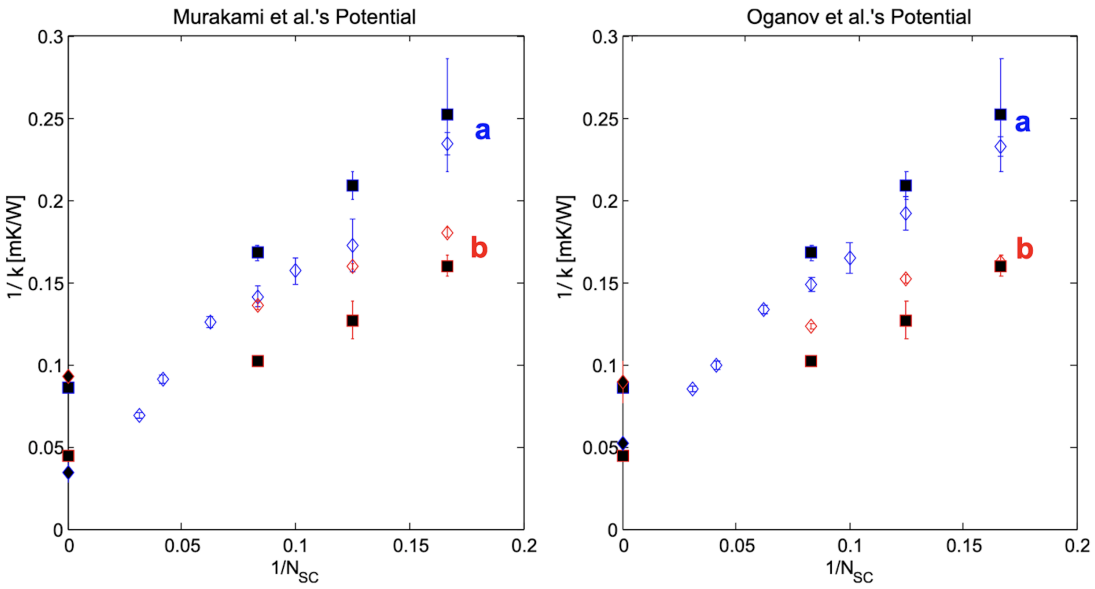

Figure 3.18: Comparison of results from interatomic potentials (empty diamonds) with those from DFT (filled squares) as a function of simulation cell length. Red shows thermal conductivity along crystal direction b, and blue along a. Values at $x = 0$ show extrapolations to infinite cell size. Reproduced with permission from *Ammann et al.* (2014).

These conclusions are specific to the conditions of 4000 K and 136 GPa, which are representative of the CMB, the area of interest in this study. I have also investigated FSE at 1000 K and at the same pressure. The results for these conditions suggest that the nature of FSE is affected by physical conditions. Agreement with Green-Kubo is only observed with the longest simulation cell lengths ($\geq$48 UC), however this fit uses only two calculated values

which limits the reliability of a linear fit (Fig. 3.15b). I do not investigate the cause of this difference within this study, but suggest it would be an important point of investigation for studies examining thermal conductivity at a range of temperature conditions. This would require the simulation of longer cell lengths (i.e., >96 UC), which would be of significant computational expense. Because the constraint of direct method FSE at 1000 K is inconclusive, I choose not to use the direct method to investigate the effect of impurities in Chapter 4 because a range of temperatures is required to create the composition-dependent conductivity model.

More broadly, I have showed the importance of performing finite-size analysis when performing direct method calculations. Direct method cells spanning a range of lengths must be considered to find the linear regime for extrapolation. Cross-sectional area must be increased until the conductivity result converges. The same can be said about the Green-Kubo method, where the result converges with increasing cell size. These effects vary with phonon mean-free path, and are sensitive to temperature, and compositional variations such as impurities. In the remainder of this thesis, I will use the Green-Kubo method to calculate thermal conductivity results. I suggest classical molecular dynamics with interatomic potentials could be an excellent way of quantifying FSE to then employ *ab initio* methods accurately, if the uncertainty in temperature-dependence of FSEs is understood.

3.4 Summary

1. In this Chapter, I presented the first comparison of Green-Kubo and direct methods for bridgmanite at lower mantle conditions.

2. I used the Green-Kubo method to calculate lattice thermal conductivity

at 136 GPa, and obtained results of 17.51 ± 0.27 $Wm^{-1}K^{-1}$ at 1000 K, and 7.07 ± 0.06 $Wm^{-1}K^{-1}$ at 4000 K. Finite-size effects associated with simulating bridgmanite at these conditions in the Green-Kubo method are mitigated by using a supercell geometry $\geq 4\times4\times3$ UC.

3. I also used the direct method to compute conductivity at the same conditions, obtaining results of 16.81 $Wm^{-1}K^{-1}$ and 6.39 ± 0.11 $Wm^{-1}K^{-1}$ respectively. Finite-size effects are much more prevalent in the direct method, where I use supercells with CSA $\geq$ 2×2 UC, and lengths of $\geq$ 48 UC at 1000 K and 8–24 UC at 4000 K, to compute conductivity results that are converged with respect to simulation size.

4. I backcalculated the MFP from results obtained from the direct method, finding values of 2.13 nm and 0.23 ± 0.03 nm, at 1000 K and 4000 K, respectively. MFPs have not previously been compared with finite-size effects in this way, and the magnitude of these values reinforces the choice of cell sizes to mitigate FSEs at each temperature.

Chapter 4

Modelling the thermal conductivity of Fe-bearing bridgmanite

As stated previously, there are significant experimental challenges in measuring thermal conductivity at the high pressures and temperatures necessary to replicate the conditions of the lower mantle. Constraining the thermal conductivity of bridgmanite at lower mantle conditions is further complicated by the addition of mineral impurities. Therefore in addition to pressure- and temperature-dependence, compositional-dependence must be considered for full evaluation of lower mantle conductivity.

The bulk of the lower mantle comprises bridgmanite (∼70%, and its high-pressure polymorph, post-perovskite), periclase (∼20%), along with other minor minerals (∼10%) such as calcium silicate perovskite ($CaSiO_3$, *Trønnes*, 2009). In bridgmanite ($MgSiO_3$, magnesium silicate perovskite), the magnesium can be replaced with Fe. Most of the lower mantle will have Fe content $< 15\%$ (*Lee et al.*, 2004), partitioned into bridgmanite as concentrations of $(Mg_{0.95}Fe_{0.05})SiO_3$, however in this study I investigate the full solid solution range between $MgSiO_3$

and $FeSiO_3$ endmembers. Knowledge of conductivity up to the Fe endmember is interesting if ultra low velocity zones have high Fe content (e.g., *Mao et al.*, 2004; *Dobson and Brodholt*, 2005). At the high Fe contents expected, electrical thermal conductivity could become important, although for simplicity this is ignored in the calculations presented here.

Additionally in bridgmanite, the aluminium can be substituted (*Zhang et al.*, 2016) for magnesium and silicon (as in *Brodholt*, 2000) where,

$$(Mg_3Al)\,(Si_3Al)\,O_{12} + 2MgO = Mg_2Al_2O_5 + 3MgSiO_3\ . \tag{4.1}$$

The introduction of impurities into lower mantle minerals reduces the thermal conductivity by introducing an extra scattering mechanism, phonon-defect scattering. A defect in crystal structure, interrupts the periodicity of the structure, much like a speed bump to a car. They have different properties to the atoms the phonon would encounter in a material with crystal periodicity, namely mass and their bonds with neighbouring atoms. For this reason the thermal conductivity of a solid solution is lower at intermediate compositions than at the endmembers. In this chapter, I investigate the effect of Fe impurities on the thermal conductivity of bridgmanite because as the most abundant mineral in the lower mantle, the conductivity of bridgmanite has the greatest effect on the overall dynamics of the lower mantle. In this study, I consider only Fe^{2+} impurities and do not consider the effect of Fe^{3+} or Al.

In Chapter 3, I showed that the Green-Kubo method produced more reliable thermal conductivity results than the direct method when considering the effects of finite simulation size. As a result of this finding, in this chapter I compute thermal conductivity results using the Green-Kubo method at pressure conditions corresponding to the core-mantle boundary (CMB), and a wide range of temperature for the full solid solution. In addition to investigating how Fe

content affects conductivity, I also investigate whether the method by which Fe atoms are modelled affects the conductivity result. These results speak to broader questions of firstly, the role of crystal defects and chemical impurities in solid solutions, and secondly, the accuracy of approaches to modelling atomic interactions.

As discussed in Section 2.4, a set of interatomic potentials exist for bridgmanite (*Oganov et al.*, 2000), i.e., the Mg endmember of the (Mg,Fe)SiO_3 solid solution. In this chapter I modify the existing potential to also model Fe defects. I do this using two methods: (1) by considering the change in atomic mass that occurs when a Mg atom is replaced by a Fe atom, and (2) by changing the atomic mass and also changing the interatomic potential to consider the effect of Fe interactions. The aim is to explore how well thermal conductivity is estimated by a model which only alters the atomic mass (i.e., an isotopic model, Fe represented by a heavy Mg isotope) compared with one that additionally updates the interatomic potential.

For example, *Ammann et al.* (2014) used an isotopic model to simulate Fe in bridgmanite and post-perovskite, when determining the thermal conductivity at the CMB. In this study, however, the validity of using an isotopic model to approximate thermal conductivity was not explored. In this chapter, I show that using an isotopic model is a good approximation. I also explore a wider composition range than *Ammann et al.* (2014).

Comparing the new Fe potential and isotopic models for Fe is particularly interesting due to the mass contrast between Fe and Mg. This is a more significant mass contrast than that arising when aluminium replaces either magnesium or silicon in bridgmanite (Equation 4.1). Previous studies (e.g., *Stackhouse et al.*, 2015) have predicted that isotopic variations will have little effect on conductivity (see Equation 4.5), where the mass differences are small (e.g., ^{24}Mg to $^{25/26}$Mg) and abundances are low (Mg standard atomic weight is 24.3, the ratio of ^{24}Mg to

heavier isotopes is roughly 4:1).

Manthilake et al. (2011) performed experiments to investigate the effect of Fe and Al on the thermal conductivity of bridgmanite and ferropericlase between 8 and 14 GPa and at 500–1200 K. The authors then extrapolated their experimental results to lower mantle conditions, calculating the conductivity for a 4 parts bridgmanite : 1 part ferropericlase composition. At lower temperatures for any pressure or composition, adding impurities up to 20 mol% reduces conductivity by a factor of around 3. The magnitude of this reduction decreases with temperature (as impurity-free conductivity decreases anyway), but impurities can have a huge effect. Conductivity decreases with temperature at a slower rate for the compositions with impurities, suggesting that reductions from impurities affect the reductions from other effects (such as temperature increase), and that there might be a minimum conductivity at which no further decrease is observed.

Using the methodologies presented in Chapter 3, in this chapter I introduce Fe impurities into my existing bridgmanite model and establish the effects on lattice thermal conductivity around the core-mantle boundary. This is in order to quantify conductivity as a function of temperature and composition. I also show that mass difference is the main factor in phonon-defect scattering. Finally, using the method presented in Section 3.2.9, I am able to determine the phonon-phonon mean free path and the phonon-defect mean free path, and how it varies with conductivity, parameter space which has not been explored before.

4.1 Adding atomic impurities

There are numerous mechanisms by which phonons scatter, and this scattering reduces the efficiency of heat transport, therefore decreasing the thermal conductivity of a material . In a chemically pure material, scattering occurs due to phonon-phonon collisions, whereas in a material with impurities, phonons can

also scatter off of defects. The effective scattering is dependent on the balance of phonon-phonon and phonon-defect scattering that occurs within the material. The phonon-defect scattering is constant with a constant composition, but the effects of phonon-phonon scattering change with pressure and temperature, therefore the relative significance of each scattering component changes with physical conditions.

4.1.1 Effect of impurities on conductivity

The effect of impurities on lattice thermal conductivity is discussed by *Klemens* (1960) and *Padture and Klemens* (1997), a review of which can be found in the Supplementary Material of *Stackhouse et al.* (2015). I outline this in this section. The lattice thermal conductivity of a binary solid solution is given as

$$\kappa_{\mathrm{SS}} = \kappa_{\mathrm{V}} \left(\frac{\omega_0}{\omega_{\mathrm{D}}} \right) \arctan \left(\frac{\omega_{\mathrm{D}}}{\omega_0} \right), \tag{4.2}$$

where ω_0 is the phonon frequency at which phonon-phonon scattering and phonon-defect scattering contributions to the mean free path are equal, and ω_{D} is the phonon frequency corresponding to the maximum of the acoustic branch in the phonon spectrum (the Debye frequency). κ_{V} is the compositionally-weighted (Voigt) average of endmember conductivities,

$$\kappa_{\mathrm{V}} = (1 - C)\, \kappa_1 + C\ \kappa_2\ , \tag{4.3}$$

where κ_1 and κ_2 are the solid solution endmember conductivities, and C is the fractional concentration of the second endmember.

When $\omega_0 \gg \omega_{\mathrm{D}}$, $\arctan(\omega_{\mathrm{D}}/\omega_0) \rightarrow (\omega_{\mathrm{D}}/\omega_0)$, so $\kappa_{SS} \rightarrow \kappa_V$, the conductivity including the effect of impurities tends toward the endmember linear average. This is the case when other scattering mechanisms, such as phonon-phonon

scattering, have caused conductivity to decrease significantly. Under such conditions, phonon-defect scattering has little effect, as the conductivity is already close to its saturated minimum.

On the other hand, when $\omega_{\mathrm{D}} \gg \omega_0$, $\arctan(\omega_{\mathrm{D}}/\omega_0) \rightarrow \pi/2$, but $(\omega_0/\omega_{\mathrm{D}}) \ll 2/\pi$, so $\kappa_{\mathrm{SS}} < \kappa_{\mathrm{V}}$, and impurity scattering has a noticeable effect on the resultant conductivity. This is the case when phonon-phonon collisions are not the dominant resistive process, like at low temperatures compared to the conditions mentioned in the above case.

4.1.2 Magnitude of impurity scattering

The factors that affect the magnitude of impurity scattering are temperature, the mass difference between the impurity and what it replaced, and the impurity concentration. The ratio of the phonon frequencies in Equation 4.2 can be expressed (Equation 4.4) as

$$\left(\frac{\omega_0}{\omega_D}\right)^2 = \frac{1}{(6\pi^2)^{1/3}} \, \frac{T}{3\varepsilon T_0} \, , \tag{4.4}$$

where T is temperature, T_0 is the temperature associated with ω_0, and ε is related to the mass difference and proportion of endmembers by

$$\varepsilon = \frac{(M_2 - M_1)^2}{\overline{M}^2} \, C\,(1 - C) \, , \tag{4.5}$$

where M_i is the atomic mass of the i-th endmember, $\overline{M}$ is the mean atomic mass of the solid solution, and C is the proportion of the impurity endmember (Equation 4.5). These equations describe how phonon processes are affected by temperature and a variable composition (*Leibfried and Schlömann*, 1954), which can subsequently be used to show how lattice conductivity varies with these parameters (in Equation 4.2).

As the temperature increases, so too does the left-hand side of Equation 4.4. As discussed earlier, this reduces the effect of scattering caused by impurities, which will be relevant at CMB conditions where temperature is large (∼4000 K).

ε increases with the mass difference of the endmembers, and the impurity concentration. Increasing ε reduces the phonon frequency ratio, meaning impurity scattering will affect the resultant conductivity more. The atomic masses of Mg and Fe are 24 and 56, so $FeSiO_3$ is 1.32 times heavier than $MgSiO_3$.

The composition control term in Equation 4.5, $C(1-C)$, increases from 0 to 0.25, when $C = 0.5$. ε increases with composition up to 50%, the furthest point away from both endmembers, therefore the condition of most disorder in the model.

4.1.3 Phonon frequency and relaxation time

The compositional model presented by *Klemens* (1960) considers the ratio of phonon frequencies, and the contribution of these frequencies to the effective relaxation time of the system. ω_0 is defined (by *Klemens*, 1960, Equation 11) as the frequency at which

$$\tau_{ph-d}\left(\omega_0\right) = \tau_{ph-ph}\left(\omega_0\right), \tag{4.6}$$

where τ_{ph-d} and τ_{ph-ph} are the contributions of phonon-defect scattering and phonon-phonon scattering to the effective phonon relaxation time (*Klemens*, 1960, Equations 2 & 3), where the authors assume

$$1/\tau_{ph-d} = A\omega^4, \tag{4.7}$$

and

$$1/\tau_{ph-ph} = B\omega^2. \tag{4.8}$$

Equation 4.7 was first defined by *Klemens* (1955), and considers the effects on phonon relaxation time from: mass difference of the defect, differences in the binding between the defect and its neighbours, and anharmonic effects of the distortion about the defect. The exponent in Equation 4.8 indicates that two phonons have collided and their frequencies multiplied (*Klemens*, 1951). The effective phonon relaxation time of the system, using the Matthiesen Rule (modified from *Klemens*, 1960, Equation 7), is

$$\frac{1}{\tau\left(\omega\right)} = \frac{1}{\tau_{ph-ph}} + \frac{1}{\tau_{ph-d}} \ . \tag{4.9}$$

When Equation 4.6 is satisfied, the effective relaxation time is equal to half of either its constituents,

$$\frac{1}{\tau\left(\omega_0\right)} = \frac{1}{\tau_{ph-ph}} + \frac{1}{\tau_{ph-d}} = \frac{1}{\tau_{\omega_0}} + \frac{1}{\tau_{\omega_0}} = \frac{2}{\tau_{\omega_0}} \ , \tag{4.10}$$

When $\tau_{ph-d} \neq \tau_{ph-ph}$, the effective relaxation time will tend toward the smaller of the two as the difference increases. I illustrate in Figure 4.1 that a process' relaxation time will dominate the other when it is around 1,000 times smaller. At the point where the contribution is equal (i.e., 0.5), the ω_0 criterion is satisfied (Equation 4.6). The contribution varies linearly when the magnitudes of the relaxation times are comparable, adopting an arctan-like form when they vary greatly.

For a CMB-like condition of high temperature, the phonon-phonon scattering relaxation time is short (left hand side of Fig. 4.1). Adding impurities (reducing τ_{ph-d}) doesn't contribute much to an already large scattering effect. Where the phonon-phonon scattering relaxation time is longer (temperatures decreasing towards Debye temperature), even adding a small amount (2%) of atomic impurity can influence the thermal conductivity. Considering the average phonon

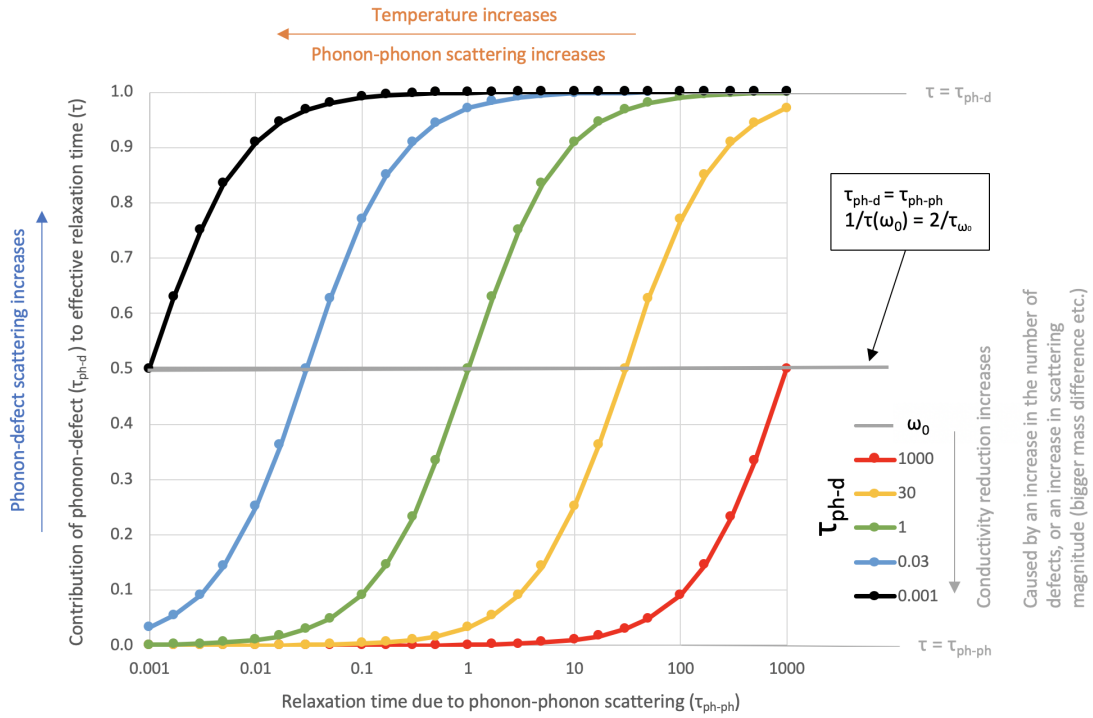

Figure 4.1: For a series of τ_{ph-d}, their contribution to the effective phonon relaxation time is plotted against τ_{ph-ph}. The quantity on the y-axis is the normalised difference in effective phonon relaxation time, comparing phonon-phonon scattering to phonon-phonon and phonon-defect scattering (as in Equation 4.9).

velocity, a longer relaxation time means a greater distance travelled, or phonon mean free path.

In Equations 4.7 & 4.8 , A and B are constants. The constant A is related to phonon-defect scattering and is constant with temperature (varying with composition). The constant B, however, is temperature-dependent, because it relates to phonon-phonon scattering, which increases with temperature. It is the relative magnitude of phonon-phonon scattering to phonon-defect scattering, and therefore τ_{ph-ph} to τ_{ph-d}, that influences the effect of impurities on thermal conductivity (see Equation 4.9). As τ_{ph-ph} is temperature-dependent, via B, the effect of impurities on thermal conductivity is similarly temperature-dependent.

The two relaxation time terms above can be equated via Equation 4.6, showing

ω_0 is similarly temperature-dependent

$$A{\omega_0}^4 = B\left(T\right){\omega_0}^2,$$

$${\omega_0}^2 = B\left(T\right)/A\ ,$$

$$\omega_0 \propto T\ . \tag{4.11}$$

The Debye frequency is a constant, so

$$\left(\frac{\omega_0}{\omega_\mathrm{D}}\right) \propto T\ . \tag{4.12}$$

As temperature increases (above the Debye temperature), conductivity decreases as phonon-phonon scattering increases. The significance of phonon-defect scattering (but not the magnitude of its relaxation time) decreases as the effect of phonon-phonon scattering increases. Therefore the relative conductivity decrease due to impurities is inversely proportional with temperature, and less important as conductivity tends towards its saturated minimum.

4.2 Methodology

In this section, I present the parameterisation of a Buckingham potential for Fe in bridgmanite. I also discuss how I construct my models of Fe-bearing bridgmanite.

4.2.1 Behaviour of iron

As described earlier, I will model the inclusion of Fe^{2+} in bridgmanite in two ways. The first approach is to fit a new interatomic potential. An in-depth review of these approaches can be found in Section 4.5.1. I adapted the *Oganov*

et al. (2000) $MgSiO_3$ Buckingham interatomic potential (U, as introduced in Section 2.3.2) to include the Fe-O interaction (see Table 4.1). I determined two short-range potential parameters, b and ρ, shown in Equation 11 from *Oganov et al.* (2000),

$$U_{ij}\left(R_{ij}\right) = \frac{z_i z_j}{R_{ij}} + b_{ij}\,\exp\left(-\frac{R_{ij}}{\rho_{ij}}\right) - \frac{c_{ij}}{{R_{ij}}^6}, \tag{4.13}$$

where ij refers to an atom pair, R is interatomic distance, z is atomic charge, and c relates to the Van der Waals force (zero for non O-O interactions). I determine ρ in the same fashion as *Oganov et al.* (2000), calculated from the atomic first ionisation potentials,

$$\rho_{ij} = \frac{1.85}{\sqrt{I_i} + \sqrt{I_j}}. \tag{4.14}$$

b is constrained using the GULP code (*Gale*, 1997), using the calculated ρ value for Fe-O. Within GULP, I use a constant volume optimisation method, i.e., adjusting the interatomic potential to minimise the energy. I fit b to structural information (lattice parameters) obtained by *Parise and Wang* (1990), who carried out an experimental study of $(Mg_{0.9},Fe_{0.1})SiO_3$ bridgmanite at ambient conditions. This study was chosen as it matches the conditions at which *Oganov et al.* (2000) fit their potential.

Table 4.1: Parameters used to define *Oganov et al.* (2000)'s bridgmanite potential, including fit Fe-O values from this study.

Bond ij	b_{ij} (eV)	ρ_{ij} (Å)	c_{ij} (eV.Å^6)	Source
Mg-O	1041.435	0.2866	0	*Oganov et al.* (2000)
Si-O	1137.028	0.2827	0	*Oganov et al.* (2000)
O-O	2023.800	0.2674	13.83	*Oganov et al.* (2000)
Fe-O	1440.437	0.2846	0	This study

Table 4.2 shows how well the new Fe potential predicts the lattice parameters of $(Mg_{0.9}Fe_{0.1})SiO_3$ used to constrain the fit. Lattice parameters from *Parise and Wang* (1990) were measured from samples synthesised at 26 GPa and 1973 K. I determined the lattice parameters for this study from an NPT simulation run at

the same conditions. Comparison of the lattice parameters shows good agreement, with all differences between the data from *Parise and Wang* (1990) and this study falling below 4%, suggesting that the parameters representing the interatomic potential are accurate.

Table 4.2: Table showing how well the Fe-model fits the data used to constrain fit, where a, b, c are the lattice parameters (Å), and V is the unit cell volume (Å^3).

	Values from *Parise and Wang* (1990)	Values from this study	Percentage difference (%)
a	4.7918	4.7506	0.86
b	4.9312	4.8429	1.79
c	6.9050	6.8272	1.13
V	163.1605	157.0712	3.73

The second approach to add Fe^{2+} into bridgmanite is to simply create a Mg atom with the mass of an Fe atom, without changing any coefficients of the interatomic potentials from *Oganov et al.* (2000). I will show in Section 4.5.1 this 'isotopic model' is a reasonable first-order approximation. As the variation in mass number from Mg to Fe is large (24 to 56, a 133% increase), it is likely to change the behaviour of the system more than a subtle change in the atomic interactions.

Approximating Fe with heavier Mg atoms is used by *Ammann et al.* (2014) to investigate the effect of impurity content at conditions of 20 GPa and 2000 K. They found the effect of impurities varied according to a number of factors (crystallographic direction, interatomic potential), and they observed saturation in the conductivity decreased with concentration.

4.2.2 Simulated impurity distribution

Iron is substituted with magnesium into the bridgmanite structure. The unit cell contains 4 Mg atoms, and the smallest direct method cell I employ is a

6×2×2 supercell. Therefore the smallest amount of iron that can be added is 1/96 atoms, a concentration just over 1%. I use a simple MATLAB script to produce LAMMPS input files, randomly selecting a specified proportion of Mg atoms to be replaced with Fe.

To avoid clumping of iron within the model, I group Mg atoms by position within the supercell, so that Fe atoms are added with a homogeneous distribution on the scale of the supercell. At a smaller scale, changing 1/4 atoms is different to changing 24/96. The latter has a higher variance in Fe distribution, and the former replaces one Mg atom in every group of four.

4.3 Results

Lattice thermal conductivities obtained from Green-Kubo calculations are plotted against temperature in Figure 4.2, for Mg and Fe endmembers and the 50/50 solid solution mix. Each Green-Kubo data point is obtained from 8 initial temperature conditions, each producing 10 ACFs/integrals, totalling 80 ns of simulation time.

Conductivity decreases with temperature, approximately following $\kappa \propto 1/T^{0.9}$ at the pressure of 136 GPa considered here. This is in contrast to the typically expected $\kappa \propto 1/T$ relation, indicating some kind of saturation in conductivity decrease with temperature.

$FeSiO_3$ has a consistently lower conductivity than $MgSiO_3$, although both endmembers may converge given a high enough, albeit unphysical, lower mantle temperature. This suggests there is a minimum conductivity associated with the crystal structure, reached first by $FeSiO_3$ with its inherently lower conductivity.

The decrease in conductivity from Mg to Fe-endmember can be attributed to the increased atomic mass, which tends to reduce phonon velocities (i.e., Equation 1.5). The effect of electron conductivity is not included here, but it may reduce the conductivity difference between endmembers by increasing the

conductivity at high Fe% compositions.

The intermediate composition (i.e., $Mg_{0.5}Fe_{0.5}$) has lower thermal conductivity than either endmember at 1000 K, and a similar thermal conductivity to the Fe endmember at higher temperatures. This is to be expected because conductivity decreases from endmember to intermediate compositions as impurity concentration increases. The conductivities become more similar at temperatures at and above 3000 K. The conductivity differences become similar (Fig. 4.2) at high temperatures for $FeSiO_3$ and the solid solution. If $FeSiO_3$ has already reached its theoretical minimum, adding Mg impurities will do little to decrease it further.

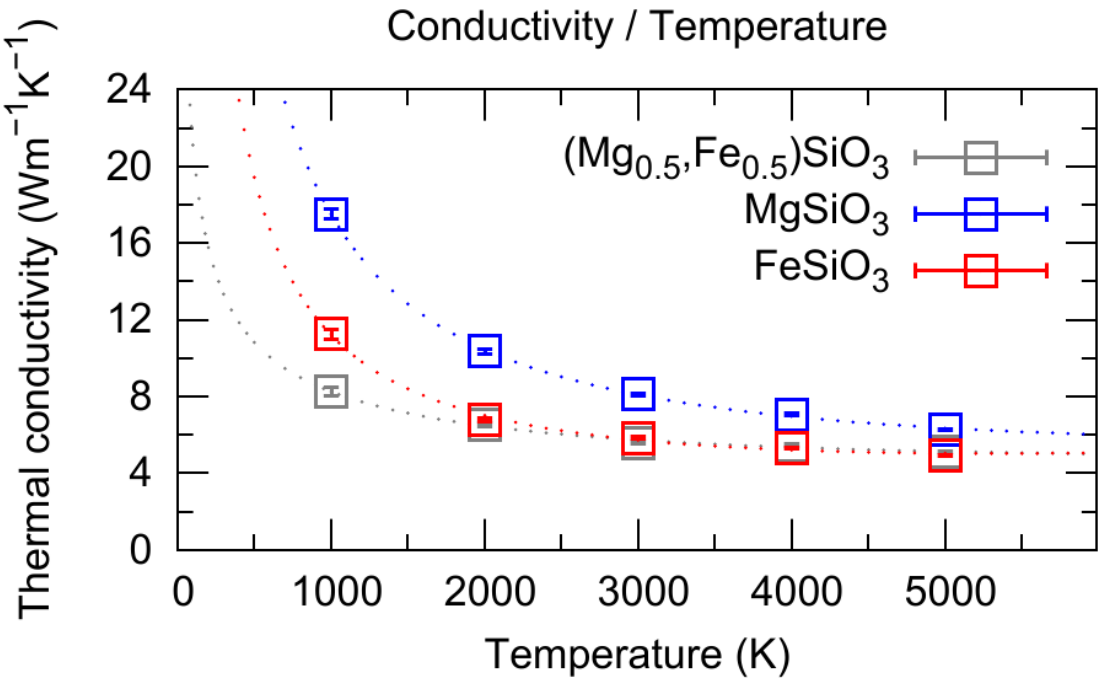

Figure 4.2: Thermal conductivity as a function of temperature for the $MgSiO_3$(blue squares), $FeSiO_3$ (red squares) and $(Mg_{0.5},Fe_{0.5})SiO_3$ (grey squares). Results are obtained using Green-Kubo at 136 GPa (Table 4.6). The dotted lines show fits to data using Equation 4.24, and constants from Table 4.4.

An alternative perspective to Figure 4.2 is presented in Figure 4.3, where Green-Kubo conductivity results are plotted as a function of Fe impurity content for several temperature series. Conductivity generally decreases with increasing temperature at all compositions, though the change becomes minimal at temperatures above 3000 K (Fig. 4.4).

The $MgSiO_3$ endmember has a consistently higher conductivity than the $FeSiO_3$. This can be explained by the increase in atomic mass as Mg is replaced with Fe, as this lowers the phonon velocities and thus decreases the conductivity.

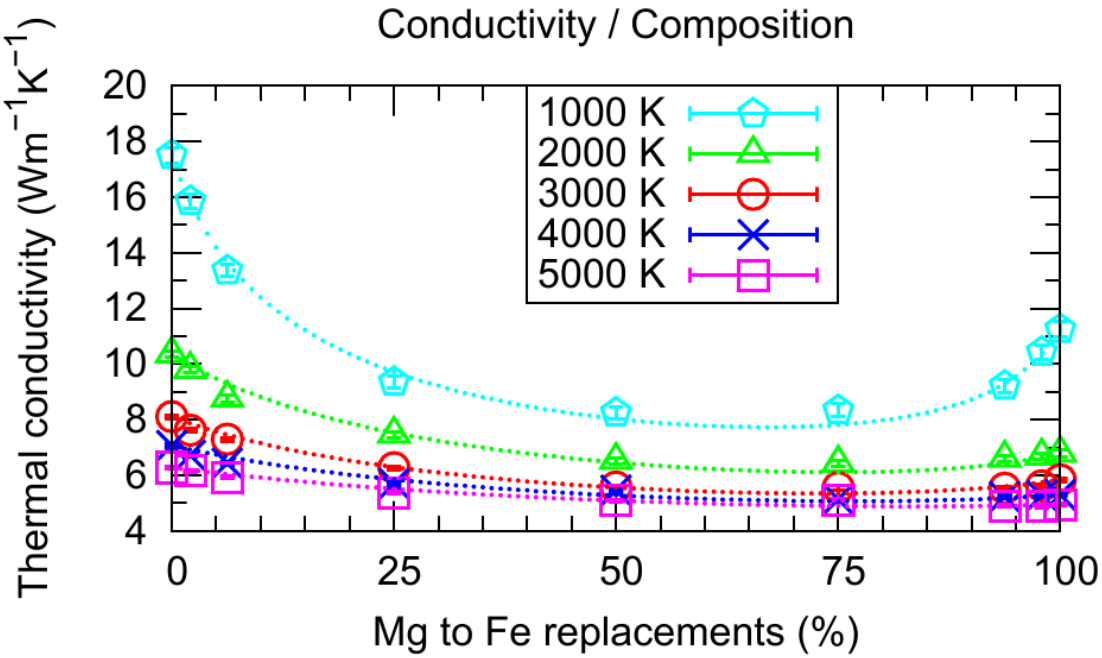

Figure 4.3: Computed thermal conductivities plotted as a function of Fe concentration for 1000 K (turquoise pentagons), 2000 K (green triangles), 3000 K (red circles), 4000 K (blue crosses) and 5000 K (pink squares). Dotted line represents the model fit for each series.

A simple interpolation between endmember conductivities is insufficient (Fig. 4.3), the presence of a compositional mix has an effect. This effect is itself temperature-dependent, the trough-like trend flattens with increasing temperature. These temperature and compositional dependences can be combined, allowing conductivity to be determined for a range of possible CMB conditions.

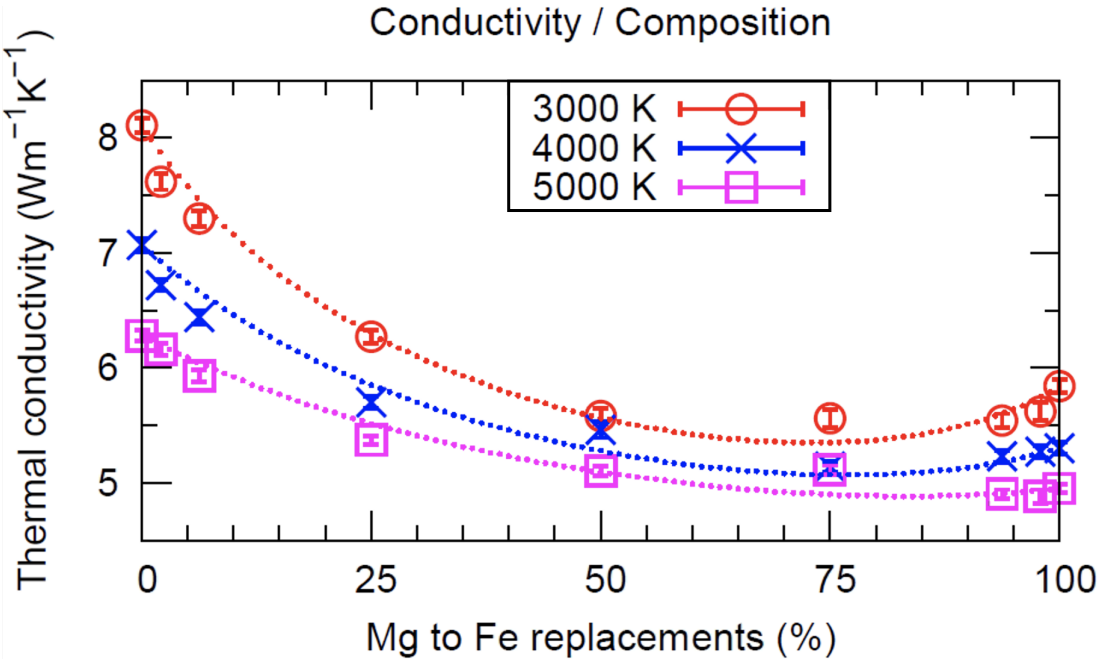

Figure 4.4: Enlarged scale version of Figure 4.3, showing computed thermal conductivities plotted as a function of Fe concentration for 3000 K (red circles), 4000 K (blue crosses) and 5000 K (pink squares). Dotted line represents the model fit for each series.

4.4 Parameterising composition and temperature effects on conductivity

In this section I develop a model for the lattice thermal conductivity of (Mg,Fe)SiO_3 perovskite at CMB conditions. Whilst the CMB is a small section of the lower mantle, it marks the heat flow boundary from core to mantle. Mantle-side thermal conductivity controls the nature of this heat flow, making it an important parameter in studies of both sides of the CMB interface.

Equations and functional forms exist for the temperature- and compositional-dependence of thermal conductivity, and it is possible to combine the two. They are based on the conductivity of $MgSiO_3$ and $FeSiO_3$ endmembers.

Padture and Klemens (1997) proposed a model for how impurities affect

lattice thermal conductivity of a solid solution, which *Ohta et al.* (2017) used to fit experimental ferropericlase data. Following a similar methodology, I fit the functional form to my (Mg,Fe)SiO_3 perovskite results at various temperatures (1000 K, 2000 K, 3000 K, 4000 K, and 5000 K). In an additional step, I establish how the functional forms change with temperature, i.e., the temperature-dependence of the compositional-dependence.

Okuda et al. (2017) present a temperature scaling relation for lattice conductivity (originally from *Manthilake et al.*, 2011), fit to their experimental results of bridgmanite. I apply this temperature scaling to computational results of $MgSiO_3$ and $FeSiO_3$ at 136 GPa. Through use of an exponent on the temperature term, the model is allowed to deviate from the theoretically-expected T^{-1} relation. With the temperature-dependence of these endmembers and of the compositional effect, I am able to determine the conductivity of any composition, interpolating to temperatures in the range 1000 K to 5000 K, at 136 GPa pressure representative of the CMB.

The aforementioned temperature-dependence from *Manthilake et al.* (2011) considers density, allowing conductivity to be determined as a function of temperature and pressure. In the examples I will present, I am only concerned with systems at 136 GPa. All density changes will result from thermal expansion, and the equations will be altered to accommodate this. Again through the use of an exponent, conductivity is allowed to deviate from its theoretically-expected linear relation with density. This flexibility allows correction for the fact that conductivities computed here are at constant pressure, not constant volume (*Manthilake et al.*, 2011).

4.4.1 Compositional-dependence of thermal conductivity

As described in Section 4.1.1, the lattice thermal conductivity of a solid-solution can be approximated as a function of temperature and composition (Equation 4.2). κ_{V} is the conductivity of the solid solution in the absence of impurity scattering (previously as Equation 4.3, modified here for the specific (Mg,Fe)SiO_3 endmembers),

$$\kappa_{\mathrm{V}} = (1 - C)\,\kappa_{\mathrm{Mg}} + C\;\kappa_{\mathrm{Fe}}\;, \tag{4.15}$$

where C is the fraction of Fe inclusions, and κ_{Mg} and κ_{Fe} are the temperature-dependent conductivities of the $MgSiO_3$ and $FeSiO_3$-endmembers respectively. The ratio of the phonon frequencies can be approximated (*Padture and Klemens*, 1997) using

$$\left(\frac{\omega_0}{\omega_{\mathrm{D}}}\right)^2 = \frac{\chi T}{C\,(1 - C)}\;, \tag{4.16}$$

where χ is a temperature-dependent constant, and T is the temperature of interest. χ can be thought of as a measure of resistance to the effects of impurity scattering. Although χ has not been explicitly calculated in this study, future work could determine χ by obtaining values for ω_0 and ω_{D}, e.g., by using a lattice dynamics approach to access phonon frequencies. The κ against C relationship (Fig. 4.3) shows a larger effect of impurity scattering in the form of greater curvature when T and χ are lower (see Table 4.3). For a given T and C, increasing χ causes the phonon frequency ratio $\left(\frac{\omega_0}{\omega_{\mathrm{D}}}\right)$ to increase which, as discussed in Section 4.1.1, means κ_{SS} tends towards κ_{V}. χ is fit to the data at each temperature, but for the model it needs to be a function of temperature. I fit χT against T with either a exponential or power law relationship (Fig. 4.5), as this term is used directly in Equation 4.16.

To describe the temperature-dependence of χT, I choose use the following

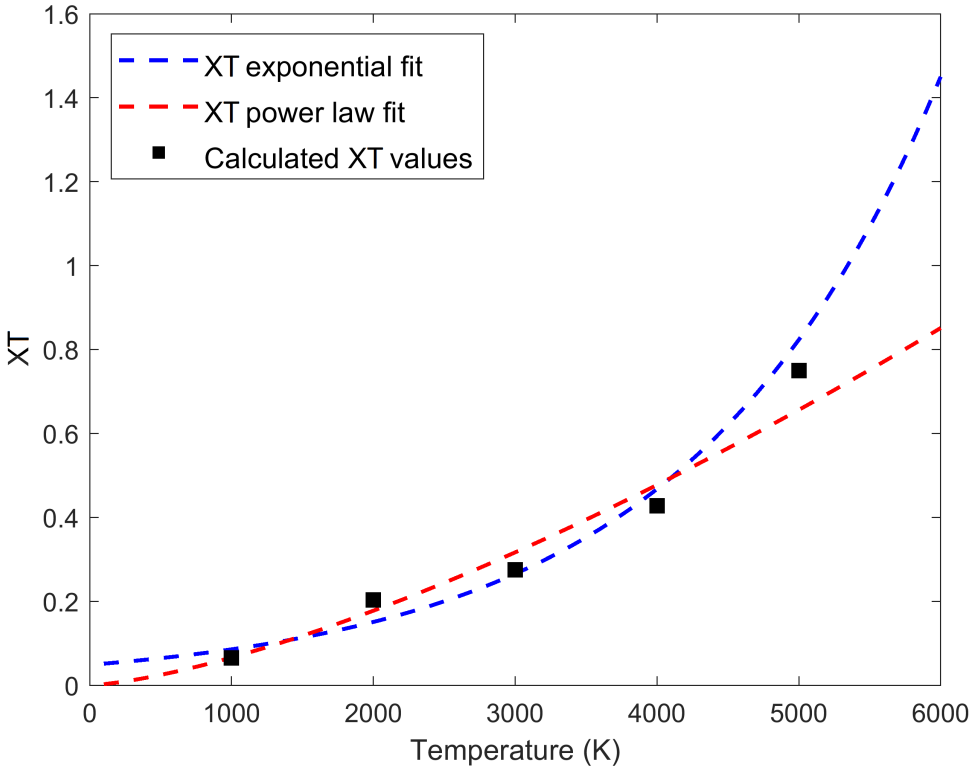

Figure 4.5: χT as a function of temperature, shown with exponential fit (blue) and power law fit (red).

Table 4.3: Variation with temperature of parameters used to fit the chemical and temperature-dependences. Reference volume from 1000 K for both endmembers.

		Temperature (K)				
		1000	2000	3000	4000	5000
Conductivity	Mg	17.51	10.36	8.11	7.07	6.28
($\mathrm{Wm^{-1}K^{-1}}$)	Fe	11.26	6.79	5.84	5.30	4.95
Volume ($\mathrm{Å^3}$)	Mg	5960	6017	6075	6136	6199
	Fe	6253	6310	6369	6431	6500
$V_{\mathrm{ref}}/V(T)$	Mg	1	0.9906	0.9811	0.9714	0.9616
	Fe	1	0.9909	0.9817	0.9723	0.9619
χ		6.49E-5	1.02E-4	9.16E-4	1.07E-4	1.50E-4
χT		0.0649	0.2035	0.2748	0.4277	0.7494

power law-relationship,

$$\chi T = AT^B, \tag{4.17}$$

where A is the coefficient and B is an exponent to be determined. Fitting of my data constrains these parameters to be 3.468×10^{-6} and 1.426 respectively.

This fit represents the temperature-dependence better, both statistically and sensitivity-wise compared to an exponential relationship $\left(\chi T = Ae^{BT}\right)$. The value of χT at high T has a lesser effect on the conductivity-composition relationship than at low T, where the power law fit matches the data better (Fig. 4.5).

At this point, I can qualitatively describe how the equation for modelling a solid solution's thermal conductivity (Equation 4.2) works and why. The first step is to calculate the conductivity for the composition of interest by linear interpolation of the endmembers. This (κ_{V}, Equation 4.15) is an overestimate of the true value.

Increasing mass difference and concentration (towards ∼50%) increase the importance of phonon-defect scattering. Mass difference is constant in this study. Concentration varies, but as discrete values across the various temperatures. For a given concentration, the mass difference and thus magnitude of point defect scattering is constant. Despite this, this decrease in conductivity due to adding impurities is not constant with temperature.

As temperature increases (through the range of conditions considered here) the degree of phonon-phonon scattering increases, decreasing conductivity (Fig. 4.2). The key thing in determining the effect of impurities is to consider the relative magnitudes of thermal scattering and defect scattering. As this ratio increases, with temperature, the importance of the defect scattering diminishes. An increase in thermal scattering reduces conductivity directly, but also reduces the change in conductivity associated with adding impurities.

This can be seen in Figure. 4.3, where the conductivity and compositional-dependence decrease with temperature. The model becomes more similar to the straight line through the endmember values as temperature increases, as the effect of thermal scattering increases relative to defect scattering. Figure 4.6 shows how the relative magnitudes of defect and thermal scattering

affect conductivity.

In the context of the model, the effect of this ratio is related to the arctan segment of Equation 4.2. The (ω_0/ω_D) term (Equation 4.16) contains the temperature and chemical (χ), and concentration (C) variables to control the scaling effect on κ_V.

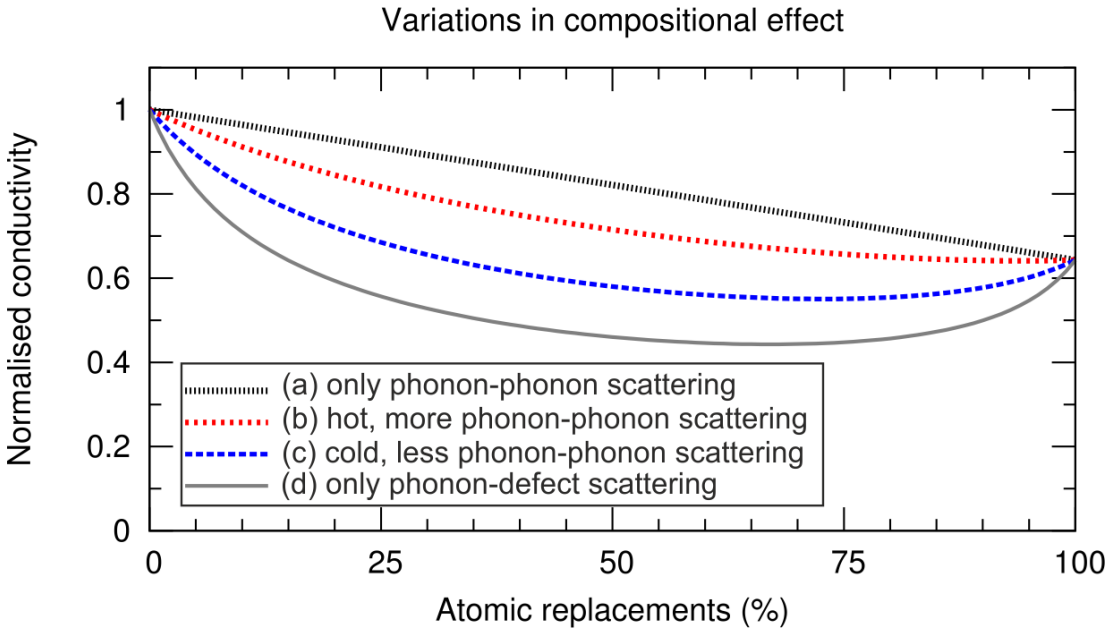

Figure 4.6: A graph showing how the relative magnitudes of phonon-phonon and defect scattering affect the resultant conductivity. Conductivity values are normalised to the maximum, the $MgSiO_3$ value in this case. This figure does not show how the magnitude of conductivity varies with temperature, but the magnitude of conductivity changes from adding impurities.
a. shows the compositionally-weighted average of endmember conductivities. It represents the conductivity due to phonon-phonon scattering in absence of defect scattering, where the reduction in conductivity comes with the addition of heavier Fe atoms over Mg.
b. & **c.** represent a solid solution at hot and cold conditions respectively. **b.** would be found at a higher temperature, where increased phonon-phonon scattering reduces the significance of defect scattering. **c.** represents a colder condition with phonon-phonon scattering, where impurities are more relevant and there is a larger decrease relative to **a.**, compared to the hot case (**b.**).
d. represents conductivity if impurity scattering were to dominate over phonon-phonon scattering. As with **a.**, this series is hypothetical, and the physical result lies somewhere between the two.

4.4.2 Temperature-dependence of thermal conductivity

Previous studies (*Stackhouse and Stixrude*, 2010; *Manthilake et al.*, 2011; *Okuda et al.*, 2017) have shown that the thermal conductivity of lower mantle minerals can be modelled by the following relation:

$$\kappa = \kappa_{\mathrm{ref}} \left(\frac{\rho}{\rho_{\mathrm{ref}}} \right)^{g} \left(\frac{T_{\mathrm{ref}}}{T} \right)^{a}, \tag{4.18}$$

where κ is the thermal conductivity at density ρ and temperature T, κ_{ref} is the thermal conductivity at reference density ρ_{ref} and reference temperature T_{ref}, and g and a are exponents. This equation is fit to the data, anchored around the values of the reference data point (the fit is shown in Fig. 4.2). I used the value at 1000 K as the reference value, as the conductivities at higher temperatures become more similar, converging towards a minimum point. Using this data point reduces the error in the fit, on account of the relatively larger conductivity at this temperature.

For a given composition, the mass of the simulated system does not change with temperature. The number and type of atoms remains constant, while thermal effects cause density variations. The density relation in Equation 4.18 can be reformulated as

$$\frac{\rho}{\rho_{\mathrm{ref}}} \equiv \frac{V_{\mathrm{ref}}}{V}, \tag{4.19}$$

because $\rho \propto V^{-1}$, where V is the volume of the system in question. This leads to a modified version of Equation 4.18

$$\kappa = \kappa_{\mathrm{ref}} \left(\frac{V_{\mathrm{ref}}}{V} \right)^{g} \left(\frac{T_{\mathrm{ref}}}{T} \right)^{a}. \tag{4.20}$$

κ represents the conductivity value adjusted for temperature, and is determined for both the $MgSiO_3$ and $FeSiO_3$-endmembers (by adjusting the reference values

and exponents). The temperature-dependent conductivities for both endmembers are then inserted into Equation 4.15 (as κ_{Mg} and κ_{Fe}), to determine the effect of composition. The exponent g (*Manthilake et al.*, 2011) represents the rate of change of lattice thermal conductivity with density, at a constant temperature,

$$g = (\partial \ln \kappa / \partial \ln \rho)_T \ . \tag{4.21}$$

The density changes that I observe result from thermal effects, i.e., not at a constant temperature and not pressure-driven. The rate of change in conductivity with density in my data are better represented as

$$h \sim (\partial \ln \kappa / \partial \ln \rho)_P \ , \tag{4.22}$$

where pressure (P) is the condition kept constant. The significance here is that pressure-driven and temperature-driven density changes affect the conductivity differently. At constant temperature, conductivity and density increase with pressure. The opposite is true at constant pressure for the temperatures considered here, conductivity and density decrease with increasing temperature. The result is g and h having opposite signs based on the scenarios they describe.

Volume does not need to be an input variable for the model, as all the data are obtained from constant pressure (136 GPa) calculations and any volume variations relate to thermal expansion. I express the volume ratio in Equation 4.20 as

$$\frac{V_{\mathrm{ref}}}{V(T)} \approx mT + c \ , \tag{4.23}$$

a simple linear function of temperature (Fig. 4.7), where m is the gradient and c the intercept.

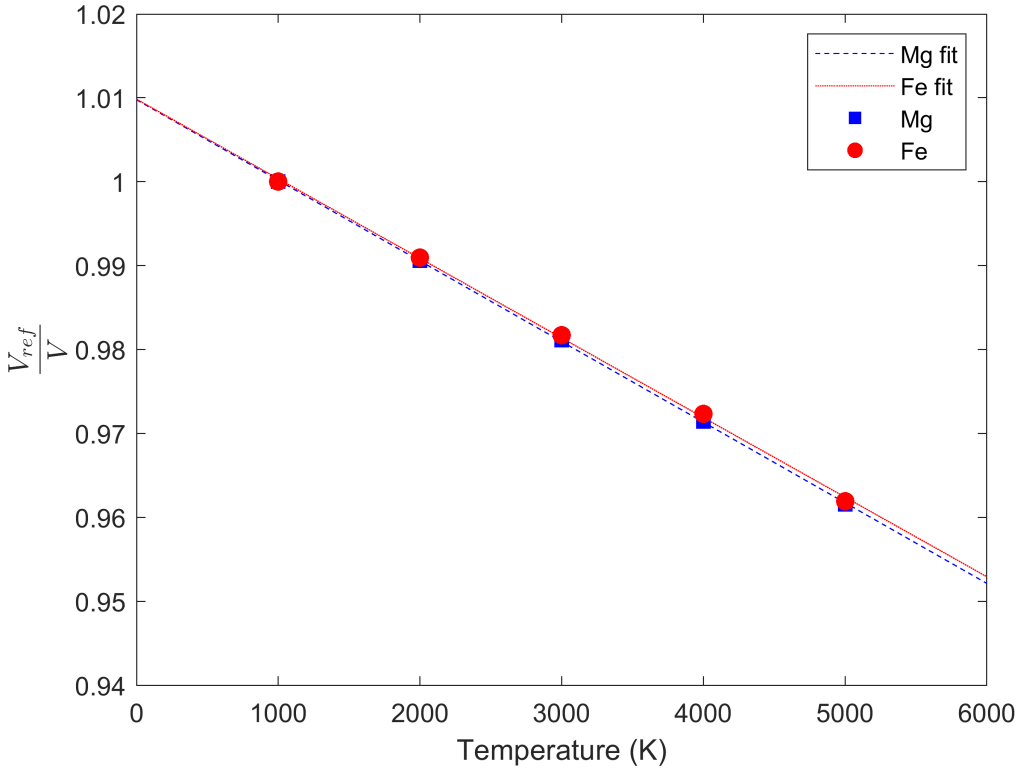

Figure 4.7: V_{ref}/V, expressed as a simple linear function of T.

With Equation 4.23, I rewrite Equations 4.18 and 4.20,

$$\kappa_j = \kappa_j^{\text{ref}} \left(m_j T + c_j\right)^{h_j} \left(\frac{T_j^{\text{ref}}}{T}\right)^{a_j}, \tag{4.24}$$

where subscript j refers either to the $MgSiO_3$ or $FeSiO_3$-endmember. Using this equation, I predict a conductivity value at any temperature within the fit range, from a reference conductivity and constants (m, c, h, & a, unique to each endmember, see Table 4.4). The constants are obtained by fitting data across all temperatures, for both endmembers.

4.4.3 Review of equations and constants in $\kappa(T, C)$ model

In this section, I present a review of the equations used to construct the $\kappa(T, C)$ model in this work. Subsequent equations explain terms in the first equation,

Table 4.4: Constants obtained by fitting Equation 4.24 to all data at 136 GPa. Mg and Fe refer to $MgSiO_3$ and $FeSiO_3$ endmembers, SS the solid solution with a 50% mix. κ_{ref} obtained at $T_{ref} = 1000$ K. $\kappa(T)$ is plotted for these compositions in Figure 4.2.

	Composition		
	Mg	SS	Fe
κ_{ref}	17.51	8.26	11.26
m	-9.60×10^{-6}	-9.47×10^{-6}	-9.48×10^{-6}
c	1.00975	1.00965	1.00983
h	-10.93	-5.52	-17.32
a	0.896	0.428	0.913

with a full expanded equation at the end. Also provided is a table with necessary constants to apply this model to calculate conductivity of (Mg,Fe)SiO_3 at 136 GPa. The conductivity of a given solid solution is given by

$$\kappa_{\mathrm{SS}} = \kappa_{\mathrm{V}} \left(\frac{\omega_0}{\omega_{\mathrm{D}}} \right) \arctan \left(\frac{\omega_{\mathrm{D}}}{\omega_0} \right), \tag{4.25}$$

which depends on the linear average of endmember conductivities in the absence of phonon-phonon scattering and the ratio of phonon frequencies. The compositionally weighted conductivity is given by

$$\kappa_{\mathrm{V}} = (1 - C)\, \kappa_{\mathrm{Mg}} + C\ \kappa_{\mathrm{Fe}}\ , \tag{4.26}$$

where the conductivity of each endmember is given by

$$\kappa_{\mathrm{Mg}} = \kappa_{\mathrm{Mg}}^{\mathrm{ref}} \left(m_{\mathrm{Mg}} T + c_{\mathrm{Mg}} \right)^{h_{\mathrm{Mg}}} \left(\frac{T_{\mathrm{Mg}}^{\mathrm{ref}}}{T} \right)^{a_{\mathrm{Mg}}} \tag{4.27}$$

and

$$\kappa_{\mathrm{Fe}} = \kappa_{\mathrm{Fe}}^{\mathrm{ref}} \left(m_{\mathrm{Fe}} T + c_{\mathrm{Fe}} \right)^{h_{\mathrm{Fe}}} \left(\frac{T_{\mathrm{Fe}}^{\mathrm{ref}}}{T} \right)^{a_{\mathrm{Fe}}}, \tag{4.28}$$

respectively. The ratio of phonon frequencies is expressed as

$$\left(\frac{\omega_0}{\omega_{\mathrm{D}}}\right)^2 = \frac{\chi T}{C\,(1-C)}\ , \tag{4.29}$$

where I model χT as a function of temperature

$$\chi T = AT^B, \tag{4.30}$$

which leads to

$$\left(\frac{\omega_0}{\omega_{\mathrm{D}}}\right) = \sqrt{\frac{AT^B}{C\,(1-C)}} \tag{4.31}$$

and

$$\left(\frac{\omega_{\mathrm{D}}}{\omega_0}\right) = \sqrt{\frac{C\,(1-C)}{AT^B}}\ . \tag{4.32}$$

Referring back to Equation 4.25, fully expanded it takes the form

$$\begin{aligned}\kappa_{\mathrm{SS}}(T,C) = \Bigg(\Bigg((1-C)\,\kappa^{\mathrm{ref}}_{\mathrm{Mg}}\,(m_{\mathrm{Mg}}T + c_{\mathrm{Mg}})^{h_{\mathrm{Mg}}}\left(\frac{T^{\mathrm{ref}}_{\mathrm{Mg}}}{T}\right)^{a_{\mathrm{Mg}}}\Bigg) \\ + \left(C\,\kappa^{\mathrm{ref}}_{\mathrm{Fe}}\,(m_{\mathrm{Fe}}T + c_{\mathrm{Fe}})^{h_{\mathrm{Fe}}}\left(\frac{T^{\mathrm{ref}}_{\mathrm{Fe}}}{T}\right)^{a_{\mathrm{Fe}}}\right)\Bigg)\left(\sqrt{\frac{AT^B}{C\,(1-C)}}\right)\arctan\left(\sqrt{\frac{C\,(1-C)}{AT^B}}\right).\end{aligned} \tag{4.33}$$

All of the constants used in this equation to calculate $\kappa(T,C)$ are given in Table 4.5.

Table 4.5: All the constants from Table 4.4 and Equation 4.17 used to calculate $\kappa(T,C)$ in Equation 4.33.

	Composition	
	Mg	Fe
κ_{ref}	17.51	11.26
m	-9.60×10^{-6}	-9.48×10^{-6}
c	1.00975	1.00983
h	-10.93	-17.32
T_{ref}	1000	
] a	0.896	0.913
A	3.468×10^{-6}	
B	1.426	

4.5 Discussion

Before I can apply this model to the Earth, I look at the implications of these results for the simulation of thermal conductivity of solid solutions, and estimate the MFP of phonons within the solid solution.

4.5.1 Significance of mass and atomic interactions

To determine the importance of mass difference in phonon-defect scattering, I run calculations where the mass of the impurities are kept the same as Mg, only changing their potential to match my fitted Mg-Fe interaction. I predict conductivity will be largely unchanged with varying composition.

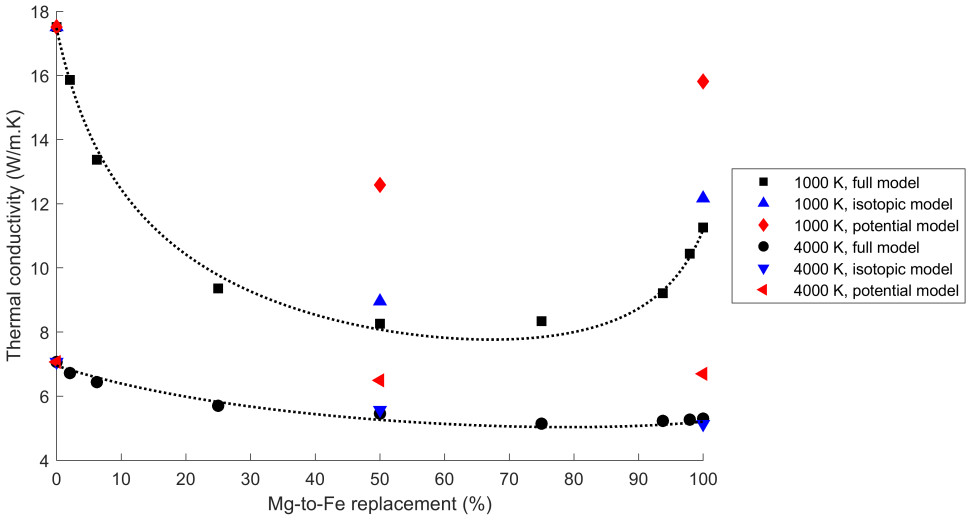

Figure 4.8: Green-Kubo conductivity results and model fits for 1000 K and 4000 K. The Fe in these series have the correct atomic mass, and the calibrated interatomic potential. The partial series show how conductivity changes when the atomic interactions are altered.

Figure 4.8 shows the Green-Kubo results of this study as a function of composition for 1000 and 4000 K, with the model fit to data. The other partial series represent the results of additional calculations, where the iron impurities only have the correct mass (the isotopic model, akin to *Ammann et al.*, 2014),

or with my calibrated Fe-O pair potential but the Mg mass. The isotopic atomic model is much closer to the results of the full model than the potential for Fe with the mass of Mg. Both atomic masses and chemical bonding play a roll in determining the interaction, albeit mass is more significant.

Intuitively, the potential and the mass is more representative than only changing the atomic mass, however I do not vary atomic charge from Mg to Fe. Predicting the thermal conductivity of bridgmanite at lower mantle conditions is additionally complicated by the Fe-partitioning between $MgSiO_3$ and MgO, the effect of ferrous vs. ferric iron, and how spin state affects properties such as conductivity as it varies along the geotherm (e.g., *Ohta et al.*, 2017). These additional complexities are beyond the scope of this project, where only ferrous iron is considered.

4.5.2 Comparison of simulated and modelled conductivities

Figure 4.9a shows the absolute percentage errors between the simulated conductivity data and the model fit and it shows good agreement between the two. Percentage errors are consistently less than 1.5%.

As mentioned in Section 4.4.2, I fit the temperature data using a reference point of 1000 K. In Table 4.6 , the modelled and computed data for 1000 K are different, as I have also incorporated the approximation for $\frac{V_{\text{ref}}}{V}$.

Table 4.7 and Figure 4.9 show the simulated and model values for the composition-dependence of conductivity. I show that the model is most closely fitted to the data at the endmembers, but there is overall good agreement with errors consistently below 3.1%.

Table 4.6: Simulated conductivity values, and values determined using the conductivity model fit, for temperature-dependent conductivity at a range of compositions.

	Temperature (K)	Simulated conductivity ($Wm^{-1}K^{-1}$)	Conductivity from model fit ($Wm^{-1}K^{-1}$)
Mg	1000	17.51 ± 0.27	17.44
	2000	10.36 ± 0.13	10.45
	3000	8.11 ± 0.06	8.10
	4000	7.07 ± 0.06	6.96
	5000	6.28 ± 0.05	6.33
Fe	1000	11.26 ± 0.27	11.15
	2000	6.79 ± 0.12	7.02
	3000	5.84 ± 0.07	5.74
	4000	5.30 ± 0.05	5.21
	5000	4.95 ± 0.04	5.01
$(Mg_{0.5}Fe_{0.5})SiO_3$	1000	8.26 ± 0.22	8.24
	2000	6.53 ± 0.11	6.47
	3000	5.58 ± 0.07	5.74
	4000	5.46 ± 0.05	5.35
	5000	5.10 ± 0.04	5.12

4.5.3 Scaling MFP to quantify phonon-defect scattering

MFP is directly proportional to conductivity (Equation 2.15) assuming that heat capacity and phonon velocity are constant with composition. Therefore I propose scaling the 4000 K GK conductivity results to quantify the phonon-defect scattering associated with adding iron. When considering the effect of impurities on conductivity, the effective MFP depends on phonon-phonon and phonon-defect interactions

$$\frac{1}{\Lambda} = \frac{1}{\Lambda_{\mathrm{ph-ph}}} + \frac{1}{\Lambda_{\mathrm{ph-d}}} \ . \tag{4.34}$$

The MFP for $MgSiO_3$ determined from the direct method extrapolation can be matched with the equivalent 0% Fe, 4000 K Green-Kubo result on Figure 4.3. If 7.07 $Wm^{-1}K^{-1}$ is proportional to an effective MFP of 0.23 nm, I can scale this MFP value by the $MgSiO_3$ endmember-normalised conductivities (Fig. 4.10).

I make the assumption that the data points/curve of Figure 4.10 represent

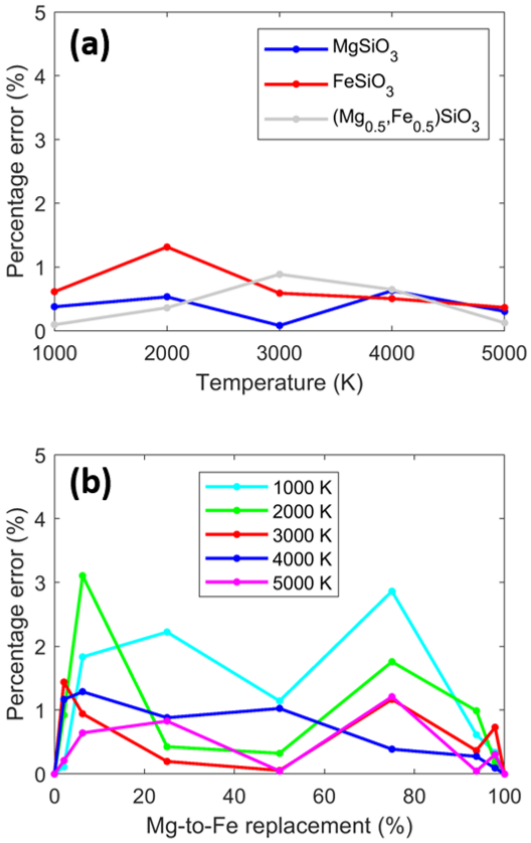

Figure 4.9: Absolute percentage errors between the computed thermal conductivity values and the model fit, for (a) temperature-dependent conductivity, and **b** composition-dependent conductivity.

the effective MFP, and that the linear interpolation between endmembers the phonon-phonon scattering MFP. The interpolated conductivities do not capture the non-linear effects of defect scattering, at constant temperature the change in conductivity is proportional to the change in mass associated with changing Mg to Fe.

The deficit between computed and interpolated conductivity can be imagined as phonon-defect contribution to Λ, the bigger the gap at a given composition, the greater significance of $\Lambda_{\mathrm{ph-d}}$. I will obtain the phonon-defect MFP by subtracting the inverse of the two, as in

$$\frac{1}{\Lambda_{\mathrm{ph-d}}} = \frac{1}{\Lambda} - \frac{1}{\Lambda_{\mathrm{ph-ph}}} \ . \tag{4.35}$$

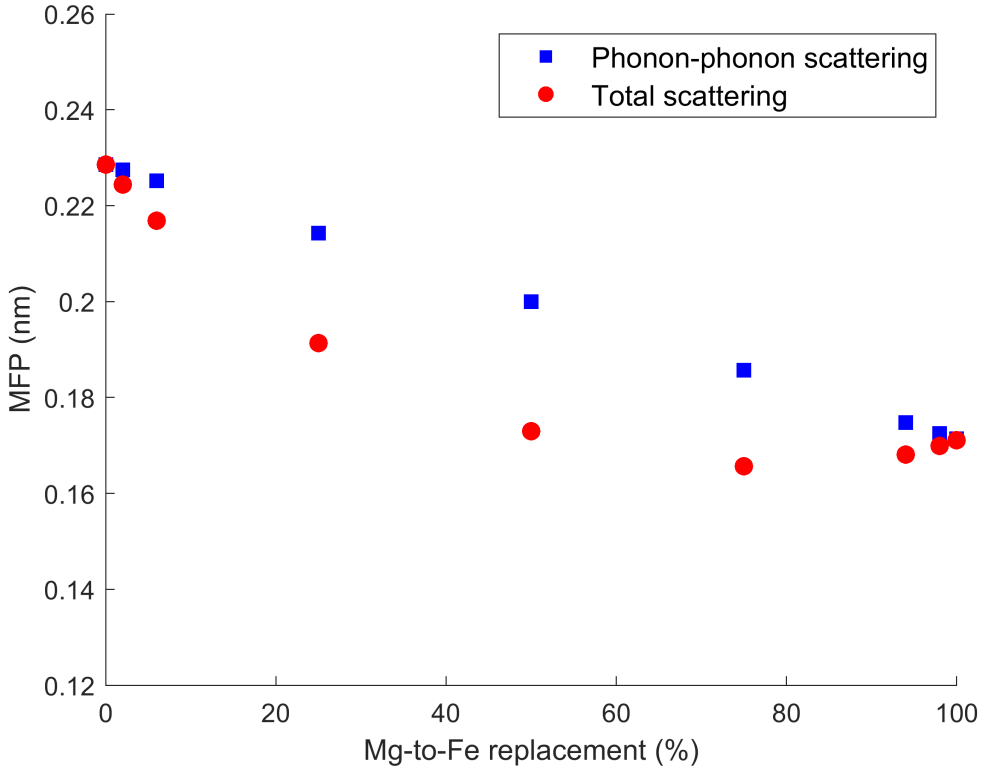

Figure 4.10: Green-Kubo conductivity results from 4000 K, scaled to the MFP determined from analysis of direct method results. The linear interpolation between endmembers gives the MFP of phonon-phonon scattering, which decreases as Fe is introduced and the mass of the system increases.

Table 4.8 shows how properties change across the range of compositions studied. The results are the computed conductivity, the interpolated conductivity as a function of composition, this difference between this two value, and the conductivity result normalised. This conductivity is then converted to a mean-free path value as discussed earlier, as is the interpolated conductivity to obtain my proxy for phonon-phonon scattering MFP. I then calculate the phonon-defect scattering MFP as in Equation 4.34. This value is then inverted and normalised, showing relative significance of scattering as conductivity varies.

If the mean free path is the distance between scattering events, then the inverse (as presented in Equation 4.35) is the amount of scattering events per unit distance. The total number of scattering events combines the number of

phonon-phonon and phonon-defect collisions, as shown for 4000 K and 1000 K respectively in Figures 4.11 & 4.12. Where phonon-phonon scattering is high because of 4000 K temperature, impurity scattering influences, but is not the dominant control on the magnitude of scattering. This behaviour is different at 1000 K, where the effect of phonon-defect scattering is of comparable magnitude to the decreased phonon-phonon scattering for high impurity contents (i.e., around 50%). The largest phonon-defect scattering coincides with the largest difference between computed and interpolated conductivity, as might be expected.

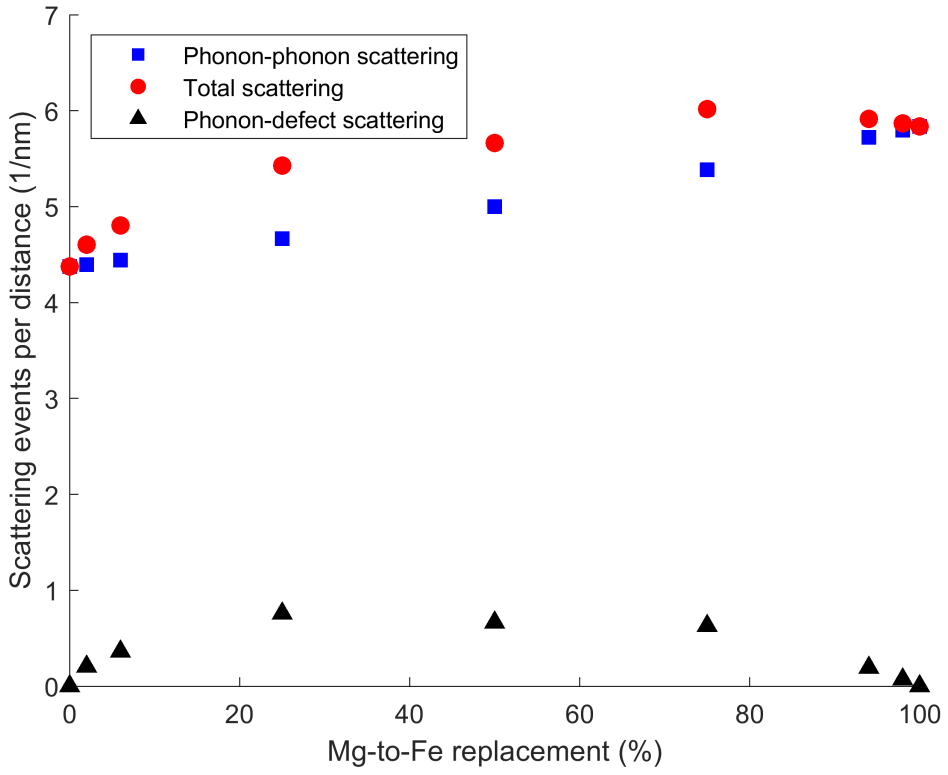

Figure 4.11: Scattering events per distance, or inverse of MFP, plotted against composition at 4000 K. The total scattering behaves like the inverse of the conductivity. Phonon-phonon scattering increases with composition, as the mass of the system increases. Phonon-defect scattering increases from each endmember, to a maximum point at an intermediate composition. The ph-ph scattering is high compared to ph-d, the 4000 K temperature dominates the MFP behaviour.

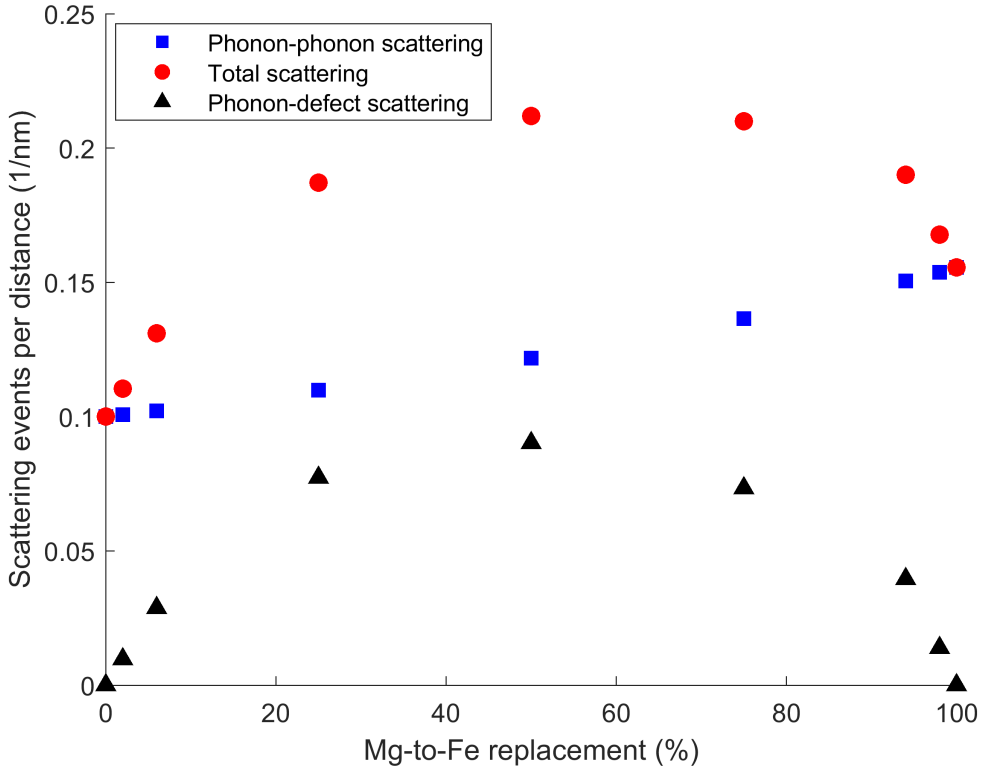

Figure 4.12: An illustrative measure of scattering significance, plotted against composition at 1000 K. The total scattering behaves like the inverse of the conductivity. Phonon-phonon scattering increases with composition, as the mass of the system increases. Phonon-defect scattering increases from each endmember, to a maximum point at an intermediate composition. While the magnitude of phonon-defect scattering is similar to that at 4000 K, ph-ph scattering is smaller due to the lower temperature. The relative significance of ph-d increases, meaning impurities have a greater effect on the conductivity.

4.5.4 $C\,(1-C)$ model limitations

Despite the good agreement between the simulated and modelled data, there are still limitations to following this methodology to determine conductivity at all temperatures and compositions.

Using the method discussed in Section 3.2.9 to determine $\Lambda_{\mathrm{ph-d}}$, I am able to observe how the mean free path of phonon defect scattering changes with composition. Table 4.8 presents both calculated values and those predicted using my model. When the data is used to determine $\Lambda_{\mathrm{ph-d}}$, the greatest effect is at a

composition between 25% and 50% (albeit closer to 25%).

Taking the 4000 K conductivity model however, the largest effect of phonon-defect scattering (smallest MFP) is at a composition around 50% (see Fig. 4.13). This is to be expected, and is set by the $C\,(1-C)$ term in Equation 4.16. The $C\,(1-C)$ model is assuming that an equal proportion of each type of atom (i.e., 50/50 composition) creates the most phonon-defect scattering, but my results indicate that it is weighted by the masses of the atoms in question. This requires further investigation. The composition at which the mass contribution is equal can be calculated by

$$C_{\text{mass}} = \frac{A_{\text{Mg}}}{A_{\text{Mg}} + A_{\text{Fe}}} \,, \tag{4.36}$$

where A is atomic mass, Mg corresponds to $C = 0$ and Fe to $C = 1$. For Mg and Fe, $C_{\text{mass}} = 0.3$, or 30% Fe to 70% Mg (Fig. 4.14), which appears here to be the turning point in phonon-defect scattering. Defect scattering increases from zero up to its maximum at this composition, and decreases to zero as Fe content tends towards 100%. Even if conductivity decreases overall due to phonon-phonon scattering effects with increasing temperature, this composition will be the point of minimum $\Lambda_{\text{ph-d}}$.

4.6 Conclusion

In this chapter I have considered how the conductivity of bridgmanite varies with temperature and iron content at 136 GPa, using a dense sampling of data points. I first showed that conductivity decreases with increasing temperature, for varying compositions (Fig. 4.2). I showed that the $MgSiO_3$ end member has a higher thermal conductivity across all temperatures, compared to the $FeSiO_3$ end member. When I considered the conductivity of $(Mg_{0.5}Fe_{0.5})SiO_3$ across a range of

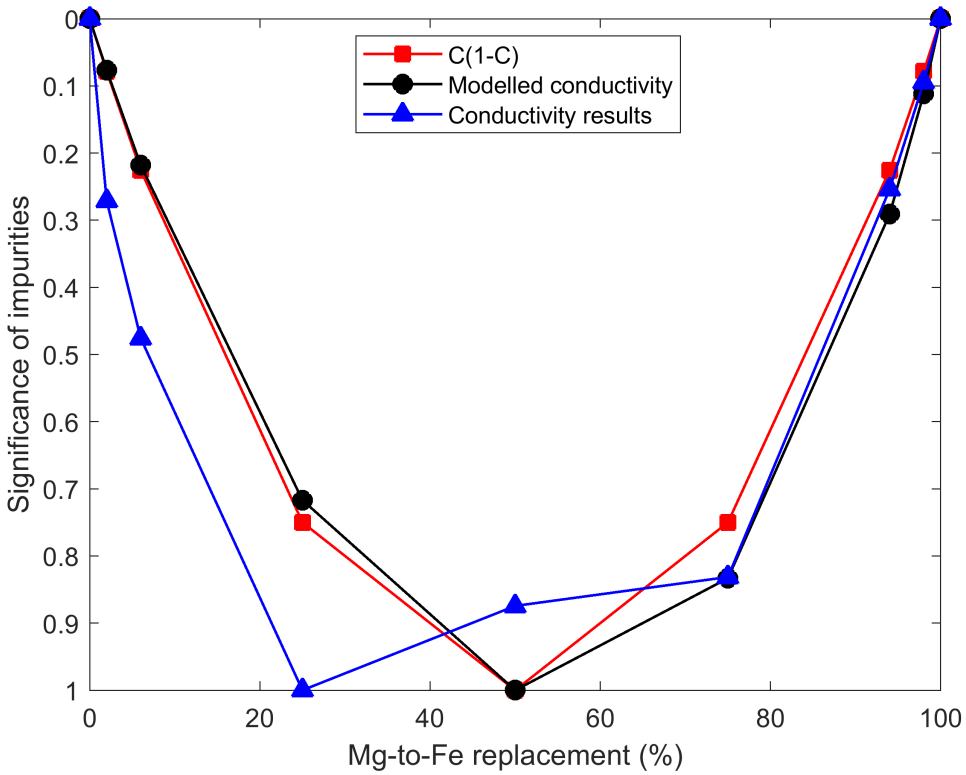

Figure 4.13: An illustration of how the significance of ph-d scattering changes with composition depending on the data. Determining the ph-d MFP from the model gives a result similar to $C\,(1-C)$, as might be expected (not exactly though, error is introduced by the model not being fixed to the endmembers). However the data shows that the largest effect of defects is between 25% and 50%, presumably closer to 25%.

temperatures, the conductivity did not fall between the Mg and Fe endmembers, but rather is approximately equal to or lower than the Fe endmember.

Next, I investigated the relationship between thermal conductivity of bridgmanite and composition. The intermediate solid solution compositions have lower conductivity values than the respective Mg and Fe endmembers (Fig. 4.3) and I showed that the conductivity values cannot be linearly interpolated between the endmember compositions. The effect of impurities on conductivity changes with temperature, because impurity scattering has a larger effect at higher initial conductivities. When conductivity decreases with temperature, the addition of impurities still further decreases conductivity, but the effect is smaller at higher

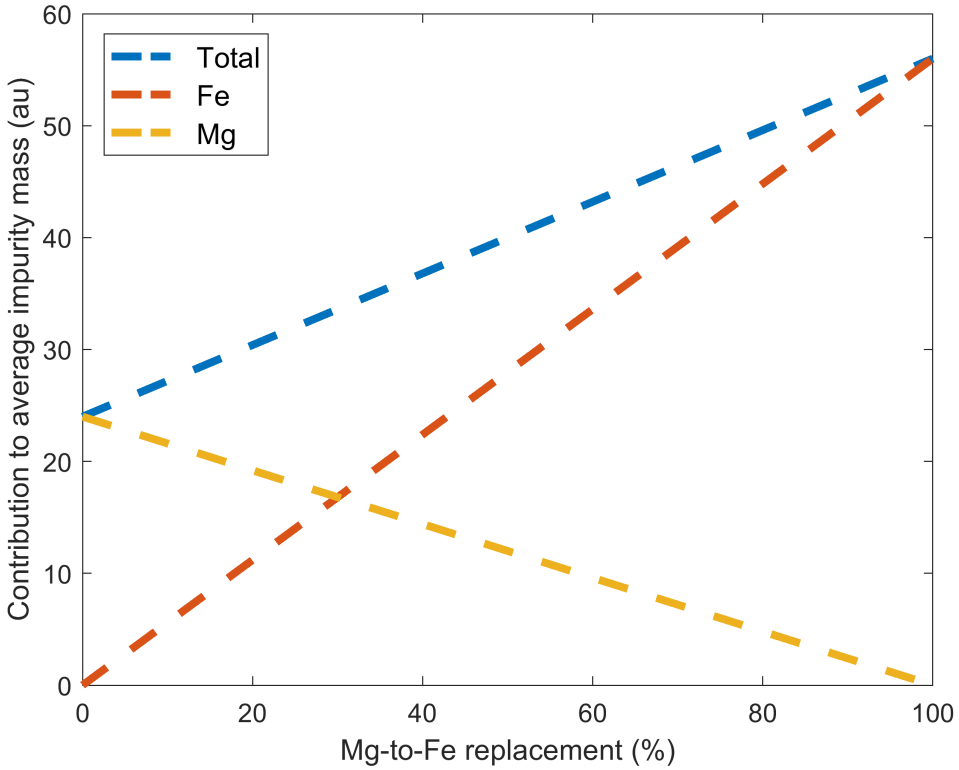

Figure 4.14: An illustration of contributions to the average mass of all Mg and Fe in the system. They contribute equally when 30% of Mg is replaced with Fe.

temperatures.

Impurities have a less significant effect on thermal conductivity at higher temperatures. This suggests that the thermal conductivity does not reduce further because it has already approached its minimum; this effect is referred to as saturation, a concept which has been debated in the literature (e.g., *Ammann et al.*, 2014; *Ghaderi et al.*, 2017). I show that the initial inclusion of small amounts (∼5%) of iron impurities into bridgmanite causes a significant drop in conductivity, but the effect plateaus with further iron addition, as found by *Tang et al.* (2014). This is because the phonon-phonon scattering is dominant at higher temperatures (i.e., the relative differences between phonon-phonon and phonon-defect scattering between Fig. 4.11 and 4.12).

More broadly, my investigation has implications for how impurities affect solid

solutions above the Debye temperature. I suggest that the concept of saturation is likely to be present with impurities other than iron. The magnitude of the effect may be smaller or larger than that observed in iron within bridgmanite, if the the atomic mass change or initial conductivity differ.

I combined the composition-dependent conductivity model of *Padture and Klemens* (1997) and the temperature-dependent model of *Okuda et al.* (2017). This produced a complete model of thermal conductivity across all possible lower mantle temperatures and iron concentrations, at CMB pressure.

I investigated the difference between methods of modelling iron - a simple isotopic model, and updated potential. I show that for simulating the conductivity of bridgmanite at lower mantle conditions, the isotopic model better approximates the full model than using only the potential model, both at 1000 K and 4000 K. I suggest therefore that if a potential is not available for a given impurity, using only an isotopic model could be a suitable approximation. This supports the results of the isotopic model used by *Ammann et al.* (2014).

In Chapter 3, I obtained the phonon mean free path. In this chapter, I expand on this method and show that it is also possible to determine the phonon-phonon mean free path and the phonon-defect mean free path. By assuming that the Green-Kubo calculations in this chapter produce thermal conductivities corresponding to the same MFPs calculated in Section 3.2.9, and that conductivity is directly proportional to MFP, I scale the compositional-dependent Green-Kubo results into MFPs. I calculate the phonon-phonon scattering by linearly interpolating between endmember compositions, and subtracting the phonon-phonon scattering from the effective scattering determines the phonon-defect scattering. This shows that the phonon-defect mean free path is smaller at low temperatures, and that it varies with composition.

The composition model from *Padture and Klemens* (1997) assumes that the effect of impurities on conductivity increases up to a 50% solid solution, and

then decreases towards the other endmember. By quantifying the phonon-defect mean free path, I show that this turning point does not occur when the number of Fe-replacements is equal to number of Mg atoms (as assumed by *Padture and Klemens* (1997) in the $C\,(1-C)$ term), but rather when Mg atoms and Fe atoms contribute equally to the mass of the system. I therefore suggest that a more complex model would allow better estimation of conductivity for a given impurity content.

The conclusions from this chapter have broader implications for the study of impurities across a range of temperatures. I suggest that to obtain a full picture of the lower mantle, similar studies to this would need to be undertaken for other impurities and/or minerals. For example, the combined composition-temperature conductivity model that I produced in this chapter could also be used to model how iron content affects the conductivity of ferropericlase. Following the analysis of isotopic and potential models, this could be done using purely an isotopic model.

The main aim of developing a model of the temperature- and compositional-dependence of the thermal conductivity of bridgmanite is to include it in a numerical study of core-mantle boundary heat flux. Therefore, the combined model from this chapter will be taken forward into Chapter 5 to investigate the effects of temperature, composition and conductivity on core-mantle boundary heat flux, thus drawing conclusions in terms of whole mantle dynamics.

4.7 Summary

1. I investigated the ways in which impurities can be added to, and affect, a crystalline structure. I showed that changing atomic mass to represent impurities is a reasonable method for Fe in bridgmanite, and may be

considered for other systems if a full interatomic potential model is unavailable.

2. By considering the full range of impurity inclusion (i.e., from 0 to 100%) I showed that the effect of adding an impurity depends on the ratio of its mass with the atom it is replacing, a potential shortcoming unidentified in previous models.

3. Using the Green-Kubo method, I computed lattice thermal conductivity at 136 GPa and a range of lower mantle temperatures, from bridgmanite to its $FeSiO_3$-endmember. I obtain results of 7.07 ± 0.06 $Wm^{-1}K^{-1}$ for bridgmanite, 5.30 ± 0.05 $Wm^{-1}K^{-1}$ for the $FeSiO_3$ endmember, and 5.46 ± 0.05 $Wm^{-1}K^{-1}$ for the 50% (Mg,Fe)SiO_3 solid solution, at CMB conditions of 136 GPa and 4000 K.

4. I fit a model to the data obtained, allowing determination of thermal conductivity for temperatures between 1000–5000 K at 136 GPa. This is the first time such an extensive model has been developed across the full range of (Mg,Fe)SiO_3 composition.

5. Computation of this series of results reveals that lattice thermal conductivity tends to saturate towards a minimum value at CMB conditions. If conductivity is reduced (e.g., increasing temperature, adding Fe) to a certain point, then changing conditions to increase it (e.g., increasing pressure) have minimal effect. This effect is significant when considering temperature in the lowermost mantle, lateral variations only have a small effect on conductivity if all temperatures are > 3000 K.

Table 4.7: Simulated conductivity values, and values determined by model fit, for compositional-dependent conductivity at a range of temperature values.

	Composition (Mg-to-Fe replacement %)	Simulated conductivity ($Wm^{-1}K^{-1}$)	Conductivity from model fit ($Wm^{-1}K^{-1}$)
1000 K	0.00	17.51 ± 0.27	17.51
	2.08	15.86 ± 0.26	15.84
	6.25	13.37 ± 0.25	13.69
	25.00	9.36 ± 0.22	9.75
	50.00	8.26 ± 0.22	8.06
	75.00	8.34 ± 0.24	7.84
	93.75	9.21 ± 0.25	9.32
	97.92	10.44 ± 0.26	10.38
	100.00	11.26 ± 0.27	11.26
2000 K	0.00	10.36 ± 0.13	10.36
	2.08	9.80 ± 0.12	9.96
	6.25	8.76 ± 0.11	9.30
	25.00	7.47 ± 0.11	7.54
	50.00	6.53 ± 0.11	6.47
	75.00	6.43 ± 0.11	6.12
	93.75	6.61 ± 0.11	6.44
	97.92	6.68 ± 0.12	6.65
	100.00	6.79 ± 0.12	6.79
3000 K	0.00	8.11 ± 0.06	8.11
	2.08	7.62 ± 0.07	7.87
	6.25	7.30 ± 0.07	7.46
	25.00	6.27 ± 0.06	6.30
	50.00	5.58 ± 0.07	5.57
	75.00	5.56 ± 0.06	5.36
	93.75	5.54 ± 0.06	5.60
	97.92	5.62 ± 0.07	5.75
	100.00	5.84 ± 0.07	5.84
4000 K	0.00	7.07 ± 0.06	7.07
	2.08	6.72 ± 0.06	6.92
	6.25	6.44 ± 0.06	6.67
	25.00	5.70 ± 0.06	5.85
	50.00	5.46 ± 0.06	5.28
	75.00	5.14 ± 0.06	5.07
	93.75	5.23 ± 0.06	5.18
	97.92	5.27 ± 0.06	5.25
	100.00	5.30 ± 0.06	5.30
5000 K	0.00	6.28 ± 0.05	6.28
	2.08	6.16 ± 0.05	6.20
	6.25	5.93 ± 0.05	6.04
	25.00	5.37 ± 0.04	5.51
	50.00	5.10 ± 0.04	5.09
	75.00	5.11 ± 0.04	4.90
	93.75	4.90 ± 0.04	4.91
	97.92	4.88 ± 0.04	4.93
	100.00	4.95 ± 0.04	4.95

Table 4.8: Conductivities within this table are obtained from simulations at 4000 K. Inferred MFPs change subtly depending on whether the raw data, or values from the model are considered. Conductivity difference represents the significance of impurities, shown by the MFP of phonon-defect scattering and its relative influence.

	Fe content (100%)	Conductivity result ($Wm^{-1}K^{-1}$)	Interpolated conductivity ($Wm^{-1}K^{-1}$)	Conductivity difference ($Wm^{-1}K^{-1}$)	Normalised conductivity ($Wm^{-1}K^{-1}$)	Conductivity-scaled MFP (nm)	Scaled ph-ph scattering MFP (nm)	Inferred ph-d scattering MFP (nm)	Relative ph-d scattering
Data	0.00	7.07	7.07	0.00	1.00	0.229	0.229	INF	0.00
	0.02	6.72	7.03	0.31	0.95	0.217	0.227	4.86	0.27
	0.06	6.44	6.96	0.52	0.91	0.208	0.225	2.77	0.48
	0.25	5.70	6.63	0.93	0.81	0.184	0.214	1.32	1.00
	0.50	5.46	6.19	0.73	0.77	0.177	0.200	1.51	0.87
	0.75	5.14	5.74	0.60	0.73	0.166	0.186	1.58	0.83
	0.94	5.23	5.41	0.18	0.74	0.169	0.175	5.19	0.25
	0.98	5.27	5.34	0.07	0.75	0.170	0.172	13.90	0.09
	1.00	5.30	5.30	0.00	0.75	0.171	0.171	INF	0.00
Model	0.00	6.95	6.95	0.00	1.00	0.229	0.229	INF	0.00
	0.02	6.83	6.92	0.09	0.98	0.224	0.227	16.77	0.08
	0.06	6.60	6.85	0.25	0.95	0.217	0.225	5.88	0.22
	0.25	5.82	6.52	0.70	0.84	0.191	0.214	1.79	0.72
	0.50	5.26	6.08	0.82	0.76	0.173	0.200	1.28	1.00
	0.75	5.04	5.64	0.60	0.72	0.166	0.186	1.54	0.83
	0.94	5.11	5.31	0.20	0.74	0.168	0.175	4.40	0.29
	0.98	5.17	5.24	0.07	0.74	0.170	0.172	11.46	0.11
	1.00	5.20	5.20	0.00	0.75	0.171	0.171	INF	0.00

Chapter 5

Simulating core-mantle boundary heat flux

Many variables affect heat flux across the core-mantle boundary (CMB). As explained in Chapter 4, thermal conductivity is dependent on the temperature and composition of a mineral. Heat is transferred between the convective core and the convecting mantle by conduction across the CMB. This leads to the formation of a thermal boundary layer (TBL) on both sides (Fig. 5.1), but as the mantle layer limits the cooling of the core, it is conduction at the base of the mantle that controls the heat flux from the core. On the other hand, it is the core that sets the temperature at the base of the mantle.

The temperature difference across the TBL is controlled by thermal conduction, and follows the form

$$\Delta T = T_{CMB} - T_{LM}, \tag{5.1}$$

where T_{CMB} is the core-mantle boundary temperature, and T_{LM} is the temperature of the lower mantle. We expect the temperature distribution in

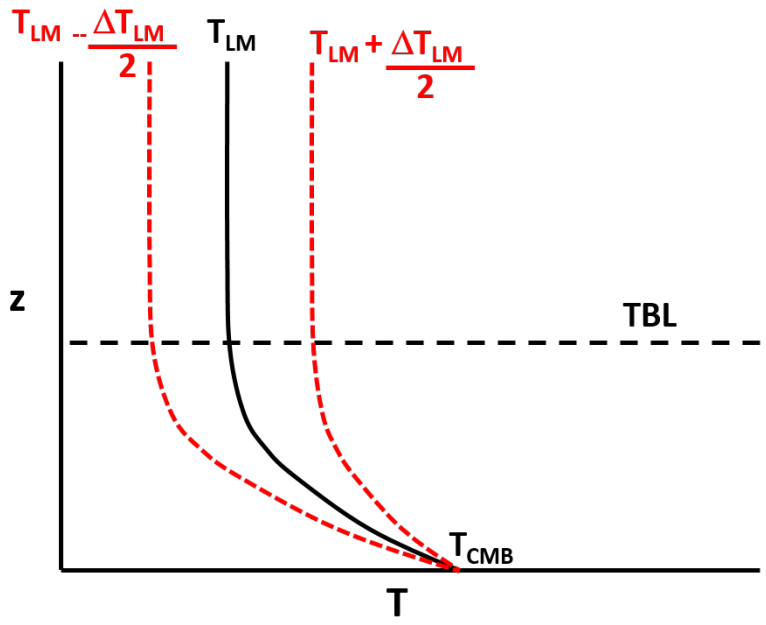

Figure 5.1: **(a)** An illustration of how temperature varies with depth (z) in LEMA, showing the transition to an isothermal CMB temperature. T_{LM} shows average lower mantle temperature, with ΔT_{LM} giving the range in lateral variation.

the TBL to follow an error function (*Wu et al.*, 2011) by

$$T_z = T_{CMB} - \Delta T erf \frac{z}{\delta(t)}, \tag{5.2}$$

where T_z is depth-dependent temperature, z is height above the CMB, and t is time.

In Chapter 4, I derived model fits to simulated data, which provided me with thermal conductivity as a continuous function of composition and temperature. This has a significant advantage over the derivation of discrete conductivity-temperature or conductivity-composition data points. In this chapter, I pair this data with a model built using the Leeds Earth Modelling Apparatus (LEMA) (*Walker et al.*, In prep). I am able to simulate variations in temperature and composition within the lower mantle, because the continuous functions from Chapter 4 allow calculation of thermal conductivity for any

combination of temperature-composition conditions. This means that within a mantle model, I am able to calculate conductivity changes due to minor variations in temperature or composition. This provides a more comprehensive view of the lower mantle than would be available using discrete data points, and limits the need for interpolation between discrete mantle states.

For example, the thickness of the thermal boundary layer determines the temperature gradient directly above the CMB (Fig. 5.1). A profile of conductivity for a continuous range of temperatures means that any changes to the TBL thickness can be appropriately simulated, i.e., thermal conductivity can be recalculated on the fly.

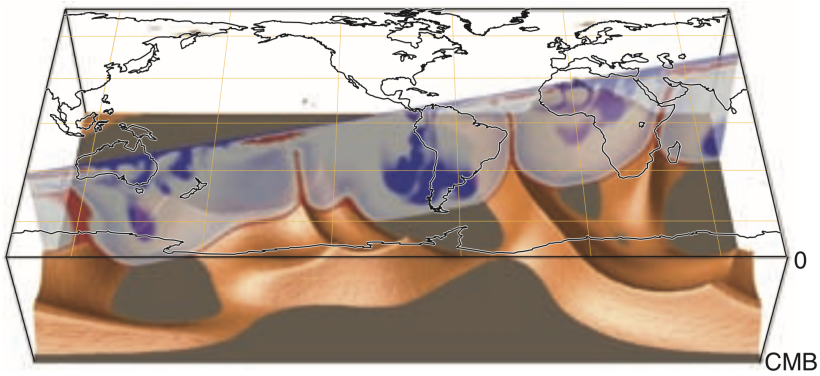

Figure 5.2: 3D thermochemical piles shown in gold, with a whole-mantle temperature cross section (red and blue denote hot and cold, respectively), based on geodynamical modelling. Reproduced with permission from *Garnero and McNamara* (2008).

In the lower mantle, there are complex three-dimensional features that render simple one-dimensional Earth models insufficient. For example, hot upwellings and cold subducted slabs (e.g., *Garnero and McNamara*, 2008, Fig. 5.2) would not be appropriately captured using only a one-dimensional model. There are two large low shear velocity provinces (LLSVPs; Section 1.1.2) that sit approximately on opposite sides of the core, and require 3D modelling to understand further.

A two-dimensional model, around the equator perhaps, would better describe the lower mantle, but the CMB is spherical and thus exceeds the complexity

provided by 2D simulations. A more sophisticated model with varying latitudes and longitudes is required to replicate changes in CMB structure.

As discussed in Section 1.2.1, *Tosi et al.* (2013) modelled two-dimensional lower mantle dynamics with depth-dependent conductivity, recreating lower mantle features observed using the seismic record. In this chapter, I take the first step towards a comprehensive three-dimensional mantle model. My primary aim is to determine the heat flux at the CMB, as a function of temperature and composition, using the thermal conductivity profiles calculated in Chapter 4.

Specifically, I do this by considering simplified representations of LLSVPs with different characteristics. LLSVPs were initially thought to be hot thermal upwellings in an isochemical mantle (*Thompson and Tackley*, 1998). They have more recently been considered as thermochemical features, which are driven by a denser mantle material (*McNamara and Zhong*, 2005; *Bull et al.*, 2009). However, this thermochemical explanation is not universally accepted, and a solely thermal explanation may be sufficient (*Davies et al.*, 2012; *Schuberth and Bunge*, 2009). In this chapter, I test various thermal and thermochemical scenarios, alongside a hypothetical purely chemical scenario. My aim is to inform on the range of parameters needed to produce a model that matches observations, and infer what such a model might tell us about how LLSVPs differ from the surrounding mantle.

5.1 Methodology

LEMA is a collection of software and tools designed to model the lower mantle and allow comparison with observations from a wide range of discipline. It models the mantle as spherical layers, such that properties can vary both laterally and radially. A flowchart of the steps undertaken in a typical LEMA calculation from this study can be found in Figure 5.3.

The magnitude of the heat flux changes with position on the CMB, as the

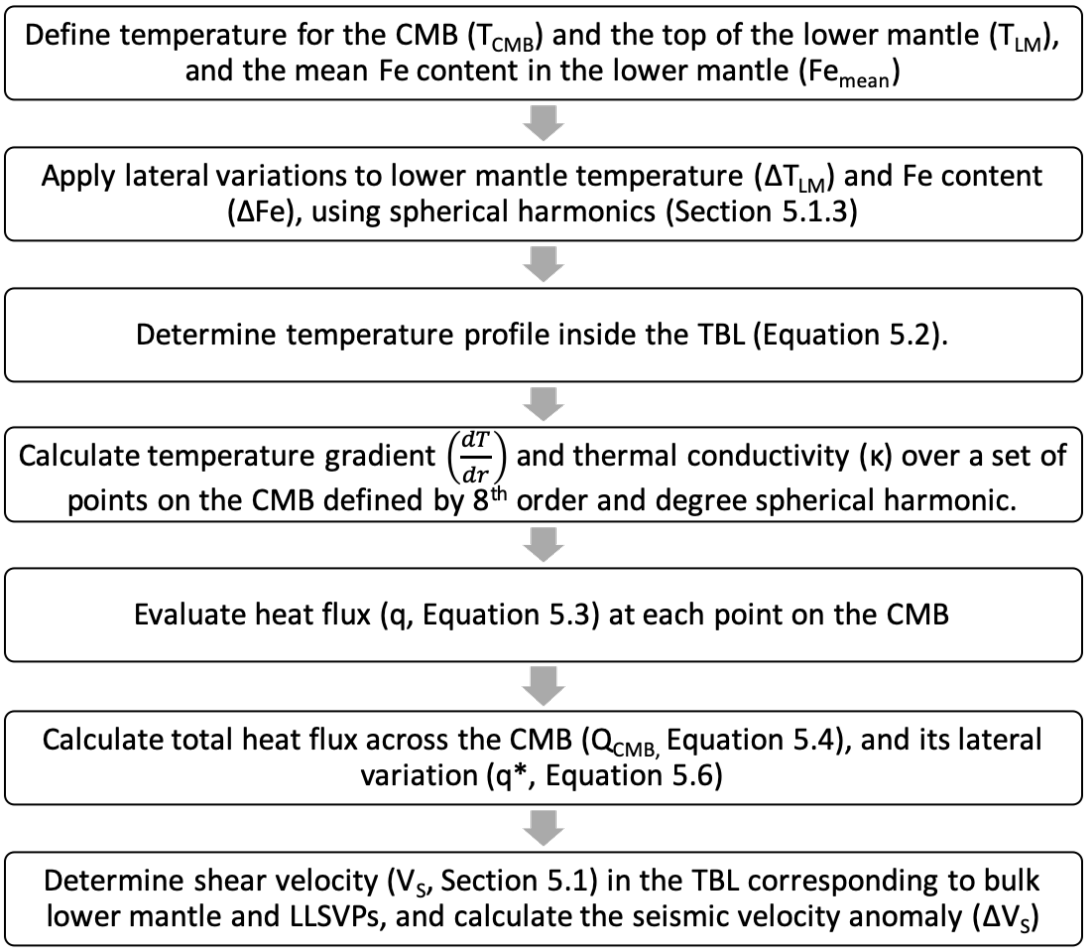

Figure 5.3: Flowchart showing the processes involved in a typical LEMA calculation, as performed in this study.

TBL characteristics change. Local heat flux (q_i) is given by solving Fourier's law at a point i by

$$q_i = -\kappa(T_{CMB}, C_i)\left(\frac{dT}{dr}\right)_i . \tag{5.3}$$

The heat flux is found directly from the radial temperature gradient ($\frac{dT}{dr}$) at point i on the CMB and the mantle thermal conductivity, which as discussed in Chapter 4, is a function of composition (C_i) and temperature (T_{CMB}).

Once the heat flux is calculated for over all points, the number of which is given by (n_p), I integrate over the CMB surface area ($4\pi r_{CMB}^2$) to find the total

heat flux across the CMB (Q_{CMB}) by

$$Q_{CMB} = \sum_{i=0}^{n_p} \frac{4\pi r_{CMB}^2}{n_p} q_i, \tag{5.4}$$

and to determine a measure of heat flux variability via lateral variations.

Lateral variations in heat flux can show how heat flux is sensitive to the lower mantle conditions, and what condition or combination of conditions has the greatest effect on heat flux. The calculated heat flux and its lateral variations can then be compared to observables (e.g., expected CMB heat flux from global heat budget estimates, and lateral variation in shear wave velocities as a proxy), dismissing scenarios which are unfeasible or unstable.

The lateral variations in temperature considered in this study cannot be explicitly compared with observations of temperature variations, because there is a trade off between the temperature and the thickness of the TBL. The temperature at the top of the TBL only serves to influence temperature gradient.

The shear wave velocity (V_S) is also calculated in LEMA by

$$V_S = \sqrt{\frac{G}{\rho}}\,, \tag{5.5}$$

where G is the shear modulus and ρ is mantle density. The shear wave velocity is calculated in a laterally and radially varying mantle given parameters for finite strain from the Mie-Grüneisen-Debye equations of state (*Stixrude and Lithgow-Bertelloni*, 2005). The laterally and radially varying shear modulus and mantle density of *Stixrude and Lithgow-Bertelloni* (2005) are used, as modified by *Zhang et al.* (2013). The velocity calculation is done using BurnMan, a lower mantle mineral physics toolkit from *Cottaar et al.* (2014), and the velocities are available on the same parameterisation as used for the temperature. It is important to note that thermodynamic equilibrium is not forced between

phases (for element partitioning) within LEMA. Instead phase boundaries in the $(MgFe)(SiAl)O_3$ and $(AlSi)O_3$ systems can be included and do account for the composition, but this feature (i.e., the post-perovskite phase transition) is turned off in this study. Therefore, the model used here considers bridgmanite only.

Using LEMA, I specify the temperatures at the CMB and at the top of the lower mantle (T_{LM}). The temperature gradient in the TBL is determined by specifying the thickness of the TBL and calculating the temperature difference between the bottom of the TBL (i.e., the CMB) and the top of the TBL (i.e., the lower mantle temperature).

In all models, I consider the CMB to be isothermal. This is a reasonable assumption because the convection within the core occurs on a much faster timescale than in the mantle (e.g., *Gibbons and Gubbins*, 2000). Although the temperature profile above the thermal boundary layer is constant with depth, there are lateral temperature variations, determined by ΔT_{LM} within LEMA. The parameter ΔT_{LM} controls the range in variations of mean temperature.

I consider the lower mantle in LEMA as bridgmanite with an average Fe content, that does not undergo the pressure-driven phase transition to post-perovskite. Variation in Fe is controlled by the ΔFe parameter, which gives the range of Fe concentration when compared with a mean value. This allows consideration of LLSVPs in the model, which are enriched in iron compared with the depleted surrounding lower mantle. Implementation of laterally-varying Fe content into the model will be explained in Section 5.2.2.

5.1.1 Modelling heat flux in the lower mantle

I use LEMA to explore how different assumptions about the origin of LLSVPs affect CMB heat flux. I present three methods by which LLSVPs can be considered in a model, and compared to the surrounding mantle material, in

order to calculate heat flux variations around the CMB. These methods consider

1. Temperature (i.e., a thermal model)

2. Composition (i.e., a chemical model)

3. Temperature *and* composition (i.e., a thermochemical model)

If no lateral variations in temperature exist in the lower mantle (i.e., a constant radial temperature), the heat flux is controlled solely by variations in composition, leading to a varying conductivity. If no lateral variations in composition exist, heat flux is controlled by lateral variations in temperature gradient.

Either scenario is, however, a vast oversimplification of conditions in the lower mantle. In reality, both temperature and compositional factors affect heat flux. Additionally, thermal conductivity has temperature-dependence and compositional-dependence, as shown in Chapter 4, thus further complicating modelling of the lower mantle.

One of the ways of modelling LLSVPs is to assume they are thermochemical piles (i.e., like Fig. 5.2), meaning that they are hotter and have higher Fe content than the surrounding lower mantle. Increasing temperature reduces conductivity, as does adding impurities up to the compositions expected in the lower mantle (∼15%; *Lee et al.* (2004)). By altering temperature and composition in tandem, I generate heat flux estimates for varied lower mantle conditions, and then compare these with observations.

5.1.2 Lateral variations in heat flux

While there are limitations to the use of this model in calculating CMB heat flux, inferences can be made on the relative lateral variations in heat flux. By creating an LLSVP model and comparing the heat flux to independent estimates, I infer how the distribution of heat flow is affected by temperature and composition

variations. I determine the lateral variation in heat flux ($q*$) as

$$q* = \frac{q_{\text{max}} - q_{\text{min}}}{q_{\text{mean}}} \ , \tag{5.6}$$

where q_{max} and q_{min} refer to the calculated extremes of heat flux (q_i, Equation 5.3). The maximum q value refers to the heat flux in the lower mantle, whilst the minimum q refers specifically to LLSVP heat flux. Higher values of $q*$ give lower heat fluxes through the LLSVPs, which are hotter, thus reducing thermal conductivity. By determining $q*$, I comment on the significance of thermal conductivity in the Earth's heat engine for a wide range of possible lower mantle conditions.

5.1.3 Using spherical harmonics to replicate CMB features

One way in which LEMA can describe the variation in temperature and composition in the mantle is to use spherical harmonics. I use this method to generate structures that resemble LLSVPs.

The centres of LLSVPs are approximately located on the equator, antipodal at 0° and 180° longitude (the African and Pacific LLSVPs respectively). A first order approximation for this geometry is the spherical harmonic Y_2^2, four quadrants of varying polarity around the polar axis (Fig. 5.4a). This is a good first approximation, but the circular projection is misleading, and the spherical harmonics extend to the poles, which would misrepresent LLSVPs. The approximation can be improved by stacking Y_2^0 on top of it (Fig. 5.4), enhancing regions on the equator and reducing everything towards the poles. When two spherical harmonics are stacked in this way, both values at every coordinate are averaged (mean) to produce a new stacked harmonic. The result is two circular

patterns, each located at opposite sides of the equator (Fig. 5.5).

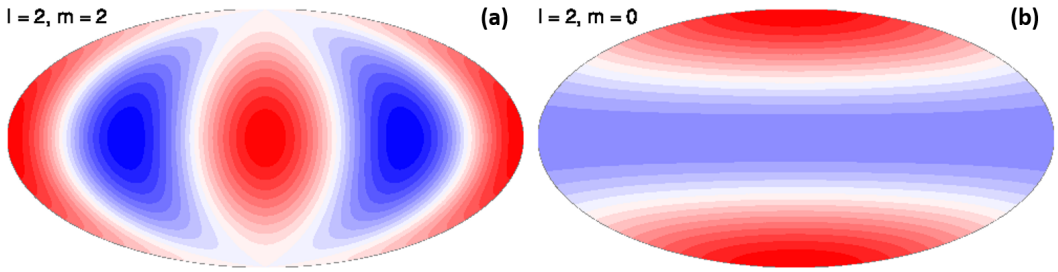

Figure 5.4: Spherical harmonic patterns corresponding to **(a)** Y_2^2 and **(b)** Y_2^0. Blue and red regions show positive and negative amplitudes, respectively.

For the Y_2^2 pattern, the areas of positive and negative amplitude regions are equal. For the Y_2^0-combined model (Fig. 5.5), the areas of positive and negative polarity are unequal. The temperature distribution in the model is weighted by the areas given by the stacked spherical harmonic. If the areas of positive and negative amplitude are equal, the ΔT_{LM} (i.e., the lateral variation in temperature) parameter is evenly distributed (i.e., $T_{max} = T_{LM} + \frac{1}{2}\Delta T_{LM}$ and $T_{min} = T_{LM} - \frac{1}{2}\Delta T_{LM}$; Fig. 5.1). However, the uneven distribution of areas with positive and negative amplitudes from the stacked harmonic means that ΔT_{LM} can also be distributed according to the areas of high or low amplitude (i.e., $T_{max} > T_{LM} + \frac{1}{2}\Delta T_{LM}$ and $T_{min} > T_{LM} - \frac{1}{2}\Delta T_{LM}$). Qualitatively, this leads to hotter hots, and warmer colds.

The parameters (T_{CMB}, T_{LM}, TBL thickness) and the lateral variation allow generation of a set of temperatures. A function f can be written as

$$f = \sum_{n=0}^{N_{MAX}} \sum_{l=1}^{L_{MAX}} \sum_{m=0}^{l} c_{nl}^m T_n(r) Y_l^m(\theta, \phi), \tag{5.7}$$

where $Y_l^m(\theta, \phi)$ are the real spherical harmonics of degree l and order m, $T_n(r)$ are the Chebyshev polynomials of the first kind, and the c_{nl}^m are coefficients. The radial temperature gradient is obtained by analytical differentiation of the Chebyshev polynomials (Fig. 5.6). This radial parameterisation can then

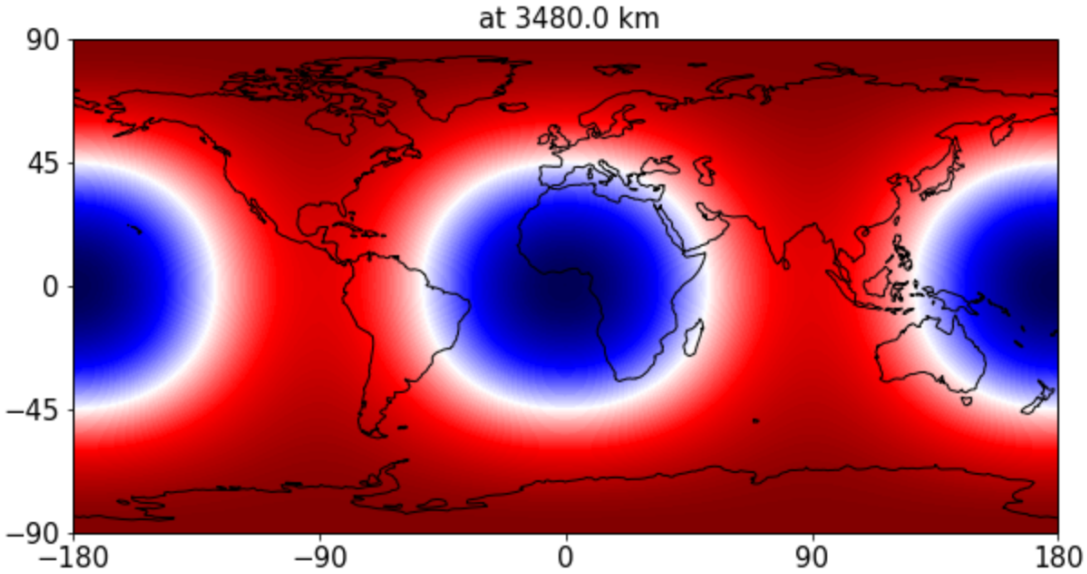

Figure 5.5: Combined spherical harmonics (the sum of Y_2^2 and Y_2^0), showing how LLSVPs are represented in LEMA for this study. Blue and red regions show positive and negative amplitudes, respectively.

be checked against an analytical solution for the heat flux (Q_{CMB}) in a one-dimensional model (i.e., no lateral variation in temperature or Fe content) calculated by determining the heat flow (q_{CMB}) by

$$q_{CMB} = 4\pi R_{CMB}^2 \; Q_{CMB} = \frac{8\sqrt{\pi}\kappa \Delta T R_{CMB}^2}{\delta} \; , \tag{5.8}$$

where R_{CMB} is CMB radius, ΔT is the temperature difference between the lower mantle and the CMB, and δ is TBL thickness (*Wu et al.*, 2011).

The effect of the lateral parameterisation is likely to be minor. The calculation is done on a HEALPix grid (*Gorski et al.*, 2005) and this gets finer as the spherical harmonic degree increases. Model resolution is therefore determined by the L_{MAX} and N_{MAX}, the maximum degrees of the spherical harmonic and the Chebyshev polynomial, respectively. Table 5.1 gives a full list of LEMA input parameters, with the symbols used and default values where necessary.

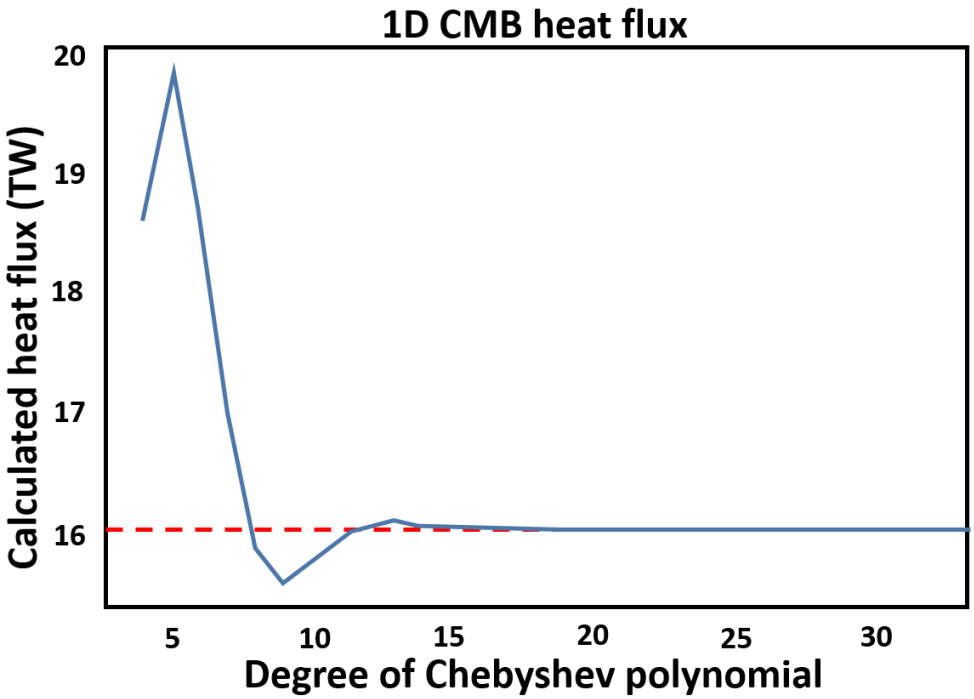

Figure 5.6: Convergence of calculated heat flux with degree of Chebyshev polynomial, where blue line indicates the heat flux calculated in LEMA, and the red dotted line represents the analytical solution using Equation 5.8.

5.2 Results

In the initial set-up of LEMA, I set the CMB temperature at 4000 K and the temperature at the top of the thermal boundary layer at 2600 K. The thickness of the TBL is set at 150 km. In each simulation, I obtain results for the core-mantle boundary heat flux (Q_{CMB}), lateral variation in heat flux (q^*), mean shear wave velocity (V_{S}) and the variation in mean shear wave velocity, i.e., the LLSVP seismic anomaly (ΔV_{S}).

Of these, I compare the Q_{CMB} and ΔV_{S} with observational data. The core-mantle boundary heat flux is compared with estimates from *Jaupart et al.* (2015) of 11 ± 6 TW. The mean shear wave velocity anomaly is compared with common estimates for the LLSVP, which are generally around 3% (e.g., *Lay and Garnero*, 2011; *Ni et al.*, 2005). The estimated velocity anomalies output from

Table 5.1: A list of LEMA input parameters with symbols and default values. Spherical harmonic degree refers to sampling of the model, not the representation of LLSVP temperature and compositional anomalies. Variations in the values cover the range used in this study.

Symbol	**Parameter**	**Value**
T_{CMB}	CMB temperature	4000 K
T_{LM}	Lower mantle temperature	2600 K
δ	TBL thickness	150 km
R_{CMB}	Model CMB radius	3480 km
R_{LM}	Model lower mantle radius	4480 km
L_{MAX}	Spherical harmonic degree and order	8
N_{MAX}	Chebyshev polynomial degree	22
κ	Thermal conductivity	varies as per model (Eq. 4.33)
ΔT_{LM}	Lateral temperature variation	varies from 0–2000 K
Fe_{mean}	Mean iron content	varies from 0–0.2 (decimal)
ΔFe	Lateral iron content variation	$2\times Fe_{mean}$, 0 for thermal model

LEMA are not the same as those obtained using seismic tomography, but rather they are values calculated from the maximum and minimum velocities at a height of 80 km above the CMB, roughly in the middle of the TBL. The velocity is a function of an arbitrary depth at which it was calculated, so absolute values from LEMA should not be compared with tomography at the same depths.

5.2.1 Thermal model

I first examine a purely thermal model. In this model, there is 0% iron, and thus no compositional variation. I increase the lateral variation in temperature at the top of the TBL, ΔT_{LM}, and observe the effect of this on the output parameters. Q_{CMB} remains within the estimates from *Jaupart et al.* (2015), increasing from 12.42 TW to 12.86 TW (see Table 5.2, and Figure 5.7) as ΔT_{LM} increases from 0 K up to 2000 K (i.e., $T_{\mathrm{LM}} = 2600 \pm 1000\ K$). The variation in Q_{CMB} is likely due to the uneven distribution of LLSVP area compared to the lower mantle, as discussed in Section 5.1.3. Because there is a larger relative area of lower mantle to LLSVP, there is a larger area in which the temperature gradient increases, meaning that as the increase in temperature gradient become more significant,

so Q_{CMB} increases. As shown in Figure 5.7, the q^* value increases linearly with increasing ΔT_{LM}. In order to obtain a seismic anomaly (ΔV_{S}) of 3%, lateral temperature variations on the order of ~1700 K are required (Fig. 5.8).

Table 5.2: **Thermal model** LEMA outputs (Q_{CMB}: heat flux across the CMB; q^*: variations in heat flux; V_{mean}: mean shear wave velocity; ΔV_{S}: shear wave velocity variation), based on simulations with iron content of Fe_{mean} and lateral variations in temperature of $\Delta \mathrm{T}_{\mathrm{LM}}$.

Fe_{mean}	$\Delta \mathrm{T}_{\mathrm{LM}}$(K)	Q_{CMB}(TW)	q*	V_{mean}(m/s)	ΔV_{S}(%)
10% Fe	0	11.17	0.00	7053.7	0.0
	200	11.17	0.19	7053.7	0.4
	500	11.19	0.46	7053.6	0.9
	1000	11.24	0.91	7053.3	1.8
	1500	11.34	1.35	7052.9	2.7
	1667	11.38	1.50	7052.8	3.0
	2000	11.47	1.78	7052.4	3.6
0% Fe	0	12.42	0.00	7231.8	0.0
	200	12.42	0.19	7231.8	0.3
	1714	12.73	1.56	7230.8	3.0
	2000	12.85	1.80	7230.5	3.5

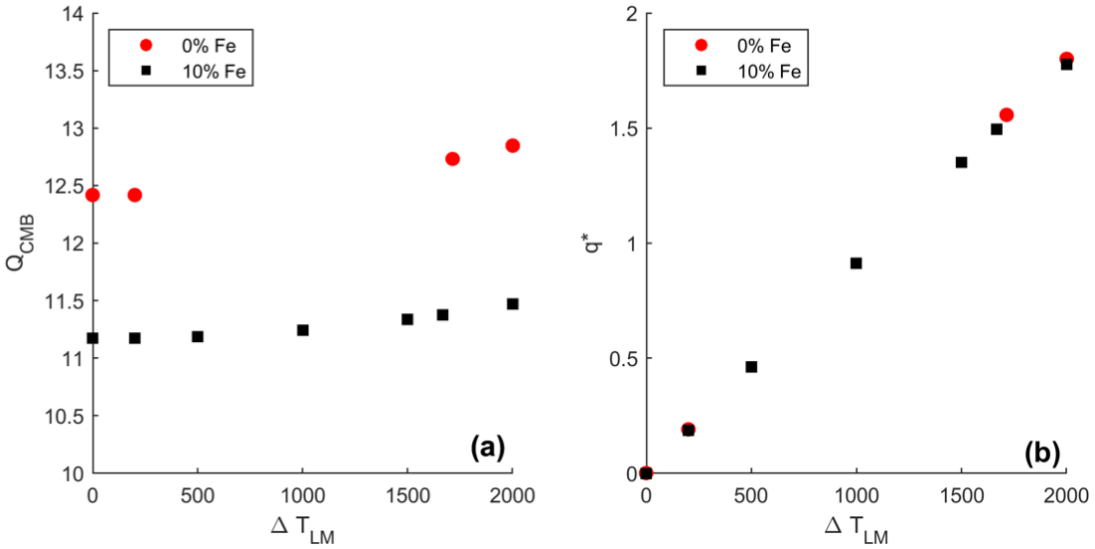

Figure 5.7: **a.** Variation in CMB heat flux (Q_{CMB}) and **b.** its lateral variation (q^*) as a function of the lateral variations in lower mantle temperature ($\Delta \mathrm{T}_{\mathrm{LM}}$) for simulations with constant 0% iron content (red circles) and constant 10% iron content (black squares).

Next, I examine a thermal model, given a constant Fe content of 10% across the lower mantle. Adding iron reduces conductivity, leading to the

observed reduction in Q_{CMB} compared with an 0% Fe case. However, adding a homogeneous distribution of iron does not significantly affect q^*, due to the lack of lateral variations. The Q_{CMB} and q^* values exhibit a similar pattern to the purely thermal model of increasing with increasing ΔT_{LM}. The increase in Q_{CMB} occurs due to the uneven area distribution from the spherical harmonics, and is likely a result of the method, rather than a physical representation. Increasing the iron content from 0% to 10% lowers the $\Delta \mathrm{T_{LM}}$ required to produce a 3% seismic anomaly, from 1714 K to 1667 K (Fig. 5.8).

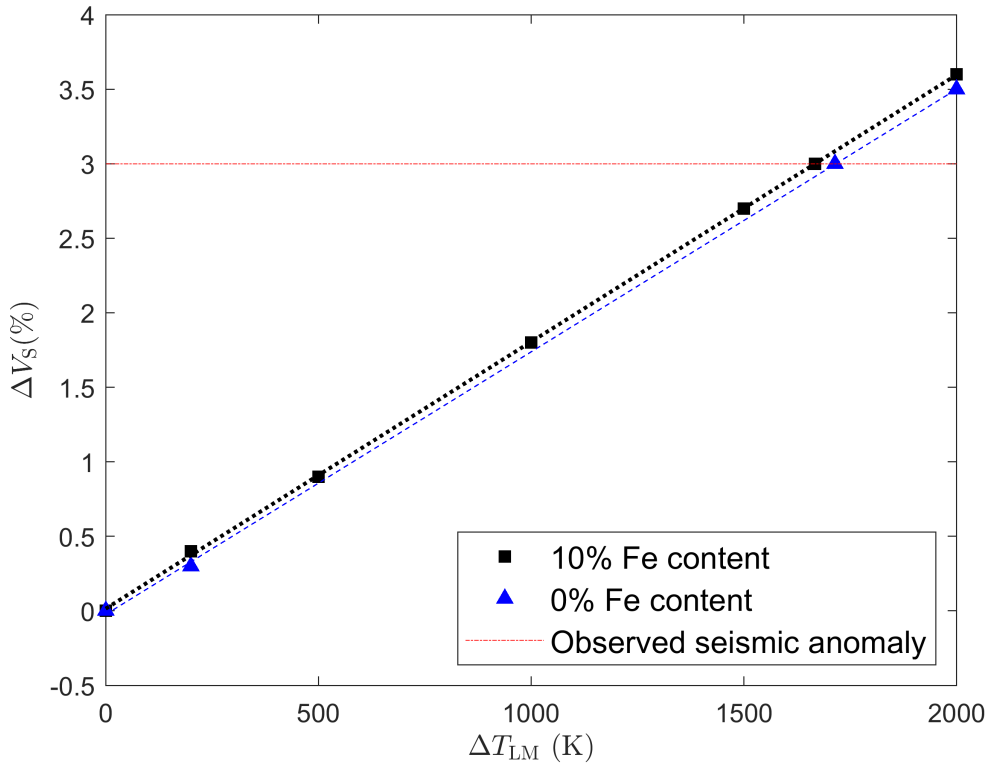

Figure 5.8: Variation in mean shear wave velocity (ΔV_{S}) as a function of the lateral variations in lower mantle temperature ($\Delta \mathrm{T_{LM}}$) for simulations with constant 10% iron content (black squares) and constant 0% iron content (blue triangles). Observed seismic anomaly from LLSVPs also indicated at 3% (red dotted line).

Table 5.3: **Chemical model** LEMA outputs (Q_{CMB}: heat flux across the CMB; q^*: variations in heat flux; V_{mean}: mean shear wave velocity; ΔV_{S}: shear wave velocity variation), based on simulations with iron content of Fe_{mean} and lateral variations in temperature ($\Delta \mathrm{T}_{\mathrm{LM}}$) of 0 K. The actual Fe contents of the LLSVP ($\mathrm{LLSVP}_{\mathrm{Fe\text{-}av}}$) and lower mantle ($\mathrm{LM}_{\mathrm{Fe\text{-}av}}$) are calculated using Equations 5.9 and 5.10, respectively.

$\Delta \mathrm{T}_{\mathrm{LM}}$	Fe_{mean}	ΔFe	$\mathrm{LLSVP}_{\mathrm{Fe\text{-}av}}$	$\mathrm{LM}_{\mathrm{Fe\text{-}av}}$	Q_{CMB}	q^*	V_{mean}	ΔV_{S}
0	0.02	0.04	3.43	0.94	12.13	0.05	7195.4	1.2
	0.05	0.1	8.58	2.35	11.76	0.12	7141.8	2.9
	0.1	0.2	17.17	4.71	11.25	0.20	7055.4	5.7
	0.2	0.4	34.33	9.41	10.51	0.32	6892.2	11.0

5.2.2 Chemical model

I then examine a purely chemical model, with no lateral temperature variations (Table 5.3). I assume a $\Delta \mathrm{T}_{\mathrm{LM}}$ value of 0 K and increase the average iron content (Fe_{mean}) up to 20%. In this model, the ΔFe is set to be twice the Fe_{mean} value. For example, if Fe_{mean} is 10% and the ΔFe value is 20%, this means the model should represent an iron content in the lower mantle of 0% and an iron content in the LLSVPs of 20%. Due to the uneven area distribution created by the spherical harmonics (see Section 5.1.3), there is a discrepancy between this idealised Fe distribution and the actual average mean LLSVP iron content ($\mathrm{LLSVP}_{\mathrm{Fe\text{-}av}}$) as

$$LLSVP_{\mathrm{Fe\text{-}av}} = \frac{Fe_{max} - Fe_{mean}}{2} + Fe_{mean}, \tag{5.9}$$

where Fe_{max} is the maxmium iron content in the LLSVP and Fe_{mean} is the mean iron content in the LLSVP. The actual average iron content in the lower mantle ($\mathrm{LM}_{\mathrm{Fe\text{-}av}}$) can be determined by

$$LM_{\mathrm{Fe\text{-}av}} = \frac{Fe_{mean} - Fe_{min}}{2}. \tag{5.10}$$

Table 5.3 and Figure 5.9 show that with a mean iron concentration of 5%,

the Q_{CMB} decreases, as expected with increasing iron content causing a decrease in conductivity. The lateral variation in heat flux (q^*) increases as the lateral variation in iron increases. The ΔV_{S} increases from 1.2% at 2% average iron to 11.0% at 20% iron (Fig. 5.10). From this, I suggest that lateral variations in composition have a far greater effect on ΔV_{S} than lateral temperature variations. For this model with 0 K lateral temperature variation, the expected seismic anomaly of 3% is reproduced with an average iron content of 5%, and therefore a ΔFe of 10%.

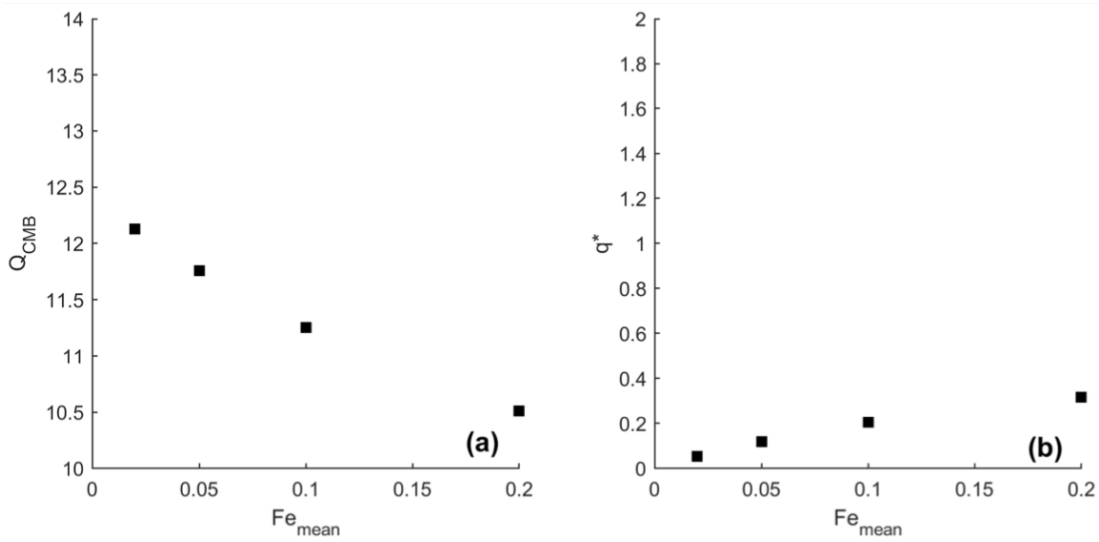

Figure 5.9: **a.** Variation in CMB heat flux (Q_{CMB}) and **b.** its lateral variation (q^*) as a function of lower mantle Fe content (Fe_{mean}) for simulations with constant lower mantle temperature.

5.2.3 Thermochemical model

Now that the independent thermal and chemical models have been evaluated, I can investigate the combined thermochemical model.

First, I create constant temperature scenarios, with varying average iron content (Fe_{mean}), and no lateral variations in iron content ($\Delta\mathrm{Fe} = 0$). I do this for temperature differences of 200 K, 500 K, and 1500 K, and iron contents across a range of 0–40% (Table 5.4). As illustrated in the purely thermal models

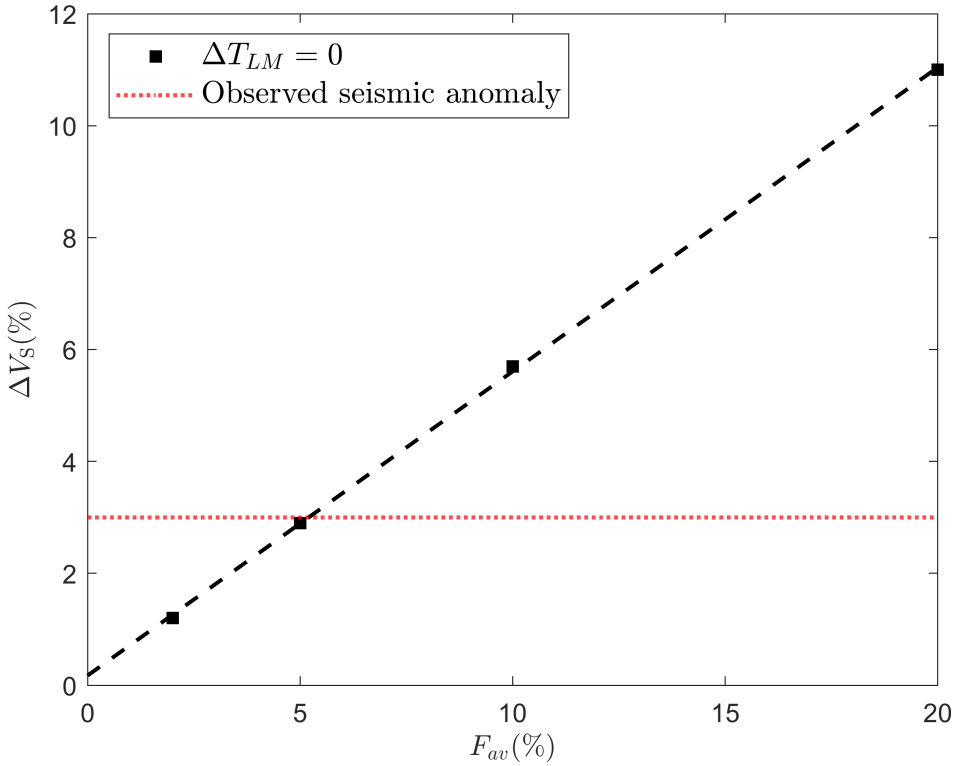

Figure 5.10: Mean shear wave velocity (ΔV_S) as a function of the lateral variations in lower mantle iron content (F_{av}) for simulations with constant lateral temperature variations of 0 K. Observed seismic anomaly from LLSVPs also indicated at 3% (red dotted line).

(Section 5.2.1), increasing the temperatures leads to an increase in q^*. Increasing the mean iron content at a fixed temperature has no impact on q^*, because $q^*$is dependent upon lateral variations. Lateral variations in temperature do not affect the mean shear wave velocity (V_{mean}), but increasing Fe_{mean} leads to a reduction in V_{mean}. In the same way that q^* remains constant with increasing Fe_{mean} but no lateral variations in Fe_{mean}, the values of ΔV_S behave in the same way and stay constant across the range of iron content.

The second suite of thermochemical models are designed to investigate the effect of simultaneous lateral variations in iron content (i.e., changing Fe_{mean}) and lateral variations in temperature (i.e., changing $\Delta \mathrm{T_{LM}}$). I do this for temperatures in the range of 100–1000 K and for iron contents up to 10% (Table 5.5).

Table 5.4: LEMA outputs for the **thermochemical model** with no lateral chemical variation. ΔT_{LM}: lateral variations in temperature; Fe_{mean} average iron content; ΔFe: lateral variation in iron content; Q_{CMB}: heat flux across the CMB; $LLSVP_{Fe\text{-}av}$: average iron content in the LLSVP regions; $LM_{Fe\text{-}av}$: average iron content in lower mantle; q^*: variations in heat flux; V_{mean}: mean shear wave velocity; ΔV_S: shear wave velocity variation.

ΔT_{LM}	Fe_{mean}	ΔFe	$LLSVP_{Fe\text{-}av}$	$LM_{Fe\text{-}av}$	Q_{CMB}	q^*	V_{mean}	ΔV_S
200	0	0	0	0	12.42	0.19	7231.8	0.3
200	0.1	0	0.1	0.1	11.17	0.19	7053.7	0.4
200	0.2	0	0.2	0.2	10.31	0.18	6885.1	0.4
200	0.4	0	0.4	0.4	9.21	0.18	6573.5	0.4
500	0	0	0	0	12.44	0.47	7231.7	0.9
500	0.1	0	0.1	0.1	11.19	0.46	7053.6	0.9
500	0.2	0	0.2	0.2	10.32	0.46	6885.0	0.9
500	0.4	0	0.4	0.4	9.21	0.45	6573.4	0.9
1500	0.1	0	0.1	0.1	11.34	1.35	7052.9	2.7
1500	0.4	0	0.4	0.4	9.29	1.32	6572.8	2.7

Table 5.5: LEMA outputs for the **thermochemical model** with added lateral chemical variation. ΔT_{LM}: lateral variations in temperature; Fe_{mean} average iron content; ΔFe: lateral variation in iron content; Q_{CMB}: heat flux across the CMB; $LLSVP_{Fe\text{-}av}$: average iron content in the LLSVP regions; $LM_{Fe\text{-}av}$: average iron content in lower mantle; q^*: variations in heat flux; V_{mean}: mean shear wave velocity; ΔV_S: shear wave velocity variation.

ΔT_{LM}	Fe_{mean}	ΔFe	$LLSVP_{Fe\text{-}av}$	$LM_{Fe\text{-}av}$	Q_{CMB}	q^*	V_{mean}	ΔV_S
100	0.04	0.08	6.87	1.88	11.89	0.19	7159.5	2.5
100	0.05	0.1	8.58	2.35	11.77	0.21	7141.8	3.1
200	0.01	0.02	1.72	0.47	12.28	0.22	7213.5	0.9
200	0.03	0.06	5.15	1.41	12.02	0.26	7177.4	2.1
200	0.04	0.08	6.87	1.88	11.90	0.28	7159.5	2.7
200	0.05	0.1	8.58	2.35	11.79	0.30	7141.8	3.3
200	0.1	0.2	17.17	4.71	11.30	0.38	7055.4	6.1
500	0.03	0.06	5.15	1.41	12.06	0.54	7177.3	2.7
500	0.04	0.08	6.87	1.88	11.95	0.56	7159.5	3.2
1000	0.01	0.02	1.72	0.47	12.40	0.95	7213.1	2.4
1000	0.02	0.04	3.43	0.94	12.28	0.97	7195.0	2.9

Table 5.6: LEMA outputs for the **thermochemical model**, where the seismic anomaly is 3%. ΔT_{LM}: lateral variations in temperature; Fe_{mean}: average iron content; ΔFe: lateral variation in iron content; Q_{CMB}: heat flux across the CMB; $LLSVP_{Fe\text{-}av}$: average iron content in the LLSVP regions; $LM_{Fe\text{-}av}$: average iron content in lower mantle; q^*: variations in heat flux; V_{mean}: mean shear wave velocity; ΔV_S: shear wave velocity variation.

ΔT_{LM}	Fe_{mean}	ΔFe	$LLSVP_{Fe\text{-}av}$	$LM_{Fe\text{-}av}$	Q_{CMB}	q^*	V_{mean}	ΔV_S
100	0.05	0.1	8.58	2.35	11.77	0.21	7141.8	3.1
200	0.045	0.09	7.725	2.115	11.84	0.29	7150.65	3
500	0.035	0.07	6.01	1.645	12.01	0.55	7168.4	2.95
1000	0.02	0.04	3.43	0.94	12.28	0.97	7195	2.9

As temperature increases, the amount of iron required to reproduce the observed shear wave seismic anomaly decreases. For example at ΔT_{LM} of 100 K, an iron content (Fe_{mean}) of 5% is required to reproduce the observed seismic anomaly of 3%, however when the ΔT_{LM} is increased to 1000 K, iron content of only 2% reproduces the seismic anomaly. It is clear here that there is a trade off between lateral temperature and compositional variations required to produce seismic anomalies.

I calculate the conditions required to produce seismic anomalies of 3% in the thermochemical model (Table 5.6). For simultaneously increasing temperature and decreasing iron, the value of q^* systematically increases. This is because the temperature-dependence of q^* dominates the trend, effectively eliminating the compositional-dependence. In the purely chemical model, increasing the iron content increases q^*. Here we observe the opposite: as iron content increases, the value of q^* decreases. This is not a function of the iron, but rather because the temperature-dependence of q^* dominates and the decrease in iron is insufficient to counteract the increase in temperature.

Finally, I investigate the effect of temperature-dependent conductivity on the model of heat flux considered in LEMA. To do this, I vary the temperature of the isothermal CMB by 500 K, with a final suite of temperatures of 3500 K, 4000 K, and 4500 K (Table 5.7 and Figure 5.11). I choose these values to show

the extreme possibilities of the CMB temperature both past and present (*Hilst et al.*, 2007; *Kawai and Tsuchiya*, 2009; *Andrault et al.*, 2016). In each case, I also vary the temperature of the lower mantle by 500 K. By keeping a constant ΔT between the lower mantle and LLSVPs, and maintaining a TBL thickness of 150 km, I keep the temperature gradient equal in all simulations. This means that I can isolate the effect of absolute temperature on heat flux by using the temperature-dependence of conductivity calculated in Chapter 4. Although not explored in this study, varying the TBL thickness would change the temperature gradient across the lower mantle, for example increasing thickness would decrease the temperature gradient. This would cause a decrease in Q_{CMB}, similar to the effect of changing T_{LM} (which changes the temperature difference between the lower mantle and the core-mantle boundary).

I find that as T_{CMB} and T_{LM} increase, the heat flux calculated in LEMA decreases. A decrease in Q_{CMB} is expected because as temperature increases, conductivity decreases, as previously shown in Figure 4.2. For example, for a lateral temperature range of 1000 K and a laterally varying iron content of 2%, Q_{CMB} ranges from 13.52 TW at 3500 K to 11.41 TW at 4500 K. q^* also decreases with increasing CMB temperature, indicative of the range of heat flux decreasing relative to the mean heat flux value. This means that there is a smaller overall range in heat flux. This can be attributed to the temperature-dependence of conductivity, because the effect of temperature on conductivity is smaller at higher temperatures, i.e., the difference between 5000 K and 4000 K is 0.23 $\mathrm{Wm^{-1}K^{-1}}$, whereas the conductivity difference between 4000 K and 3000 K is 0.39 $\mathrm{Wm^{-1}K^{-1}}$ (model fit for solid solution, Table 4.6).

Table 5.7: LEMA outputs for the **thermochemical model**, where the CMB temperature is varied from 3500 K to 4500 K. T_{CMB}: CMB temperature; T_{LM}: lower mantle temperature; TBL thickness; ΔT_{LM}: lateral variations in temperature; Fe_{mean}: average iron content; ΔFe: lateral variation in iron content; Q_{CMB}: heat flux across the CMB; $\mathrm{LLSVP}_{\mathrm{Fe\text{-}av}}$: average iron content in the LLSVP regions; $\mathrm{LM}_{\mathrm{Fe\text{-}av}}$: average iron content in lower mantle; q^*: variations in heat flux; V_{mean}: mean shear wave velocity; ΔV_{S}: shear wave velocity variation.

T_{CMB}	T_{LM}	$TBLthickness$	ΔT_{LM}	Fe_{mean}	ΔFe	$\mathrm{LLSVP}_{\mathrm{Fe\text{-}av}}$	$\mathrm{LM}_{\mathrm{Fe\text{-}av}}$	Q_{CMB}	q^*	V_{mean}	ΔV_{S}
3500	2100	150	100	0.05	0.1	8.58	2.35	12.83	0.24	7237.0	3.1
3500	2100	150	200	0.045	0.09	7.73	2.12	12.92	0.32	7245.8	3.0
3500	2100	150	500	0.035	0.07	6.01	1.65	13.14	0.57	7263.7	2.9
3500	2100	150	1000	0.02	0.04	3.43	0.94	13.52	1.00	7290.6	2.8
4000	2600	150	100	0.05	0.1	8.58	2.35	11.77	0.21	7141.8	3.1
4000	2600	150	200	0.045	0.09	7.73	2.12	11.84	0.29	7150.7	3.0
4000	2600	150	500	0.035	0.07	6.01	1.65	12.01	0.55	7168.4	3.0
4000	2600	150	1000	0.02	0.04	3.43	0.94	12.28	0.97	7195.0	2.9
4500	3100	150	100	0.05	0.1	8.58	2.35	11.01	0.19	7043.1	3.1
4500	3100	150	200	0.045	0.09	7.73	2.12	11.06	0.27	7051.9	3.0
4500	3100	150	500	0.035	0.07	6.01	1.65	11.19	0.53	7069.4	3.0
4500	3100	150	1000	0.02	0.04	3.43	0.94	11.41	0.94	7095.9	3.0

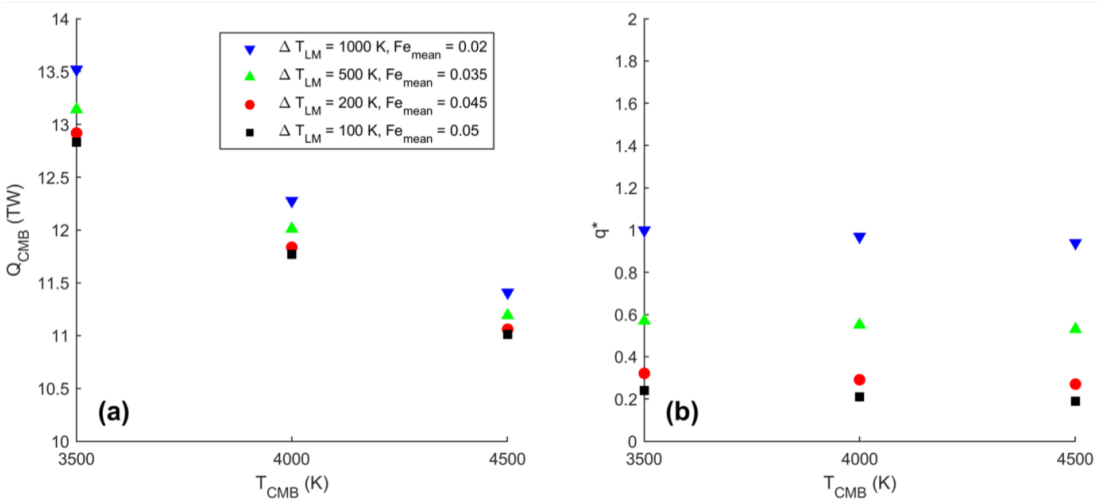

Figure 5.11: **a.** Variation in CMB heat flux (Q_{CMB}) and **b.** its lateral variation (q^*) as a function of CMB temperature for a variety of thermochemical LLSVP models.

5.2.4 Ultra-low velocity zones

While the LEMA model considered here is explicitly set up to consider the heat flux through LLSVPs, it can be used to inform on ultra-low velocity zone (ULVZ) properties. To do this, I consider different input parameters until the shear wave velocity anomaly of the ULVZs is reproduced. Heat flux, however, cannot be calculated in this way, because the model is effectively set up to have ULVZs with the area of LLSVPs, which is an overestimation of what is expected in reality.

ULVZs are observed around the edges of LLSVPs, as regions with a 25% reduction in shear velocity (*Rost et al.*, 2005, as discussed in Section 1.1.2). By trying to reproduce this 25% anomaly instead of the 3% expected from LLSVPs, I can inform on ULVZ temperature and composition. Considering a thermal model, a ΔT_{LM} of 14000 K is required, i.e., 2600±7000 K at the top of the TBL. The chemical model requires a ULVZ Fe-content of around 92%. A thermochemical model with ΔT_{LM} of 1000 K requires a ULVZ Fe-content of 78% to reproduce a shear velocity anomaly of 25%.

From these models, I show that thermal models are unable to represent ULVZs, because a feasible model requires a large Fe-content. While this utilisation of the LLSVP model is unable to quantify the heat flux through the ULVZ, the magnitude will be lower than the flux through the LLSVP. The increase in temperature variation and Fe-content required to reproduce the expected seismic velocity anomaly in the region reduces the heat flux. Thermal conductivity in an ULVZ is unlikely to significantly differ from the rest of the lower mantle, due to the saturation effects at high temperature and high Fe-content, unless the non-LLSVP lower mantle is Fe-free and on the order of 1000 K cooler than the ULVZs.

5.3 Discussion

In this chapter, I have explored the difference between using a thermal model, a chemical model, and a thermochemical model to replicate LLSVP-like features. There are, however, many oversimplifications in the methodologies presented here that must be considered before drawing conclusions from the results.

The thermal boundary layer is given a constant thickness in this model, which may not be accurate as temperature perturbations are likely to affect the TBL layer thickness, and therefore the temperature gradient. An additional simplification here is within the compositional model I use to represent the lower mantle. I only incorporate bridgmanite, without periclase and/or calcium perovskite (Fig. 1.2). In addition, I do not incorporate the phase transition from bridgmanite to post-perovskite, which is expected to occur in the lowermost mantle (*Oganov and Ono*, 2004). The model only considers Fe^{2+}, and does not consider Fe^{3+} or Al, as discussed in Chapter 4 and shown in Equation 4.1. Although the model simplifies composition, it allows a first investigative look at the effect of impurities on various lower mantle properties.

The spherical harmonics approach used here oversimplifies the shape and structure of the LLSVP features. The amplitude of the spherical harmonics is continuous from maximum to minimum, but changes in the lower mantle could be more abrupt. For example, LLSVPs have been suggested to have "sharp boundaries" (*Davies et al.*, 2015). As previously discussed, the stacking of two spherical harmonics leads to an uneven distribution of positive and negative amplitude. Although stacking two spherical harmonics gives a more appropriate LLSVP shape, a disadvantage is that there is less area representative of LLSVPs than if only one spherical harmonic pattern were used. While this is not a problem in reproducing LLSVP geometry, it affects the distribution of temperature and iron in the model. When an average variation is given to the model, this is not uniformly distributed across the model space, but rather is weighted by the uneven spherical harmonic areas, e.g., an increase in temperature is focussed in a smaller area and thus has a greater magnitude of temperature increase.

Despite the assumed simplifications incorporated into LEMA, the main advantage of the model is the qualitative comparisons that can be made for different hypothetical scenarios. Although the absolute values for Q_{CMB} and q^* depend upon the input values (e.g., T_{CMB}, $\Delta \mathrm{T}_{\mathrm{LM}}$), the way in which these outputs are affected by different parameters can be well explored using LEMA. I focus here on the effect of average lower mantle temperature (and its lateral variation) and average iron content (and its lateral variation) on the output values for Q_{CMB} and q^*.

In a thermal model, large lateral variations (range on the order of 1700 K) in thermal boundary layer temperature are required to produce seismic anomalies which match tomography. The results of the chemical model in this study show that only a 5% average iron content with a 10% range in lateral variation is required in order to produce a 3% seismic anomaly. This would mean a largely Fe-free lower mantle, and an Fe-enriched LLSVP.

Lateral temperature variations and lateral iron variations both tend to create shear wave anomalies between lower mantle material and the material in LLSVPs. In this chapter, I showed that even a small amount of iron (5%) reduces the temperature needed to produce a shear wave anomaly of 3% (Table 5.3) LLSVPs likely have a thermal component, due to their association with mantle plumes (e.g., *Garnero et al.*, 2007), but I show here that the addition of iron allows LLSVPs to exist at lower temperature variations than in an iron-free thermal model, and still match the observed changes in S-wave velocity.

By comparing the thermal and chemical models, I observe that variations in iron content affect the seismic anomaly (ΔV_S) more than they affect lateral variations in heat flux (q^*). Conversely, variations in temperature affect lateral variations in heat flux more than they affect the seismic anomaly. This exploration of parameter space exemplifies where LEMA can newly inform on the physical and chemical conditions that affect LLSVPs. The purely chemical model which produces a seismic anomaly of 3% has a q^* value of 0.12, whereas the thermal model producing the same seismic anomaly has a q^* of 1.56, thus demonstrating the sensitivity of q^* to lateral variations in temperature gradient. Considering a thermal model which gives a q^* of 0.19, the ΔV_S is 0.3%. For a chemical model with q^* of 0.2, the ΔV_S is 5.7%. This shows that for the same value of q^* , the chemical model has a much larger seismic anomaly than the thermal model, showing the sensitivity of ΔV_S to lateral variations in iron content. This is because seismic velocities are more sensitive to iron content than conductivity; this is supported by the data shown in Chapter 4 indicating that the effect of adding iron saturates with increasing temperature. An important conclusion here is that the relative importance of variations in temperature and iron content are different on ΔV_S and q^*, and this can only be observed using a combined thermochemical model.

I then used LEMA to investigate the different parameters that are able to

produce a seismic anomaly of 3%. Again, this exploits the advantages of LEMA, as the comparison between unique scenarios is more important than the absolute output values. By performing a suite of fully combined thermochemical scenarios (Table 5.6), I show that several scenarios reproduce the observed seismic anomaly, suggesting that there is a non-unique solution for the temperature/composition profile of the lower mantle. LEMA can be used with observations to investigate the full parameter range, for example, if ΔV_{S} and $\Delta \mathrm{T}_{\mathrm{LM}}$ are assumed as known values, LEMA can be used to explore the feasible mean iron content and its distribution in the lower mantle. Equally, if ΔV_{S} and Fe_{mean} are known, the full range of $\Delta \mathrm{T}_{\mathrm{LM}}$ can be explored. The results from the thermochemical models show that in order to get a shear velocity anomaly of 3% and a reasonable Q_{CMB} value, the values of $\Delta \mathrm{T}_{\mathrm{LM}}$ and LLSVP Fe content range from 100 K and 10% Fe, to 1000 K and 4% Fe (Table 5.6).

Lastly in this chapter, I showed the effect of temperature-dependent conductivity on heat flux and its lateral variation. Heat flux decreases with increasing CMB temperature, but q^* also decreases with increasing temperature. This shows the importance of understanding thermal conductivity as both a function of temperature and composition, because the decrease in q^* means the range of CMB heat flux decreases relative to its mean value as CMB temperature increases. This means that if the CMB temperature is higher, the variations in heat flux resulting from lateral variations in temperature are smaller, due to the saturation effect that is observed in the temperature-dependence of thermal conductivity of bridgmanite. From this, I can say that if the value of thermal conductivity was fully saturated and did not change with temperature, the CMB heat flux would be a constant value assuming a constant temperature gradient.

Calculating a heterogeneous heat flux at the CMB has been shown to have implications for the outer core (*Mound et al.*, 2019). Lateral variations in heat flux have been shown, through outer core dynamics simulation, to lead to regional

stratification in the top of the Earth's core. The presence of such a stratified layer would influence thermal and chemical features of the core, thus informing on core dynamics and evolution. Heat flux variation has also been shown to alter the pattern of the magnetic field (*Gubbins et al.*, 2007; *Aubert et al.*, 2008; *Sarson et al.*, 1997; *Olson and Christensen*, 2002). Ultimately the calculation of CMB heat flux depends on a thorough understanding of the lateral variations in conductivity in the lower mantle, and this relies on knowledge of the temperature and compositional-dependence of conductivity determined in this thesis.

5.4 Summary

1. Using LEMA, I show the sensitivity of lower mantle heat flux and shear wave velocity to a variety of LLSVP models, considering thermal, chemical, and thermochemical origin. Thermal models require large lateral variations in temperature (around 1700 K) to reproduce observations of seismic velocity anomaly, whereas a thermochemical model is more reasonable in terms temperature and composition variation (from 100 K and 10% Fe, to 1000 K and 4% Fe) between LLSVPs and the surrounding bulk lower mantle.

2. The heat flux computed here depends on the temperature- and composition-dependent thermal conductivity, as obtained from the model in Chapter 4. Heat flux across the CMB and its lateral variation are strongly dependent on temperature and its lateral variation. Shear velocity and the anomaly between lower mantle and LLSVP are much more sensitive to Fe-content. I suggest ULVZs are predominantly a chemical feature (78% Fe with 1000 K lateral temperature variation), in order to reconcile the large shear velocity anomaly.

Chapter 6

Summary and Conclusions

6.1 Summary

My overall aim in this thesis was to model thermal conductivity at the core-mantle boundary. In order to calculate the thermal conductivity, I use the Green-Kubo method and the direct method, and compare results to thoroughly investigate the effects of finite system size to validate my results. Here, I summarise the results of my thesis, by commenting on how I met each objective set out in Chapter 1.

Establish method of simulating bridgmanite at lower mantle conditions

The *Oganov et al.* (2000) potential describes the atomic interactions within bridgmanite. In Chapter 2, I incorporated the potential into LAMMPS and I calculated structural parameters (e.g., lattice parameters, unit cell volume, elastic constants, and the bulk and shear moduli). I compared my structural data from LAMMPS with other calculations using the same potential (which had been previously compared with experimental data) and found very good agreement (within 0.0001 Å). I also compared my unit cell parameters at lower mantle conditions with those of *Ammann et al.* (2014), and found percentage

differences consistently below 0.2%. I therefore concluded that bridgmanite was well replicated at the atomic scale using the *Oganov et al.* (2000) potential in LAMMPS.

Determine the accuracy of various atomic-scale modelling approaches.

I determined that for using the Green-Kubo method to calculate bridgmanite thermal conductivity, auto-correlation functions and their integrals were converged on the order of 10 ps. Using the Green-Kubo method, I calculated thermal conductivity values of 17.51 ± 0.27 $Wm^{-1}K^{-1}$ at 1000 K and 136 GPa, and 7.07 ± 0.06 $Wm^{-1}K^{-1}$ at 4000 K and 136 GPa. For both temperature conditions, Green-Kubo conductivity results are converged with respect to simulation size when a system is used with volume of 4×4×3 UC.

Next I used the direct method and I observed that the simulation time required to obtain a converged conductivity result increased with increasing cell length. I observed that a simulation length must be long enough to produce a conductivity result that is converged, but also that it must be short enough that it is not subjected to drift due to an error in the numerical integrator.

To obtain a conductivity result using the direct method, different cell lengths must be simulated, but for each length, I also considered various simulation cell cross-sectional areas. I found that large enough cross-sectional area is required, or the result is an unrealistic overestimate of conductivity. This is because narrow simulation cells do not reproduce the thermal resistivity of the bulk material. In direct method calculations, I also observe that simulation cells can be too short. When cells are too short, conductivity is also overestimated. To extrapolate the conductivity results to the bulk material, I ignore the cells that are too small or too short (<2×2 UC and <8 UC, respectively at 4000 K).

There is an additional effect of cross-sectional area size observed at long system lengths, which have not previously been described. The conductivity results

diverge away from the expected behaviour as cell length increases (e.g., > 24 UC at 4000 K). This is a re-emergence of the cross-sectional area effect, where thermal resistivity is not being replicated for high aspect ratio systems. This study is the first time that such finite-size effects have been identified for materials and conditions representative of the deep Earth.

I evaluated the thermal conductivity results of bridgmanite from *Ammann et al.* (2014) and showed how their results also display the same divergence as identified in my study. I also compared the observed finite-size effects to those observed by *Hu et al.* (2011). I was able to add to their analysis by identifying that cells which are too short produce unrealistic conductivity values. I showed how this has an effect for conductivity estimates in existing literature (e.g., *Stackhouse et al.*, 2015).

At 4000 K and 136 GPa, using the direct method with cross-sectional areas of 2×2 or larger, and cell lengths in the range of 8–24 UC reproduce the thermal conductivity results calculated using the Green-Kubo method ($\kappa = 6.39 \pm 0.11$ $\mathrm{Wm^{-1}K^{-1}}$). At 1000 K and 136 GPa, I show that cell lengths >48 UC produce conductivity results that agree with Green-Kubo ($\kappa = 16.81$ $\mathrm{Wm^{-1}K^{-1}}$).

In the process of calculating direct method results, I showed how the phonon mean free path can be calculated. I calculated mean free paths of 0.23 ± 0.03 nm at 4000 K and 2.13 nm at 1000 K. These mean free paths were on the same order of magnitude as those from *Stackhouse et al.* (2015), and corresponded well with the cell lengths that I ignored for being too short at both temperatures.

Investigate how impurities affect conductivity at lower mantle conditions

Iron can be added into the bridgmanite structure by increasing the mass of some magnesium atoms to that of iron in a heavy magnesium isotope model. It is also possible to determine the iron-oxygen potential parameters. In Chapter

4, I used both methods and showed that the heavy isotope model is a good approximation for a full potential model.

After calculating conductivity at temperatures in the range of 1000–5000 K, I observe saturation in conductivity with increasing temperature. Conductivity results for bridgmanite and $FeSiO_3$ are shown in Figure 6.1, with bridgmanite conductivity from previous studies for comparison. My results fall within the expected range at high pressures, with $FeSiO_3$ conductivities consistently lower for the same pressure/temperature conditions as expected.

I also calculated conductivity across the $MgSiO_3$ to $FeSiO_3$ solid solution. Initially increasing iron content in bridgmanite decreases conductivity until iron contributes the same mass to the system as magnesium, at which point conductivity saturates. Once iron contributes more mass, the conductivity increases again towards the value of the iron endmember. The effect of saturation with composition decreases with temperature, because conductivity is already saturated due to temperature effects, and thus cannot decrease further.

I combined the compositional model from *Padture and Klemens* (1997) and the temperature model of *Okuda et al.* (2017) to produce a more comprehensive numerical form, that allows conductivity to be calculated for any lower mantle temperature *and* iron content.

Finally in Chapter 4, using the mean free paths determined from the direct method, I scaled the conductivity values computed as a function of composition to corresponding mean free path values. This allowed me to distinguish the phonon-phonon scattering and the phonon-defect scattering, the latter a parameter that has not been explored in previous literature.

Incorporate the thermal conductivity results into a model of core-mantle boundary heat flux to investigate LLSVP conditions.

Using LEMA, I used the continuous forms from Chapter 4 and a simple

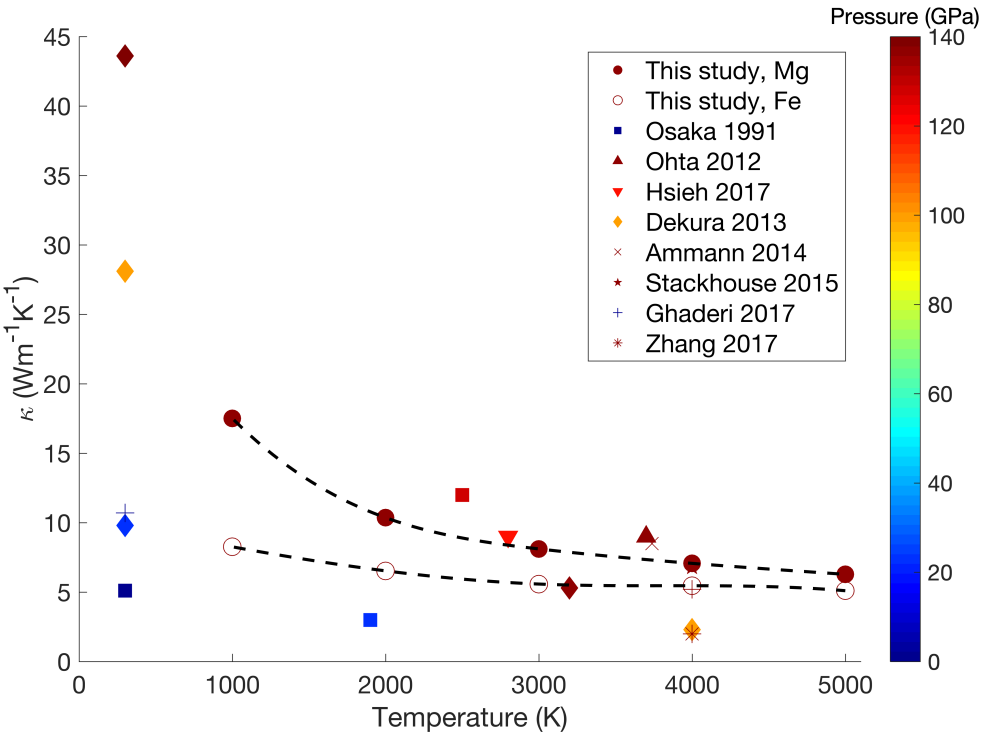

Figure 6.1: A comparison of bridgmanite thermal conductivity results across a range of lower mantle conditions from existing literature, including my results for bridgmanite and $FeSiO_3$ conductivity (see Table 4.6 alongside experiments and calculations as shown in Table 1.1.

spherical harmonic model, to represent LLSVPs and the lower mantle. I modelled LLSVPs with variations in iron content and temperature, where enrichments in iron content affects the thermal conductivity as described in Chapter 4, thus influencing the heat flux at the core-mantle boundary. I found that lateral variations in heat flux are more sensitive to thermal effects within LLSVPs, whereas seismic velocity anomalies are more sensitive to variations in iron content between LLSVPs and the lower mantle. I find that purely thermal LLSVPs require large lateral variations in temperature gradient to reproduce seismic anomalies (>1650 K), whereas in a thermochemical LLSVP model, the addition of iron reduces the lateral temperature variations required to reproduce observed seismic anomalies of 3%. I also used LEMA to show the effect of temperature-dependent conductivity, and I showed that as temperature increases,

conductivity decreases, and thus so does Q_{CMB}. However, the lateral variation in heat flux also decreases with temperature, which means that the range of Q_{CMB} decreases relative to its mean value. This is because of the saturation in conductivity at higher temperatures.

6.2 Future work

A major simplification in the work presented in this thesis is that I have only considered bridgmanite. If behaviour of the full lower mantle is to be considered, it would also be necessary to simulate ferropericlase, calcium perovskite, and the phase transition of bridgmanite to post-perovskite. Similar methods could be used as those presented here, but modifications would be required. For example, the potentials for ferropericlase and calcium perovskite would need to be validated. Once the potentials for different minerals have been validated, it would also be necessary to repeat the finite-size effect analysis for each different mineral before computing the conductivity. The consideration of more minerals would allow a more detailed analysis in LEMA, as the full composition of the lower mantle could be considered.

The thermal conductivity of ferropericlase has been estimated by *Stackhouse et al.* (2010) as 20 ± 5 $\mathrm{Wm^{-1}K^{-1}}$ at CMB conditions. *Trønnes* (2009) estimated that the lower mantle composition constitutes 20% ferropericlase (Fig. 1.2). By combining these estimates with my estimate of bridgmanite conductivity at CMB conditions (7.07 ± 0.06 $\mathrm{Wm^{-1}K^{-1}}$), I can calculate a compositionally-weighted average to estimate thermal conductivity considering both bridgmanite and ferropericlase. This provides a new estimate for thermal conductivity at CMB conditions of 9.6 ± 1.0 $\mathrm{Wm^{-1}K^{-1}}$. A higher conductivity estimate would cause an increase in Q_{CMB}.

Stackhouse et al. (2015) estimate the lattice thermal conductivity of calcium

silicate perovskite ($CaSiO_3$), using scaling from the Liebfreid-Schlmann relation (*Stackhouse et al.*, 2015, Supplementary material Eq. 5). They find $CaSiO_3$ has a very similar conductivity to bridgmanite, where the former is approximately 2% higher. Such an increase is negligible when considering compositionally-weighted averages, as $CaSiO_3$ only comprises around 10% of the lower mantle (*Trønnes*, 2009, Fig. 1.2). While $CaSiO_3$ does not significantly affect lattice thermal conductivity, it may affect other properties, and should be considered for a fully comprehensive lower mantle model.

Bridgmanite is expected to undergo a pressure-driven phase change to post-perovskite towards the CMB. *Ammann et al.* (2014) estimated that the thermal conductivity of post-perovskite is approximately 50% higher than that of bridgmanite, increasing from 8.5 $Wm^{-1}K^{-1}$ to 12 $Wm^{-1}K^{-1}$. Applying the same relationship to the conductivity calculated here, I estimate the conductivity of post-perovskite to be approximately 10.5 $Wm^{-1}K^{-1}$ at CMB conditions. The phase transition to post-perovskite does not occur in the hottest regions of the mantle (due to the double crossing effect, as discussed in Section 1.1.2). Therefore, the estimate of 10.5 $Wm^{-1}K^{-1}$ can be considered as a minimum conductivity value where post-perovskite is present, because the presence of post-perovskite suggests a cooler mantle. Therefore, including post-perovskite in the model would further increase the lateral variation in heat flux (q^*) between the colder mantle regions and the hotter LLSVPs.

I have also only considered Fe^{2+} as an impurity. Other impurities would also need to be simulated, such as Fe^{3+} and Al. I suggest that Fe^{3+} would have a similar effect, because the mass is the same as Fe^{2+} and I showed in Chapter 3 that mass is a significant determining factor. By the same logic, aluminium would likely have a lesser effect than iron because it is of similar mass to magnesium (Al mass of 27 compared to 24 for Mg). Additionally, iron undergoes a spin transition with depth through the lower mantle. This is not

considered in the models presented here, and I suggest that consideration of the spin transition would alter the properties of iron and lead to a decrease in conductivity (*Ohta et al.*, 2017). In this thesis, the finite-size effects were only determined for pressures of 136 GPa (i.e., core-mantle boundary pressure). It is possible that the finite-size effects vary with pressure and this would therefore need to be investigated further. In this study, I was primarily focussed on the heat flux at the core-mantle boundary, so assuming a constant pressure was a reasonable assumption. For a mantle model that examines the effect of thermal conductivity at various depths, a comprehensive review of finite size effects across pressure would be important.

The effect of anisotropic thermal conductivity was not included in this study, where all conductivity values correspond to the *a* crystallographic direction. *Ammann et al.* (2014) explored the anisotropy of thermal conductivity in bridgmanite along a lower mantle geotherm and found that the difference in conductivity between the *a* and *c* crystallographic directions was on the order of 1 $\mathrm{Wm^{-1}K^{-1}}$ at shallow depths within the lower mantle. *Ammann et al.* (2014) found that the difference in conductivity between crystallographic directions decreases toward the CMB, to the point of becoming negligible, possibly due to the effect of saturation with increasing temperature. Post-perovskite, however, was found to be strongly anisotropic, so if considering a more complex composition for the lower mantle, anisotropy would need to be included.

In addition, I have considered only the effects of lattice thermal conductivity. As discussed in Section 1.6, lattice conductivity must be summed with radiative conductivity to gain a full understanding of the thermal conductivity of the lower mantle. The radiative component is estimated to be between 0.54 $\mathrm{Wm^{-1}K^{-1}}$ (*Goncharov et al.*, 2008) and 10 $\mathrm{Wm^{-1}K^{-1}}$ (*Keppler et al.*, 2008). *Lobanov et al.* (2017) recently estimated radiative conductivity at 2.2 ± 0.4 $\mathrm{Wm^{-1}K^{-1}}$ for CMB conditions with 10% Fe. Compared to the lattice conductivity calculated here

(7.07 ± 0.06 $\mathrm{Wm^{-1}K^{-1}}$), this range of radiative conductivity estimates is on the same order of magnitude as the lattice conductivity, and would affect the resultant Q_{CMB}. If LLSVPs have significant Fe content, as suggested by the thermochemical models presented in Chapter 5, radiative thermal conductivity could be inhibited by impurities in the same way as lattice conductivity, leading to the radiative conductivity becoming negligible. However, heat flux associated with radiative thermal conductivity would still be high in the bulk lower mantle outside of Fe-enriched regions (i.e., outside of the LLSVPs), leading to an increase in q^*.

The contribution of the electronic component to thermal conductivity is very poorly constrained for CMB conditions. High Fe contents (up to the Fe-endmembers) are not often considered, as they are not expected to be present in the lower mantle. Some studies consider electrical conductivity, and its contribution to thermal conductivity, but only for ferropericlase. *Ohta et al.* (2017) measure electrical conductivity in a diamond anvil cell up to 140 GPa and 2730 K, finding that ferropericlase with 19% Fe remained an insulator and thus its electronic thermal conduction is negligible. *Holmström et al.* (2018) used density functional theory to calculate electronic conductivity, and found that contributions to the thermal conductivity were negligible for ferropericlase again with 19% Fe at conditions up to and beyond those expected at the CMB.

These two studies suggest the contribution of the electrical component to thermal conductivity is unimportant, but this is only considering conservative amounts of Fe in one mineral. If the electrical component from high Fe content regions were to contribute significantly to thermal conductivity, it would tend to increase heat flux through these regions. This would be within LLSVPs, following a thermochemical model as discussed in Section 5.2.3. This is interesting as adding Fe tends to reduce lattice thermal conductivity, but increasing the electrical component would reverse this reduction. This could serve to reduce q* by increasing conductivity and heat flux through regions of very high Fe

content (i.e., tending towards 100%), which is opposite to the effect observed in regions with low Fe content (>5%, where conductivity is markedly decreased, as in Figure 4.3). Therefore, the potential role of electron-electron interactions would need to be considered for a full understanding of thermal conductivity in iron-rich regions of the mantle.

Density Functional Theory, or *ab initio* methods, are a more accurate way of calculating the atomic interactions than the classical interatomic potential methods used in this study. Computations using DFT, however, are significantly more computationally expensive. As a consequence, smaller system sizes are typically used in DFT studies to obtain results on a feasible timescale. The results in this thesis show the importance of considering finite-size effects within the direct method when undertaking DFT calculations. For example, I have shown in this thesis that at 1000 K, using cell lengths of <48 UC gives thermal conductivity values that do not agree with the Green-Kubo calculations. This conclusion can be used in DFT studies to constrain the minimum appropriate cell length for given conditions.

Bibliography

Alfè, D., M. J. Gillan, and G. D. Price (2007), Temperature and composition of the Earth's core, *Contemp. Phys.*, *48*(2), 63–80, doi:10.1080/00107510701529653.

Allègre, C. J., J. P. Poirier, E. Humler, and W. Hofmann, A (1995), The chemical composition of the Earth, *Earth Planet. Sci. Lett.*, *134*, 515–526, doi:10.1093/astrogeo/atv065.

Allen, M. P., and D. J. Tildesley (2017), *Computer simulation of liquids*, Oxford University Press.

Ammann, M. W., A. M. Walker, S. Stackhouse, J. Wookey, A. M. Forte, J. P. Brodholt, and D. P. Dobson (2014), Variation of thermal conductivity and heat flux at the Earth's core mantle boundary, *Earth Planet. Sci. Lett.*, *390*, 175–185, doi:10.1016/j.epsl.2014.01.009.

Andrault, D., J. Monteux, M. Le Bars, and H. Samuel (2016), The deep Earth may not be cooling down, *Earth and Planetary Science Letters*, *443*, 195–203, doi:10.1016/j.epsl.2016.03.020.

Aubert, J., J. Aurnou, and J. Wicht (2008), The magnetic structure of convection-driven numerical dynamos, *Geophysical Journal International*, *172*(3), 945–956, doi:10.1111/j.1365-246X.2007.03693.x.

Balandin, A. A., S. Ghosh, W. Bao, I. Calizo, D. Teweldebrhan, F. Miao, and C. N. Lau (2008), Superior thermal conductivity of single-layer graphene., *Nano Lett.*, *8*(3), 902–907, doi:10.1021/nl0731872.

Bloxham, J. (2000), Sensitivity of the geomagnetic axial dipole to thermal core-mantle interactions, *Nature*, *405*, 63–65, doi:10.1038/35011045.

Bloxham, J., and D. Gubbins (1985), The secular variation of earth's magnetic field, *Nature*, *317*(6040), 777–781, doi:10.1038/317777a0.

Brodholt, J. P. (2000), Pressure-induced changes in the compression mechanism of aluminous perovskite in the Earth's mantle, *Nature*, *407*(6804), 620–622, doi:10.1038/35036565.

Brown, J. M. (1986), Interpretation of the D" zone at the base of the mantle: dependence on assumed values of thermal conductivity, *Geophys. Res. Lett.*, *13*(13), 1509–1512.

Bull, A. L., A. K. McNamara, and J. Ritsema (2009), Synthetic tomography of plume clusters and thermochemical piles, *Earth Planet. Sci. Lett.*, *278*(3-4), 152–162, doi:10.1016/j.epsl.2008.11.018.

Cai, Y., Y. Li, and J. Cheng (2016), Synthesis, crystal structure, and physical properties of the perovskite iridates, *Intech Open*.

Carrez, P., A. M. Goryaeva, and P. Cordier (2017), Prediction of mechanical twinning in magnesium silicate post-perovskite, *Scientific reports*, *7*(1), 17,640.

Chen, Y., A. Chernatynskiy, D. Brown, P. K. Schelling, E. Artacho, and S. R. Phillpot (2012), Critical assessment of classical potentials for MgSiO3 perovskite with application to thermal conductivity calculations, *Phys. Earth Planet. Inter.*, *210-211*, 75–89, doi:10.1016/j.pepi.2012.08.002.

Christensen, U., and P. Olson (2003), Secular variation in numerical geodynamo models with lateral variations of boundary heat flow, *Physics of the Earth and Planetary Interiors*, *138*, 39–54, doi:10.1016/S0031-9201(03)00064-5.

Cottaar, S., T. Heister, I. Rose, and C. Unterborn (2014), BurnMan: a lower mantle mineral physics toolkit, *Geochemistry, Geophysics, Geosystems*, *15*, 4692–4711, doi:10.1002/2014GC005563.

Dalton, D. A., W. Hsieh, G. T. Hohensee, D. G. Cahill, and A. F. Goncharov (2013), Effect of mass disorder on the lattice thermal conductivity of MgO periclase under pressure., *Sci. Rep.*, *3*, 2400–2405, doi:10.1038/srep02400.

Davies, D., S. Goes, and H. Lau (2015), Thermally dominated deep mantle LLSVPs: a review, in *The Earth's Heterogeneous Mantle: A Geophysical, Geodynamical, and Geochemical Perspective*, pp. 441–477, Springer, Cham., doi:10.1007/978-3-319-15627-9.

Davies, D. R., S. Goes, J. H. Davies, B. S. Schuberth, H. P. Bunge, and J. Ritsema (2012), Reconciling dynamic and seismic models of Earth's lower mantle: The dominant role of thermal heterogeneity, *Earth Planet. Sci. Lett.*, *353-354*, 253–269, doi:10.1016/j.epsl.2012.08.016.

Davies, G. F. (2001), Dynamic earth: Plates, plumes and mantle convection.

de Koker, N. (2009), Thermal conductivity of MgO periclase from equilibrium first principles molecular dynamics, *Phys. Rev. Lett.*, *103*(12), 1–4, doi:10.1103/PhysRevLett.103.125902.

Dekura, H., T. Tsuchiya, and J. Tsuchiya (2013), Ab initio lattice thermal conductivity of MgSiO3 perovskite as found in Earth's lower mantle, *Phys. Rev. Lett.*, *110*, 1–5, doi:10.1103/PhysRevLett.110.025904.

Di Paola, C., and J. P. Brodholt (2016), Modeling the melting of multicomponent systems: the case of mgsio 3 perovskite under lower mantle conditions, *Scientific reports*, *6*, 29,830.

Dobson, D. P., and J. P. Brodholt (2005), Subducted banded iron formations as a source of ultralow-velocity zones at the core-mantle boundary, *Nature*, *434*, 371–374, doi:10.1038/nature03385.1.

Dong, H., Z. Fan, L. Shi, A. Harju, and T. Ala-Nissila (2018), Equivalence of the equilibrium and the nonequilibrium molecular dynamics methods for thermal conductivity calculations: From bulk to nanowire silicon, *Phys. Rev. B*, *97*(9), 1–8, doi:10.1103/PhysRevB.97.094305.

Dove, M. (1993), *Introduction to lattice dynamics*, Cambridge University Press.

Dubuffet, F., and D. A. Yuen (2000), A thick pipe-like heat-transfer mechanism in the mantle: Nonlinear coupling between 3D convection and variable thermal conductivity, *Geophys. Res. Lett.*, *27*, 17–20.

Ewald, P. P. (1921), Die berechnung optischer und elektrostatischer gitterpotentiale, *Annalen der physik*, *369*(3), 253–287.

Fowler, C. (1990), *The Solid Earth: An Introduction to Global Geophysics*, Cambridge University Press, doi:10.1142/9781860949210_0011.

Gale, J. D. (1997), GULP: A computer program for the symmetry-adapted simulation of solids, *J. Chem. Soc.*, *93*, 629–637.

Garnero, E. J., and A. K. McNamara (2008), Structure and dynamics of Earth's lower mantle, *Science (80-.).*, *320*, 626–629.

Garnero, E. J., T. Lay, and A. Mcnamara (2007), Implications of lower-mantle structural heterogeneity for the Existence and Nature of Whole-Mantle Plumes, *Geol. Soc. Am. Spec. Pap.*, *430*(05), 79–101, doi:10.1130/2007.2430(05).For.

Gavezzotti, A. (1994), Are crystal structures predictable?, *Accounts of chemical research*, *27*(10), 309–314.

Ghaderi, N., J. Xian, D. Zhang, H. Zhang, R. M. Wentzcovitch, and T. Sun (2017), Lattice Thermal Conductivity of MgSiO3 Perovskite from First Principles, *Sci. Rep.*, *7*(1), 1–9, doi:10.1038/s41598-017-05523-6.

Gibbons, S. J., and D. Gubbins (2000), Convection in the Earth's core driven by lateral variations in the core-mantle boundary heat flux, *Geophys. J. Int.*, *142*(2), 631–642, doi:10.1046/j.1365-246X.2000.00192.x.

Goncharov, A. F., B. D. Haugen, V. V. Struzhkin, P. Beck, and S. D. Jacobsen (2008), Radiative conductivity in the Earth's lower mantle., *Nature*, *456*, 231–234, doi:10.1038/nature07412.

Goncharov, A. F., P. Beck, V. V. Struzhkin, B. D. Haugen, and S. D. Jacobsen (2009), Thermal conductivity of lower-mantle minerals, *Phys. Earth Planet. Inter.*, *174*, 24–32, doi:10.1016/j.pepi.2008.07.033.

Gorski, K. M., E. Hivon, A. J. Banday, B. D. Wandelt, F. K. Hansen, M. Reinecke, and M. Bartelmann (2005), Healpix: a framework for high-resolution discretization and fast analysis of data distributed on the sphere, *The Astrophysical Journal*, *622*(2), 759.

Goryaeva, A. M., P. Carrez, and P. Cordier (2017), Modeling defects and plasticity in mgsio 3 post-perovskite: Part 3screw and edge [001] dislocations, *Physics and Chemistry of Minerals*, *44*(7), 521–533.

Green, M. S. (1954), Markoff random processes and the statistical mechanics of time-dependent phenomena. II. Irreversible processes in fluids, *J. Chem. Phys.*, *22*(3), 398–413, doi:10.1063/1.1740082.

Gubbins, D. (2003), *Thermal Core-Mantle Interactions: Theory and Observations*, 163-179 pp., American Geophysical Union (AGU), doi:10.1029/GD031p0163.

Gubbins, D., and J. Bloxham (1985), Geomagnetic field analysisIII. Magnetic fields on the coremantle boundary, *Geophysical Journal International*, *80*(3), 695–713, doi:10.1111/j.1365-246X.1985.tb05119.x.

Gubbins, D., D. Alf, G. Masters, G. D. Price, and M. J. Gillan (2003), Can the Earths dynamo run on heat alone?, *Geophysical Journal International*, *155*(2), 609–622, doi:10.1046/j.1365-246X.2003.02064.x.

Gubbins, D., A. P. Willis, and B. Sreenivasan (2007), Correlation of Earth's magnetic field with lower mantle thermal and seismic structure, *Phys. Earth Planet. Inter.*, *162*, 256–260, doi:10.1016/j.pepi.2007.04.014.

Haigis, V., M. Salanne, and S. Jahn (2012), Thermal conductivity of MgO, MgSiO3 perovskite and post-perovskite in the Earth's deep mantle, *Earth Planet. Sci. Lett.*, *355-356*, 102–108, doi:10.1016/j.epsl.2012.09.002.

Hilst, R. D. V. D., M. V. D. Hoop, P. Wang, L. Tenorio, and B. C. America (2007), Seismostratigraphy and Thermal Structure of Earth's Core-Mantle Boundary Region, *Science*, *315*(March), 1813–1817.

Hofmeister, A. M. (1999), Mantle values of thermal conductivity and the geotherm from phonon lifetimes, *Science (80-.).*, *283*, 1699–1706, doi:10.1126/science.283.5408.1699.

Holmström, E., L. Stixrude, R. Scipioni, and A. Foster (2018), Electronic conductivity of solid and liquid (mg, fe)o computed from first principles, *Earth and Planetary Science Letters*, *490*, 11 – 19, doi:https://doi.org/10.1016/j.epsl.2018.03.009.

Hoover, W. G. (1985), Canonical dynamics: Equilibrium phase-space distributions, *Phys. Rev. A*, *31*, 1695–1697, doi:10.1103/PhysRevA.31.1695.

Horai, K. (1971), Thermal conductivity of rock-forming minerals, *Earth Planet. Sci. Lett.*, *76*(5), 359–368, doi:10.1016/0012-821X(69)90186-1.

Howell, P. C. (2012), Comparison of molecular dynamics methods and interatomic potentials for calculating the thermal conductivity of silicon., *J. Chem. Phys.*, *137*(22), 224,111, doi:10.1063/1.4767516.

Hsieh, W.-P., F. Deschamps, T. Okuchi, and J.-F. Lin (2017), Reduced lattice thermal conductivity of fe-bearing bridgmanite in earth's deep mantle, *Journal of Geophysical Research: Solid Earth*, *122*(7), 4900–4917.

Hu, L., W. J. Evans, and P. Keblinski (2011), One-dimensional phonon effects in direct molecular dynamics method for thermal conductivity determination, *J. Appl. Phys.*, *110*(11), 113,511, doi:10.1063/1.3660234.

Hu, Y., B. Kiefer, C. R. Bina, D. Zhang, and P. K. Dera (2017), High-pressure γ-camgsi2o6: Does penta-coordinated silicon exist in the earth's mantle?, *Geophysical Research Letters*, *44*(22).

Jackson, A., A. R. T. Jonkers, and M. R. Walker (2000), Four centuries of geomagnetic secular variation from historical records, *Philosophical Transactions: Mathematical, Physical and Engineering Sciences*, *358*(1768), 957–990.

Jaupart, C., S. Labrosse, F. Lucazeau, and J. C. Mareschal (2015), *Temperatures, Heat, and Energy in the Mantle of the Earth*, vol. 7, 223–270 pp., Elsevier B.V., doi:10.1016/B978-0-444-53802-4.00126-3.

Kawai, K., and T. Tsuchiya (2009), Temperature profile in the lowermost mantle from seismological and mineral physics joint modeling, *Proceedings of the National Academy of Sciences*, *106*(52), 22,119–22,123, doi:10.1073/pnas.0905920106.

Keppler, H., L. S. Dubrovinsky, O. Narygina, and I. Kantor (2008), Optical absorption and radiative thermal conductivity of silicate perovskite to 125 gigapascals, *Science (80-.).*, *322*, 1529–1532.

Kittel, C. (2005), *Introduction to Solid State Physics*, John Wiley Sons, doi:10.1021/ja01569a094.

Klemens, P. G. (1951), The thermal conductivity of dielectric solids at low temperatures, *Proc. R. Soc. London. Ser. A. Math. Phys. Sci.*, *208*(1092), 108–133.

Klemens, P. G. (1955), The Scattering of Low-Frequency Lattice Waves by Static Imperfections, *Proceedings of the Physical Society A*, *68*, 1113–1128, doi:10.1088/0370-1298/68/12/303.

Klemens, P. G. (1959), Deviation from Matthiessen's rule and lattice thermal conductivity of alloys, *Aust. J. Phys.*, *12*(2), 199–202, doi:10.1071/ph590199.

Klemens, P. G. (1960), Thermal resistance due to point defects at high temperatures, *Phys. Rev.*, *119*(2), 507–509, doi:10.1103/PhysRev.119.507.

Knittle, E., and R. Jeanloz (1989), Melting curve of (mg, fe) sio3 perovskite to 96 gpa: Evidence for a structural transition in lower mantle melts, *Geophysical Research Letters*, *16*(5), 421–424.

Knittle, E., R. Jeanloz, E. K. N. I. Itle, and R. Jeanloz (1991), Earth's Core-Mantle Boundary : Results of Experiments at High Pressures and Temperatures, *Science*, *251*(5000), 1438–1443.

Korte, M., F. Donadini, and C. G. Constable (2009), Geomagnetic field for 03 ka: 2. a new series of time-varying global models, *Geochemistry, Geophysics, Geosystems*, *10*(6), doi:10.1029/2008GC002297.

Kraych, A., P. Carrez, and P. Cordier (2016), On dislocation glide in mgsio3 bridgmanite at high-pressure and high-temperature, *Earth and Planetary Science Letters*, *452*, 60–68.

Kubo, R. (1957), Statistical-mechanical theory of irreversible processes. I., *J. Phys. Soc. Japan*, *12*(6), 570–586, doi:10.1143/JPSJ.12.570.

Kubo, R. (1966), The fluctuation-dissipation theorem, *Rep. Prog. Phys.*, *29*(1), 255.

Lay, T., and E. J. Garnero (2011), Deep Mantle Seismic Modeling and Imaging, *Annu. Rev. Earth Planet. Sci.*, *39*(1), 91–123, doi:10.1146/annurev-earth-040610-133354.

Lay, T., J. Hernlund, E. J. Garnero, and M. S. Thorne (2006), A post-perovskite lens and D" heat flux beneath the central Pacific., *Science (80-.).*, *314*, 1272–1276, doi:10.1126/science.1133280.

Lay, T., J. Hernlund, and B. A. Buffett (2008), Coremantle boundary heat flow, *Nat. Geosci.*, *1*, 25–32, doi:10.1038/ngeo.2007.44.

Leach, A. R. (2001), *Molecular modelling: principles and applications*, Pearson Education.

Lee, D., P. C. Stevens, S. Q. Zeng, and A. J. Hunt (1995), Thermal characterization of carbon-opacified silica aerogels, *J. Non. Cryst. Solids*, *186*, 285–290, doi:10.1016/0022-3093(95)00055-0.

Lee, K. K. M., B. O'Neill, W. R. Panero, S. H. Shim, L. R. Benedetti, and R. Jeanloz (2004), Equations of state of the high-pressure phases of a natural peridotite and implications for the Earth's lower mantle, *Earth Planet. Sci. Lett.*, *223*, 381–393, doi:10.1016/j.epsl.2004.04.033.

Leibfried, G., and E. Schlömann (1954), *Wärmeleitung in Elektrisch Isolierenden Kristallen, von Günther Leibfried und Ernst Schlömann*, Vandenhoeck und Ruprecht.

Lobanov, S. S., N. Holtgrewe, J. Lin, and A. F. Goncharov (2017), Radiative conductivity and abundance of post-perovskite in the lowermost mantle, *Earth Planet. Sci. Lett.*, *479*, 43–49, doi:10.1016/j.epsl.2017.09.016.

Manthilake, G. M., N. de Koker, D. J. Frost, and C. A. McCammon (2011), Lattice thermal conductivity of lower mantle minerals and heat flux from Earth's core., *Proc. Natl. Acad. Sci. U. S. A.*, *108*, 1–4, doi:10.1073/pnas.1110594108.

Mao, W. L., G. Shen, V. B. Prakapenka, Y. Meng, A. J. Campbell, D. L. Heinz, J. Shu, R. J. Hemley, and H. Mao (2004), Ferromagnesian post-perovskite silicates in the D" layer of the Earth, *Proc. Natl. Acad. Sci.*, *101*(45), 15,867–15,869, doi:10.1073/pnas.0407135101.

McCammon, C. A. (1997), Perovskite as a possible sink for ferric iron in the lower mantle, *Nature*, *387*(6634), 694–696, doi:10.1038/42685.

McNamara, A. K., and S. Zhong (2005), Thermochemical structures beneath Africa and the Pacific Ocean, *Nature*, *437*(7062), 1136–1139, doi:10.1038/nature04066.

Mound, J., C. Davies, S. Rost, and J. Aurnou (2019), Regional stratification at the top of Earth's core due to coremantle boundary heat flux variations, *Nat. Geosci.*, doi:10.1038/s41561-019-0381-z.

Muir, J. M. R., and J. P. Brodholt (2016), Ferrous iron partitioning in the lower mantle, *Phys. Earth Planet. Inter.*, *257*, 12–17, doi:10.1016/j.pepi.2016.05.008.

Müller-Plathe, F. (1997), A simple nonequilibrium molecular dynamics method for calculating the thermal conductivity, *J. Chem. Phys.*, *106*(14), 6082, doi:10.1063/1.473271.

Murakami, M., K. Hirose, K. Kawamura, N. Sata, and Y. Ohishi (2004), Post-perovskite phase transition in MgSiO_3, *Science (80-.).*, *304*, 855–858.

Naliboff, J. B., and L. H. Kellogg (2006), Dynamic effects of a step-wise increase in thermal conductivity and viscosity in the lowermost mantle, *Geophys. Res. Lett.*, *33*, 1–4, doi:10.1029/2006GL025717.

Ni, S., D. V. Helmberger, and J. Tromp (2005), Three-dimensional structure of the African superplume from waveform modelling, *Geophys. J. Int.*, *161*(2), 283–294, doi:10.1111/j.1365-246X.2005.02508.x.

Nieto-Draghi, C., and J. B. Avalos (2013), Non-equilibrium momentum exchange algorithm for molecular dynamics simulation of heat flow in multicomponent systems, *Mol. Phys.*, *101*(14), 2303–2307, doi:10.1080/0026897031000154338.

Nosé, S. (1984), A unified formulation of the constant temperature molecular dynamics methods, *The Journal of Chemical Physics*, *81*(1), 511–519, doi:10.1063/1.447334.

Oganov, A. R., and S. Ono (2004), Theoretical and experimental evidence for a post-perovskite phase of MgSiO3 in Earth's D" layer, *Nature*, *430*, 445–448.

Oganov, A. R., J. P. Brodholt, and D. G. Price (2000), Comparative study of quasiharmonic lattice dynamics, molecular dynamics and Debye model applied to MgSiO3 perovskite, *Phys. Earth Planet. Inter.*, *122*, 277–288.

Ohta, K., T. Yagi, N. Taketoshi, K. Hirose, T. Komabayashi, T. Baba, Y. Ohishi, and J. Hernlund (2012), Lattice thermal conductivity of MgSiO3 perovskite and post-perovskite at the coremantle boundary, *Earth Planet. Sci. Lett.*, *349-350*, 109–115, doi:10.1016/j.epsl.2012.06.043.

Ohta, K., T. Yagi, and K. Hirose (2014), Thermal diffusivities of MgSiO3 and Al-bearing MgSiO3 perovskites, *Am. Mineral.*, *99*, 94–97.

Ohta, K., T. Yagi, K. Hirose, and Y. Ohishi (2017), Thermal conductivity of ferropericlase in the Earth's lower mantle, *Earth Planet. Sci. Lett.*, *465*, 29–37, doi:10.1016/j.epsl.2017.02.030.

Okuda, Y., K. Ohta, T. Yagi, R. Sinmyo, T. Wakamatsu, K. Hirose, and Y. Ohishi (2017), The effect of iron and aluminum incorporation on lattice thermal conductivity of bridgmanite at the Earth's lower mantle, *Earth Planet. Sci. Lett.*, *474*(September), 25–31, doi:10.1016/j.epsl.2017.06.022.

Olson, P., and U. R. Christensen (2002), The time-averaged magnetic field in numerical dynamos with non-uniform boundary heat flow, *Geophysical Journal International*, *151*(3), 809–823, doi:10.1046/j.1365-246X.2002.01818.x.

Osako, M., and E. Ito (1991), Thermal diffusivity of MgSiO3 perovskite, *Geophys. Res. Lett.*, *18*, 239–242.

Padture, N. P., and P. G. Klemens (1997), Low thermal conductivity in garnets, *J. Am. Ceram. Soc.*, *80*(4), 1018–1020, doi:10.1111/j.1151-2916.1997.tb02937.x.

Parise, J. B., and Y. Wang (1990), Crystal structure and thermal expansion of (Mg,Fe)SiO_3 perovskite, *Geophysical Research Letters*, (12), 2089–2092.

Plimpton, S. (1995), Fast parallel algorithms for shortrange molecular dynamics, *J. Comput. Phys.*, *117*, 1–19, doi:10.1006/jcph.1995.1039.

Pozzo, M., C. Davies, D. Gubbins, and D. Alfè (2012), Thermal and electrical conductivity of iron at Earth's core conditions, *Nature*, *485*(7398), 355–358, doi:10.1038/nature11031.

Robie, R. A., B. S. Hemingway, and H. Takei (1982), Heat capacities and entropies of Mg2SiO4, Mn2SiO4, and Co2SiO4between 5 and 380 K., *Am. Mineral.*, *67*(5-6), 470–482.

Ross, N. L., and R. M. Hazen (1989), Single crystal x-ray diffraction study of mgsio 3 perovskite from 77 to 400 k, *Physics and Chemistry of Minerals*, *16*(5), 415–420.

Rost, S., E. J. Garnero, Q. Williams, and M. Manga (2005), Seismological constraints on a possible plume root at the core-mantle boundary, *Nature*, *435*(7042), 666–669, doi:10.1038/nature03620.

Sarson, G. R., C. A. Jones, K. Zhang, and G. Schubert (1997), Magnetoconvection dynamos and the magnetic fields of Io and Ganymede, *Science*, *276*(5315), 1106–1108, doi:10.1126/science.276.5315.1106.

Schelling, P. K., S. R. Phillpot, and P. Keblinski (2002), Comparison of atomic-level simulation methods for computing thermal conductivity, *Phys. Rev. B*, *65*(14), 144,306, doi:10.1103/PhysRevB.65.144306.

Schubert, G., D. L. Turcotte, and P. Olson (2001), *Mantle convection in the Earth and planets*, Cambridge University Press.

Schuberth, B. S., and H. P. Bunge (2009), Tomographic filtering of high-resolution mantle circulation models: Can seismic heterogeneity be explained by temperature alone?, *Geochemistry, Geophys. Geosystems*, *10*(5), doi:10.1029/2009GC002401.

Sellan, D. P., E. S. Landry, J. E. Turney, A. J. H. McGaughey, and C. H. Amon (2010), Size effects in molecular dynamics thermal conductivity predictions, *Phys. Rev. B*, *81*, 1–10, doi:10.1103/PhysRevB.81.214305.

Snyder, G. J., and E. S. Toberer (2008), Complex thermoelectric materials, *Nat. Mater.*, *7*(2), 105–114, doi:10.1038/nmat2090.

Stackhouse, S., and L. Stixrude (2010), Theoretical methods for calculating the lattice thermal conductivity of minerals, *Rev. Mineral. Geochemistry*, *71*, 253–269, doi:10.2138/rmg.2010.71.12.

Stackhouse, S., L. Stixrude, and B. B. Karki (2010), Thermal Conductivity of Periclase (MgO) from First Principles, *Phys. Rev. Lett.*, *104*(20), 208,501, doi:10.1103/PhysRevLett.104.208501.

Stackhouse, S., L. Stixrude, and B. B. Karki (2015), First-principles calculations of the lattice thermal conductivity of the lower mantle, *Earth Planet. Sci. Lett.*, *427*, 11–17, doi:10.1016/j.epsl.2015.06.050.

Stixrude, L., and C. Lithgow-Bertelloni (2005), Thermodynamics of mantle minerals - I. Physical properties, *Geophysical Journal International*, *162*(2), 610–632, doi:10.1111/j.1365-246X.2005.02642.x.

Su, C., Y. Liu, W. Song, D. Fan, Z. Wang, and H. Tang (2018), Thermodynamic properties of San Carlos olivine at high temperature and high pressure, *Acta Geochim.*, *37*(2), 171–179, doi:10.1007/s11631-018-0261-z.

Tadano, T., Y. Gohda, and S. Tsuneyuki (2014), Anharmonic force constants extracted from first-principles molecular dynamics: applications to heat transfer simulations., *J. Phys. Condens. Matter*, *26*, 1–12, doi:10.1088/0953-8984/26/22/225402.

Tang, X., and J. Dong (2009), Pressure dependence of harmonic and anharmonic lattice dynamics in MgO: A first-principles calculation and implications for lattice thermal conductivity, *Phys. Earth Planet. Inter.*, *174*, 33–38, doi:10.1016/j.pepi.2008.10.003.

Tang, X., and J. Dong (2010), Lattice thermal conductivity of MgO at conditions of Earth's interior, *Proc. Natl. Acad. Sci.*, *107*(10), 4539–4543, doi:10.1073/pnas.0907194107.

Tang, X., M. C. Ntam, J. Dong, E. S. G. Rainey, and A. Kavner (2014), The thermal conductivity of the Earth's lower mantle, *Geophys. Res. Lett.*, *41*, 2746–2752, doi:10.1002/2014GL059385.Received.

Thompson, P. F., and P. J. Tackley (1998), Generation of mega-plumes from the core-mantle boundary in a compressible mantle with temperature-dependent viscosity, *Geophys. Res. Lett.*, *25*(11), 1999–2002, doi:10.1029/98gl01228.

Tosi, N., D. A. Yuen, N. de Koker, and R. M. Wentzcovitch (2013), Mantle dynamics with pressure- and temperature-dependent thermal expansivity and conductivity, *Phys. Earth Planet. Inter.*, *217*, 48–58, doi:10.1016/j.pepi.2013.02.004.

Touloukian, Y. S., R. W. Powel, C. Y. Ho, and P. G. Klemens (1970), Thermal conductivity of nonmetallic solids, *Thermophys. Prop. Matter*, *2*, 183–193.

Trønnes, R. G. (2009), Structure, mineralogy and dynamics of the lowermost mantle, *Mineral. Petrol.*, *99*, 243–261, doi:10.1007/s00710-009-0068-z.

Turney, J. E., E. S. Landry, A. J. McGaughey, and C. H. Amon (2009), Predicting phonon properties and thermal conductivity from anharmonic lattice dynamics calculations and molecular dynamics simulations, *Phys. Rev. B - Condens. Matter Mater. Phys.*, *79*(6), 1–12, doi:10.1103/PhysRevB.79.064301.

Verlet, L. (1967), Computer "experiments" on classical fluids. i. thermodynamical properties of lennard-jones molecules, *Physical review*, *159*(1), 98.

Walker, A., C. Davies, A. Nowacki, and P. Koelemeijer (In prep), Lema: a framework to integrate models of mantle mineralogy, seismology and dynamics.

Wang, Z., and X. Ruan (2017), On the domain size effect of thermal conductivities from equilibrium and nonequilibrium molecular dynamics simulations, *J. Appl. Phys.*, *121*(044301), 1–8, doi:10.1063/1.4974884.

Wu, B., P. Driscoll, and P. Olson (2011), A statistical boundary layer model for the mantle D" region, *Journal of Geophysical Research: Solid Earth*, *116*(12), 1–17, doi:10.1029/2011JB008511.

Xu, Y., T. J. Shankland, S. Linhardt, D. C. Rubie, F. Langenhorst, and K. Klasinski (2004), Thermal diffusivity and conductivity of olivine, wadsleyite and ringwoodite to 20 GPa and 1373 K, *Phys. Earth Planet. Inter.*, *143*(1-2), 321–336, doi:10.1016/j.pepi.2004.03.005.

Yeganeh-Haeri, A. (1994), Synthesis and re-investigation of the elastic properties of single-crystal magnesium silicate perovskite, *Physics of the Earth and Planetary Interiors*, *87*(1-2), 111–121.

Zhang, D.-B., P. B. Allen, T. Sun, and R. M. Wentzcovitch (2017), Thermal conductivity from phonon quasiparticles with subminimal mean free path in the $mgsio_3$ perovskite, *Phys. Rev. B*, *96*, 100,302, doi:10.1103/PhysRevB.96.100302.

Zhang, S., S. Cottaar, T. Liu, S. Stackhouse, and B. Militzer (2016), High-pressure, temperature elasticity of Fe- and Al-bearing MgSiO3: Implications for the Earth's lower mantle, *Earth and Planetary Science Letters*, *434*, 264–273, doi:10.1016/j.epsl.2015.11.030.

Zhang, Z., L. Stixrude, and J. Brodholt (2013), Elastic properties of MgSiO3-perovskite under lower mantle conditions and the composition of the deep Earth, *Earth and Planetary Science Letters*, *379*, 1–12, doi:10.1016/j.epsl.2013.07.034.